Engineered Metal Oxide and Chalcogenide Nanomaterials for Sensitized Solar Cells and Solar Photoelectrochemical Water Splitting

Thesis Submitted to AcSIR for the Award of
the Degree of

DOCTOR OF PHILOSOPHY
In Chemical Sciences

By

Reshma Bhosale

Registration Number: 10CC13J26011

Under the Guidance of

Dr. Satishchandra Ogale
Research Guide

Dr. Sarika Bhattacharyya
Research Co-guide

CSIR- National Chemical Laboratory, Pune-411008, India.

July 2015

Certificate

This is to certify that the work incorporated in this Ph.D. thesis entitled **"Engineered Metal Oxide and Chalcogenide Nanomaterials for Sensitized Solar Cells and Solar Photoelectrochemical Water splitting."** submitted by **Ms. Reshma Bhosale** to Academy of Scientific and Innovative Research (AcSIR) in fulfillment of the requirements for the award of the Degree of **Doctor of Philosophy in Chemical Sciences,** embodies original research work under my supervision. I further certify that this work has not been submitted to any other University or Institution in part or full for the award of any degree or diploma. Research material obtained from other sources has been duly acknowledged in the thesis. Any text, illustration, table etc., used in the thesis from other sources, have been duly cited and acknowledged.

Research Student
Reshma Bhosale

Research Guide
Dr. Satishchandra B. Ogale
Chief Scientist

Declaration

I hereby declare that the thesis entitled **"Engineered Metal Oxide and Chalcogenide Nanomaterials for Sensitized Solar Cells and Solar Photoelectrochemical Water splitting."** submitted for the degree **Doctor of Philosophy** in Chemical Sciences to the Academy of Scientific & Innovative Research (AcSIR), has been carried out by me at the Physical and Materials Chemistry Division of National Chemical Laboratory, Pune under the guidance of **Dr. Satishchandra B. Ogale**. Such material as has been obtained by other sources has been duly acknowledged in this thesis. The work is original and has not been submitted in part or full by me for any other degree or diploma to other University.

Date: July 2015

National Chemical Laboratory,

Pune - 411008

Reshma Bhosale

(Research Student)

Dedicated to

My Beloved Child…

Acknowledgements

I take this opportunity to express my sincere gratitude to all those people who have made this thesis possible and because of whom my Ph.D. experience has been one which I will cherish forever.

I express my foremost and deepest gratitude to my supervisor, Dr. Satishchandra Ogale who gave me opportunity to work under his guidance. I have been amazingly fortunate to have such an advisor who gave me the freedom to explore on my own and at the same time the guidance to recover when my steps faltered. His keen observation, analysis and positive approach towards the research has blessed me with valuable experiences. His innovative and out of the box ideas have helped to set my publications a new and high standard. He became my ideal who taught me as to how to fight and overcome in difficult situations. His energetic, eager to learn tendency and optimistic nature towards the work and life has not only inspired me to strive to be a good researcher but also to become a good human being.

I sincerely thank the Council of Scientific and Industrial Research (CSIR) and the Department of Information Technology (DIT) for their funding support. I would also like to express my gratitude to Dr. Sourav Pal and Dr. Sivaram (former Directors, CSIR-NCL), Dr. Anil Kumar (Head of the Physical and Materials Chemistry Division) for providing the infrastructure and advanced facilities for research and giving me an opportunity to work at CSIR NCL.

I am indebted to my Doctoral Advisory Committee (DAC) members Dr. Satyanaryana Chilukuri (chairman), Dr. Prakash Wadgaonkar and Dr. Jayaraj Nithyanandhan for regular assessment of my Ph.D. work including courses. Their judicious suggestions have helped me to improve my research work.

I am also thankful to all collaborators, especially Prof. S .H. Han and Dr. Wanjoo Lee, Hanyang University, Seoul, Prof. Bèatrice Hannoyer, Université de Rouen, France, Dr. Deodatta Phase, UGC-DAE Consortium for Scientific Research, Indore, Dr. Dushyant Kothari, University of Mumbai for their timely experimental help.

I admire and appreciate Student Academic Office (SAO) staff initially led by Dr. C. G. Suresh and now by Dr. C. J. Gadgil for their kind help and co-operation, through this journey. I also acknowledge and admire the efficiency of the Deans of AcSIR (headquarters) and their staff.

I deeply acknowledge my laboratory seniors/friends Dr. Tushar Jagdale, Dr. Sarfaraj Mujawar, Dr. Subas Muduli, Dr. Abhimanyu Rana, Dr. Anup Kale, Dr. Arif, Dr. Parvez Shaikh, Dr. Vivek Antad, Dr. Harish Gholap, Dr. Ashish, Dr. Mukesh, Dr. Megha, Dr. Prasad, Dr. Meenal Deo, Dr. Shruti, Satish, Vishal, Dr. Abhik, Aniruddha, Dr. Rohan, Dhanya, Dipti, Dr. Onkar, Dr. Lily, Dr. Mandakini, Dr. Datta, Anil, Pradeep, Yogesh, Wahid, Umesh, Rounak, Satyawan, Sambhaji, Divya, Pooja, Shraddha, Mukta, Dr. Menakshi, Supriya, Ketaki, Nilima, Aparna, Rupali, Shital, Poonam, Srashti, Ishita, Swati and Golu. I am grateful to Dr. Rajesh Hyam, Dr. Vivek Dhas and Dr. Sarika Phadke for their constant support and encouragement.

I whole heartedly thank my family Pappa, Mummy and Didi for their constant support and unconditional love. My father is the one who always boosted me for the higher studies and gave all sorts of freedom in my life to choose whatever I desired along with the timely direction. I would also like to thank Anna (father-in-law), Nana, Nani, kaka, kaku, Amit (brother-in law) and my cute niece Ridhi for their inspiration and affection. Thanks to my extended family and relatives for understanding and appreciating my efforts in all my achievements. I would further like to thank my school and college friends - Swati, Vidya, Tejal and Nilu for always being there for me.

A countless thanks to my sweet little prince – Rishabh, for bringing so much of joy, love and affection in my life. Precious thanks to his direct/indirect sacrifices, adjustments and support throughout my Ph.D. research work. He is the one who became my strength and motivation in all kinds of situations. Finally and most importantly, very warm thanks to my dear husband Navnath for his patience, love, support and for believing in my dreams.

Finally, I thank almighty God for providing a good life for me !

Reshma Kanta Bhosale

List of Abbreviations

AFM	Atomic Force Microscopy
AM	Air Mass
BHJ	Bulk Heterojunction
CB	Conduction Band
CE	Counter electrode
CIS	$CuInS_2$
CIGS	$Cu(In,Ga)Se_2$
CV	Cyclic Voltammetry
DOS	Density of States
DRS	Diffuse Reflectance Spectroscopy
DSSC	Dye Sensitized Solar Cell
EIS	Electrochemical Impedance Spectroscopy
FESEM	Field Emission Scanning Electron Microscope
FB	Flat Band
FF	Fill Factor
FTIR	Fourier Transform Infra-red
FTO	Fluorine doped Tin oxide
FWHM	Full Width at Half Maximum
HOMO	Highest Occupied Molecular Orbital
HRTEM	High Resolution Transmission Electron Microscope
HTM	Hole Transporting Material
IPCE	Incident photon-to-current conversion efficiency

ITO	Indium doped Tin Oxide
J_{SC}	Short circuit current density
LH	Light Harvesting
LHE (λ)	Light harvesting efficiency at wavelength λ
LUMO	Lowest Unoccupied Molecular Orbital
MEG	Multiple Exciton Generation
NHE	Normal Hydrogen Electrode
OPD	Optical Path Difference
PEC	Photoelectrochemical
PL	Photo-luminescence
P_{max}	Maximum power
PV	Photovoltaic
QDSSC	Quantum Dot Sensitized Solar Cell
SAED	Selected Area Electron Diffraction
STM	Scanning Tunneling Microscope
SEM	Scanning Electron Microscope
TIP	Titanium tetra isopropoxide
TEM	Transmission Electron Microscope
VB	Valence Band
V_{OC}	Open circuit potential
XPS	X-ray Photoelectron Spectroscopy
XRD	X-ray Diffraction

Content

Abstract **i - iii**

Chapter 1: Introduction **1- 76**

1.1. Energy demand and need of alternative sources of energy 2

1.2. Renewable energy sources 5

1.2.1. Wind Energy 6

1.2.2. Hydro energy 7

1.2.3. Biomass energy 8

1.2.4. Geothermal energy 9

1.2.5. Solar energy 10

1.3. Solar electricity: Photovoltaics 11

1.3.1. Generations of Solar cell

1.3.1.1. Classic Silicon Solar cell 12

1.3.1.2. Thin Film Solar Cell 13

1.3.1.3. Organic and hybrid Solar cell 14-16

1.4. Hydrogen: A clean fuel from solar driven water splitting 17-18

1.5. Nanotechnology 19-22

1.6. Nano-effect

1.6.1. High surface to volume ratio 23

1.6.2. Quantum Confinement effect 24-27

1.7. Metal oxides and their nanostructures 28-29

1.7.1. Titanium dioxide (TiO_2) 30-31

1.7.1.1. Engineered size of TiO_2 32

1.7.1.2. Engineered morphologies of TiO_2 33

1.7.1.3. Engineered composition /band gap of TiO_2 34

1.7.1.4. Engineered surface of TiO_2 35

1.8. Metal Chalcogenides and their nanostructures 36

1.8.1. $CuInS_2$ 37

1.8.1.1. Engineered size of $CuInS_2$ 38

1.8.1.2. Engineered morphologies of $CuInS_2$ 39

1.8.1.3. Engineered composition of $CuInS_2$ 40
1.8.2. NiS_2 41
1.9. Metal oxide & Chalcogenide for Dye Sensitized Solar Cell application
1.9.1 Dye Sensitized Solar Cell (DSSC)
1.9.1.1. Working principle 42-43
1.9.1.2. Components of DSSC 44-47
1.9.1.3. Governing parameters of DSSC performance 48-50
1.9.2 Engineered metal oxide (TiO_2) for DSSC application 51
1.9.2.1. Size: Double-layered Structure 52
1.9.2.2. Shape: Kinetics of DSSC 53-55
1.10. Metal Chalcogenide for Quantum Dot Sensitized Solar Cell application
1.10.1 Quantum dot Sensitized Solar Cell (QDSSC)
1.10.1.1. Working principle 56
1.10.1.2. Engineered metal chalcogenide QDs 57-58
1.10.1.3. Components of QDSSC 59-60
1.11. Metal oxide and Chalcogenide for Photoelectrochemical water splitting
1.11.1. Water electrolysis 61
1.11.2. Solar driven water splitting
1.11.2.1. Photo-catalytic (PC) water splitting 62
1.11.2.2. Photoelectrochemical (PEC) catalytic water splitting 63-65
1.12. Outline of thesis 66-67
1.13. References 68-76

Chapter 2: Fabrication of Sensitized Solar Cell, Experimental Methods and Characterization Techniques **77-115**

Section I: Fabrication of Sensitized Solar cell
2.1. Fabrication of DSSC 78-86
2.2. Fabrication of QDSSC 87-89
Section II: Experimental methods
2.3. Anodization method 90-91
2.4. SILAR method 92-93

2.5. Hydrothermal method 94

Section III: Characterization techniques

2.6. X-ray Diffraction 95-96

2.7**.** Scanning Electron Microscopy 97

2.8. Transmission Electron Microscopy 98-99

2.9. Ultraviolet - visible Spectroscopy 100-101

2.10. Photoluminescence Spectroscopy 102-103

2.11. Fourier Transform Infra –red Spectroscopy 104-105

2.12. Raman Spectroscopy 106-107

2.13. X-ray Photoelectron Spectroscopy 108-110

2.14. DSSC characterization tool: Solar Simulator 111-112

2.15. References 113-115

Chapter 3: Room Temperature Synthesis of Rutile TiO_2 Hierarchical Nanoneedle Flower Morphology for Dye Sensitized Solar Cell **116-133**

3.1. Introduction 117-118

3.2. Experimental Section

3.2.1. Anodization method 119

3.2.2. Fabrication of DSSC 120

3.3. General Characterizations 120

3.4. Results and Discussion

3.4.1. X-ray Diffraction pattern 121

3.4.2. Thermogravimetric analysis 122

3.4.3. Field Emission Scanning Electron Microscopy (FESEM) images 123

3.4.4. Transmission electron Microscopy (TEM) images 124

3.4.5. Diffused Reflectance Spectra 125

3.4.7. Mechanism of nanoneedle formation 126-127

3.4.8. Mechanism of rutile nuclei formation 128-130

3.5. Solar Cell Characterization 131

3.6. Conclusion 132

3.7. References 132-133

Chapter 4: Chlorate ion mediated rutile to anatase reverse phase transformation in the TiO_2 nanosystem **134-150**

4.1. Introduction 135

4.2. Experimental Section

4.2.1. Anodization method 135

4.2.2. Fabrication of DSSC 136

4.3. General Characterizations 136

4.4. Results and Discussion

4.4.1. X-ray Diffraction pattern 137-138

4.4.2. Raman spectra 139

4.4.3. Transmission electron Microscopy (TEM) images 140-141

4.4.4. Fourier Transform Infra red Spectra 142

4.4.5. Mechanism of reverse phase transformation 143-146

4.5. Solar Cell Characterization 147

4.6. Conclusion 148

4.7. References 148-150

Chapter 5: Nanophase $CuInS_2$ nanosheets/CuS composite grown by the SILAR method leads to high performance as a counter electrode in dye sensitized solar cells **151-183**

5.1. Introduction 152-154

5.2. Experimental Section

5.2.1. SILAR method 154

5.2.2. Fabrication of DSSC 155

5.3. General Characterizations 155

5.4. Results and Discussion

5.4.1. X-ray Diffraction pattern 156-157

5.4.2. Raman spectra 158-160

5.4.3. Field Emission Scanning Electron Microscopy (FESEM) images 161-164

5.4.4. Transmission electron Microscopy (TEM) images 165
5.4.5. Mechanism of CIS nanosheet formation 166-168
5.4.6. Electrochemical analysis 169-170
5.4.7. Photovoltaic performance 171-173
5.4.8. Stability data 174-175
5.4.9. Electrochemical impedance analysis 176
5.4.10. Tafel Polarization Curve 177
5.4.11. Diffusion Co-efficient Calaculation 178-179
5.5. Conclusion 180
5.6. References 180-182

Chapter 6: Aqueous colloidal $CuInS_2$/CdS sensitizer for Quantum dot sensitized solar Cell 183-196

6.1. Introduction 184-185
6.2. Experimental Section
6.2.1. TGA assisted aqueous synthesis of CIS and CIS /CdS 186
6.2.2. Fabrication of QDSSC 187
6.3. General Characterizations 187
6.4. Results and Discussion
6.4.1. CQD Characterization 188
6.4.2. Optical Characterization 189
6.4.2.1. Photoluminescence (PL) 190
6.4.2.2. Diffuse Reflectance Spectra (DRS) 191
6.5. Solar Cell Characterization 192-193
6.6. Conclusion 194
6.7. References 194-196

Chapter 7: $NiS_{1.97}$: A new highly efficient photo-electrochemical catalyst for hydrogen generation **197-223**

7.1. Introduction 197-198

7.2. Experimental Section 199-201

7.2.1. Synthesis of HYD-NiS_2

7.2.2. Synthesis of HYDS-NiS_2

7.2.3. Synthesis of SUL-$NiS_{1.97}$

7.2.3.1. Synthesis of Ni $(OH)_2$

7.2.3.2. Synthesis of NiO

7.2.3.3. Sulfurization of NiO

7.3. Characterization 202

7.4. Results and discussion

7.4.1. X-ray diffraction 203-205

7.4.2. Diffuse Reflectance Spectroscopy 206

7.4.3. Photoluminescence spectroscopy 207

7.4.4. X-ray photoelectron spectroscopy 208-211

7.4.5. Field emission Scanning Electron microscopy (FESEM) 212

7.4.6. Photoelectrochemical (PEC) measurement 213-214

7.4.7. Mott Schottky analysis 215-217

7.4.8. Stability data 218-219

7.5. Conclusion 220

7.6. References 220-223

Chapter 8: Summary and Future scope **224-229**

8.1. Summary

8.2. Future scope of work

List of Publications, patents & awards **230-231**

Abstract

Development of modern society largely depends on energy supply which is currently available from non-renewable sources that are not only depleting rapidly but are also creating environment hazards. To resolve this issue, the abundant and omnipresent solar energy can be utilized as a clean and green source which is required to be converted to other forms of energy with high efficiency. In the present state of art in photovoltaics, silicon solar cell is most robust and commercial but highly expensive. Towards this end, third generation solar cell systems such as Dye-sensitized solar cells (DSSCs) and the green approach to create hydrogen fuel by photoelectrochemical (PEC) water splitting are emerging as two promising concepts. With the unique combination of nanotechnology and solar energy, cost effective nanodevices can be fabricated for light harvesting and generating clean future fuel.

For realizing higher performance features of DSSC and PEC systems that are acceptable for practical technological implementation the search for new materials that are earth abundant and inexpensive is essential. Moreover tuning of their optoelectronic properties by nano-engineering is highly desirable. The present thesis is an attempt in this direction. We have synthesized metal oxide and chalcogenide nanostructures for the application of DSSc and PEC. This topic makes the brief introduction of **Chapter 1.**

Chapter 2 includes three sections: Fabrication of sensitized solar cell, experimental methods used for synthesis of nanomaterials and characterization techniques used in the present thesis.

Chapter 3 deals with successful synthesis and characterization of electrochemically active photoanode material, namely TiO_2 which is the heart of DSSC device.TiO_2 has three crystal forms- Anatase, Rutile and Brookite. Out of these rutile TiO_2 is a high temperature phase (above

600°C) due to which it is hard to control particle size, porosity, surface area, grain boundaries and orientated 1D nanostructure which are essential parameters for light harvesting, charge transport and charge collection in DSSC. In light of this we have synthesized rutile TiO_2 nanoneedle flowers (concurrent nano-micro hierarchical morphology) at room temperature by using a simple and efficient one step process of anodic dissolution. DSSCs configured using such rutile TiO_2 flowers are shown to exhibit appreciable power conversion efficiency of 3.6%.

In **Chapter 4,** the synthesis, characterization and application of TiO_2 photoanode nanomaterial, namely Anatase TiO_2 is presented and discussed. Rutile TiO_2 nanoneedles synthesized by anodization in perchloric acid (pH < 1) are shown to undergo an interesting reverse phase transformation to anatase nanoparticles (8 nm) at 300^0C only if the chlorate ions are maintained in the ambient medium. When chlorate ions are removed by multiple washing, the rutile phase and the needle morphology are maintained. The mechanism of formation of the ion-stabilized solid and its thermal evolution are discussed in detail. When such anatase TiO_2 nanoparticle powder is used in DSSC, a respectable efficiency of 6% is achieved.

In **Chapter 5**, we have tried to replace high cost counter electrode material commonly used in DSSC, namely platinium, with dichalcogenide $CuInS_2$ (CIS). Obtaining stoitiometric bimetallic sulfide is a great challenge till today. In our present work we have not only successfully achieved phase pure CIS by a simple Successive Ionic Layer Adsorption Reaction (SILAR) method but have also obtained graphene-like thin sheet morphology. Temperature dependant formation of CIS is also studied which indicates that at a particular temperature composite of CIS with CuS is formed. Only CIS counter electrode delivered 5% and its composite with CuS gave 6% efficiency in reduction of iodine/tri-iodide species of DSSC due to synergistic effect of both on the catalytic performance.

In **Chapter 6**, we have attempted to replace the commonly used dye sensitizer with quantum dots (QD) as the ruthenium based organic dyes are expensive and have degradation issues over time. QDs are efficient candidates for sensitizer as they make use of the concepts of quantum confinement effect and multiple exciton generation. Here we synthesized colloidal solution of $CuInS_2$ QDs of 3-4 nm for use as sensitizers. These were rendered stable and protective by passivating them with CdS and gave an efficiency of 3% when used with mesoporous TiO_2 film as an active layer in DSSC.

In **Chapter 7**, we report sulfur deficient dichalcogenide, $NiS_{1.97}$ as a efficient photoelectrochemical catalyst for H_2 evolution. Phase pure $NiS_{1.97}$ nanomaterial is obtained by converting nickel oxide into sulfide by controlled sulfurization method, which is otherwise difficult to establish. The ordered defect states (sulfur vacancies) in this material increase the carrier density and in turn lead to favorable band line-up with respect to redox potential of water, rendering it to be an effective photoelectrochemical catalyst. The material exhibits a remarkable PEC performance with hydrogen evolution equivalent of 1.25 mA/cm^2 vs NHE at 0.68V in neutral pH, which is almost 1000 times superior as compared with that of the stoichiometric phase of NiS_2. The latter is well known to be a co-catalyst but not as a primary PEC catalyst.

Chapter 8 summarizes the present thesis with its significant features along with avenues of future prospective.

Chapter 1

Introduction

The primary focus of the present thesis was to engineer and study metal oxide and chalcogenide nanostructures, their phase transformations and their optical, electronic and catalytic properties for energy applications such as sensitized (dye or quantum dot) solar cells and solar driven water splitting to generate hydrogen fuel. This chapter initially presents the overview of current energy scenario and the necessity of harnessing solar energy. Further it deals with the strengths of the excellent combination of nanoscience and solar energy for the development of low cost, eco-friendly and commercially viable technologies, namely the Dye/QD Sensitized Solar Cells (DSSC/QDSSC) and photoelectrochemical water splitting (PEC). An introduction to both these concepts, their components, working principles, their dependence upon engineered nanostructures and their properties for the cases of metal oxide and chalcogenide systems are discussed in the context of the said applications. Finally the outline of the chapters to follow is provided.

1.1. Energy demand and need of alternative sources of energy

Energy is part and parcel of the human civilization and without adequate and sustainable energy availability the progress in social and economic spheres is an impossible task. Development demands energy for industrial, residential, commercial or transport sectors as seen from **Figure 1.1a).** The growth and strength of industry, the speed of transportation, comfort zone of homes, hotels, workplace, and the security of the nation need provision of adequate energy sources. In

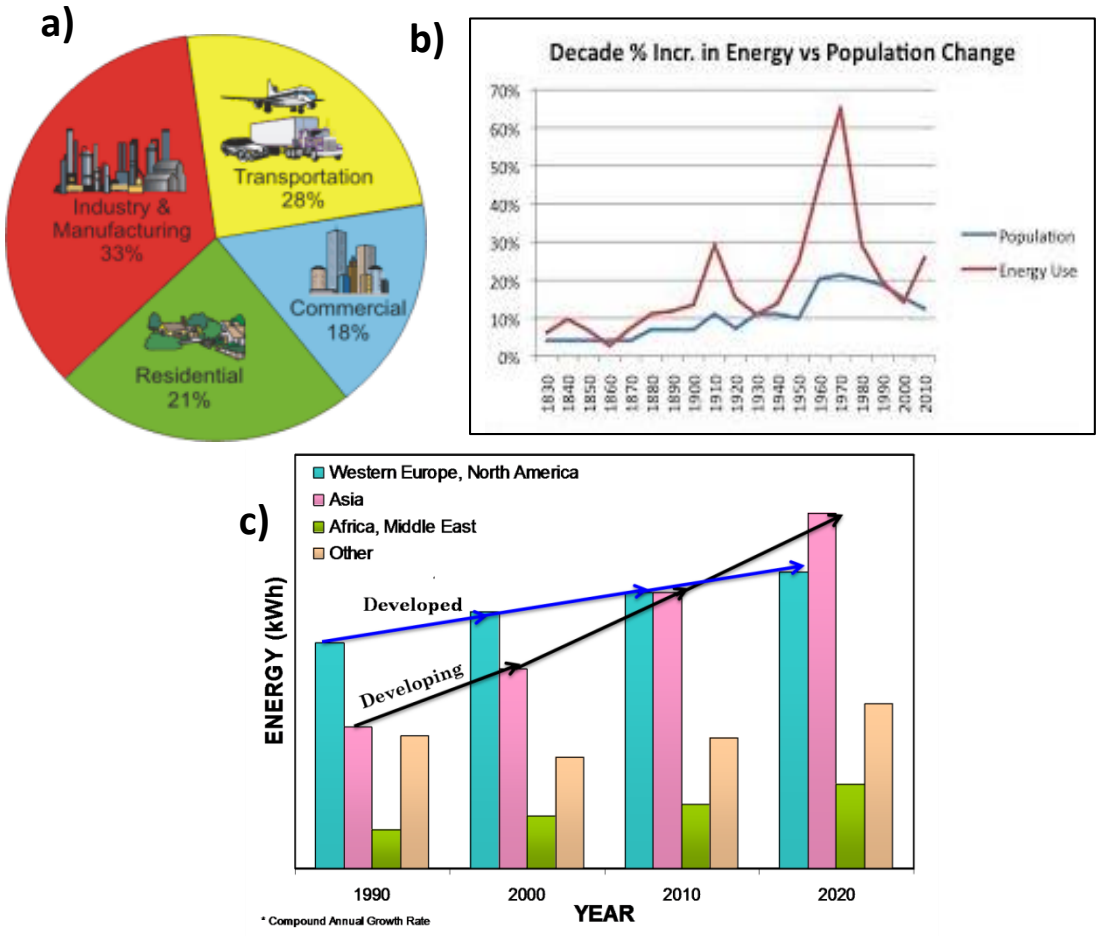

Figure1.1. Global energy demand with a) various sectors b) increasing population c) region

http://energyconservation.wiki.lovett.org/Increasing+Energy+Efficiency

http://ourfiniteworld.com/2012/03/12/world-energy-consumption-since-1820-in-charts/

recent decades with increasing population per capita energy usage and its demand have also increased by 40% as per the survey done till 2010.[1] Also from the point of various regions, developing or under-developed countries will need more energy as compared to the developed countries as shown in **Figure1.1.c).** Overall it is predicated that worldwide energy consumption will increase to 762 exajoules (2, 12,201treawatt) by 2030.[2] To fulfill this huge energy demand we are mainly (86%) dependant on fossil fuels like oil (36%), natural gas (25%), coal (20%).[3] Theses are the primary sources of energy occurring in nature. They are formed by very slow and gradual decomposition of dead plants and animals deep under the earth's crust. Due to this reason they are neither earth abundant nor renewable sources of energy.

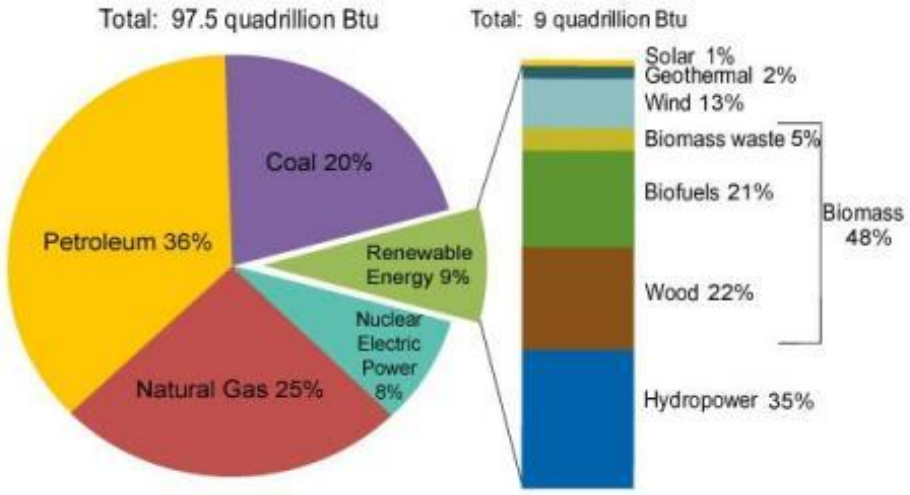

Source: U.S. Energy Information Administration, *Monthly Energy Review*, Table 10.1 (March 2012), preliminary 2011 data.

Figure1.2. Global energy consumption in terms of sources of energy.[3]

http://www.colorado.edu/ecenter/energy-us/renewable-energy

Their feed stock is limited and they are at the edge of depletion. For instance, energy reservoir of coal may last for 120 years but natural gas and oil will be depleted in 65 and 45 years, respectively.[2] Even though they had lasted longer and satisfied the current energy demand their major drawback is that they create various kind of serious environmental pollutions. 40% of world electricity comes from burning of coal. Burning of fossil fuels in automobiles and power plants releases toxic gases into the environment such as CO_2, CO, N_xO, SO_2 which give rise to serious air pollution and health hazard. CO_2 is a greenhouse gas which is the primary reason for global warming. For climate scientists global warming is the foremost critical issue as it is responsible for sudden changes in climate, melting of glaciers at the poles, rising of sea levels and doughtiness. Due to these gases the protective layer of earth-ozone is worn out and ozone holes are created. From the ozone holes harmful UV rays enter the earth and cause disease like cancer.

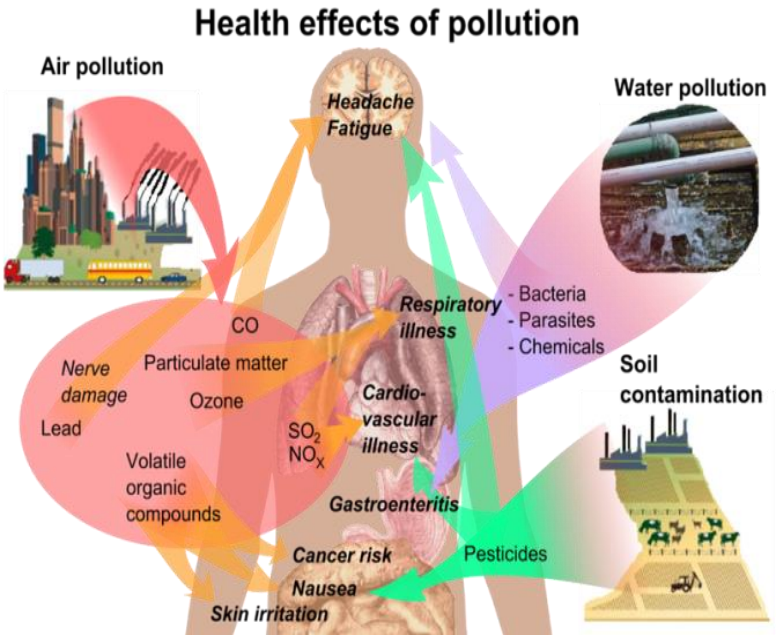

Figure1.3. Ill effects of burning fossil fuels.

http://commons.wikimedia.org/wiki/File:Health_effects_of_pollution.png

SO_2 gas is responsible for acid rain which not only has very adverse effect on human and animal health but also on historic monuments. On an average a coal based thermal plant generates tons of ash, sludge and waste material which contain extremely heavy and toxic metals like cadmium, mercury, arsenic. These kinds of toxic substances are dumped in open land fill or drained in rivers and lakes which in turn create soil and water pollution. Initially, all such pollutions have minor symptoms on human health like headache, restless, nausea, cough, vomiting, asthma but prolonged exposure can lead to serious diseases related to liver, kidney, lungs and heart.[4] Even though fossil fuels are major sources of energy their end product and by-product are difficult to manage and dispose. Needless to say that a limited supply of fossil fuels and their ill effects are an alarm for the need for alternative sources of energy.

1.2. Renewable energy sources

To have a clean, sustainable and low cost energy alternative, renewable sources of energy, which include wind, hydro, biomass, geothermal and solar energy, need to be tapped.

1.2.1. Wind Energy:

Wind turbines utilize the wind's kinetic energy to generate electrical energy that can be used in homes. Blowing wind causes the angled blades to rotate which convert the wind's kinetic energy into mechanical energy. Sensors attached with turbines detect the direction of wind and project or turn the rotor automatically to face the wind, and automatically brake in dangerously high winds to protect the turbine from damage. A shaft is connected to the generator through a rotor which in turn rotates a generator (**Figure1.4.**). Generators convert mechanical energy into electrical energy through application of electromagnetic field. This generated electricity is passed through cables to particular stations and finally converted to a high voltage.

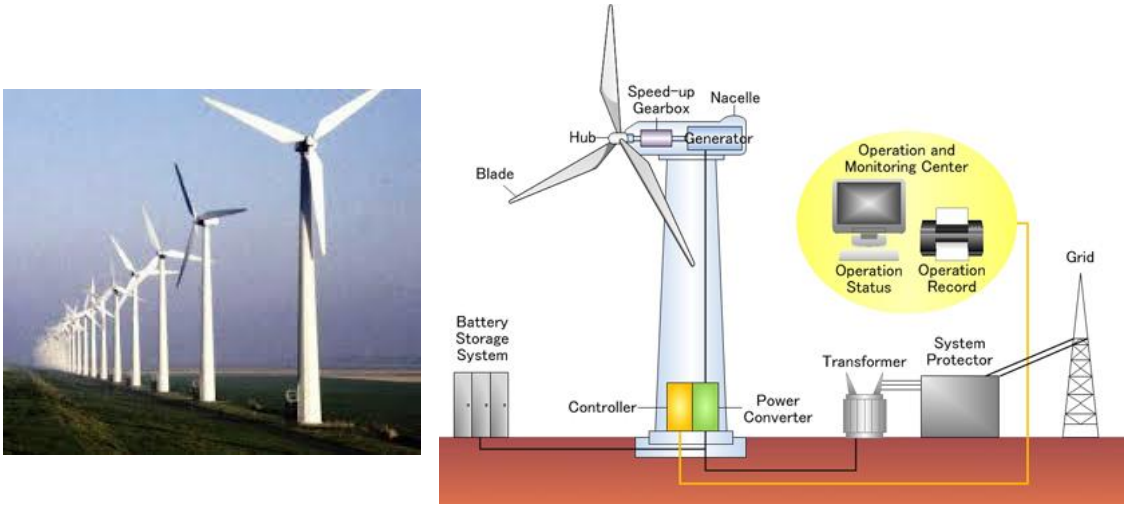

Figure1.4. Electricity generation from wind energy

http://www.fiddlersgreen.net/models/miscellanous/Wind-Turbine.html

http://www.yokogawa.com/industry/renewable_energy/wind_power/index.htm?nid=megadlist

The national grid uses high voltages to transmit electricity efficiently through the power lines to the homes. Here, other transformers reduce the voltage back down to a usable level.[5] Electricity production from wind energy was only 13% earlier but now it is growing rapidly. It has expanded to 336GW till 2014. Now at least 83 countries worldwide are using wind energy supply for their electricity grid. Denmark has set a good example by generating its 40% of electricity from wind energy .[6]

1.2.2. Hydro energy:

In hydro energy, power is generated by utilizing energy of falling water to move turbines. Damming the river converts its kinetic energy into potential energy and this stored form of turbines uses its electromagnetic field to convert mechanical energy into electricity (**Figure 1.5.**).[7] This is the most widely used renewable form of energy which generates about 16% of the global electricity, that is 3427 TW-hr. Around 150 countries uses hydroelectricity and China is the largest hydroelectricity producer, at 721TW-hr. Hydroelectricity is the most reliable way of

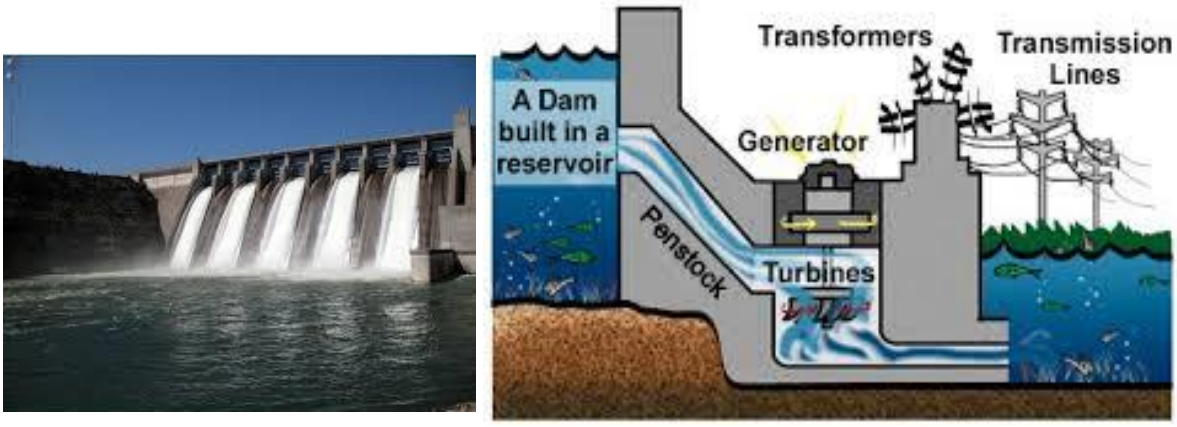

Figure1.5. Electricity generation from hydro energy

http://eurogroupconsultingenergy.com/?p=413

https://www.pinterest.com/pin/153685406006217562/

producing energy, since once the hydropower plant is built then no further investment is required. Moreover, it is flexible for operating, low cost and has no direct waste or air pollution.[8]

1.2.3. Biomass energy:

The word "biomass" comprises of variety of materials like wood, agricultural waste, forest debris, animal and human waste. Energy derived from biomass is also called "biopower" as it has stored energy which can be released as heat. This heat from biomass can be converted into power in many ways. Most commonly and conventionally used method comprises biomass like wood being directly combusted to produce high pressure steam as shown in **Figure 1.6.** The biomass feed stock is burnt in excess of air in furnace to heat water. This heated water in boiler is converted into steam to run turbine. In U.S. about 50 billion KW-hr of electricity is produced rom biomass. Due this reason they grow energy crops like *switch grass* and *bigblue stem* in marginal lands which can be harvested till 10 years even before they are planted. Thick perinnal

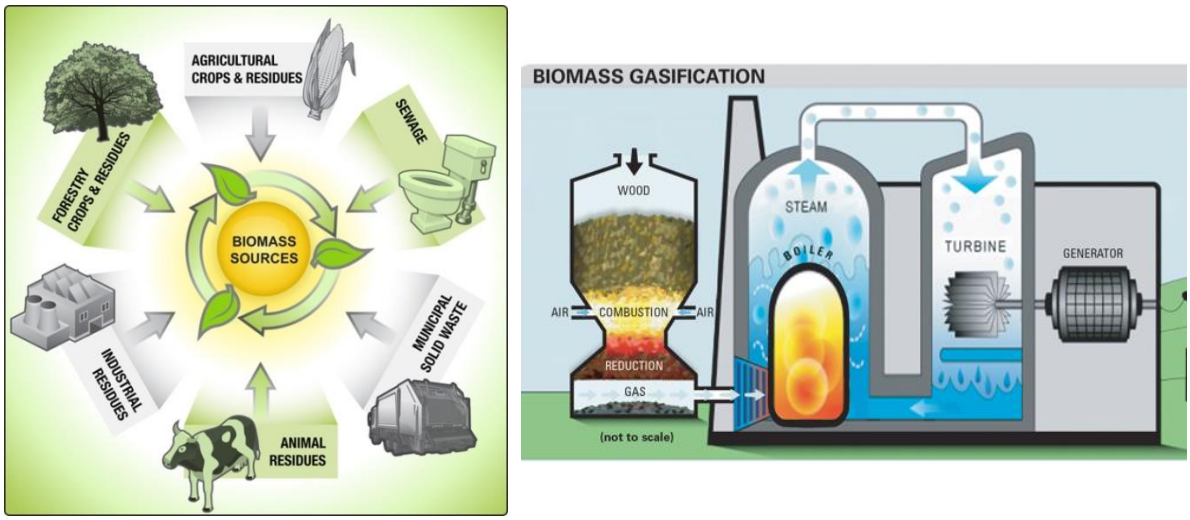

Figure1.6. Electricity generation from biomass

http://efergy.com/blog/beginners-guide-to-renewable-energy-technologies/

http://greenenergy.reviewforcash.com/

grasses like *sugar cane* and *elephant grasses* can be grown in wet and hot climates such as in India, Hawaii and Florida.

The most important advantage of biopower is that sources which are used for power generation indirectly clean up the industrial, agricultural and municipal waste. But compared to hydro and wind power it is not in much practice because it needs availability and storage of biomass as well as an initial investment in power plant which is higher. Also combustion of biomass leads to emission of toxic gases in air.[9]

1.2.4. Geothermal energy:

Heat produced and stored in earth crust is called as *geothermal energy* which is also a renewable source of energy. Earth's internal heat content is 10^{31} joules which is 100 billion times of the world energy consumption. Many parts of the world like U.S., Philippines and Indonesia use geothermal energy for electricity generation which is about 2687 MW, 1967 MW and 992 MW,

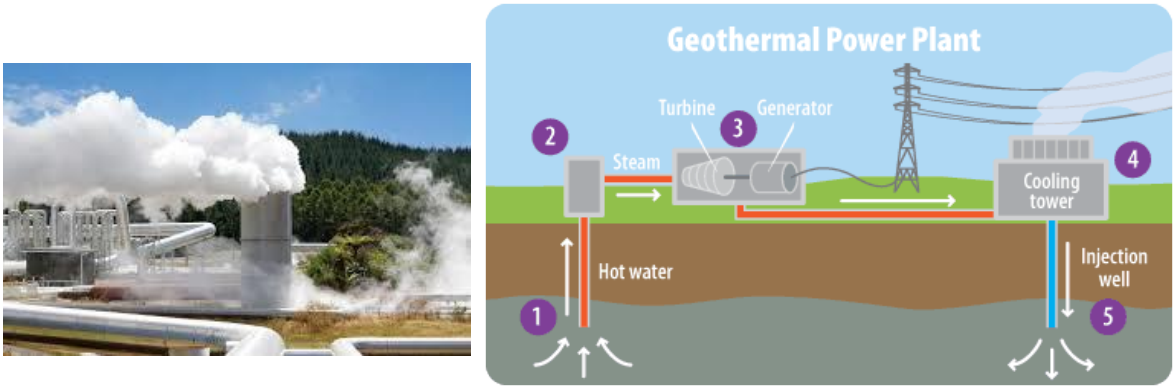

Figure 1.7. Electricity generation from geothermal energy

http://renewables.seenews.com/news/costa-rica-to-advise-bolivia-on-geothermal-energy-461305

http://www.epa.gov/climatestudents/solutions/technologies/geothermal.html

respectively.

This power makes up about 27% of global electricity accounted from geothermal energy. Country like Iceland gets 50% of its energy from geothermal power. Generally a stream of hot water or dry steam is allowed to flow through turbines to produce electricity. The only concern in this type of energy source is that some toxic air pollutants like hydrogen gas, CO_2, and ammonia are produced from earth crust which has trace amounts of toxic element arsenic.[10]

1.2.5. Solar energy:

Among all the renewable sources of energy sun energy is perhaps the most reliable and practical alternative form of energy as it is available in plenty at free of cost. It is also fruitful in meeting the current global energy demand because sun energy striking the earth produces approximately 120,000 TW per annum. Energy from sunlight can be directly converted into electricity by a harvesting medium or a device. This can be done in many ways as given below:

- Direct solar to electricity conversion (Photovoltaic)
- Direct solar to fuel (H_2) conversion (Photoelectrochemical water splitting)
- Solar thermoelectric
- Solar heating and cooling.

The present thesis mainly deals with the first two topics of solar light harvesting- Photovoltaics and Photoelectrochemical water splitting. The direction of the work was to synthesize and engineer metal oxides (TiO_2) and dichalcogenides into unique nanostructures and study their properties in the context of the above mentioned applications. Nanoscience and solar energy together represent a formidable combination that has made way to the emergence and rapid growth of new and novel technologies for solar energy harvesting during the past couple of decades. In the following sections brief discussion of the components, working principles, fundamental issues, and challenges pertaining to these applications is presented.

1.3. Solar electricity: Photovoltaics

The conversion of solar energy emerged as an energy harvesting possibility with the discovery of *"Photovoltaic effect"* observed by Bacquerel. [11] Indeed, this was the beginning of the solar cell technology. It is generally defined as the generation of photovoltage across two electrodes connected to solid or liquid system when light shines on it. Practically all the photovoltaic devices are accounted for in terms of p-n junction based semiconductor systems. In a semiconductor material having both the n-type and p-type material regions joined together lead to a p-n junction. Near the interface, the electrons from n- type material diffuse in low electron concentration (p-type region) leaving behind positively charged ions and holes from p-type

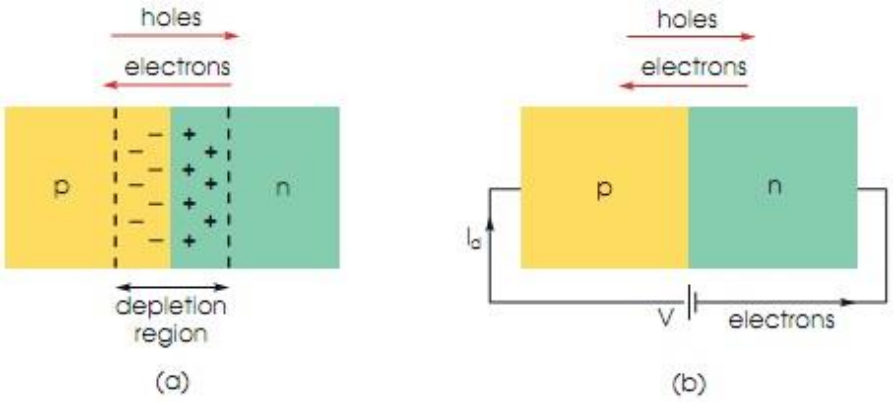

Figure1.8. a) p-n junction b) applying forward bias

http://learning-hi-tech.blogspot.in/2013/01/solar-cell-p-n-junction.html

region diffuse in n-type region leaving behind negatively charged ions. This process continues till the large enough electric charge densities are developed in both cases to repel further charge transfer.

This diffusion of charges in the opposite directions creates an electric field called as the "built-in potential". Ultimately a neutral state or equilibrium is achieved where no mobile charge carries pass across the junction creating a "potential barrier" over an interface region (width) termed as the **depletion region**. This depletion region turns a p-n junction into a diode which conducts current in one direction as shown in **Figure 1.8.** In a photovoltaic cell when light strikes this region it creates free electrons and holes in and around the depletion region. The built-in potential drives the two types of charges in the opposite directions leading to a photo-voltage. The p and n region are connected to an external load which carries the current.

Although the concept of converting solar light into electricity existed even before 1900, the real practical silicon solar cell demonstration was given by Bells lab in 1954 which gave overall power conversion efficiency of 6%.[12] Since then many generations of silicon-based and non-silicon type solar cells have evolved and developed as shown in **Figure 1.9.**

1.3.1. Different generations of Solar cell

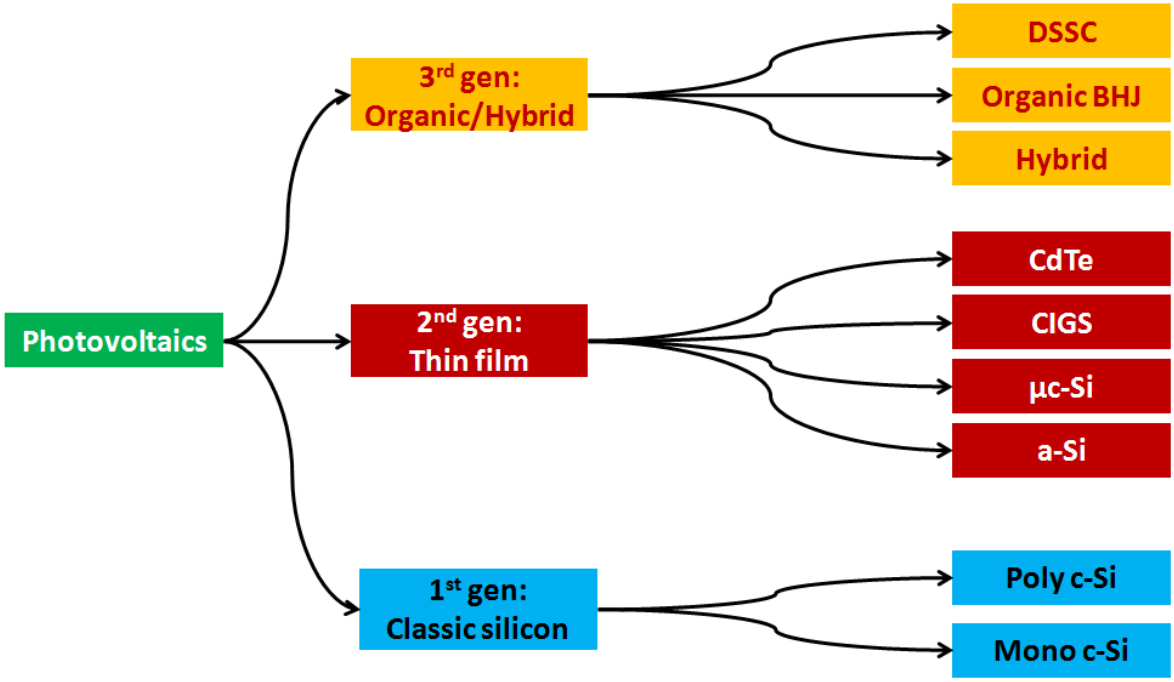

Figure1.9. Historical development of different generations of solar device.[13]

http://www.heliatek.com/technologie/organische-photovoltaik/?lang=en.

1.3.1.1. Classic Silicon Solar cell: Current photovoltaic production uses 90% of first generation solar cells which are composed of single junction solar cells made up of monocrystalline silicon (c-Si) wafers or multi-crystalline silicon (mc-Si), as given in **Figure 1.10**. On the module level, the single crystal silicon cells show 18-20% efficiency, whereas ploycrystalline silicon solar cells deliver about 12-14%.[14] These cells dominate the PV market as they are robust, most reliable and well established. However, the silicon wafers, their desired high purity and the manufacturing process are extremely expensive. Hence the high cost of first generation solar cells severally restricts their wide spread applicability for the future expansion. This gave rise to the second generation solar cells called as Thin film solar cells.

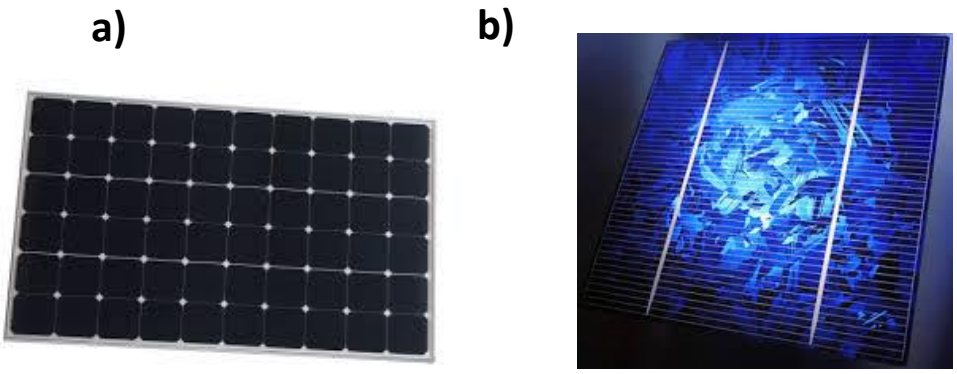

Figure1.10. Images of a) Monocrystalline b) Multicrystalline silicon solar cell.

http://www.sharp.co.uk/cps/rde/xchg/gb/hs.xsl/-/html/sharp-to-begin-mass-production-of-new-

http://www.wifinotes.com/energy/types-of-solar-cells.html

1.3.1.2. Thin Film Solar Cells: Thin film solar cells are also single junction solar cells which utilize materials such as amorphous silicon (a-Si), CdTe, CIGS and microcrystalline silicon (µc-Si) on low cost substrates like glass. These materials absorb the solar spectrum much more efficiently than c-Si and mc-Si while using only 1-10µm of the active material. They are flexible and light weight (**Figure 1.11**) enabling their use in creative applications like wearable device systems. Unlike the first generation solar cells they can also work in poor light conditions and are not affected by shading issues. Up till now good conversion efficiencies have been reported for the a-Si (6-9%) [15] CdTe (20%) [16], CIGS (20%) [17] and µc-Si (11%) cells.[18] Although these second generation solar cells have reduced the cost by some extent, the poor material reproducibility and uniformity for large area devices limit their applicability on the commercial scale. Moreover the materials used are toxic and harmful to environment.

1.3.1.3. Organic and hybrid Solar cell: The third generation solar cells are multi-junction solar cell which utilizes organic materials like small molecules or polymers. These are inexpensive, flexible and readily available for use. Moreover they can be simply and quickly applied for large

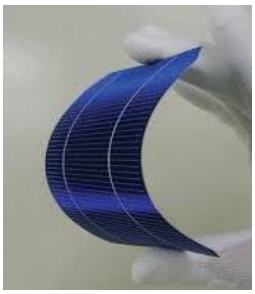

Amorphous silicon solar cell

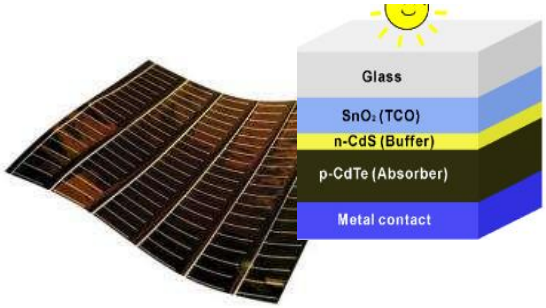

CdTe solar cell

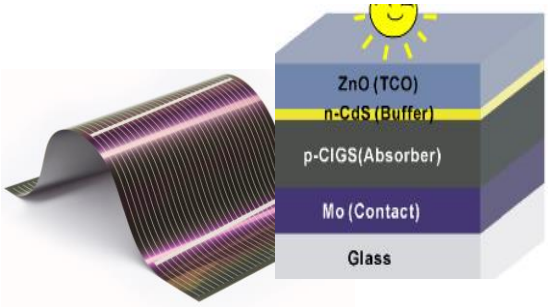

CIGS solar cell

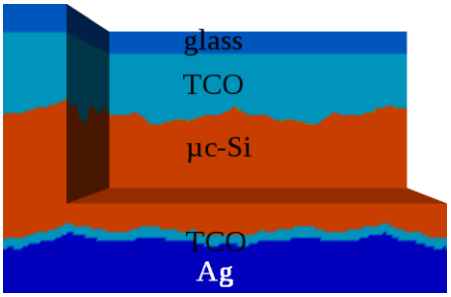

µc silicon solar cell

Figure1.11. Images of different thin film solar cells

http://pixgood.com/amorphous-silicon-solar-cell.html

http://phys.org/news/2011-06-efficiency-flexible-cdte-solar-cell.html

http://fabricalo.net/index.php/how-are-thin-film-solar-cells-cigs-made/

http://www.aot.uni-erlangen.de/saot/research/activities-in-progress/simulation-of-optical-waves-in-thin-film-solar-cells.html

scale production by roll to roll printing technique. In the simplistic *single layer organic photovoltaic* cell electronically active polymer is sandwiched between two conducting electrodes (**Figure 1.12a**) and the exicton is separated due to difference in their work function. For example, ITO/PPV/Al can give 0.1% efficiency under white light illumination.[19]

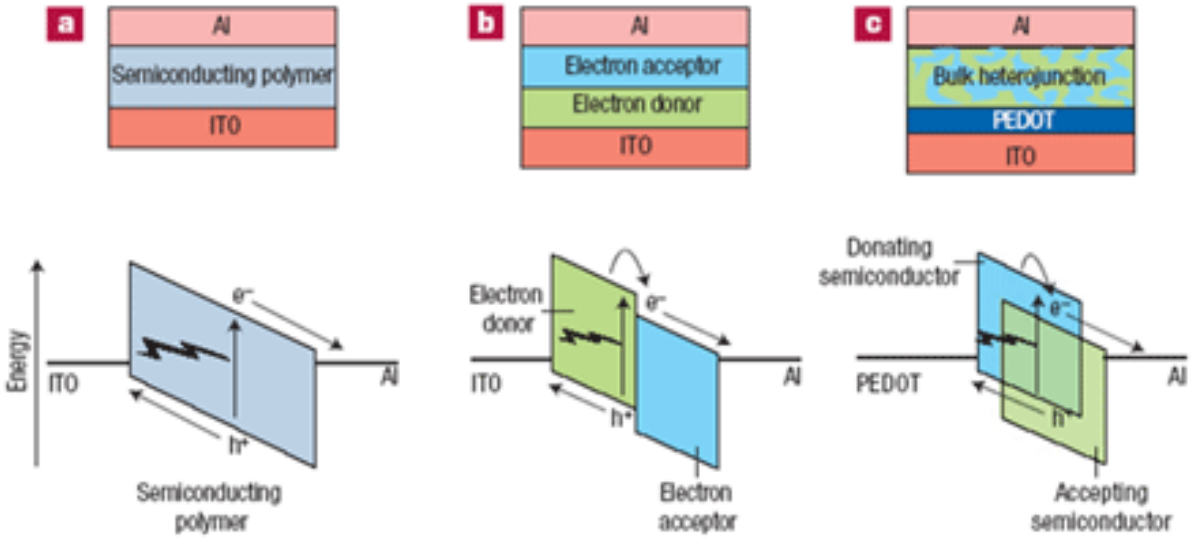

Figure1.12. Representative Organic solar cell.

http://www.sneresearch.com/eng/info/show.php?c_id=4561&pg=2&s_sort=2&sub_cat=&s_type=&s_word=

In *bilayer type*, active region contains two materials, one electron donor and other electron acceptor. The exciton is separated between their interface due to difference in electron affinity and ionization potential. For example, PPV/C_{60} system showed 1% efficiency.[20] Both these types suffer from low efficiency due to recombination and short diffusion length of 10nm, respectively. The third type is *Bulk Heterojunction solar cell (BHJ)* where electron donor material and acceptor material are mixed together to form a blend, and if the modulation length scale of the blend constitution is equal to the diffusion length of exciton then they can migrate to

the interface and break. Electrons and holes are pulled in the opposite direction generating photovoltage and current. A good example of bulk heterojunction solar cells is silicon nanorod as acceptor and Spiro as a donor rendering efficiency of 10.3%.[21]

Third generation solar cells include another class called *hybrid solar cells* where both organic and inorganic materials are assembled together in hetero-junction type. Organic part is a conjugated polymer which absorbs light and transport hole whereas the inorganic material carries the electron. These hybrid solar cells are mainly of three types: Polymer-nanocomposite hybrid solar cell, Dye Sensitized Solar Cell and Quantum Dot Solar Cell. Polymer-nanocomposite cell is based on mixing of nanomaterials and polymers. It takes the advantages of the high surface area of nanoparticles which facilitates better charge transfer processes. The nanomaterials used in these type of cells are usually CdS, CdSe, TiO_2 (size range 6-20 nm) etc. and common polymers used are P3HT, MEH-PPV etc. which have extended conjugation and are also hydrophobic.[22]

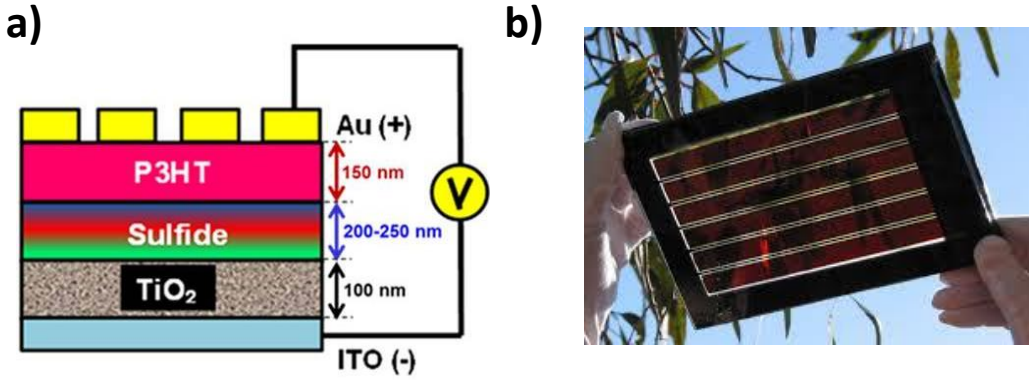

Figure1.13. Representative hybrid solar cell a) polymer nano-composite based solar cell [22] and b) DSSC device. Reproduced by the permission of reference 22: *RSC Adv.*, **2013**, 3, 5412-5421.

http://www.asknature.org/product/b57e64dd3a2a1a9d36a92a5a51ef7293

Amongst the leading third generation technologies of solar cells, the Dye Sensitized Solar Cell and Quantum Dot sensitized Solar cell stand out for their unique architecture and form the major part of this thesis. These are discussed in more details in later sections.

1.4. HYDROGEN: A clean fuel from solar driven water splitting

To minimize our dependence on fossil fuels for energy, hydrogen is considered a promising alternative. It is a cost effective and eco-friendly fuel. It does not exist as fuel rather it occurs in chemical form of water or hydrocarbon which needs to be transformed into usable form as H_2. H_2 like electricity is carrier of energy which can be stored and used for any application.

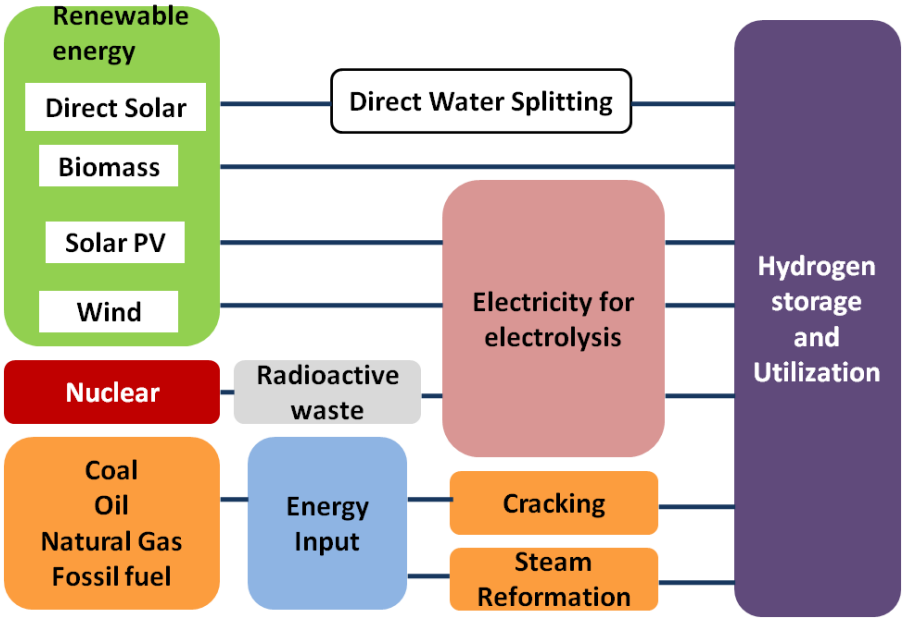

Figure1.14. Renewable and non-renewable sources of energy and pathways for H_2 production [23]

http://www.fsec.ucf.edu/en/consumer/hydrogen/basics/production.htm

At present, world's 50% of the H_2 is generated from natural gas by the process of steam reforming and 18% by coal gasification.[24] However, producing H_2 from fossil fuels reduces its economy and releases massive toxic gases in air like CO_2. H_2 economy involves three steps- H_2

production, storage and use. Even if the production cost, performance and reliability are achieved other two technical steps should also be economic. Thus to achieve the benefits of H_2 economy; we should produce it from non-fossil resource like water, and renewable sources of energy. Biomass is also renewable source of energy but availability and storage of biomass is a major problem. Moreover amount of H_2 gas generated is not that great; hence the conversion efficiency is low. Direct or solar thermal splitting of water requires temperature greater than 2000°C and produces back reaction rapidly by combining the mixture of H_2 and O_2. Wind energy and PV systems coupled to electrolyzer are the most versatile approaches but are very expensive. Photolysis combines the two processes of electricity generation and electrolysis into a single system.

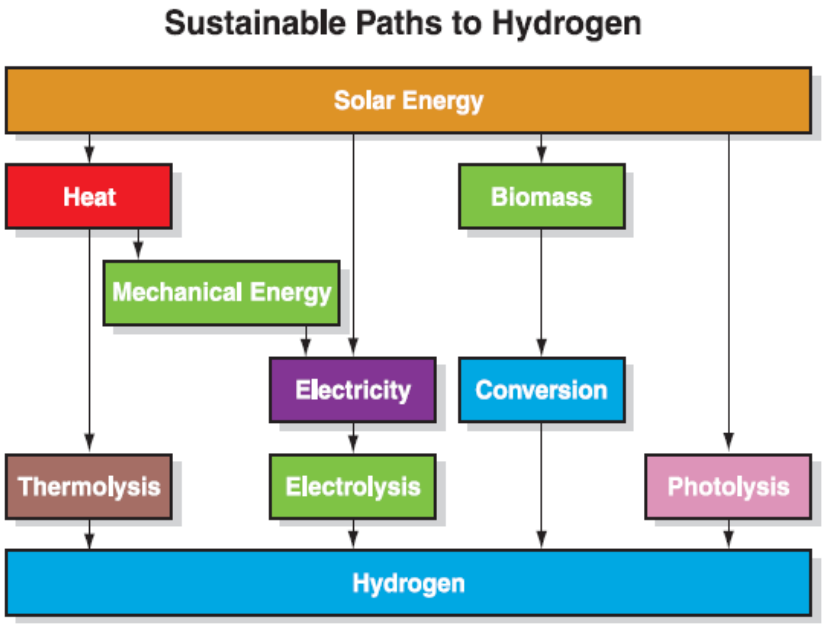

Figure1.15. Sustianble pathways for H_2 production [25] Reproduced by the permission of reference 25: *Science*, **1999**,285, 687-689.

These direct conversion systems include photoelectrolysis and photobiological systems which are based on the fact that visible light should have sufficient amount of energy to split water. [25] Among all these methods H_2 generation from electrolysis of water from solar energy has attracted tremendous attraction as water is clean and sun is inexhaustible source of energy (10000 times greater energy than current energy demand-16TW) and by product of solar driven water splitting is again water. Solar energy used as light is the most efficient solar to hydrogen path because it does not have the inefficiencies associated with thermal transformation or with the conversion of solar energy to electricity followed by electrolysis. Water decomposition by means of sunlight mimics photosynthesis by converting water into H_2 and O_2 using inorganic photo-semiconductors that catalyze the water-splitting reaction:

$$H_2O \rightarrow 1/2\ O_2 + H_2\ (g)$$

Fundamentals and workings of solar driven water splitting and Photoelectrochemical water splitting which are also a prime part of this thesis are discussed in details in later sections.

1.5. Nanotechnology

A simple and basic definition of nanotechnology is "engineering functional systems at atomic, molecular or at supramolecular scale". In other words it is defined as manipulation of matter with at least one dimension size of about 1-100 nm. Actually '*Nano*' is a *Greek* word; meaning dwarf. Mathematically 'Nano' means one billionth. Thus, 1 nm = 10^{-9} m. To get a sense of the nano scale, a human hair measures 80,000 nanometers across or just ten hydrogen atoms in a line make up one nanometer. The concept of new science and devices on such a length scale was seeded first by renowned physicist Richard Feynman in1959 but the term "nanotechnology" was

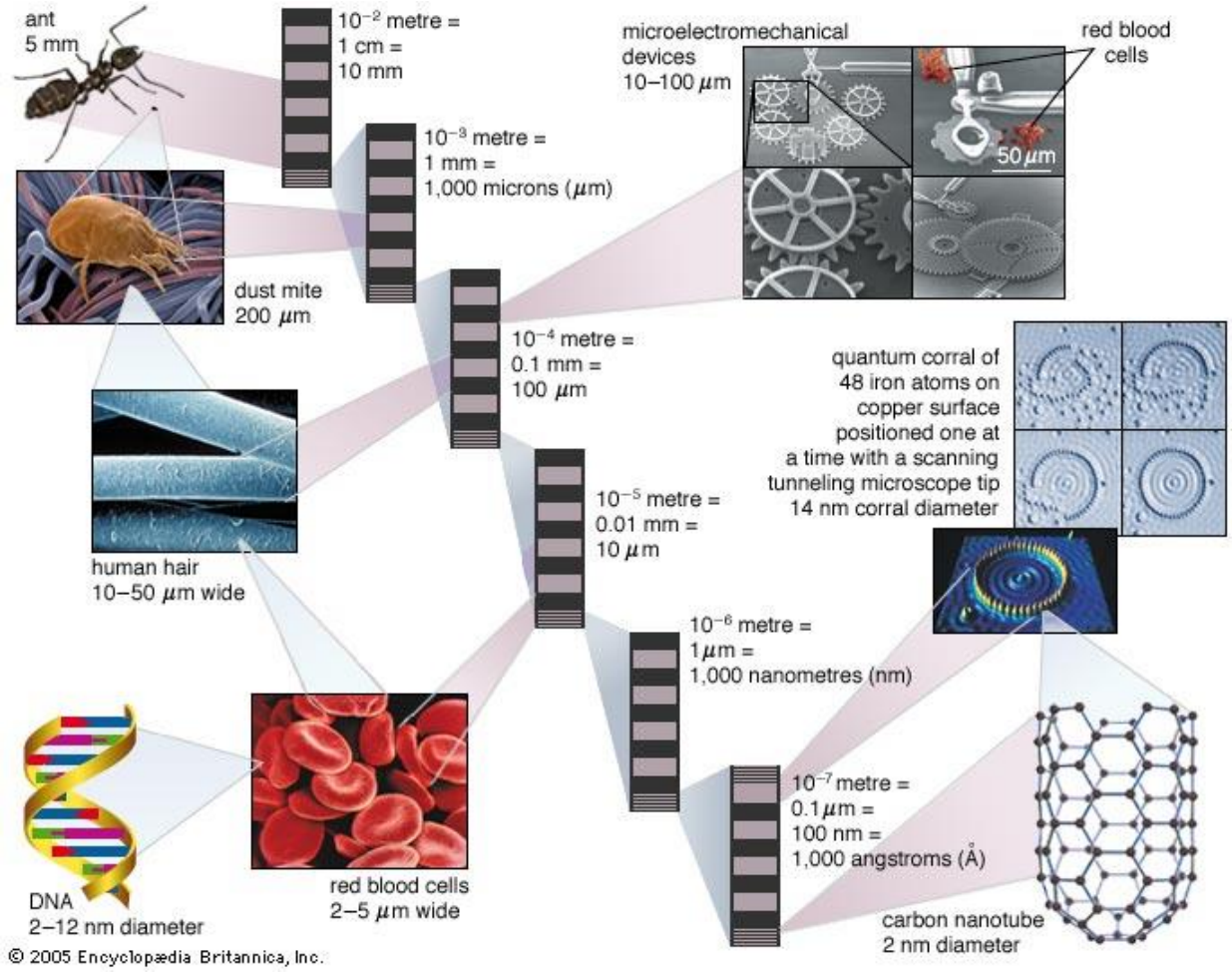

Figure1.16. Visual examples of naturally occurring and man-made materials at nanoscale level

http://blogs.britannica.com/2010/12/nanotechnology-the-science-of-miniaturization-picture-essay-of-the-day

assigned by Norio Taniguchi in1974.[26] Nanotechnology involves nanoscience, engineering, and technology which enable in imaging, measuring, modeling and controlling matter at the nm length scale. **Figure 1.16** shows systems occurring on the nanoscale. These cannot be seen by naked eye, not even by an optical microscope. For this scientist have to use techniques such as transmission electron microscopy, scanning electron microscopy, scanning tunneling microscopy (STM) and Atomic Force Microscopy (AFM).

Nanotechnology involves a new and broad science where diverse fields such as chemistry, physics, biology, computational science, materials science, and engineering converge. Although the research frontier of nanoscience and nanotechnology is quite new, examples of nanomaterials were seen from the past centuries as shown in **Figure 1.17. a)** and **b)** without the civilization at that time having any idea of the length scale involved.

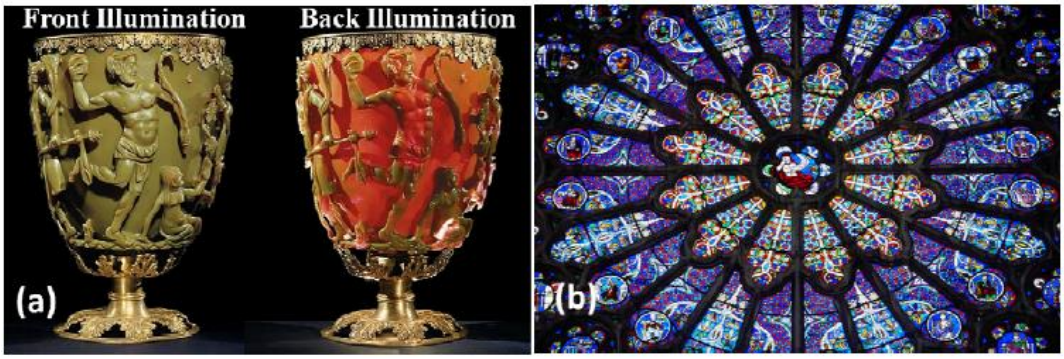

Figure1.17. Ancient examples of nanomaterials used a) Lycurgus cup b) European cathedral window glass

http://www.nano.gov/timeline

In the 4th century Lycurgus glass cup found in Rome contains colloidal gold and silver which allow it look opaque green when lit from outside but translucent red when light shines from inside. Another example was seen in 6-15th century where vibrant stained glass windows were used in European cathedrals which were composed of nanoparticles of gold, metal oxides and chlorides. Later in the modern era much more developed and advanced examples of nanotechnology were seen as shown in **Figure 1.18.**

In 1985 researchers from Rice University discovered Buckminsterfullerene (C_{60}), commonly called as bucky ball which is entirely composed of carbon. In the same year, Louis Brus from Bell lab discovered colloidal semiconductor nanocrystals. Again in 1991, a breakthrough discovery of tubular carbon nanotubes (CNT) by Sumio lijima, turned the direction of nanotechnology to a higher level. Later concurrent and rapid developments occurred in the field of nanotechnology with the arrival of sophisticated instruments like Transmission Electron Microscopy (TEM) and Scanning Tunneling Microscopy (STM) for imaging and probing the chemical bonding in nanomaterials. In the last few years nanotechnology has grown at a fast pace both in laboratories as well as in industry and has begun to affect each aspect of life. The promises and achievements in various applications through nanotechnology have begun to prove their potential for commercialization.[26]

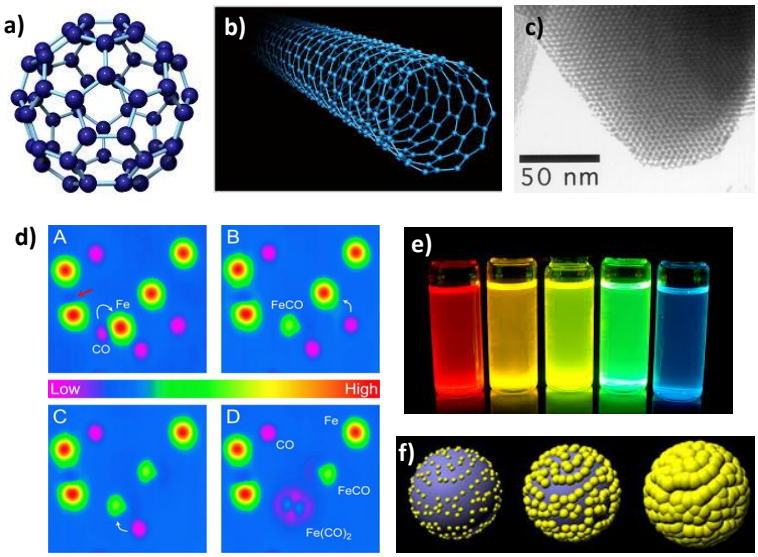

Figure1.18. Modern era examples of nanomaterials a) C_{60} b) CNT c) HRTEM image of SiO_2 nanoparticle d) STM image of inorganic molecule e) Colloidal quantum dots d) Computational modeling of gold shell on silica nanoparticle.

http://www.nano.gov/timeline

1.6. The "Nano-effect"

Significance of nanoscience and nanotechnology lies in the nanometer length scale of the size of the material and the unique "nano-effect" it shows. There are two major and strong nano-effects which affect and govern the physical, chemical, optical, electrical, mechanical and magnetic properties of material which are: a) High surface to volume (S/V) ratio with reduction in size to nanosacle, and b) Confinement effect: i) Increased band gap and ii) Discrete energy levels.

1.6.1. High surface to volume ratio:

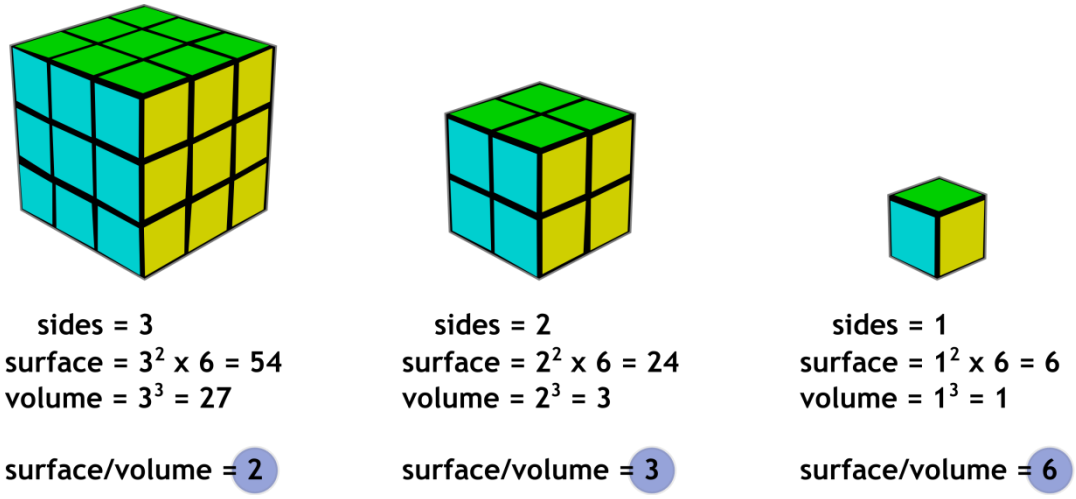

Figure1.19. Surface to volume ratio with reduction in size.

http://sustainable-nano.com/2014/09/23/nano-sensors-small-size-big-impact/

When a material is reduced to nano dimension, maximum numbers of atoms are present on surface. The bulk material is sub-divided into individual nano material whereby the overall volume remains the same but collective surface area increases greatly as shown in **Figure. 1.19.** The corresponding consequence is that the surface to volume ratio increases. The identity of atoms present on the surface is different than that of interior of bulk material and in many

materials the physical and chemical properties are governed by surface phenomena. As the surface area increases it facilitates high adsorption, adhesion or storage ability. On the other hand atoms at surface are reactively unstable with high surface energy which makes them chemically highly reactive. It enables potential application of nano materials in catalytic reactions, detection reaction, chemisorption reactions etc.

1.6.2. Quantum Confinement effect: Optoelectronic properties of nanomaterials

When there is reduction in particle size to the nanoscale level the motion of charge carriers in particular dimension(s) is restricted/ confined making the energy levels discrete and widening the band gap in the case of nano-solids. In a bulk semiconductor, electronic states are so closely packed that they appear as a continuous band but in the case of nanosystems (e. g. quantum dots) the carrier dynamics are restricted along one or more dimensions.

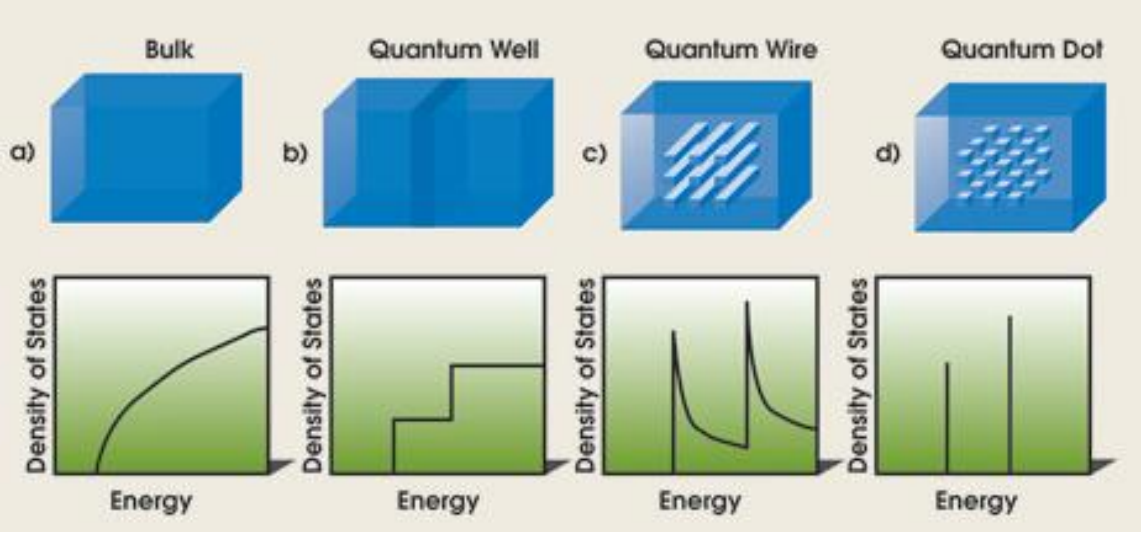

Figure1.20. Graphics representing density of states (*bottom*) as function of dimensions (*top*)

http://www.photonics.com/Article.aspx?AID=31908

For instance, in quantum dots the motion of charge carriers is restricted in all directions (**Figure1.20)** making the energy levels discrete like in an atom. Over all, when the particle size reduces close to exciton radius then the wave function is limited by the quantum confinement and the corresponding effects are felt more strongly. This increases the energy of lowest optical transition from top of the valence band and bottom of conduction band, ultimately increasing the band gap, leading to blue shift in the absorption spectra. This confinement effect plays crucial role in deciding optoelectronic properties of nanomaterials.[27]

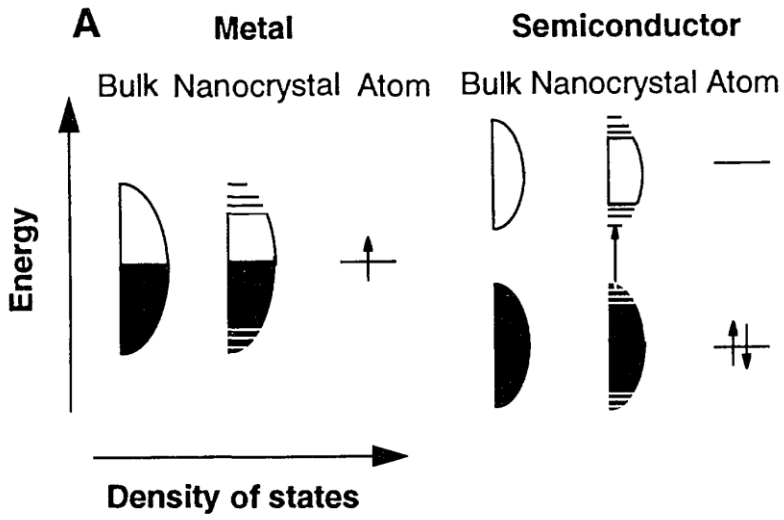

Figure1.21. Density of states in metal and semiconductors.[27] Reproduced by the permission of reference 27: *Science*, New Series, **1996**,271, 933-937.

https://s100.copyright.com/CustomerAdmin/PLF.jsp?ref=f6b3f320-91a2-4628-919d-b7ad129d42b7

Optical properties deal with color and transparency of material. It is actually interaction of matter with electromagnetic waves which involves absorption, emission, transmission and scattering. Absorption and emission of light are affected by discreteness of energy levels which is the reason for the origin of color in nanomaterials whereas scattering of light by different sizes of

nano materials gives rise to specific transparency behavior. Optical properties are also significantly affected by the size, shape, surface features and other aspects like doping. For example, in CdSe quantum dots, as the size decreases it shows ***"Quantum size effect"*** and photoluminescence intensity (PL) shifts to lower wavelength (higher energy) due to increase in band gap. Thus the color of the nanomaterial can be tuned by controlling its size as shown in **Figure 1.21.**[28]

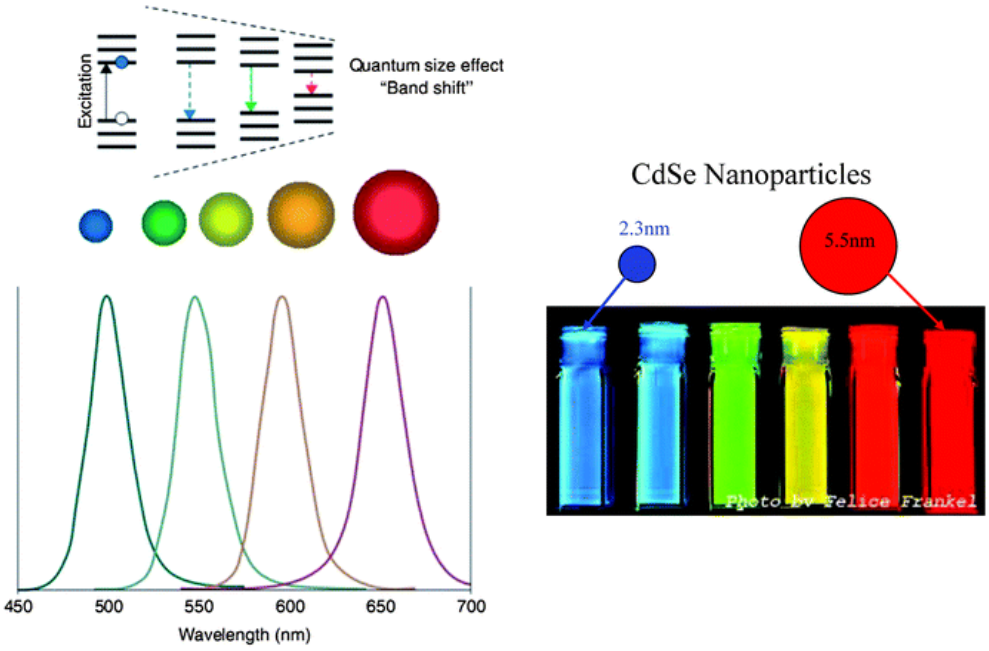

Figure1.22. Size dependant PL and color of CdSe nanoparticles.[28] Reproduced by the permission of reference 28: *Wiley Interdiscip. Rev.: Nanomed. Nanobiotechnol.*, **2010**, 2, 113–129

https://s100.copyright.com/CustomerAdmin/PLF.jsp?ref=198cc411-c2a9-480f-85fe-34c3bb9dd58a

Not only size but the shape also alters the optical properties of nanomaterials. For example, growth of gold nanoparticles of different dimensions shows different absorption properties as shown in **Figure 1.22.a**[29] Some peculiar surface characteristics called as ***"Localised Surface Plasmon Resonance (LSPR)*** shown by metal nanoparticles affect the optical behavior as seen by

gold nanoparticles. When light of wavelength larger than the particle size of metals is incident then it causes *surface plasmon* (a group of surface conducting electrons/electron cloud propagating paralleling in the direction of metal/dielectric interface) to oscillate and sets the free electron to oscillate as shown in **Figure 1.23.b.** LSPR is sensitive to dielectric function, surrounding, shape and size of nanoparticles. Another consequences of LSPR is that colloids of metal nanoparticles impart colors and show visible absorption which otherwise is not seen in their bulk form.[30]

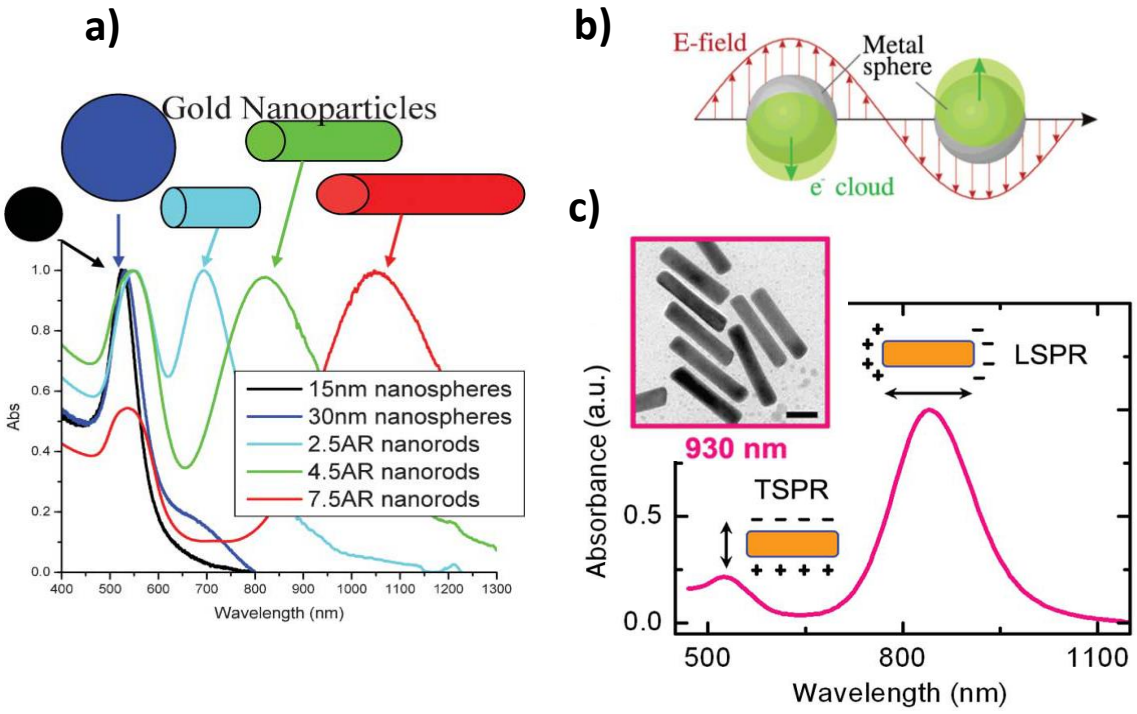

Figure1.23.a) Shape and size dependant absorption spectra of growth of Au nanopaticles.[29] Reproduced by the permission of reference 29: *Chem. Soc. Rev*., **2006**, 35, 209–217.b) Schematic diagram of plasmon oscillation of nanosphere [30] c) Transverse and longitudinal LSPR modes of gold nanorod in absorption spectra.[30]

With reduction in size tremendous nano-effects are seen in the optoelectronic properties of nanomaterials which make them potential candidates for various applications. *In the present thesis nanostructures of metal oxide and chalcogenide are synthesized, characterized and employed for the essential applications of sensitized solar cell and Photoelectrochemical water splitting for hydrogen generation, which are clean and alternative ways of harvesting energy.*

1.7. Metal oxides and their nanostructures

Metal oxide (MO) is chemical compound which contains at least one oxygen atom and one metal. Due to high electronegativity of the oxygen atom it forms a stable bond with metal atoms and have polymeric structure. For example if oxide bonds to three metals it forms rutile structure but if bond to six metal atoms it form rock salt like structure. Depending upon this bonding the metal oxides show different physical, chemical, optical and electronic properties. Due to these properties metal oxides cover a diverse and wide range of properties from superconducting to highly conducting to semiconducting to insulating. They can also be ferromagnetic, ferroelectric, piezoelectric or multiferroic. Due to such huge range of properties, they play a very important role in fields of chemistry, physics, biology, material science.

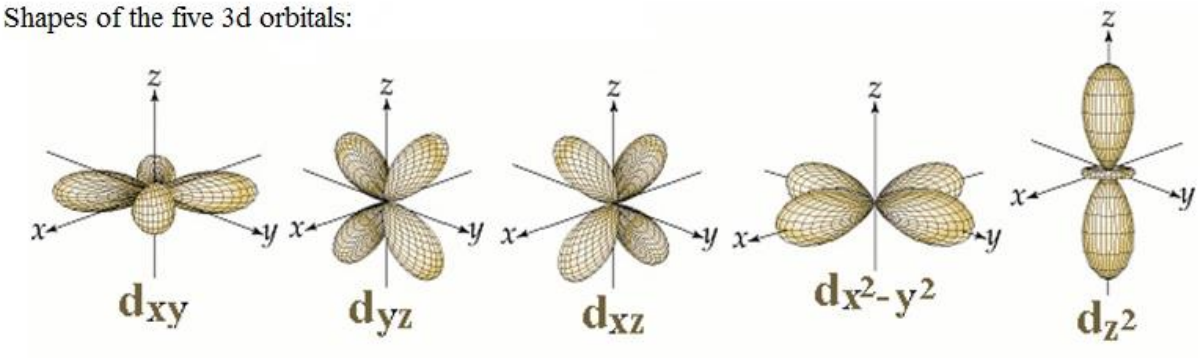

Figure1.24. Five d orbitals of metal oxides**.**

http://2012books.lardbucket.org/books/principles-of-general-chemistry-v1.0/s27-the-d-block-elements.html

Amongst metal oxides, transition metal oxides have attained a wide spread attention in various applications like solar cells, catalysis, fuel cells, microelectronics and sensors. The nature of transition metal bonding with oxygen can change from ionic to covalent to even metallic. Reason for these unusual properties observed in the case of 3d transition metal oxides is the behavior emanating from the outer d-orbital in the transition elements. Electrons in transition metal oxides have choice of several types of energetically equivalent/degenerate *orbitals* as shown in **Figure 1.24** to bond**.** The specific way this freedom is broken is reflected in the interactions of the electrons and hence in their physiochemical and magnetic properties. For example, alternating orbitals on neighboring lattice sites favors ferromagnetism, whereas uniform occupation of orbitals on all lattice sites tends to generate antiferromagnetism.[31] Other uniqueness of transistion metal oxides is that they exist in multiple oxidation states which enables rich redox reactions in the material. This makes them potential candidates for various applications like pseudocapcitor or catalysis industry.

Metal oxide at nanoscale length and the corresponding nanostructures have also attracted many researchers as they are easy to synthesize, inexpensive, stable and eco-friendly. Moreover, they can be fabricated in energy saving manner for nano-devies such as solar cells, fuel cells, light emitting diodes, lithium ion battery, transistors, photodetectors, systems for hydrogen production by electrolysis of water, sensors, and water purification systems.[32] Recently metal oxides like ZnO, TiO_2, SnO_2, Cu_2O have revolutionized the research in the field of nanomaterials due to their availability and compatibility for interesting applications.

The present thesis mainly deals with the transition metal oxide TiO_2, its optoelectronic properties and its engineered nanostructures for the application of sensitized solar cell. Detailed features of TiO_2 and its advantages in solar devices are discussed in the following sections.

1.7.1. Titanium dioxide (TiO_2):

Amongst the metal oxides TiO_2 is one of the most promising and well-studied metal oxide due to its unique optoelectronic properties. On the other hand from the material point of view it is earth abundant, cost-effective, stable, safe and eco-friendly enabling a broad range of applicability. TiO_2 is wide band gap (3-3.2eV) n-type of semiconductor which absorbs in the UV region. It shows three polymorphs: Anatase, Rutile and Brookite.[33] The corresponding crystal characteristics are given in **Table 1.** In bulk TiO_2, the rutile phase is more stable thermodynamically whereas at the nanoscale the anatase phase is stable due to contribution from surface energy. The fundamental framework/unit cell of these polymorphs is TiO_6 octahedron and depending upon different synthesis conditions and parameters their arrangement is decided giving rise to different phases of TiO_2. As seen from **Figure 1.25** anatase TiO_6 octahedra share all edges to form anatase TiO_2 whereas in the rutile case both edges and corners of octahedral are shared, but in a systematic manner. On the other hand in the Brookite case a much more complicated structure is present and octahedra shares both like rutile TiO_2**.**[34]

Anatase TiO_2 is a low temperature and higher pH medium phase whereas rutile is a high temperature, low pH phase. Conventionally rutile is produced by high temperature calcination (800-1200°C) of anatase.[35] Anatase TiO_2 is more favored in optoeletronic applications such as photocatalysis and dye sensitized solar cells because of its surface chemistry, higher conduction

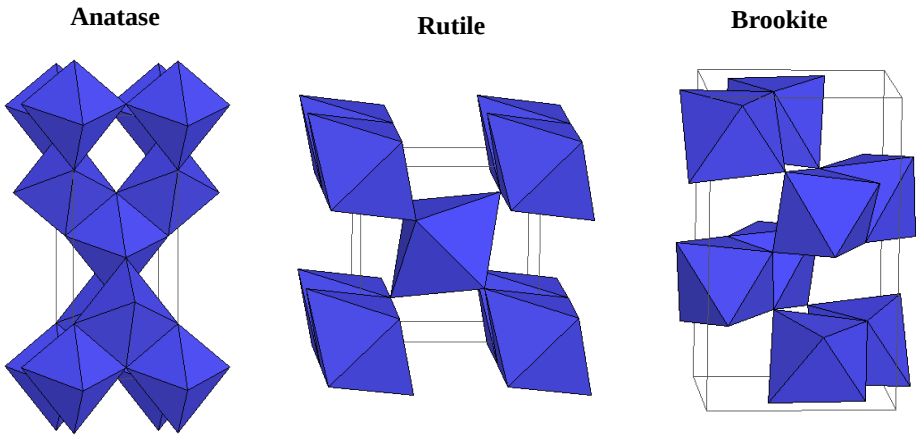

Figure1.25. Polymorphs of TiO_2 [33]

http://ruby.colorado.edu/~smyth/min/tio2.html

Polymorphs	Band gap	Space group	Cell parameter (Å)	Crystal structure
Anatase	3.23 eV	*I 4₁/amd*	a= 3.7845, c=9.5143	Tetragonal
Rutile	3.05 eV	*P 4₂/mnm*	a= 4.5937, c= 2.9587	Tetragonal
Brookite	3.26 eV	*P bca*	a= 9.1840, b= 5.4470, c= 5.1450	Orthorhombic

Table 1. Crystal characteristics of different polymorphs of TiO_2[33]

band edge energy and 10 times higher mobility than rutile TiO_2.[36] But rutile is thermodynamically the most stable and has been traditionally used in numerous application sectors because because of its good light-scattering and light reflecting properties, high refractive index, non-toxicity, and chemical inertness.[37]

TiO_2 nanomaterial is considered to be the most attractive nanomaterial for energy conversion devices due to its unique and tunable properties that can be tuned as per the requirement of a particular application. For example, the electronic structure of TiO_2 reduces the probability of

recombination in nanodevices involved in the electricity production.

The oxidation state of Ti in TiO_2 is Ti^{4+} (d^0) and the valence band is made up of hybridized O2p orbitals and 3d Ti orbitals and the conduction band comprises of 3d Ti orbitals. Due to different parity of valence and conduction band transition of electron in valence band decreases and hence the probability of e- h+ recombination.[38] TiO_2 also offers different modes to alter or engineer its size, morphology, transparency, surface area, porosity and means of surface modification (doping/sensitization). A slight variation in its electronic and structural system creates an altogether different material at nanometer level.

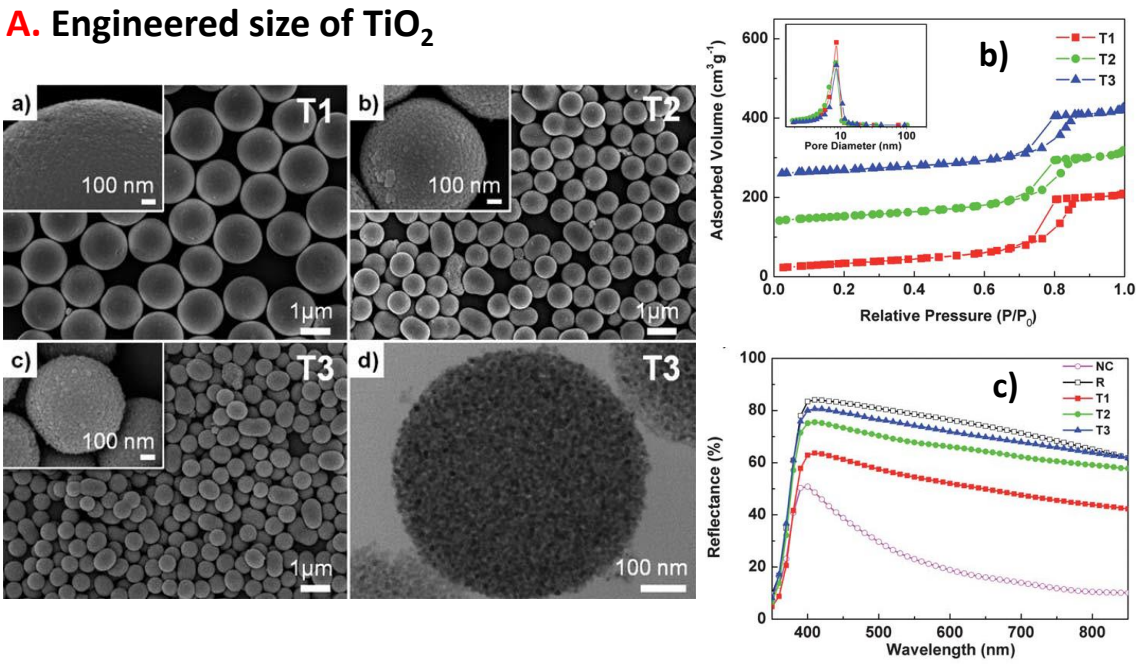

Figure1.26.a) SEM images of size tunable mesoporous spheres of TiO_2 b) N2 isotherm-from T1 to T3 as particle size decreases surface area and pore diameter decreases. (T2 and T3 are shifted by 100 and 200cm^3/g respectively for clearance.) c) Diffuse reflectance spectra.[40]

Reproduced by permission from reference 40: *J. Mater. Chem*., **2011**, 21, 9582-9586.

1.7.1.1. Engineered size of TiO_2

The exciton radius for anatase TiO_2 is nearly 1.5 nm, therefore the typical nano-sizing effects such as quantum confinement effect and the blue shift in the band gap are very difficult to observe in the case TiO_2 nanoparticles.[39] However, the properties of the nanosystems can be tuned by controlling different sizes and shapes which affect their optical properties. For example, Park et al, [40] reported size tuned mesoporous spheres (MS) as shown in **Figure 1.26** which affected the surface area, porosity and light scattering ability. As the size increased, the surface area increased and the optical scattering of light decreased. Such a size-effect in nano-assembled meso- and microscopic forms can be utilized in nanodevices which are potentially involved in light harvesting processes.

1.7.1.2. Engineered morphologies of TiO_2

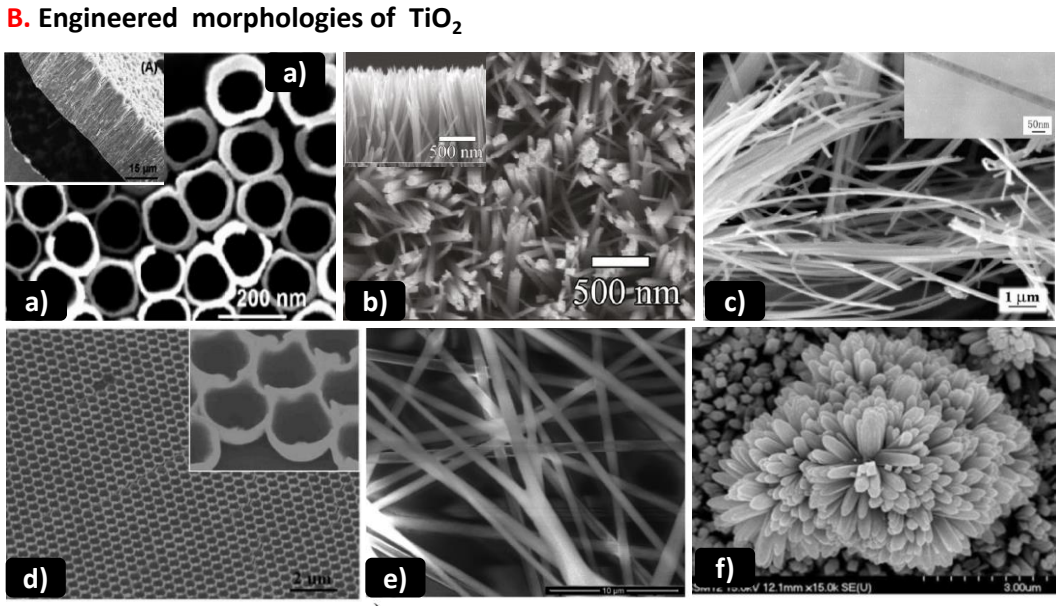

Figure1.27. SEM images of engineered morphologies of TiO_2 a) nano tubes, [41] b) nanorods, [42] c) nanowires, [43] d) nanobowls, [44] e) nanofibres[45], f) nanoflowers, [46].

Reproduced and reprinted by permission of references 41-46.

Being extensively studied as a nanomaterial, the literature contains hundreds of publications on different morphologies of TiO_2.

Depending upon different synthesis parameters (pH, temperature, precursors, capping agent, solvent system, voltage) and techniques (Hydrothermal, pulse laser deposition, electrochemical method, combustion method, spray pyrolysis) different kind of hierarchical architectures of TiO_2 can be obtained such as nanotubes,[41] nanorods,[42] nanowires,[43] nanofibres[44], nanoflowers,[45] nanobowls.[46] as shown in **Figure 1.27**. Some forms of oriented nanostructures provide direct path way for electron transfer and decrease electron hole pair recombination.

1.7.1.3. Engineered composition /band gap of TiO_2

Narrowing the wide band gap of TiO_2 either by introducing disorder or dopants for increasing its absorption range is easily feasible in TiO_2 as shown in **Figure 1.28.**

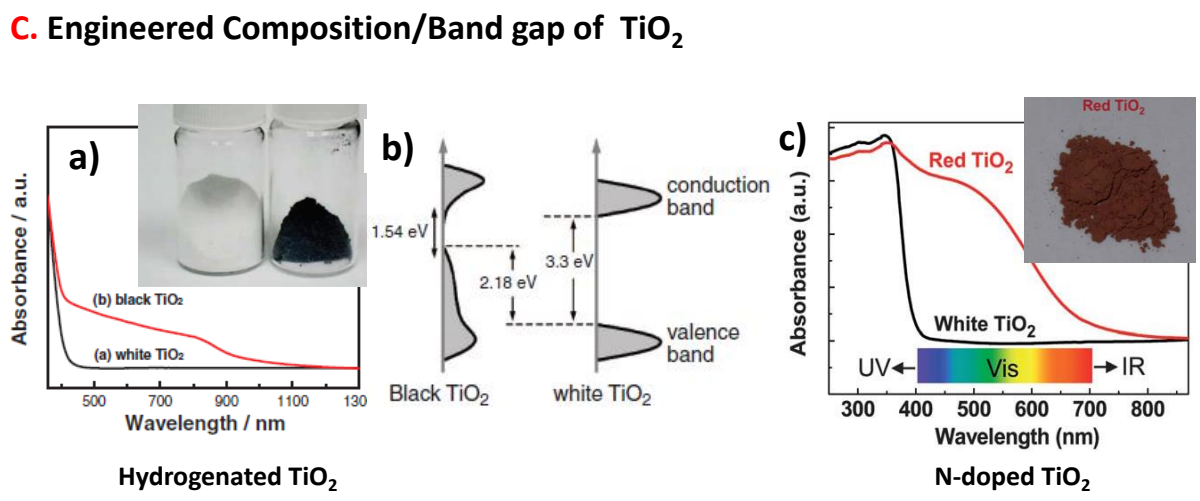

Figure1.28. Enginneered Band gap/composition of TiO_2 a) defect induce black TiO_2 [47] b) narrowing of band gap through induced defects in black TiO_2 [47] c) N-doping in TiO_2.[48] Reproduced and reprinted by permission of references 47-48.

Chen et al[47] showed engineered disordering in TiO_2 nanocrystals by hydrogenation reaction which produced black TiO_2 for photocatalysis application. The same figure also shows Red-TiO_2 due to nitrogen doping in TiO_2. This defect or dopant creates mid- gap states called as band tail states which narrow the band gap and increase absorption of TiO_2 in the visible range.

1.7.1.4. Engineered surface of TiO_2

TiO_2 surface can be engineered by sensitization method where sensitizer can be an organic dye molecule, inorganic semiconductor (QD) or metal nanoparticles. This surface modification does not narrow the band gap of TiO_2 but couples levels of sensitizers such that absorption of TiO_2 can be tuned in the visible region. Thus, surface modification can be used to alter the optical properties of TiO_2 nanoparticle based complexes. By surface engineering the photochromic properties of TiO_2 can also be tuned. For example, Ohko etal.[50] found that in Ag sensitized TiO_2 nanoparticles the color of the film could be reversely switched back and forth between brownish-

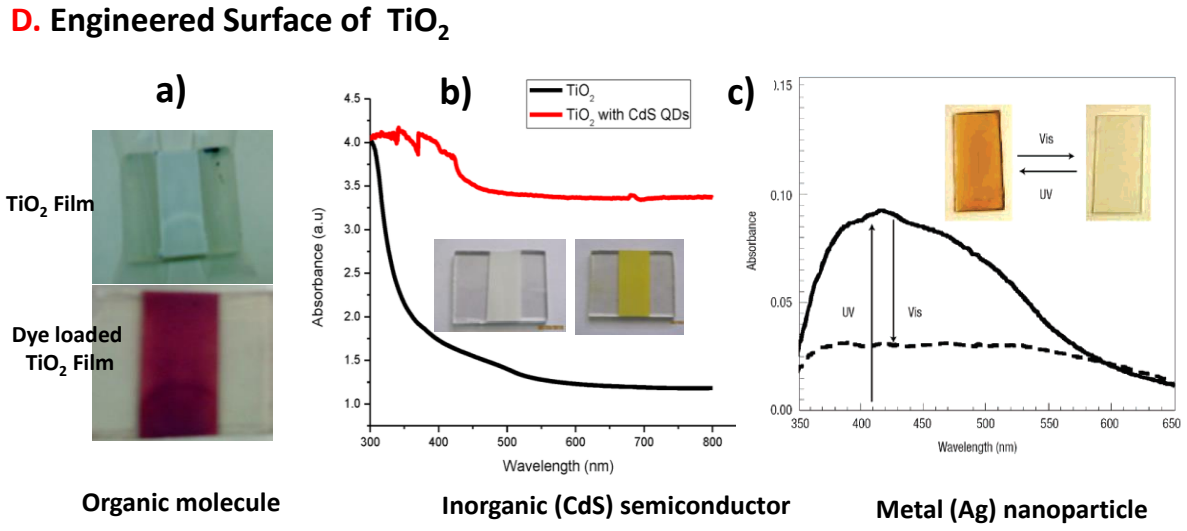

Figure1.29. Enginneered surface of TiO_2 by sensitization of a) organic dye b) inorganic semiconductor (CdS) [49] c)Metal (Ag) nanoparticle [50] Reproduced and reprinted by permission of references 49-50.

gray under UV light and the color of illuminating visible light due to the oxidation of Ag by O_2 under visible light and reduction of Ag+ under UV light as shown in **Figure 1.29.c)**

1.8. Metal Chalcogenides and their nanostructures

Chalcogenide is a chemical compound composed of at least one "chalcogen anion" and other electro positive element. The word "chalcogen" was given by Werner Fischer[51] in 1930 which was accepted later in the Committee of the International Union of Chemistry (now called as IUPAC). The chalcogen atoms represent a group of 16 elements of the periodic table which has sulfur (S), Selenium (Se) and tellurium (Te). Originally oxygen was also included but was later excluded from this family. The word chalcogen is a *Greek* word in which "*Chal*" means copper and "*gensis"* means birth. Thus the word implies ore forming elements.[51]

Out of alkali, non-alkali and transistion metal (TM) chalcogenides, TM metal chalcogenides have attracted much of attention due to their potential applications in the field of solar devices, solar coatings, microelectronics, sensors, optical fibres, catalysis etc.[52-55]. In mono chalcogenide M-X type of system is present where M is a metal atom such as Cd, Cu, Ni, Co bonded to X chalcogen- S, Se, Te. In dichalcogenides two chalcogens are covalently bonded to metal ion (X-M-X) particularly forming layered 2D structures in which adjacent X atom layer is bonded by week "Van der Waals" forces. These are of particular interest due to their remarkable properties like d-p covalent mixing, order-disorder transistion and a wide range of electrical properties. In addition, d-electrons of the metals can give rise to new physical phenomena, including excellent electrical transport properties and high on/off ratios that are ideal for use in optoelectronic and solid-state junction devices.

TiS_2, $TiSe_2$, $TiTe_2$, $ZrTe_2$, and $HfTe_2$ compounds may be roughly classified as metallic materials due to an overlap of the chalcogenide s and p states with the metal d states. The 2D layered structures of Group IV-VI transition metal dichalcogenides MX_2 (M = Ti, Zr, Hf, Nb, Ta, Mo, W) as well as of the ternary alkali metal/3d-metal systems AMX_2 (A = alkali metal; M = Ti, V, Cr, Mn, Fe, Co, Ni) are capable of intercalating various guest species.[52] Hence these can be employed in energy storing systems like batteries. SnSe, MoS_2, WS_2 nanocrystals have suitable band gap energies (0.7–1.4 eV) with high absorption coefficient, which are critical for solar energy harvesting and photocatalytic applications.[53] Also, di, tri ($CuInS_2$, $CuInSe_2$, CdSeS, CdTeSe, PbSeS, $NiCoS_2$) [54-59] and quaternary (Cu-Zn-Ti-S, Cd-Zn-Se-S, Zn-Ag-In-S) [60-62] chalcogenides also exist. They are highly luminescent making them useful in applications such as light emitting diodes, optical sensors and biological imaging. Also they have high conductivity and catalytic activity originating from synergistic effect of metals making them efficient photocatalyst.

The present thesis mainly deals with two chalcogenide systems, namely NiS_2 and $CuInS_2$, their engineered nanostructures and their optoelectronic properties for the applications of photoelectrochemical water splitting and sensitized solar cell, respectively.

1.8.1. $CuInS_2$:

$CuInS_2$ (CIS) is a ternary sulfide which is alternative to toxic cadmium or lead containing semiconductors. It is a direct band gap semiconductor with a gap of 1.45eV. It has a high extinction co-efficient of 10^5 in the visible region. Bohr radius of CIS is 4.1nm and therefore quantum confinement effect can only be seen below about 8nm.[63] $CuInS_2$ is referred to as a chalcopyrite in which each sulfur atom is surrounded by two copper atoms and two indium

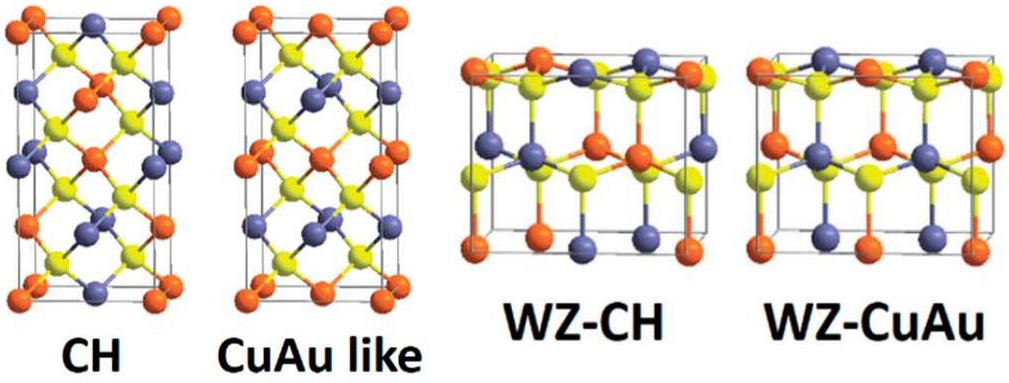

Figure1.30. Schematic diagram of $CuInS_2$ structures where red ball is symbolized for Cu, blue for In and yellow balls for S atoms.[64] Reproduced by permission from reference 64: *RSC Adv.*, **2014**, 4, 23505.

atoms, which is a doubled structure of zinc-blend system along the c-axis. A slight variation in the atomic arrangement in chalcopyrite would lead to a metastable CuAu-like structure, in which the copper layer and indium layer exist alternatively beside the sulfur layer. Likewise, other two metastable phases of $CuInS_2$ can be derived from the wurtzite phase. They are orthorhombic structures and usually referred to as wurtzite-chalcopyrite and wurtzite-CuAu-like structures. CH phase is stable at high temperature but CA phase is not.[64]

CIS shows good catalytic activity and conductivity. Depending upon the stiochiometry n or p-type conductivity is realized. At the nanoscale level CIS offers opportunities to engineer its size, morphology, and composition which alter its optical and electronic properties. This makes it potential candidate for solar cells, LEDs, biolabelling and sensors.

1.8.1.1. Engineered size of $CuInS_2$

CIS quantum dots show quantum confinement effect; hence with the size decrease the absorption can be tuned over the whole visible region as shown in **Figure 1.31.**This same effect is also seen on emission.[63]

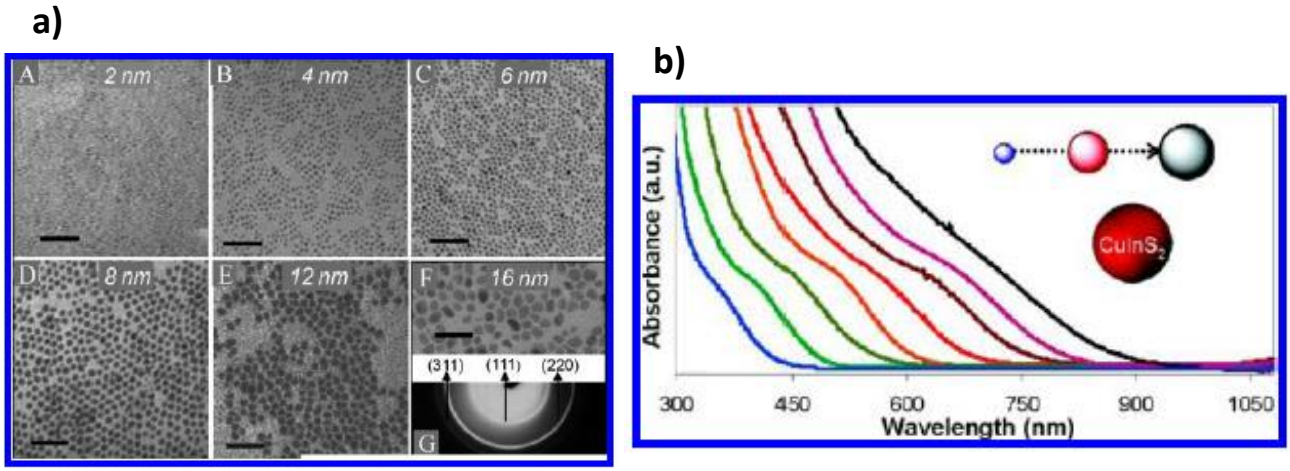

Figure1.31. a) TEM images of CIS of 2-16nm size b) Size dependant absorption spectra of CIS.[63] "Reprinted with permission from (*ACS Appl. Mater. Interfaces*,**2013**, 5, 12221−12237). Copyright (2013) American Chemical Society.

1.8.1.2. Engineered morphologies of $CuInS_2$

Different morphologies of CIS can be engineered as shown in **Figure 1.32** by controlling different combinations of parameters which provide high surface area and direct pathway for electron transfer.

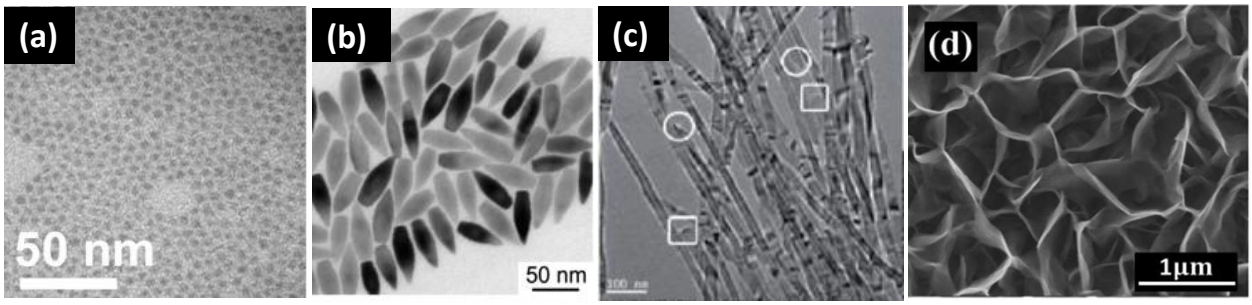

Figure 1.32.TEM images of CIS of different morphologies a) Quantum dots [65] b) nano spindle [63]nanoribbons [63] d) nanosheets [66] Reproduced and reprinted by permission of references 66, 65-66.

Their most unique form lies in the colloidal form as in this form or in solution/ink they can be easily applied to inexpensive and flexible substrates by spray or spin coating as they make better contact at junctions. Also such production is easily scalable to large production scale.

In solution processible method if organic ligand is exchanged with inorganic ligand to encapsulate and bind QD then it can be shrunk/ wrapped to small nm region where electrons can quickly and smoothly travel avoiding large distances.

1.8.1.3. Engineered composition of $CuInS_2$

Not only the size but also the composition can influence the bandgap of CIS nanocrystals. The valence band of CIS, which is composed of Cu 3d and S 3p orbitals, is lowered in copper deficient particles. Thus, the bandgap is widened in Cu poor CIS nanocrystals.[63]

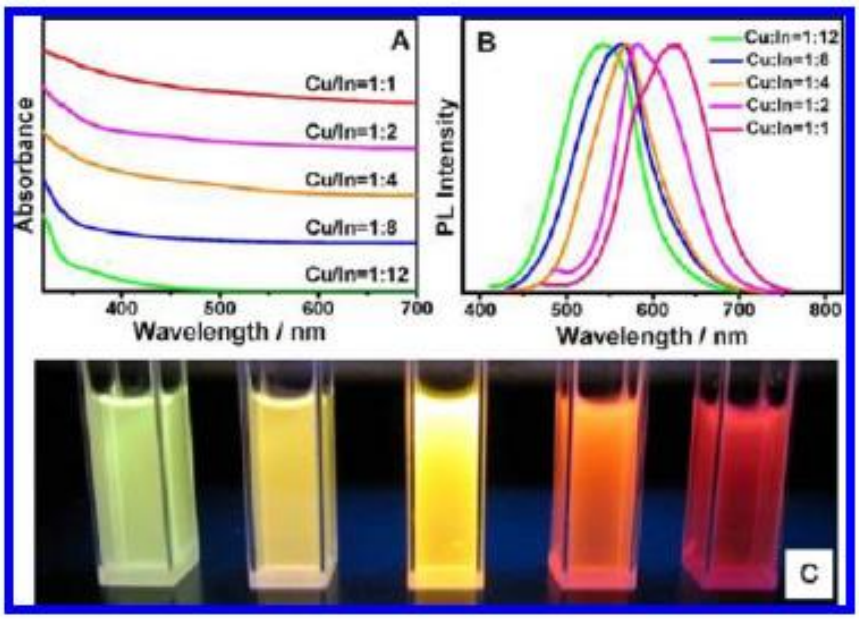

Figure1.33. Effect of composition on a) absorbance b) PL c) colour of CIS colloidal solution [63]"Reprinted with permission from (*ACS Appl. Mater. Interfaces,* **2013**, 5,12221−12237). Copyright (2013) American Chemical Society.

1.8.2. NiS_2:

Nickel disulfide, NiS_2 is a 3d transition metal dichalcogenide which exhibit pyrite structure. This structure is similar to NaCl face centred like where; Ni^{2+} is in cation site and S_2^{2-} chalcogen atomic pairs on anion site. NiS_2 is an antiferromagnetic insulator (gap, 0.3-0.8 eV), in spite of the half-filled eg band, and is therefore considered to be a Mott insulator. However, the surface of NiS_2 appears to be metallic which has been attributed to lattice relaxation near the surface. So the Hall effect and photoemission measurements support the surface property being quite different from that of bulk.[67] Due to its unique opto-electronic properties it is widely applicable as a catalyst or coating for photogalvanic cells, a metal insulator, a paramagnetic–antiferromagnetic Phase - changing material, a hydrodesulfurization catalyst, and a cathode in rechargeable lithium batteries.[68]

1.9. Metal oxides and Chalcogenides for Dye Sensitized Solar Cell application

1.9.1 Dye Sensitized Solar Cell (DSSC)

1.9.1.1. Working principle:

In a typical DSSC configuration, there are two electrodes, one is photoanode (working electrode) and the other is photocathode (counter electrode) as shown in **Figure 1.34.** The working electrode is dye loaded porous TiO_2 nanoparticle film coated on transparent conducting oxide (TCO) whereas the counter electrode is platinum NP coated TCO. These two electrodes are sandwiched together and in between a liquid electrolyte (a redox couple) is added. When light is incident on the photoanode passing through TCO, dye molecules get excited and transfer the electron to the conduction band (CB) of TiO_2 as HOMO of dye is above the CB of TiO_2. The transferred electron passes to the TCO through TiO_2 nanoparticle film by diffusion mechanism.

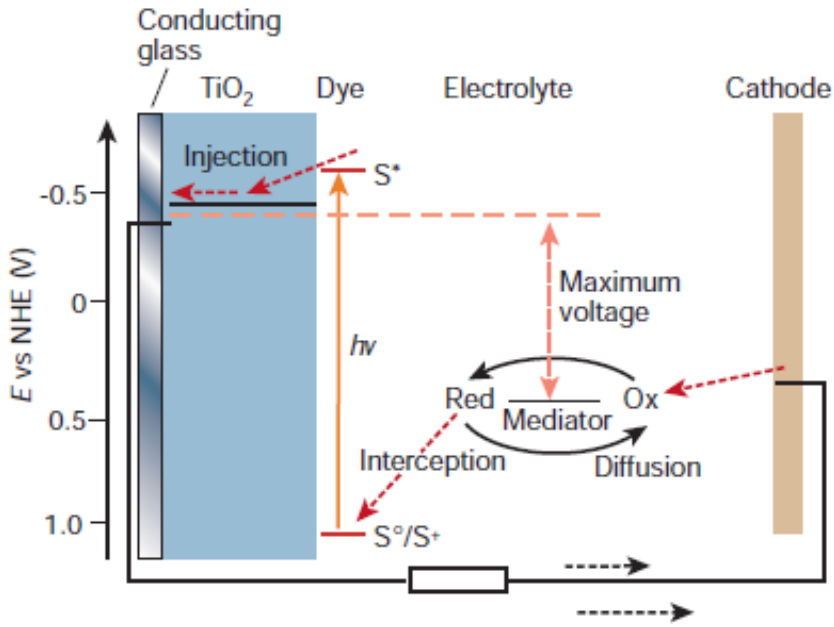

Figure1.34. Schematic energy level diagram of DSSC working [69] Reprinted with permission from (*Nature*, **2001,** 414,338-344). Copyright (2001) American Chemical Society.

On the other hand the oxidized dye molecule is regenerated by taking the electron from redox couple which is in the form of iodine /triiodide species. This redox couple is also regenerated by taking up the electron from the counter electrode coming from the external circuit. Transfer of electrons during the cell operation involves the following steps: [69, 70]

$TiO_2|\ S + h\upsilon \rightarrow\ TiO_2|S^*$ Excitation of dye upon irradiation (1)

$TiO_2|\ S^* \rightarrow\ TiO_2|S^+ +\ e^-$ Oxidation of dye due to injection of electrons into TiO_2 (2)

$TiO_2|\ S^+\ +\ e^- \rightarrow\ TiO_2|S$ Dye recovers its original ground state (3)

$TiO_2|\ S^+ + 3/2I^- \rightarrow\ TiO_2|S + 1/2I_3^-$ Oxidization of the electrolyte (4)

$1/2I_3^{-\ +}\ e^- \rightarrow 3/2I^-$ Restoration of electrolyte at the counter electrode (5)

$I_3^-\ +\ 2e^- \rightarrow\ 3I^-$ Redox reaction (6)

S: Dye sensitizer; *: excitation upon irradiation; +: Oxidation

The reason for such charge transfer is the nature of the band alignment. The working principle of DSSC mimics the naturally occurring process of photosynthesis. In photosynthesis light energy is converted into chemical energy; wherein the light absorber is green colored pigment "chlorophyll' whereas in DSSC the organic dye molecules act as light absorber. This breakthrough in solar cell was achieved in 1991 by O'Regan and Gratzel[70] whereby a power conversion efficiency of 11% was reported. DSSC is thus also called as "Gratzel cell". Compared to conventional silicon solar cells this cell is cost-effective, easy to fabricate even over large area and generally involves eco-friendly protocols.

1.9.1.2. Components of DSSC:

a) Transparent conducting substrate

In most cases, the bottom electrode substrate used is a transparent conducting oxide (TCO) coated on glass. TCO material usually used is fluorine doped tin oxide (FTO) or tin doped indium oxide (ITO). They are thin films that function as a current collector and a support of the semiconductor layer in DSSCs. Usually, FTO substrate which has low sheet resistance of (10-15 Ω /cm), high transmittance > 80% and high thermal stability is used in DSSC. The transparency and conductivity of the substrate are crucial criteria while making the choice of the substrate.

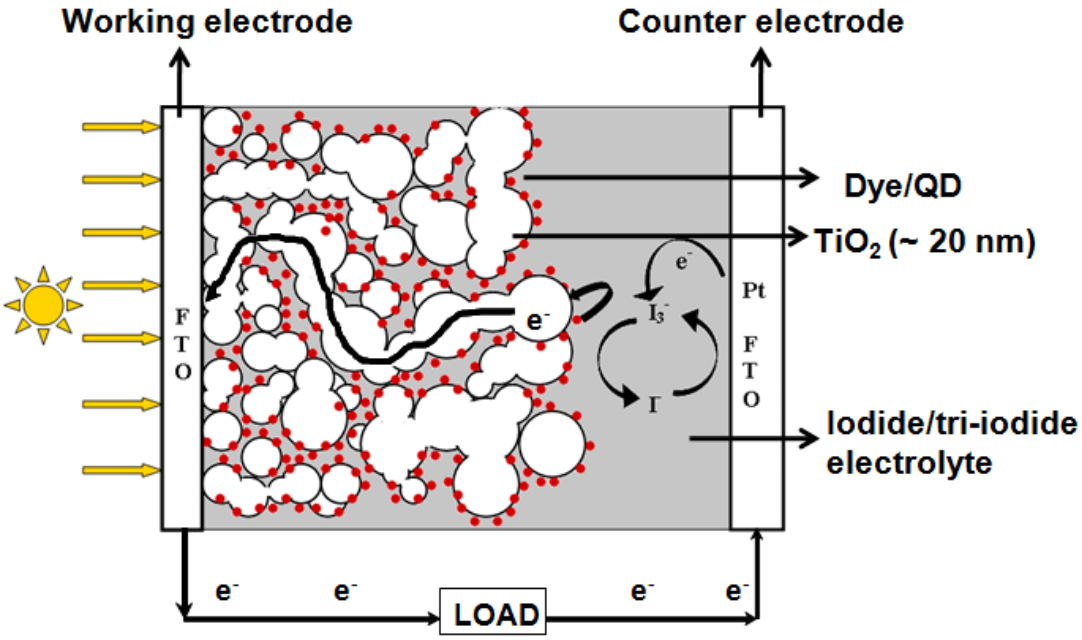

Figure1.35. Schematic architecture of DSSC

b) Semiconductor Photoanode: metal oxide coating

The photoanode is a key component for DSSC which plays an important role in dye loading, electron injection, transportation and collection, and therefore exhibits significant influence on

photocurrent, photovoltage and the power conversion efficiency. Different material structures, including zero dimensional (0D) nanoparticles, quasi-one dimensional (quasi-1D)/one dimensional (1D) nanostructures, and hierarchical nanoarchitectures, have been developed. Of these the last kind of structure shows a great potential in achieving high performance DSSCs. Therefore, the photoanode materials need to meet several conditions: First, the conduction band edge of the semiconductor should be below the LUMO of the dye molecules to ensure an effective injection of the photo-induced electrons from the dyes to the semiconductor. Second, the semiconductor film should have a high surface area to absorb more dye molecules. Third, the porosity of the semiconductor film must be high enough to ensure that the electrolyte can permeate well into the interior of the film, forming a good ohmic contact at the interfaces between them. Fourth, the electron mobility of the semiconductor should be high enough to transport the photo-injected electrons quickly to the outer circuit.

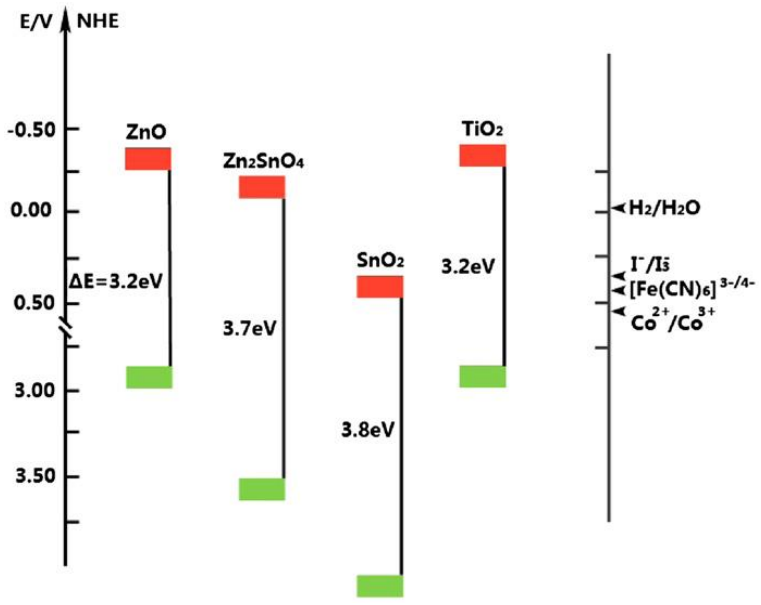

Figure1.36. Band edges of metal oxide w.r.t. to NHE and different electrolyte

Many n-type metal oxides like TiO_2, [70],ZnO, [71] SnO_2 [72] are used as photoanode material and are coated on TCO. But most widely TiO_2 is employed as it very efficiently fulfills the above mentioned criteria. Therefore it is also called as "work horse" or "vehicle" or "heart" of DSSC.

c) The Sensitizer:

The ideal sensitizer has to meet several requirements that guide effective molecular engineering: (i) the sensitizer should be able to absorb light over a broad range up to the IR wavelength; (ii) it should have a carboxylate or phosphonate group to anchor on the surface of semiconductor oxide; (iii) the lowest unoccupied molecular orbital (LUMO) of the sensitizer should be above the edge of the conduction band of the oxide to minimize the energetic potential losses during the electron transfer reaction ; (iv) the highest occupied orbital (HOMO) of the sensitizer must be sufficiently low to accept electron donation from an electrolyte or a hole conductive material ; (v) it should be stable.

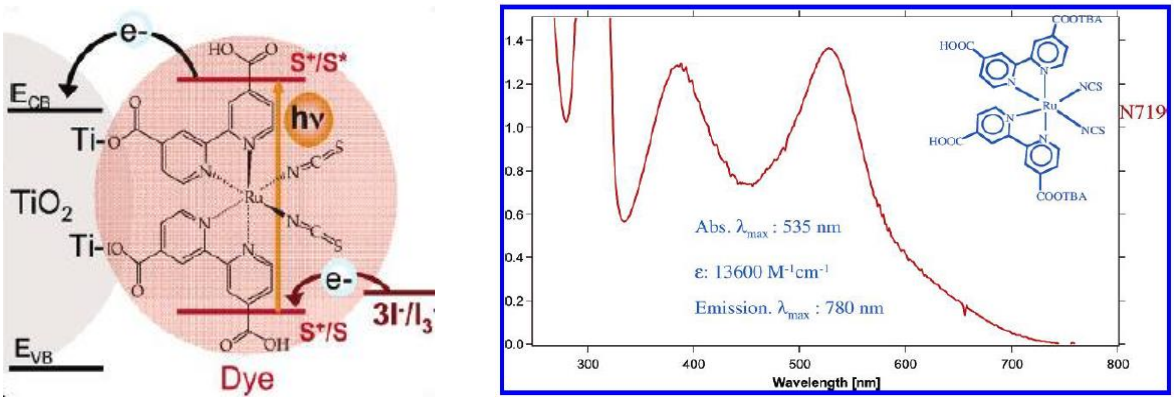

Figure1.37. Schematic diagram of TiO_2 sensitized with N719 dye with its anchoring groups and band edges (left).Absorption spectra of N719 dye. (right) [73] Reprinted with permission from (*Inorg. Chem.* **2005,** 44, 6841-6851). Copyright (2005) American Chemical Society.

Typically the metal oxide films are immersed in the dye solution for 12 to 24 hrs so that the dye molecules get adsorbed on the surface of the metal oxide nanoparticles. Standard dyes used in DSSC are ruthenium based complexes such as N719, N3 etc.[73] But the high cost, limited abundance and availability of noble metals, and also the sophisticated synthesis and purification steps have pushed the scientific community to search for some metal free organic dyes and even natural dyes as well.[74]

d) Electrolyte:

The role of electrolyte is to collect the electrons at the cathode and transport them back to the oxidized dye molecules to regenerate them. The most commonly used liquid electrolyte, namely iodide/ triiodide (I^-/I_3^-), works well mainly due to its kinetics and appropriate energy level(s).[75]For an ideal electrolyte the redox potential should be above the LUMO of dye. In the electrolyte, the I_3^- diffuses to cathode to harvest electrons and in turn produces I^- which diffuses in the opposite direction towards the TiO_2 electrode to regenerate the dye molecules. So diffusion properties of electrolyte should be good enough to avoid mass-transport limitations. It should also be non-corrosive towards collecting metals and should show good photochemical stability.

In theory, the maximum voltage generated in DSSCs is determined by the difference between the quasi-Fermi level of the TiO_2 and the redox potential of the electrolyte, which is about 0.6-0.7V under solar illumination conditions. In order to obtain a higher open circuit voltage and control the corrosion of I^-/I_3^- redox couple, a variety of alternative redox couples have been introduced in DSSCs such as Br^-/Br_3^-, $SCN^-/(SCN)_2$, $SeCN^-/(SeCN)_3^-$, $Fe(CN)_6^{3-/4-}$ [76] and Co(II)/Co(III)complex.

e) Counter electrode:

The counter electrode used in DSSC is generally platinium nanoparticles coated on FTO. Pt counter electrode is very efficient in I^-/I_3^- redox regeneration (the conversion of I_3^- to I^- occurs on the surface Pt) which in turn helps in the regeneration of oxidized dye. Thus, platinum acts as catalyst for the charge transfer reaction occurring between iodide and tri-iodide.[77] However in view of the high cost and less natural abundance of Pt, in recent years significant efforts are directed towards the replacement of this Pt catalyst with other inexpensive and earth abundant materials like CNTs, [78] functionalized graphene,[79] mesoporous carbon,[80] sulphides, carbides, nitrides and some organic inorganic composites.[81]

1.9.1.3. Governing parameters of DSSC performance:

In this section, we describe the important parameters that characterize the photovoltaic performance of DSSC and also briefly explain the factors affecting these photovoltaic parameters.

a) Open – circuit voltage (V_{OC}): Open circuit voltage in DSSC is the difference between the quasi-Fermi level of the TiO_2 and the electro-chemical potential of the electrolyte. Mathematically it is expressed as,

$$V_{oc} = E_{CB}/q + kT/q \ln(n/N_{CB}) - E_{redox}/q \qquad \text{(volts)}$$

Where, E_{CB} is the energy of TiO_2 conduction band edge, n is the concentration of injected electrons in TiO_2, N_{CB} is the effective density of trap states below the conduction band edge and E_{redox} is the redox potential of the electrolyte. Therefore, it can be understood that the V_{OC} in DSSC depends on the dye absorbance as it determines n, quality of TiO_2 nanoparticles as it

determines the trap state density N_{CB} and the redox potential of the electrolyte. Experimentally open circuit potential is obtained by measuring the potential difference between the working and counter electrodes of illuminated DSSC under the condition of infinite load attached between the two. It is the X-intercept of the JV curve of DSSC as shown in **Figure 1.38.**

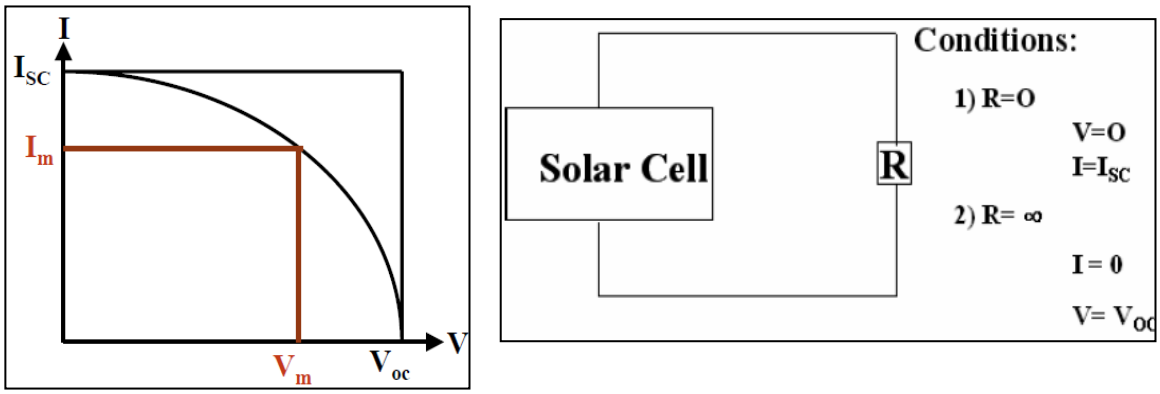

Figure1.38. I-V parameters of Solar cell

b) Short Circuit Current (J_{SC}): This is the current density obtained from an illuminated DSSC when the working and counter electrodes are short or load resistance is zero. It is the y-intercept of the J-V curve of DSSC. J_{SC} in DSSC depends on the spectral response, the absorption coefficient of the sensitizer and the recombination dynamics within the cell. Therefore, the sensitizers with high absorption coefficients, absorbance deep in the visible region (up to 800-850nm) and appropriate HOMO-LUMO levels is an ongoing quest in the field of DSSC.

c) Fill factor: Mathematically it is defined as the ratio of maximum output power from DSSC to the product of V_{OC} and J_{SC}. Thus, fill factor is given by

$$FF = V_{max} * I_{max} / V_{oc} * I_{sc}$$

Where V_{max} and I_{max} are the values of voltage and current corresponding to the maximum power of DSSC. Geometrically fill factor determines the degree of rectangular nature of JV curve. The

value fill factor is also dependent on the series resistance (Rsc) and shunt resistance (Rsh) of the DSSC. The Rsc in DSSC corresponds to the collective resistance offered by the contact resistance at the electrodes, the bulk resistance of the cell and sheet resistance of the substrates. Therefore, the high value of series resistance can affect the maximum output power of the DSSC and hence leads to lowering of FF. The Rsc of DSSC is equal to the reciprocal of the slope of the J-V curve at V_{OC}. The charge recombination within the photoactive layer gives an alternate path for removal of photogenerated electron-hole pairs which leads to the loss of photo-current and also the maximum output power. The resistance to this recombination within the photoactive layer is termed as shunt resistance, and it should have high value in order to achieve maximum photovoltaic performance. It can be obtained from the inverse of the slope of the J-V curve at J_{SC}.

d) Conversion Efficiency: Mathematically it is the ratio of maximum obtainable power from DSSC to the input power from the solar radiations which is expressed as,

$$\eta\% = (V_{oc} * I_{sc} * FF)* / P_{in}$$

The standard condition for the efficiency measurement of DSSC is under 'AM1.5 Global' solar irradiance ($100mW/cm^2$) and at a temperature of 25°C.

e) Incident Photon to Current Conversion Efficiency (IPCE)

'External Quantum Efficiency (EQE)', Quantum efficiency (QE) or sometimes also referred to as Incident Photon to Charge Conversion Efficiency (IPCE) is a measure of how efficient a solar cell is in producing photo-generated charge at a given wavelength. It is defined as the ratio of the number of incident photons to the number of charge carriers generated and is a function of the excitation wavelength:

$$IPCE\ (\lambda) = 1240 * I_{sc} / \lambda * \phi$$

where, I_{SC} is the short circuit current (mA/cm^2), λ is the wavelength (nm) and ϕ is the incident radiation light flux (W/m^2). For DSSC, the term is defined as:

$$IPCE\ (\lambda) = LHE(\lambda) * \phi(inj) * \eta(coll)$$

where, LHE(λ) is the light-harvesting efficiency for photons at wavelength λ, ϕ(inj) is the electron injection quantum yield for the excited sensitizer to the semiconductor oxide conduction band and η(coll) is the fraction of injected charges that is able to reach the back contact. J_{sc} can be calculated by integrating the product of incident photon to current efficiency (IPCE) and incident photon flux (P_{in}) over the spectral distribution.

1.9.2 Engineered metal oxide (TiO_2) for DSSC application

1.9.2.1. Size: "Double-layered Structure"

As mentioned earlier the photoanode of DSSC is made up of mesoporous TiO_2 nanoparticles coated on FTO with optimum thickness of about 14-15 μm as shown in **Figure 1.39.** In this thickness three different layers of TiO_2 are composed. The first layer is a basic thin *blocking layer coated on FTO* to avoid contact of electrolyte with FTO which will otherwise short the device. The second and third layers of DSSC are very crucial in terms of size of TiO_2 used in each layer as they are governing factors of DSSC performance. The second layer is composed of 20-30nm nanoparticles of TiO_2 whereas the third/top layer is made up of 400nm particle size. Because of these two different configurations it is also called as **"Double layered /Bi-layered structure".** Therefore, for utilizing more photons large quantity of dye molecules should be adsorbed on TiO_2. For this purpose TiO_2 nanoparticles should have maximum surface area which

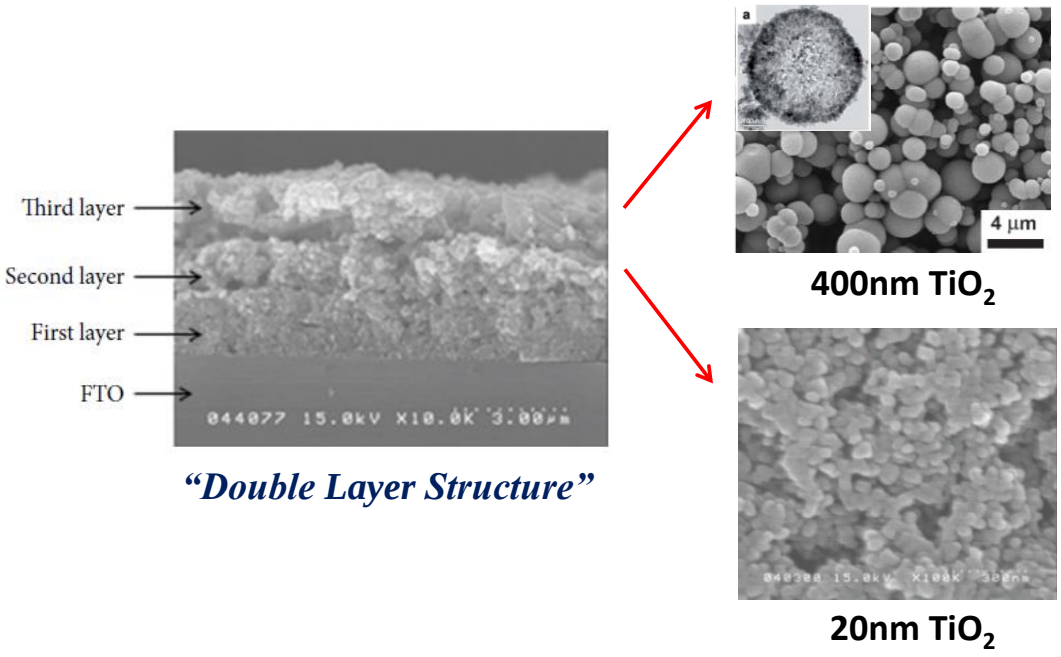

Figure 1.39. Double layer structure of DSSC.[82]

in turn is provided by 20nm particles size compared to larger particles than them. This ultimately increases the photocurrent of device. But as seen from **Figure 1.37** (right) the absorption maximum of N719 dye is only till 550nm. Beyond 550nm its absorption co-efficient decreases; that is a higher absorption length is required to harness light greater than 550nm. For this purpose the path length of light should be increased which is not achieved by transparent layer of 20nm particles of TiO_2. Thus a second layer of TiO_2 nanoparticles of 400nm is applied which shows strong back scattering (80%) of light into the underlying layer. This backscattered light is recaptured by the second layer and maximum light is absorbed which very well reflected in the IPCE is shown in **Figure 1.40.** [82, 83, 84]

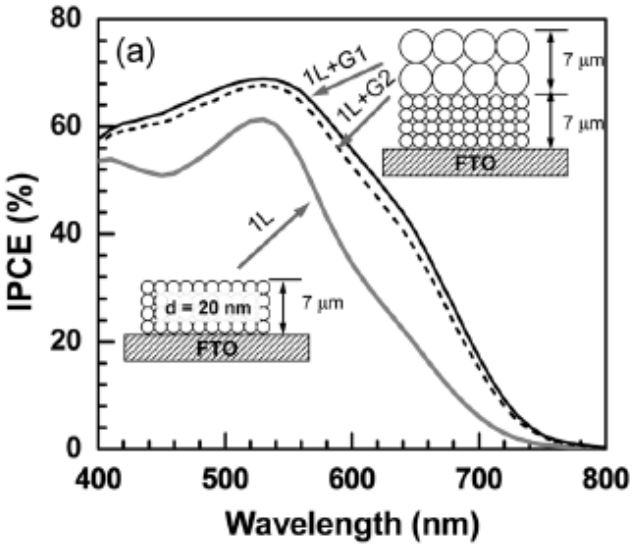

Figure 1.40. Effect of double layer structure on IPCE.[84]

Therefore, two different engineered sizes of TiO_2 are used in DSSC architecture and have a positive effect on the photocurrent density as the maximum amount of light is being captured and converted in to current.

1.9.2.2. Shape: Kinetics of DSSC

Before dye loading the FTO coated TiO_2 nanoparticles are sintered to have necking between them for electron transfer and to improve electronic conduction between TiO_2 layer and FTO. When light is incident on dye molecules they gets excited and inject electrons in the conduction band (CB) of TiO_2 within about 100 femtoseconds as shown in **Figure1.41.** The excited dye molecules get de-excited in 15ns and are also regenerated in a few microseconds. Thus the electron transfer process is faster than the dye de-excitation and regeneration avoiding recombination. When this electron is injected in CB it has to pass through the whole thickness of TiO_2 to reach TCO on the other side. Bisquert et al.[85] and Fisher et al.[86] have shown that the transport of ejected electron is purely based on multiple trapping/de-trapping model where

electron has to pass through TiO_2 by the diffusion mechanism. During its journey in necked TiO_2 the electron has to face many resistances from defects, surface states and grain boundaries as shown in **Figure 1.42**.

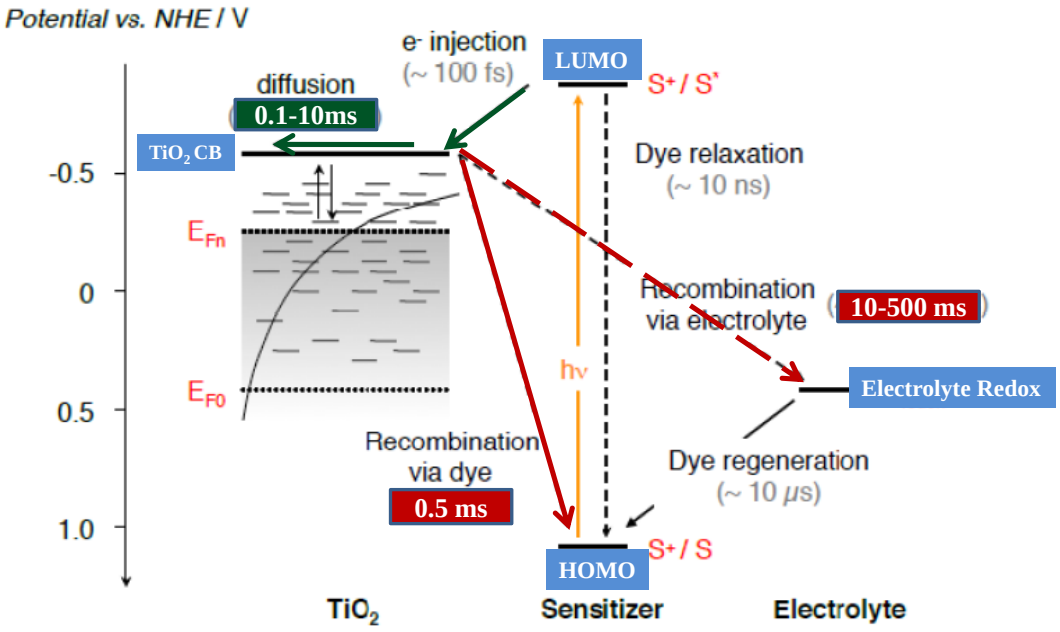

Figure1.41. Kinectics involved in DSSC [87]

This makes electron transport very slow (in about 5 milliseconds), increasing recombination and thereby diminishing charge collection at the back contact. There are two main recombinations prevailing in the system: one between injected electron and electrolyte in 10ms and the second the between electron and oxidized dye which occurs in 0.5ms. Thus the electron transfer in TiO_2 and interfacial recombination occur on about the same time scale. These both processes are under dynamic competition which makes it a rate determining step and also a major limiting factor of DSSC performance.[88] To overcome this factor electron diffusion length and hence its life time should be increased. This can be done efficiently by 1-dimensional nanostructures like nano rods,

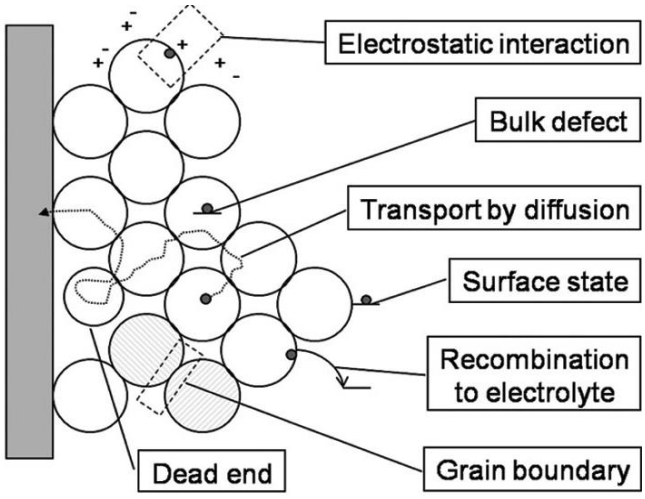

Figure1.42. Schematic diagram showing the hindrance in electron transport in DSSC.[87] Reproduced by permission from reference 87: *Chem. Rev.* **2010,** *110,* 6595–6663.

nanotubes and nano needles.

Crucial advantages provided by such 1D nanostructure are elaborated below [83]:

1) Electron diffusion length in 1D nanostructures increases up to 100μm which is much higher than that of nanoparticles (7-30μm).

2) 1D nanostructure improves the charge collection by providing direct channel (limiting random walk in TiO_2 network scaffold) for the photo-generated electrons.

3) Low number of grain boundaries and defects present in such system facilitate the electron transport and hence reduce the interfacial recombination.

4) Provides high surface area and hence enhanced light absorption due to increased dye loading.

Metal chalcogenides are good candidates for use in DSSC as a counter electrode material as they have good catalytic activity and conductivity. Moreover their nanostructured architecture

provides high surface area for electrolyte contact and direct pathway for transfer of charge carriers to redox couple. Therefore, the size and nanostructure engineering of metal oxides and chalcogenides used in photoanode material has very predominant role in enhancing the performance of DSSC.

1.10. Metal Chalcogenides for Quantum Dot Sensitized Solar Cell application

1.10.1 Quantum dot Sensitized Solar Cell (QDSSC)

1.10.1.1. Working principle:

Working of QDSSC is similar to DSSC with the only difference that the sensitizers are narrow band gap inorganic semiconductor QDs instead of dye molecules. Commercially used organic dye molecules are ruthenium based which are expensive and they degrade with time under UV.[89] Quantum Dots (QDs) are semiconductors where electrons and holes are confined to ultra-small regions of space of the order of or smaller than the exciton radius (typically 1-15 nm). Such a semiconductor structure enters the regime of size quantization, wherein the electronic energy levels become discrete rather than being quasi-continuous. Due to this fact the optical and electronic properties of the semiconductor become strongly size-dependent.[90]

1.10.1.2. Why Quantum Dots? (Engineered metal chalcogenide QDs)

QDs have unique advantages over dyes which make them viable candidates for sensitizer applications which are as follows:

(1) Their band gap can be tailored by changing the size which in turn can tune the adsorption spectra to visible region so as to utilize maximum solar spectrum.[90, 91] Also, as the size of QD decreases the band gap increases as shown in **Figure 1.40** due to ***quantum confinement effect*** which is expected to have favorable conduction band edges for electron injection, thereby

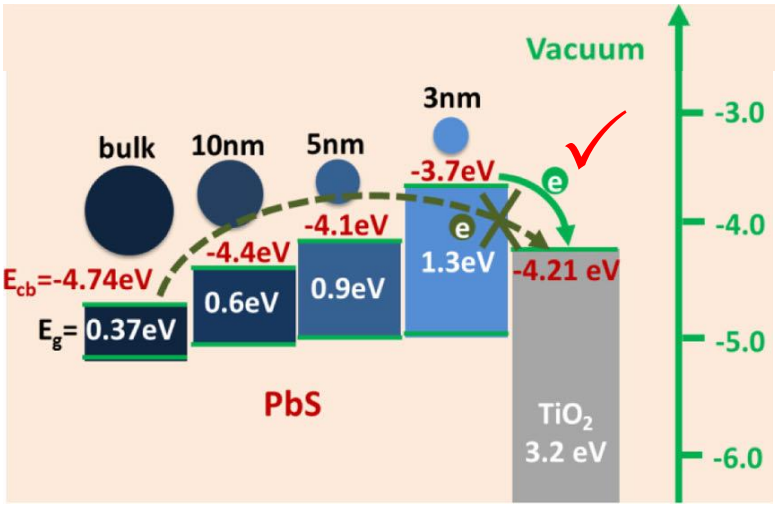

Figure1.43. Schematic illustration of the modulation of energy levels of PbS by particle size.[91] Reprinted with permission from (*ACS Nano*, **2009**, 3, 3023-3030.). Copyright (2009) American Chemical Society.

increasing rate of electron transfer.

(2) QDs have larger extinction co-efficient than organic dyes, enabling thinner device architecture, [92] and,

(3) Larger intrinsic dipole moment which leads to rapid charge separation.[93, 94]

(4) Multiple Exciton Generation (MEG) is possible by single photon absorption due to impact ionization effect (inverse Auger effect).[95, 96] Ultimately, as the number of photo generated electrons are increased the photocurrent of the device is also enhanced. Due to MEG maximum theoretical solar power conversion efficiency of QDSSC is considered to exceed the Shockley-Queisser limit (31%) to greater than 44%.[97, 98]

(5) QDs utilize the concept of ***"hot carriers"***[89], where photons with energies greater than the band gap of semiconductor generate hot carriers. If energy with such kind of QD solar cell is collected fast before they cool and relax due to phonon emission then it enhances charge transfer

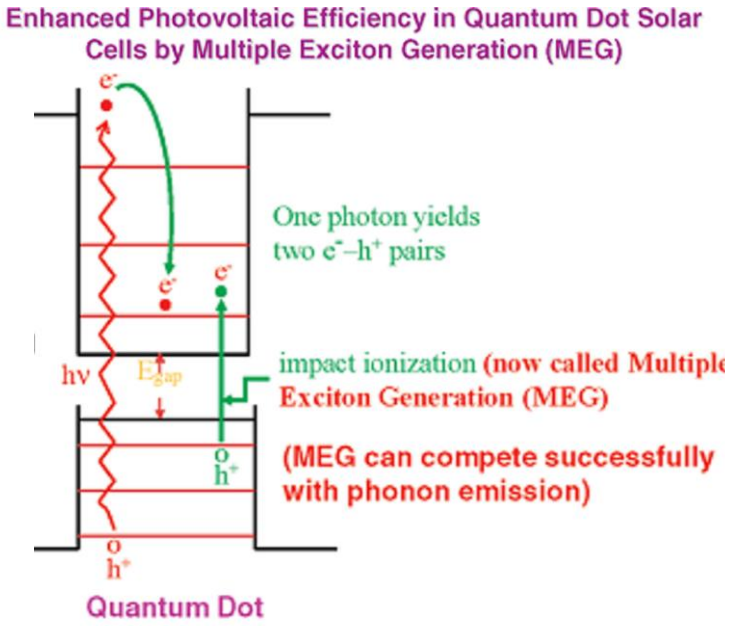

Figure1.44. Multiple Exciton generation in QDs [96] Reprinted with permission from (*Nano Lett*., **2010**, 10, 2735–2741.) Copyright (2010) American Chemical Society.

rate and V_{oc}. Both hot electrons and holes have different rate of cooling depending upon their effective masses. When hot electron is generated it gives its excess kinetic energy to a thermalized hole via an Auger process. The hole can then cool quickly because of its higher effective mass and more closely spaced quantized states. Hole is removed from the QD core by a fast hole trap at the surface, then the Auger process is blocked leading to slow electron cooling. This phenomenon was first seen in CdSe and InP where electron cooling was seen to slow down to 7ps as compared to 0.3ps.

1.10.1.2. Components of QDSSC

Working principle of QDSSC is fundamentally similar to DSSC except for some components.

a) Photoanode: A wide band gap semiconductor like TiO_2, ZnO, SnO_2 is used and fabricated same as that of DSSC.

b) Sensitizer: Unlike DSSC the sensitizer used herein is QDs of materials such as CdS, CdSe, PbS, PbSe, InAs, InP Bi_2S_3,Ag_2S. Intially used binary QDs had good coverage on TiO_2 but still they showed very less solar efficiency of about 1-3%.[99] This is due to the limited extended absorption region of QDs or may be due to poor energy level alignment making ineffective charge injection. To achieve both these factors researchers were provoked to use co-sensitizer or cascade structure like CdS/CdSe which gave remarkable enhancement in solar efficiency up to 4.15%.[100]After binary QDs, ternary QDs like $CuInS_2$, $CuInSe_2$, CdSeS, CdTeSe, PbSeS were also employed due to their high absorption co-efficient (10^5).[99] Moreover, alloying such chalcogenides, create a single panchromatic sensitizer increasing light harvesting range without hindering electron extraction. Recently, quaternary QDs have emerged as a new class of QDs as their optoelectronic properties can be tuned by changing their composition without changing the particle size. Also they are chemically more stable due to hardened lattice structure and decreased interdiffusion.[101]

c) Electrolyte: In QDSSCs polysulphide electrolyte is used containing sulphur, Na_2S and KCl or NaOH. Iodine/triiodide electrolyte used in DSSC is not compatible in QDSSC as QDs undergo photocorrosion/ degradation process in iodine. A polysulphide electrolyte is suitable as compared to others in terms of the stability of QDs and in redox activity.[102] Eventhough polysulphide electrolyte has high rate of regeneration potential, it suffers from low V_{oc}. To overcome this problem many researchers have done modification of the electrolyte by adding tetramethylammonium in 3-methoxypropionitrile (MPN) which raised the V_{oc} to 1.2V.[99] To

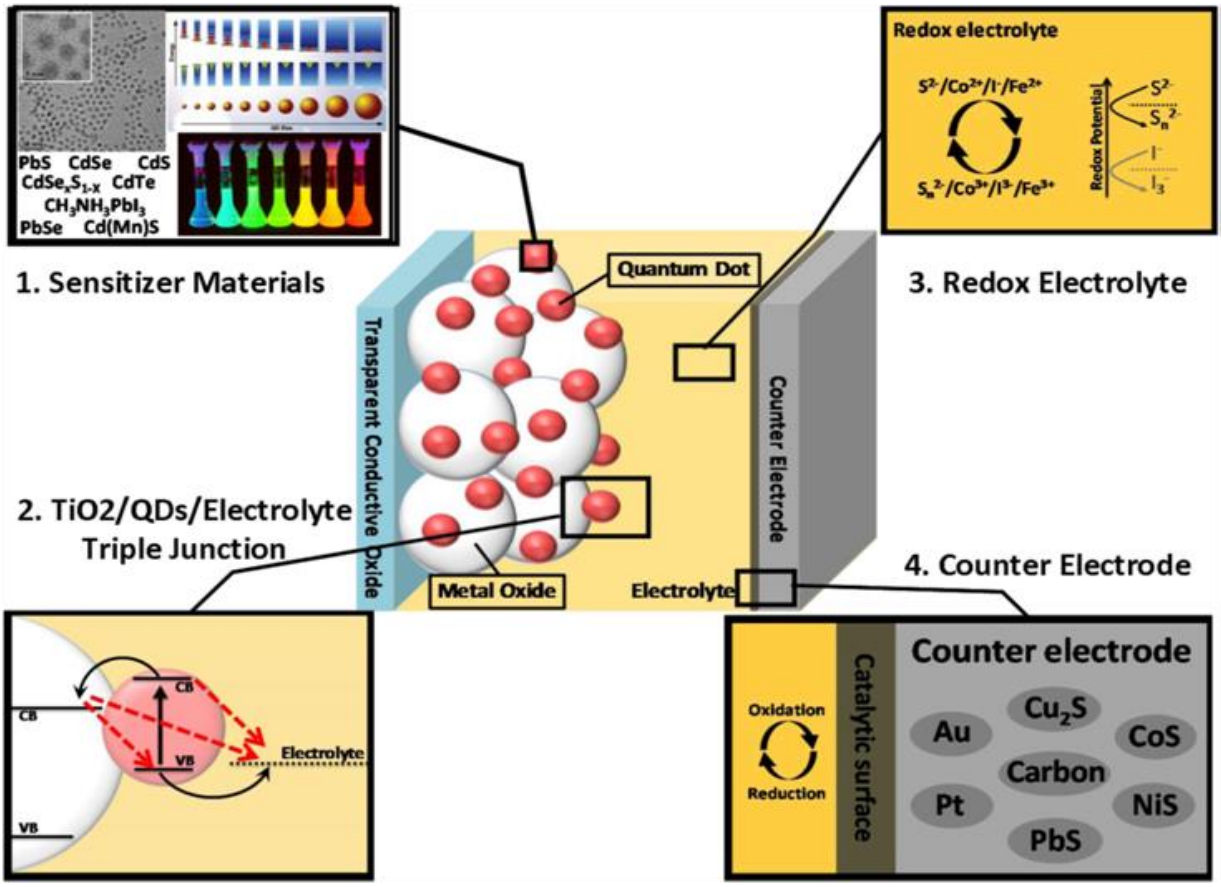

Figure1.45. Schematic representation of QDSSC components, materials and interfaces.[99] Reprinted with permission from (*Langmuir*, **2014**, 30, 7264−7273). Copyright (2014) American Chemical Society.

increase the photocurrent Bisquert et al.[99] introduced pyrrolidinium ionic liquid. In spite of all this, sulphur-based liquid electrolyte still suffers from long term stability and is tedious to commercialize which prompted search for alternative electrolyte. In this direction solid state hole conducting mediators like spiro-OMeTAD, PEDOT, CuSCN are used as they provide accessibility for easier device sealing and in turn higher photovoltage values as compared to liquid based electrolyte.[99]

e) Counter electrode: Platinium is not suitable with polysulfide electrolyte as sulphur gets strongly chemosorbed onto Pt surface and hampers its catalytic activity.[100] Hence search for alternative cheap and earth abundant materials for counter electrode for QDSSC is a recent emerging goal of research. Many materials have been tried like carbon (activated carbon, mesoporous carbon, grapheme, fullerenes), polymers (ployaniline (PAN), Ploystyrenesulfonate (PEDOT-PSS)), and sulphides (CoS,NiS,PbS,CuS,CoS_2,$CoSe_2$,$CuInS_2$,$NiCoS_2$).[99,103]As a standard, Cu_2S brass counter electrode is used which showed up till now a 4-5% conversion efficiency. [104] This is compatible with polysulfide electrolyte.

1.11. Metal oxide and Chalcogenide for Photoelectrochemical water splitting

1.11.1. Water electrolysis:

Water electrolysis means splitting of water into H_2 and O_2 by using electric potential or current. Water splitting is given the most emphasis as compared to other methods for hydrogen production as mentioned in **section 1.4** because it produces 99.99% pure hydrogen (without any pollutant) to be used in fuel cell. Moreover, the byproduct of this technique is again water which makes this system sustainable and economically viable. In water electrolysis, two electrodes (anode and cathode) is immersed in conducting electrolyte made up of water and solvent, and a potential is applied between the electrodes. The thermodynamic oxidation and reduction reactions at the electrode are:

At anode (oxidation):	$H_2O\,(l) \rightarrow O_2\,(g) + 4\,H^+\,(aq) + 4e^-$	$E_{ox} = -1.23V$
Cathode (reduction):	$2H^+\,(aq) + 2e^- \rightarrow H_2\,(g)$	$E_{red} = 0\ V$

The standard potential of water electrolysis is 1.23V under standard conditions of pressure and temperature. However, the real water splitting always requires potential higher than 1.23V as the

above equation considers the evolution of atomic hydrogen, but the enthalpy of molecular hydrogen and oxygen evolution is 286 kJ/mol which corresponds to a voltage of 1.48V. Thus, the water splitting starts on the two electrodes provided the potential difference between them is greater than or equal to 1.48V. The water electrolysis can be a renewable source of hydrogen if the required potential for water splitting is provided by any renewable energy source like a photovoltaic module or a wind turbine. The current research in the field of water electrolysis is to develop novel electro-catalyst which can split water at a potential lower than 1.48 V.[105]

1.11.2. Solar driven water splitting:

The electric energy required for water splitting can be replaced or minimized by solar energy by utilizing nanomaterials which makes the system cost effective and clean. Even electricity generated by photovoltaics can be employed for water splitting. Soar driven water splitting has two pathways: a) Photocatalytical water splitting and b) Photoelectrochemical water splitting

1.11.2.1. Photo-catalytic (PC) water splitting

In photocatalytic water splitting a semiconductor photocatalyst is immersed in water/electrolyte and irradiated with sunlight. The generated photoelectron hole pair within the semiconductor performs the function of water reduction and oxidation on its surface to produce H_2 and O_2. In order to facilitate the surface reaction and better charge separation many times photocatalyst is modified with co-catalyst or buffer layers as shown in **Figure 1.46.**

In this catalysis process, the photocatalyst has to satisfy stringent criteria to perform PC water splitting, that is, a) narrow band gap to maximize the absorption spectrum, and b) appropriate conduction and valence band edges w.r.t. to redox potential of water, and c) stability in the solution. Although many materials are available which satisfy the properties required for water

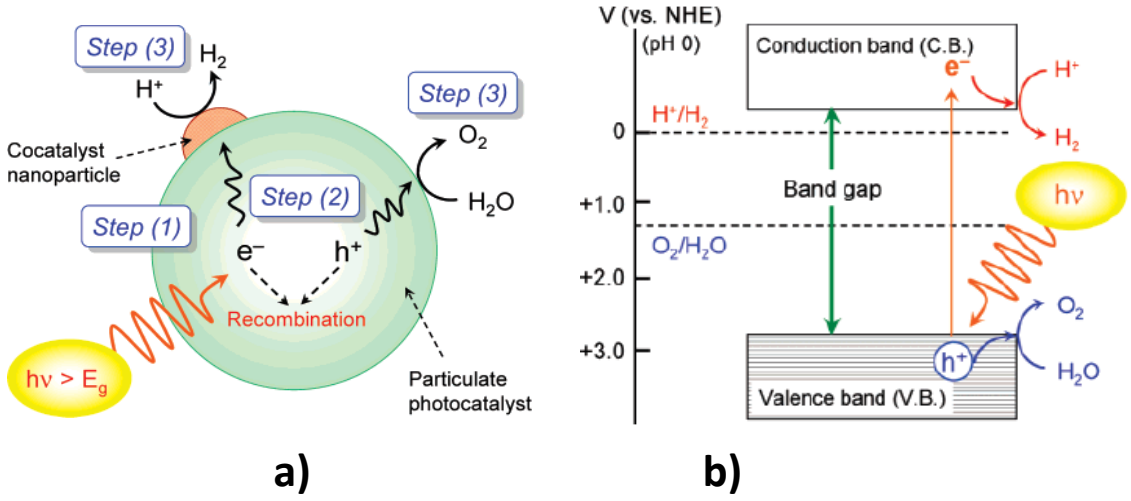

Figure1.46. a) Steps and b) Basic principle involved in photocatalytic water splitting.[106] Reprinted with permission from (*J. Phys. Chem. C*, **2007**, 111, 7851-7861). Copyright (2007) American Chemical Society.

splitting, it is difficult to have single material which can satisfy all the requirements. Moreover, the main bottleneck lies in low quantum yield where most of the photo generated charge carriers recombine after excitation.[105]To solve this issue photoelectrochemical (PEC) water splitting emerged as a efficient path way for solar driven water splitting.

1.11.2.2. Photoelectrochemical (PEC) catalytic water splitting

In PEC water splitting two (or three) electrode system immersed in a conducting electrolyte is used, where the working electrode may be n/p- type material and the counter of metallic type. Another option is n-type material as photoanode and p-type material as photocathode (**Figure 1.47**).

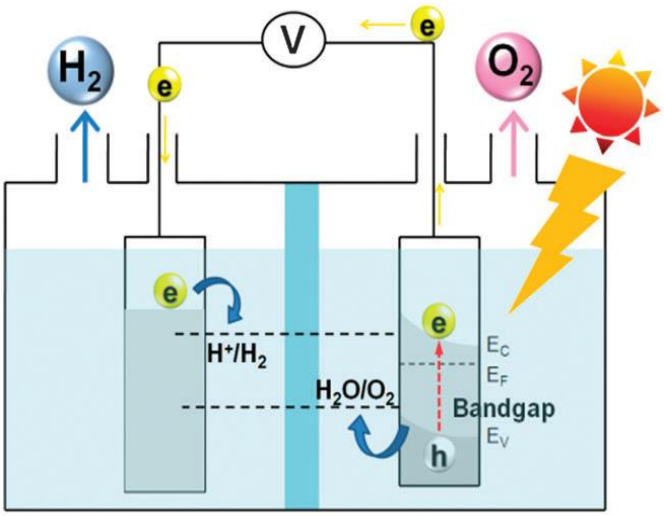

Figure1.47. Basic principle of photoelectrochemical water splitting with n-type semiconductor photoanode.[106] Reproduced by permission from reference 106: *Chem. Rev.* **2012,** 41, 5654–5671.

When sunlight is incident on the working electrode, electron hole pair is generated and these carriers migrate through the electrolyte to the respective electrodes. Electrons from external circuit reach the photocathode for water reduction and holes at photoanode do the water oxidation. The two processes occur at two different electrodes unlike photocatalytical water splitting. In this kind of water splitting small bias (V< 1.23 V) can be applied to narrow band gap materials which can absorb in visible region but their conduction band edge is below the water reduction potential. Applying small bias can separate the charges efficiently increasing the solar to fuel conversion efficiency.

When light is incident on photoanode (hv < Eg), photo-generated electron hole pair at the electrode/electrolyte interface causes built-in electric field /band bending. Due to this electric field electrons move away from electrolyte to counter electrode through external circuit for water

reduction whereas the holes move towards electrolyte for water oxidation. These two reactions at two different electrodes increase hydrogen economy as well its storage ability.[105]

The discovery of the Honda–Fujishima [107] effect in 1972 is one of the most important discoveries in chemistry and extensively promoted the research field of PEC water splitting.

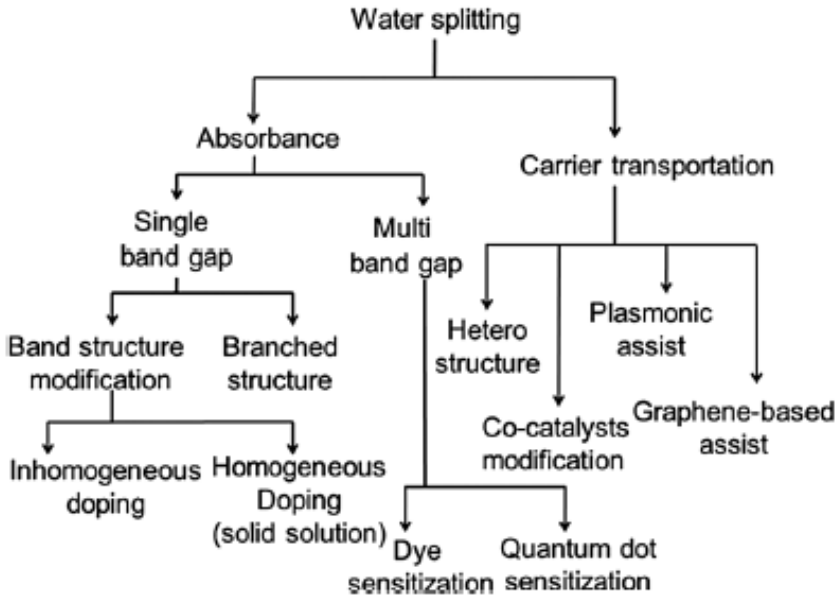

Figure 1.48. Schematic diagram for strategies to improve photo activity for water splitting. [105] Reproduced by permission from reference 105: *Chem. Rev.* **2012,** 41, 5654–5671.

Many materials have been reported since then but metal oxides and chalcogenides have attracted tremendous attraction due to their unique optoelectronic properties and feasibility to engineer or tune their properties such as band edges, size, morphology and surfaces. By following different strategies given in **Figure 1.47** PEC performances can be boosted and such strategies can be easily applied to MOs and chalcogenides. Wide band gap semiconductor like TiO_2, ZnO absorb only in UV region but still they can be efficiently used as photocatalyst either by doping (narrowing the band gap) or by surface modification as given in **section 1.6.1.**[105] On the other

hand, transition metal chalcogenide have narrow band gap like CdS or NiS but their conduction band edges are below the reduction potential of water. Therefore mostly they are established as surface modifier or as co-catalysts. But some of them like MoS_2 [108] are being reported as a PEC catalyst by band engineering through introduction of ordered defect system. Transition metal chalcogenides have high absorption co-efficient, catalytic activity and ability to lower the over-potential for water splitting.

1.12. Outline of thesis

The present thesis deals with efficient utilization of solar energy either in sensitized solar cell based nano devices to produce electricity or to split water for hydrogen generation. It also deals with engineered nanostructures for the above mentioned applications.

The **second** chapter presents and discusses DSSC and QDSSC fabrication, and the related materials synthesis protocols and characterization techniques.

The **third** chapter presents the electrochemical synthesis of rutile TiO_2 at room temperature with hierarchical nanoneedle flower morphology for DSSC photoanaode material.

The **fourth** chapter deals with reverse phase transformation of rutile TiO_2 nanoneedles to anatase nanoparticles and the related detailed mechanism. The obtained nanoparticles are shown to give good power conversion efficiency when used as a photoanode material for DSSC.

The **fifth** chapter reports the synthesis of vertically oriented nanosheets of $CuInS_2$ and theirs nanocomposite with CuS as photocathode/counter electrode material for DSSC.

The **sixth** chapter focuses on replacing the dye with a quantum dot sensitizer $CuInS_2$. The corresponding colloidal solution along with CdS quantum dots are used as sensitizer which have synergetic effect on the QDSSC performance.

The **seventh** chapter presents a first report on sulfur deficient $NiS_{1.97}$ dichacogenide as an efficient photoelectrochemical (PEC) catalyst for water splitting.

The concluding chapter **eighth** describes the future scope for this present research work.

1.12. References:

1) http://ourfiniteworld.com

2) Energy Information Administrator, *Report on 'World Consumption of Primary Energy by Energy Type and Selected Country'*, **2006**.
http://www.iea.org/publications/freepublications/publication/key_world_energy_stats-1.pdf,

3) Renewable energy, Environmental centre, University of Colorado,
http://www.colorado.edu/ecenter/energy-us/renewable-energy

4) https://www.nrdc.org

5) https://www.edfenergy.com/energyfuture/generation-wind

6) http://en.wikipedia.org/wiki/Wind_power

7) http://www.edfenergy.com/energyfuture/generation-hydro

8) http://en.wikipedia.org/wiki/Hydroelectricity#Advantages

9) Union of Concern scientist, Science for healthy planet and safer world, http://www.ucsusa.org/

10) http://en.wikipedia.org/wiki/Geothermal_energy#Economics

11) A.E. Becquerel, C. R. Acad. Sci. **1839,** 9, 561- 567.

12) a)A. Goetzberger, J. Luther, G. Willeke, *Solar Energy Materials and Solar Cells* **2002**, 74, 1-11; b) Y. J. Lee, B. S. Kim, S. M. Ifitiquar, C. Park, J. Yi, *Journal of the Korean Physical Society* **2014**, *65*, 355-361.

13) Heliatek, *Developement history of photovoltaics*, http://www.heliatek.com/technologie/organische-photovoltaik/?lang=en.

14) M. A. Green, K. Emery, Y. Hishikawa, W. Warta, E. D. Dunlop, *Prog. Photovolt: Res. Appl.* **2011**, 19, 565-572.

15) http://energyinformative.org/amorphous-silicon-solar-panels/

16) M. Gloeckler, I. Sankin, Z. Zhao, *IEEE Journal of Photovoltaics*, **2013**, 3, 1389–1393.

17) A. D. Compaan, *Solar Energy Materials & Solar Cells*, **2006**, 90, 2170–2180.

18) S. Gupta, *Understanding of Nano Science And Technology*, **2006**, Global Vision Publishing Ho.

19) S. Karg, W. Riess, V. Dyakonov, M. Schwoerer, *Synthetic Metals*, **1993**, *54*, 427-433.

20) J. J. M. Halls, K. Pichler, R. H. Friend, S. C. Moratti, A. B. Holmes, *Appl. Phys. Lett.*, **1996**, *68*, 3120-3122.

21) J. J.M. Halls, R.H. Friend, M. D. Archer, R. D. Hill, *Clean electricity from photovoltaics. London: Imperial College Press.* pp. 377–445. ISBN 1860941613.

22) B. Reeja-Jayan and A. Manthiram, *RSC Adv.*, **2013**, 3, 5412-5421.

23) FSEC, *Hydrogen Basics: Production*, http://www.fsec.ucf.edu/en/consumer/hydrogen/basics/production.htm, **2007**

24) U. Sahaym Æ M. Grant Norton, *J Mater Sci*, **2008**, 43:5395–5429.

25**)** J. A. Turner, *Science*, **1999**,285, 687-689.

26) http://www.nano.gov/timeline

27) A. P. Alivisatos, *Science*, New Series, **1996**,271, 933-937.

28) H. S. Mansur, *Wiley Interdiscip. Rev.: Nanomed. Nanobiotechnol.*, **2010**, 2, 113–129.

29) S. Eustis and M. A. El-Sayed, *Chem. Soc. Rev*., **2006**, 35, 209–217.

30) J. Li, H. Guo, and Z.-Y. Li, *Photon. Res.*, **2013**, 1, 28-41.

31) J. Chakhalian, J. W. Freeland, H.-U. Habermeier, G. Cristiani, G. Khaliullin, M. van Veenendaal, B. Keimer, *Science*, **2007,**318, 1114 – 1117.

32) S. B. Ogale, *Functional Metal Oxides*, Wiley-VCH, Singapore, **2013**.

33) Mineral structure and property data, University of Colorado http://ruby.colorado.edu/~smyth/min/tio2.html .

34) M. Landmann, E. Rauls and W. G. Schmidt, *J. Phys.: Condens. Matter,***2012,** 24**,** 195503(6pp).

35)J. Zhang, Q. Xu, M. Li, Z. Feng, and C. Li, *J. Phys. Chem. C*, **2009**, *113*, 1698–1704.

36)L. Kavan, M. Gra1tzel, S. E. Gilbert, C. Klemenz, and H. J. Scheel, *J. Am. Chem. Soc.* **1996**, 118, 6716-6723.

37) K. H. Park, H. Li, M. Dhayal, J. W. Lee, and H. B. Gu, *J. Nanosci. Nanotechnol.* , **2008**, 8, 5252-5256.

38) J.- J. Lee, Md. M. Rahman, S. Sarker, N.C. Deb Nath, A.J. S. Ahammad and J. K. Lee, Chapter 7- *Metal Oxides and Their Composites for the Photoelectrode of Dye Sensitized Solar Cells, Advances in Composite Materials for Medicine and Nanotechnology*, Dr. Brahim Attaf (Ed.), ISBN: 978-953-307-235-7, InTech, **2011,**181-210.

39) S. Pradhan, D. Ghosh, S. W. Chen, *Acs Applied Materials & Interfaces* **2009**, *1*, 2060-2065.

40) Y.-C. Park,Y.-J. Chang,B.-G. Kum,E.-H. Kong, J. Y. Son, Y. S. Kwon, T. Parkc and H. M. Jang, *J. Mater. Chem*., **2011**, 21, 9582-9586.

41) S. Banerjee, S. K. Mohapatra, and M. Misra, *J. Phys. Chem. C*, **2011**, 115, 12643–12649.

42) I. S. Cho, Z. Chen, A. J. Forman, D. R. Kim, P. M. Rao, T. F. Jaramillo and X. Zheng, *Nano Lett.* **2011**, 11, 4978–4984.

43) Y.X. Zhang, G.H. Li , Y.X. Jin, Y. Zhang, J. Zhang, L.D. Zhang, *Chemical Physics Letters*, **2002**,365,300–304.

44) X. D. Wang, E. Graugnard, J. S. King, Z. Lin Wang, and C. J. Summers, *Nano Lett.,* **2004,** 4, 2223-2226.

45) T. J. Athauda, J. G. Neff, L. Sutherlin, U. Butt, and R. R. Ozer, *ACS Appl. Mater. Interfaces*, **2012**, 4, 6917−6926.

46) S. S. Mali, H. Kim, C. S. Shim, P. S. Patil, J. H. Kim & C. K. Hong, *Sci Rep.* **2013**; 3: 3004 (8pp).

47) X. Chen, L. Liu, P. Y. Yu, S. S. Mao, *Science*, **2011**,331, 746-750.

48) G. Liu,L.-C. Yin,J. Wang, P. Niu, C. Zhen, Y. Xie and H.-M. Cheng, *Energy Environ. Sci.*, **2012**, 5, 9603-9610.

49) M. Atif, W. A. Farooq, A. Fatehmulla , M. Aslam and S. M. Ali, *Materials*, **2015**, 8, 355-367.

50) Y. Ohko, T. Tatsuma, T. Fujii, K. Naoi, C. Niwa, Y. Kubota, Fujishima, A. *Nat. Mater.* **2003**, *2*, 29-31.

51) Fischer W, A second note on the term "Chalcogen". *J Chem Educ* , **2001**,78,1333.

52) A. Paulheim. Photoemission am tern¨aren Schichthalbleitersystem ZrS_xSe_{2-x}. Diploma thesis, Humboldt Universit¨at zu Berlin, **2010**, 01.

53) J. A. Wilson and A.D. Yoffe. "The transition metal dichalcogenides discussion and interpretation of the observed optical, electrical and structural properties". *Advances in Physics*, **1969**, 18, 73,193.

54) J.Rasch, T. Stemmler, and R. Manzke. *Journal of Alloys and Compounds*, **2007**,442, 262–264.

55) A. H. Reshak and S. Auluck., *Phys. Rev. B,* **2003**, 68, 24, 245113.

56) J. H. Han, S. Lee and J. Cheon, *Chem. Soc. Rev.,* **2013**, 42, 2581-2591.

57) R. Wang, O. Calvignanello, C. I. Ratcliffe, X. Wu, D. M. Leek, Md. B. Zaman, D. Kingston, J. A. Ripmeester, and K. Yu, *J. Phys. Chem. C*, **2009**, 113, 3402–3408.

58) N. P. Benehkohal, V. Gonzalez-Pedro, P. P. Boix, S. Chavhan, R. Tena-Zaera, G. P. Demopoulos, and I. Mora-Sero , *J. Phys. Chem. C*, **2012**, 116, 16391−16397.

59) A. Banerjee, K. K. Upadhyay, S. Bhatnagar, M. Tathavadekar, U. Bansode, S. Agarkar and S. B. Ogale , *RSC Adv.*, **2014**,4, 8289-8294.

60) L. S, C. Y, H. L, P. D., *Nanotechnology* , **2013,** 24,395705.

61) Y. Wang, S. Yang, H. Yang and H. Sun, *Advanced Optical Materials*, **2015**, 3, 5, 652–657.

62) D. Deng, J. Cao, L. Qu, S. Achilefu and Y. Gu, *Phys. Chem. Chem. Phys.*, **2013**,15, 5078-5083.

63) J. K. -Olesiak and H. Weller, *ACS Appl. Mater. Interfaces*,**2013**, 5, 12221−12237.

64) J. Chang and E. R. Waclawik, *RSC Adv.*, **2014**, 4, 23505–23527.

65) T. - L. Li and H. Teng, *J. Mater. Chem.*, **2010**, 20, 3656–3664.

66) J. Yang, C. Bao, J. Zhang, T. Yu, H. Huang, Y. Wei, H. Gao, G. Fu, J. Liuac and Zhigang Zouab, *Chem. Commun.*, **2013**, 49, 2028—2030.

67) K.D. M.. Rao, T. Bhuvana, B. Radha, N. Kurra, N. S. Vidhyadhiraja and G. U. Kulkarni , *J. Phys. Chem. C*, **2011**, 115, 10462–10467.

68) S.-L. Yang,H.-B. Yao,M.-R. Gao and S.-H. Yu, *CrystEngComm*, **2009**, 11, 1383–1390.

69) M. Gratzel, *Nature*, **2001,** 414,338-344.

70) B. O'Regan and M. Gratzel, *Nature*, **1991**, 353, 737–740.

71) K. Keis, E. Magnusson, H. Lindstrom, S.E. Lindquist, A. Hagfeldt, *Solar Energy Materials and Solar Cells*, **2002**, 73, 51–8.

72) E. Ramasamy, J. Lee, *J. Phys Chem. C*, **2010**, ***114***, 22032–7.

73) M. Gratzel, *Inorg. Chem.* **2005,** 44, 6841-6851.

74) G. Calogero, G. D. Marco, S. Caramori, S. Cazzanti, R. Argazzi, C. A. Bignozzi, *Energy Environ. Sci.* **2009**, 2, 1162–1172.

75) S. Y. Huang, G. Schlichthorl , A. J. Nozik, M. Gratzel, A.J. Frank *Journal of Physical Chemistry B* ,**1997**,101,2576–82.

76) T. Daeneke, Y. Uemura, NW. Duffy, AJ. Mozer, N. Koumura, U. Bach, L. Spiccia, *Advanced Materials,* **2012**,24, 1222-1225.

77) M. Wu and T. Ma, *ChemSusChem* , **2012**, 5, 1343 – 1357.

78) W. J. Lee, E. Ramasamy, D. Y. Lee, J. S. Song, *ACS Appl. Mater. Interfaces*, **2009**, 1, 1145-1149.

79) J. D. R.-Mayhew, D. J. Bozym, C. Punckt, and I.A. Aksay, *ACS Nano,* **2010**,4, 6203-6211.

80) E. Ramasamy, J. Lee, *Carbon*, **2010,** 48, 3715-3720.

81) H.K. Mulmudi, S. K. Batabyal, M. Rao,R. R. Prabhakar, N. Mathews, Y- M Lam and S. G. Mhaisalkar, *Phys. Chem. Chem. Phys.,* **2011**, 13, 19307–19309.

82) M.-J. Jeng, Y.-L. Wung, L.B. Chang, and L. Chow, *International Journal of Photoenergy,* **2013,**563879.

83) H. Y. Chen,D.B. Kuang and C.-Y. Su, *J. Mater. Chem.*, **2012**, 22, 15475–15489.

84) N.-G. Park, *Journal of the Korean Electrochemical Society,* **2010,** 13, 10-18.

85) J. Bisquert andV. S. Vikhrenko, *J. Phys. Chem. B*, **2004**, 108, 2313– 2322.

86)A. C. Fisher, L. M. Peter, E. A. Ponomarev, A. B. Walker and K. G. U. Wijayantha, *J. Phys. Chem. B*, **2000**, 104, 949–958.

87)S. Wenger, *Ph. D thesis "Strategies to Optimizing Dye-Sensitized Solar Cells Organic Sensitizers Tandem Device Structures and Numerical Device Modeling"*, Ecole Polytechnique Fédérale de Lausanne **2010**.

88) P. Roy, D. Kim, K. Lee, E. Spieckerb and P. Schmuki, *Nanoscale,* **2010**, 2, 45–59.

89) A.J. Nozik, *Physica* , **2002,** E 14, 115 – 120.

90) P. K. Snatra, P. V. Kamat, *J. Am. Chem. Soc.*, **2012**, 134, 2508−2511.

91) I. Moreels, K. Lambert, D. Smeets, D. De Muynck, T. Nollet, JC. Martins, F. Vanhaecke , A. Vantomme , C. Delerue , G. Allan , Z. Hens, *ACS Nano* **2009**, 3,3023-3030.

92) W. Yu, L. H. Qu, W. Z. Guo, X. G Peng, *Chem. Mater.* **2003**, *15*, 2854–2860.

93) R. Vogel, K. Pohl, H. Weller, *Chem. Phys. Lett.* **1990**, *174*, 241–246.

94) R. Vogel, P. Hoyer, H. Weller, *J. Phys. Chem.*, **1994**, *98*, 3183–3188.

95) R. D. Schaller and V. I. Klimov, Phys. Rev. Lett., **2004**, 92, 186601.

96) A J. Nozik, *Nano Lett.*, **2010**, 10, 2735–2741.

97) W. Shockley, H. J. Queisser, *J. Appl. Phys.* ,**1961**, 32, 510−519.

98) V. I. Klimov, *J. Phys. Chem. B*, **2006,** 110, 16827–16845.

99) I. Hod and A. Zaban, *Langmuir,* **2014**, 30, 7264−7273.

100) Y. L. Lee and Y. S. Lo, *Adv. Funct. Mater.* **2009**, 19, 604–609.

101) Z. Pan, K. Zhao, J. Wang, H. Zhang, Y. Feng, and X. Zhong, *ACS Nano* ,**2013**, 7, 5215–5222.

102) T. L. Li, Y. L. Lee and H. Teng, *Energy Environ. Sci.*, **2012**, 5, 5315–5324.

103) S. Thomas, T. G. Deepak, G. S. Anjusree, T. A. Arun, S. V. Nair and A. S. Nair, *J. Mater. Chem. A*, **2014**, 2, 4474–4490.

104) K. Zhao, H. Yu, H. Zhang, and X. Zhong, *J. Phys. Chem. C*, **2014**, 118, 5683−5690.

105)H. M. Chen, C. K. Chen, R. S. Liu, L. Zhang, J. Zhang and. P. Wilkinsonc, *Chem. Rev.* **2012,** 41, 5654–5671.

106) K. Maeda, and K. Domen, *J. Phys. Chem. C* **2007**, 111, 7851-7861.

107) A. Fujishima, K. Honda, *Nature* **1972**,238, 37-38.

108)Z.Chen, A. J. Forman and T. F. Jaramillo, *J. Phys. Chem. C*, **2013**, 117, 9713−9722.

Chapter 2

Fabrication of Sensitized Solar Cell, Experimental Methods and Characterization Techniques

This chapter deals with a detailed discussion about the fabrication protocols for making efficient Dye Sensitized Solar cells (DSSCs) and Quantum dot sensitized solar cells (QDSSCs). Preparation and optimization protocols for each component of the sensitized solar cells are addressed carefully and discussed at length. The paste preparation of photoanode material, which is one of the vital steps in the solar cell fabrication process, is presented in details. Two specific protocols for making the full cell architecture that have been employed in this work are discussed. Further, various synthesis methods and characterization techniques used in the present research work are also presented and discussed.

The present chapter consists of three sections. First section deals with detailed fabrication of sensitized solar cell whereas second section presents experimental methods involved in the present research work. Last section deals with characterization techniques used in this thesis.

SECTION I: Fabrication of Sensitized Solar cell

Section I deals with detailed fabrication protocols for DSSC and QDSSC. The sensitized solar cell devices are composed of multiple components and they are interlinked or interdependent of each other for obtaining maximum and stable performance. Therefore, careful optimization of parameters for each component is necessary. *The most crucial and challenging task of sensitized solar cell is paste preparation of photoanode material and its coating. With initial optimization, protocol I was developed which gave about 6% of solar efficiency but with rigorous optimization of various parameters protocol II of paste making was established in our lab which gave remarkable efficiency of 10%.*

2.1. Fabrication of DSSC

2.1.1. Transparent conducting oxide (TCO) Substrate

Transparent conducting oxide (TCO) substrate plays an important role in dictating the DSSCs' performance. Transparent conducting oxide (TCO) substrate plays an important role in the DSSCs' performance. TCO is used to establish contacts and to give medium for coating of semiconductor. Two features should be used in DSSC- (1) *transparency* to allow light to pass through it to the semiconducting layer and (2) low electrical resistivity – for electron transfer. Usually Fluorine doped tin oxide (F: SnO_2, FTO) is used as transparent conducting substrate in

DSSC. It has 70–80% transmittance in the visible with sheet resistance of < 12 ohm/sq. Apart from FTO, Indium tin oxide (ITO, In_2O_3: Sn) exhibits 80% transparency and resistivity of 10^4 ohm/sq because of which it is also widely used as TCO in the field of optoelectronic devices. However, the only concern with ITO is increment of resistivity with calcination temperature applied in the DSSC fabrication. Therefore FTO is the preferred transparent conducting material for DSSCs.

2.1.1.1. FTO Substrate Cleaning.

FTO glass was cut into 2x2 cm square pieces. Cleaning of these FTO substrates is important in order to remove any organic or inorganic contaminants on its surface which in turn enhances the adhesion of subsequent layers to be deposited over it. The cleaning protocol pursued was as follows:

- Sonicate in soap solution for 15 minutes
- Rinse with deionized water
- Sonicate in deionized water for 15 minutes
- Sonicate in ethanol for 15 minutes

2.1.2. Preparation of Photoanode (*Working Electrode)*

2.1.2.1. Blocking layer of TiO_2.

The photoanode made of nanoporous TiO_2 provides high surface area for dye loading and solar light Absorption.[1] However, unfortunately it also provides abundant openings through the active layer to the bare FTO substrate, where the photo-injected electrons may recombine with I_3^- species in the redox electrolyte ($2e^- + I_3^- \rightarrow 3I^-$).[2, 3] This recombination will cause the loss of the photocurrent thus decreasing the solar cell performance. The introduction of a compact layer between the interface of FTO and nanoporous TiO_2 has been proven theoretically and practically

effective in blocking the electron recombination via this undesirable indirect route.[4,5,6] This compact layer is thus much denser than the nanoporous TiO_2 active layer. Semiconductors such as TiO_2, [7] Nb_2O_5, [8] ZnO [9] etc. have been effectively used as blocking layer materials in DSSCs. Amongst them, TiO_2 is best candidate. The role of blocking layer is not only to block the contact of electrolyte to FTO but it also provides a good contact between FTO and TiO_2 layer for efficient electron transport to increase current density of device. The procedure for making this blocking layer is described in detail here. The cleaned substrate is heated for 15 min at 450ºC to remove the residual organic contaminants and then the blocking layer is deposited.

The deposition of the blocking layer involves two steps:

1. Preparation of blocking layer solution: To prepare blocking layer solution, Titanium tetraisopropoxide (TIP) (1 mL) is added in the mixture of ethanol (5 mL) and acetic acid (0.5 mL) and sonicated for 5 minutes.

2. Spin coating and annealing: Washed FTOs are masked at both ends with scotch tape leaving the desired area in between as open. Blocking layer solution is spin coated on the exposed area at 2500 rpm for 1 minute. The scotch tape is removed and the films are then sintered at 450°C for 1 hour, which results in the formation of the compact TiO_2 layer.

2.1.2.2. TiO_2 paste making:

DSSC performance is majorly dependent on the quality of the photoanode film. The optimum thickness, porosity, uniformity and transparency of the metal oxide film are the deceive factors for generation of maximium photovoltage and photocurrent in a particular solar device. These factors can be controlled by optimizing the slurry/paste which is prepared from metal oxide powder. Also to achieve the uniform and crack free film the slurry of appropriate viscosity and

consistency should be prepared. So the paste making step in the fabrication of DSSC is not trivial but yet very essential. Ultimately the ingredients and their amount which are added to make the slurry will decide the quality of slurry and hence the photoanode film. Thus, the paste making process is a combination of nanoscience and art. So our foremost goal was to have mastery in this art. We therefore chose commercially available (Sigma Aldrich) Degussa P25 (mixture of 75% anatase and 25% rutile TiO_2, ~ 25nm nanoparticles and 50-60m^2/g surface area) to optimize the paste and to use it as standard.

Figure2.1. Photographs of steps involved in slurry preparation (Protocol I)

Protocol I:

To prepare the slurry, this powder (0.5g) was ground in an agate mortar as shown in **Figure 2.1.** Small amount of water (0.5ml) and dilute acetylacetonate (~0.8ml) is added to it to prevent re-aggregation of the particles as the primary particle size of the nanoparticles is around 25 nm, but they form aggregates of > 100 nm size. Other stabilizers such as dilute acid (dilute (0.05M) HNO_3 0.25ml) and binding agents (**Polyethylene glycol** 0.25gm of molecular weight 10,000) were also added subsequently. Small amount of **Triton X-100** (about 50µl) was also added to facilitate the spreading of the colloid on the substrate.0.5ml ethanol is added at final stage while grinding to adjust the consistency and viscosity to optimum.

Protocol II:

Protocol II is based on addition of ingredient **ethyl cellulose** (Sigma aldrich) as binder and alpha – **terpinol** (ACROS) as surfactant. Commercially available TiO_2 (Sigma Aldrich) of 21nm size anatase powder is used. Consequently many steps are involved in paste preparation which avoids agglomeration of particles and promotes uniform film formation. Following are the steps involved:

1.0.6gm of TiO_2 is mixed uniformly with 1ml of acetic acid in agate mortor for about 15mins.

2. Add 1ml water to it and grind for 1min.repaet this for 5 times.

3. Repeat the second step with ethanol.

4. Again add 1ml acetic acid in agate mortor and grind for 5mins.

5. Add ethanol of about 2.5ml and grind for 6mins.

6. After the grinding steps take all the paste in beaker and 100ml ethanol to it.

7. Stir this mix for 2hrs for homogenous mixing of ingredients with TiO_2 and finally with ultrasonic probe with 5sec of pulse.

8. In this solution add 21ml terpineol and stir for 20mins followed by sonication in ultrasonic probe with 5sec active and 5sec rest time.

9. Then add solution of 3g of cellulose dissolved in 30ml ethanol and again ultra-sonic the paste.

10. Evaporate excess of ethanol in rota till the optimum viscosity of paste is achieved.

2.1.2.3. Coating of paste:

To produce uniform film from the paste, ***"Doctor Blade"*** coating method was used as given in **Figure 2.2.** In this method, first an FTO coated glass substrate is masked with two scotch tapes (~25-30 micrometer thick). This creates an area as well as controls the thickness of the TiO_2 film

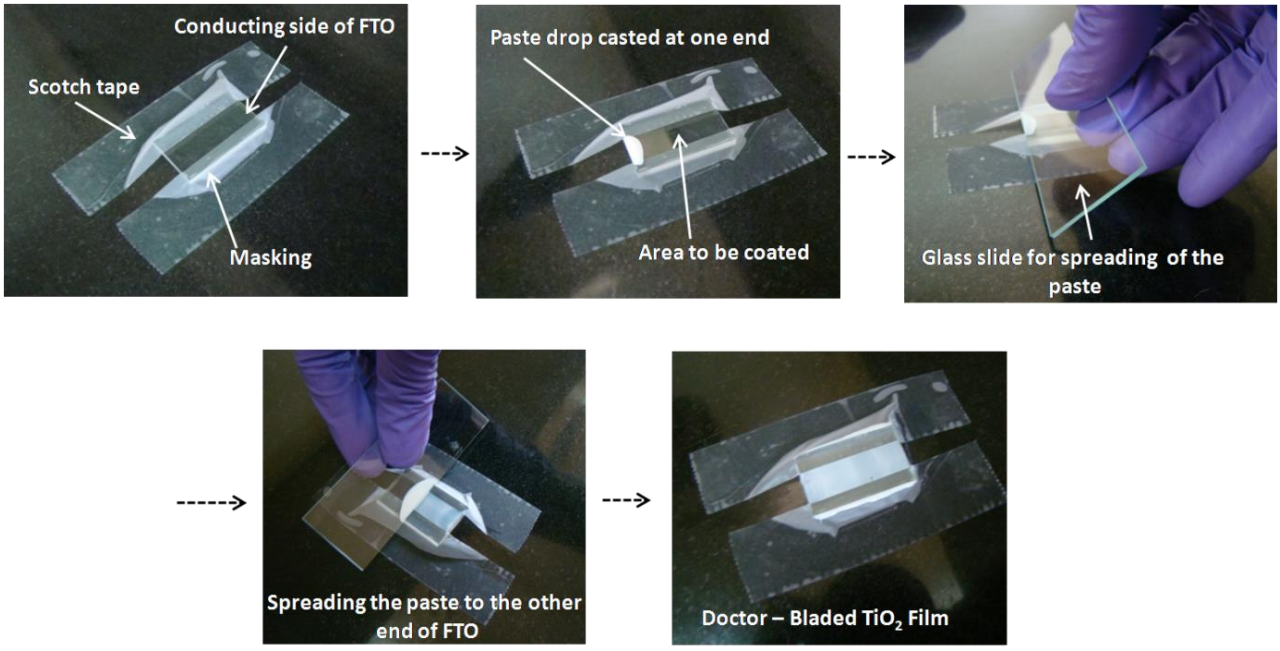

Figure2.2. Visual photographs of Doctor blade method

and the non-coated part of the substrate provides area for electrical contact. The prepared slurry is applied to one of the edges of the conducting glass and is spread over to the other end using glass slide or blade. The coated film is allowed to air dry for 10 minutes and then heated for 10 min at 450^0C.The resulting film thickness is around 6-7 µm. This process is repeated to get a film of 12-15 µm thickness. After air drying the electrode is fired for 60 min at 450 ^{O}C.

Commercially available standard Degussa P-25 powder is used initially as photoanode material for optimizing crucial parameters of paste making which gave about 4-6% solar efficiency in our lab by protocol I but with protocol II noteworthy 7-10% solar efficiency was achieved. In the chapter 3 of present thesis protocol I has been employed where as in other chapters protocol II is used.

2.1.2.4. $TICl_4$ Treatment

For post $TiCl_4$ treatment, $TiCl_4$ solution is made by adding 0.55ml of $TiCl_4$ in ice made from 100ml DI water. Ice is allowed to melt at room temperature and stirred to get homogenous aqueous solution of 40mM concentration. In this solution doctor bladed TiO_2 films are dipped and subjected to70^oC for 30 mins. This heating step provides a thin layer of about 2 nm amorphous TiO_2 on the doctor bladed film.[10, 11] Films are taken out of solution and rinsed with water and ethanol. After drying in air they are again annealed at 450^0C for 30 mins. This treatment increases connectivity and necking between the particles for efficient charge transfer. Moreover, it provides roughness factor to the film for better dye loading and light harvesting.

2.1.2.4.. Sensitization: preparation of Dye solution

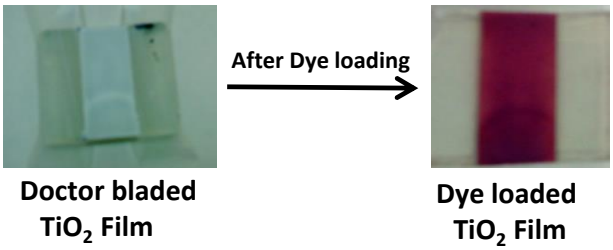

Figure2.3. Sensitization: dye loading in TiO_2 film

After $TiCl_4$ treatment photoanode film is sensitized with dye molecules for light harvesting by soaking it in dye solution for 20-24hrs.From **figure 2.3.**colour change of TiO_2 white film can seen after dye loading. Dye used in the present thesis work is N3 (chapter 3) or N719. Dye solution is prepared of concentration 0.5mM in tert. butyl alcohol and acetonitrile solvents (50/50 ratio v/v). Dye was purchased from Solaronix, Switzerland and used without further purification.

2.1.3. Preparation of Photocathode (*counter electrode)*

Counter electrode is prepared by drop casting 0.6M H_2PtCl_6 ethanolic solution on FTO. It is allowed spread evenly all over FTO and to dry for few minutes in air. Then it is fired at 450^0C for 15 min which thermally reduces it to Pt nanoparticles

.

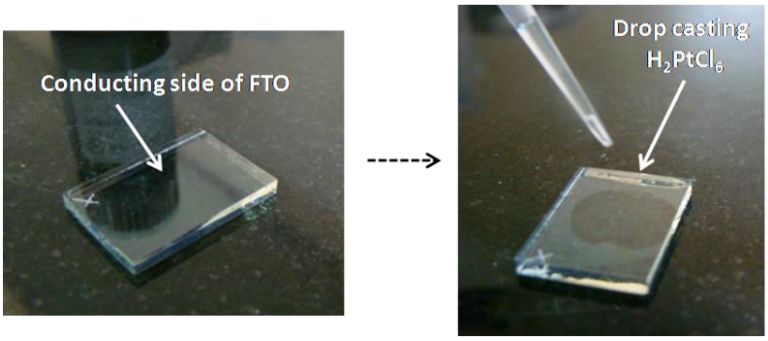

Figure2.4. Preparation of counter electrode of DSSC

2.1.4. Preparation of electrolyte solution:

The typical composition of the I^-/I_3^- redox couple was 0.05M LiI, 0.05M I_2, 1M 1-propyl-2,3-dimethyl-imidazolium iodide (DMPII), and 0.5M 4-tertbutylpyridine (TBP) in acetonitrile/valeronitrile solution (v/v 1:1). The DMPII and LiI in electrolyte are sources of iodide ions and I_2 is necessary to produce the redox couple with them. The TBP in electrolyte helps to improve V_{oc} by positively shifting the conduction band edge of TiO_2 and also by reducing the dark current.[12]

2.1.5. DSSC device assembly:

In order to evaluate the performance of DSSC device, working electrode and counter electrode is assembled together. Detailed steps involved in assembling the device is given in **Figure 2.5.**The area of dye sensitized working electrode was limited to 5 mm × 5mm (area = **0.25** cm^2) while

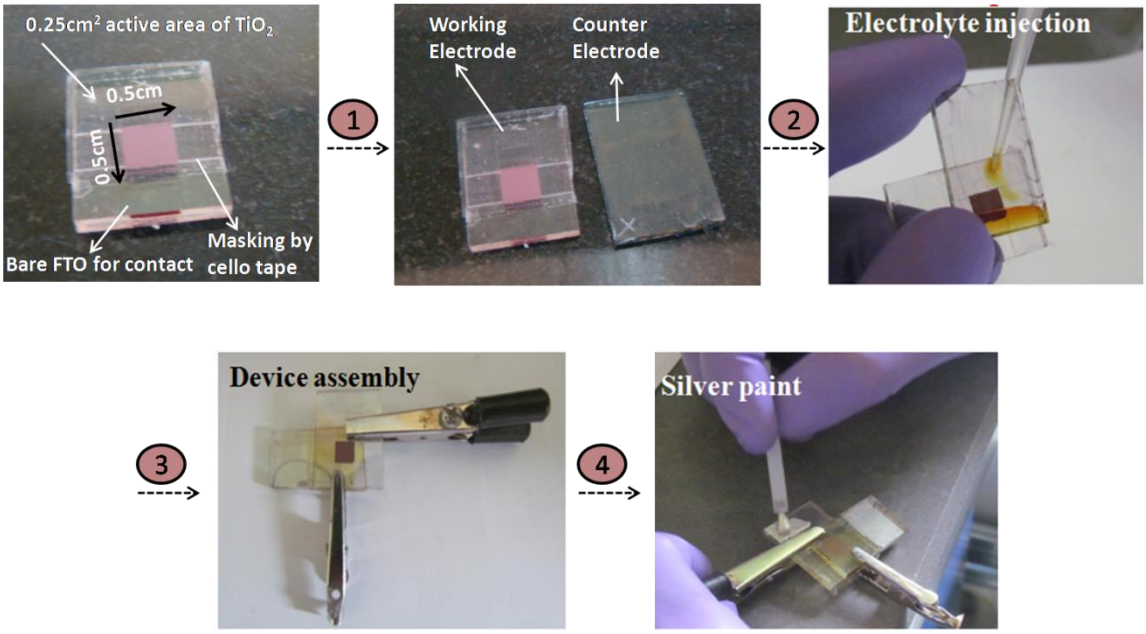

Figure2.5. Visual photographs of steps involved in assembling DSSC device for testing its photovoltaic performance.

TiO_2 film on remaining area was scratched. The bare FTO on working electrode was masked with the cello tape of thickness 40 microns which prevents the direct contact of electrolyte with FTO and also acts as spacer between working electrode and counter electrode. A small amount of electrolyte was injected between the working and counter electrodes using a syringe shown in 2^{nd} step. Then a thin layer of silver paste is applied at the ends of both electrodes where contacts are supposed to be given for better charge collection. When the paste is dried in air crocodile contacts are given. The JV curves were measured using Newport solar simulator attached to Keithley IV meter.

2.2. Fabrication of QDSSC

2.2.1. Preparation of Photoanode (*Working Electrode)*

Preparation of photoanode in QDSSC is similar to DSSC photoanode as given in **section 1.2.2.** in detail. Protocol II was followed for paste making of TiO_2 for QDSSC photoanode.

2.2.2. Sensitizer:

The major difference between DSSC and QDSSC lies in sensitizer where organic dyes are replaced by narrow band gap semiconductors called as Quantum dots. Many binary (CdS, CdSe, CdTe) or ternary ($CuInS_2$, CdTeSe) QDs are used as sensitizer.[13] There are two approaches of assembling QDs to wide band gap semiconductors like TiO_2

1) ***Ex situ* sensitization** –With and without linker assisted absorption of QDs on TiO_2 mesoporous film from pre-synthesized colloidal solution of QDs.[14] Sensitization of Colloidal Quantum Dots (CQD) occurs in two consecutive steps. In first step CQDs are grown with appropriate size, shape, crystallinity and capping and in second step they are attached to photoelectrode. This attachment may be assisted or direct. In assisted sensitization a bifunctional linker is used in which one end of linker attaches to TiO_2 electrode by carboxylic group and other to QDs by thiol group.[15] In direct sensitization QDs attach directly without linker by simply dipping TiO_2 films in CIS colloidal QD solution.[16] Linker assisted sensitization is preferred as it avoids agglomeration of QDs and hence increases QD loading.

2) ***In situ* sensitization** – Direct nucleation and *in situ* growth of QDs in mesoporous TiO_2 film by Successive Ionic Layer Adsorption Reaction (SILAR) [17, 18] or by Chemical Bath deposition (CBD) [18]

2.2.3. ZnS treatment

A thin passivation layer of ZnS is coated on sensitized photoanode by SILAR method to protect QDs from photocorrosion, passivate the surface trap states/defects and to inhibit interfacial recombination (leakage of current) from QD/electrolye interface.[20] With the SILAR, QDs get

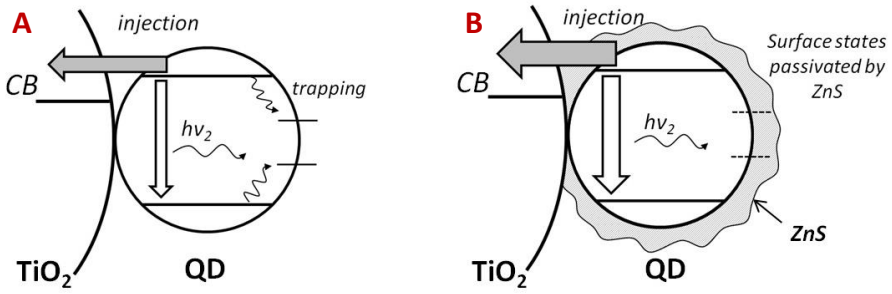

Figure 2.6. Radiative recombination and surface trapping states of QD attached to TiO_2 semiconductor A. without ZnS coating, B. with ZnS coating.[20] Reprinted with permission from (*Phys. Chem. Chem. Phys.*, **2011**, 13, 12024–12032). Copyright (2011) American Chemical Society.

covered heterogeneously with flat nanoparticles of size 10-15nm diameter of ZnS.[20] ZnS treatment not only increases stability of device but also increases $J_{sc.}$ Ethanolic solution of $Zn(NO_3)_2$ and Na_2S of 0.5M concentration is prepared in two separate beakers and two cycles of SILAR is performed with1min dipping time.

2.2.4. Preparation of Polysulfide electrolyte:

Polysulfide electrolyte used in QDDSC is Sulphur saturated. It is prepared by dissolving 0.6M Na_2S, 0.2M Sulfur and 0.2M KCl in1:1v/v water/methanol mixture.Na_2S is source of S_2- for hole recovery, sulphur is source of S_x^- which improve hole recovery ability and ionic salts is added to enhance the conductivity of solution. Mixed solvent system is preferred to minimize the high surface tension of water making its penetration difficult through TiO_2 to inhibit recombination.[21]

Iodine/triiodide electrolyte used in DSSC is not compatible in QDSSC as QDs undergo photocorrosion/degradation process in iodine. A polysulphide electrolyte is suitable compared to others in terms of stability of QDs and in redox activity.[20]

2.2.5. Preparation of Photocathode (*counter electrode)*

Pt counter electrode used in DSSC cannot be used in QDSSC as it undergoes corrosion with polysulfide electrolyte. Therefore, sulfide based counter electrode is prepared. A brass sheet (Zn-Cu alloy) of 5mm thickness is immersed in 0.1M acid (HCL) at 80°C for 20mins to etch the surface and to expose clean Cu surface. Then it is taken out and rinsed with D.I water. After drying it is masked with scotch tape leaving 1cm*1cm area exposed as shown in **Figure 2.7.**In the exposed area one drop of polysulfide electrolyte is added. As soon as drop is added area turns into black colour indicating formation of Cu_2S.It is dried in air and used as counter electrode.

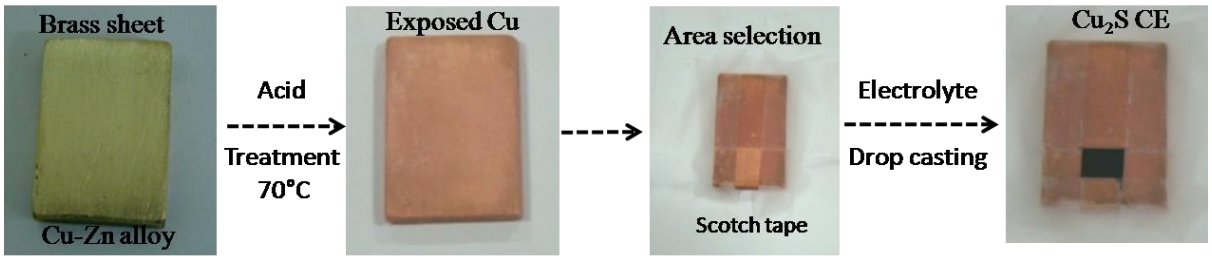

Figure2.7. Preparation of counter electrode of QDSSC

2.2.6. QDSSC device assembly:

Device assembly of QDSSC is similar to DSSC assembly with difference in components.

SECTION II: Experimental methods

2.3. *Anodization Method*

Anodization is an electrochemical method which is well established surface modification technique to form metal oxide protective layer on metals. In nanotechnology it is widely used as "top-down" synthesis process for engineering nanostructures of metal oxides and other nanomaterials. It is a simple, cheap and one step process for obtaining ordered and self-organized nanostructures even on large scale.

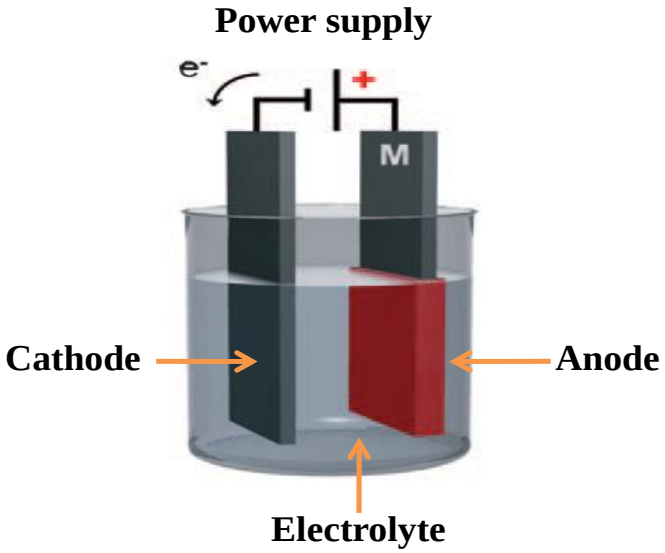

Figure2.8. Anodization set up

A typical anodization process involves two-electrode assembly comprising of a anode and a conducting metal as cathode dipped in a weak electrolyte solution (acidic or alkaline) and connected by DC power supply as depicted by **Figure 2.8.**As the voltage is applied across the electrodes hydrogen ion gets reduced at cathode and hydrogen gas is produced where as a anode reactive species from electrolyte oxidizes or corrodes the anode forming stable oxidation state of

metal ion. This process is also abbreviated as "Anodic Oxidation" or "anodic dissolution" as the part of the electrode which is going to be oxidized or corroded is anode. The properties of resultant oxide film or product after anodic oxidation such as size, roughness, morphology and surface area are purely affected by parameters used for anodization process. Anode thickness, composition of electrolyte, pH of solution, applied voltage and temperature are the governing factors for the anodization.

Specifically, by anodization method 1D self – evolved, oriented and ordered nanostructures like nanotubes, nanoneedles, nanowires are produced due to unique process of etching of anode by reactive species. Usaually, three mechanisms are prevailing in this process - chemical dissolution, field assisted dissolution and oxidation. Out this field assisted dissolution is considered to be the most predominant one responsible for tubular structure. In the intial stage of anodization a thin metal oxide layer is formed on the surface of anode. The active species present in the electrolyte say ClO_4^- or F^- ions chemically corrodes the surface and forms small pits as.

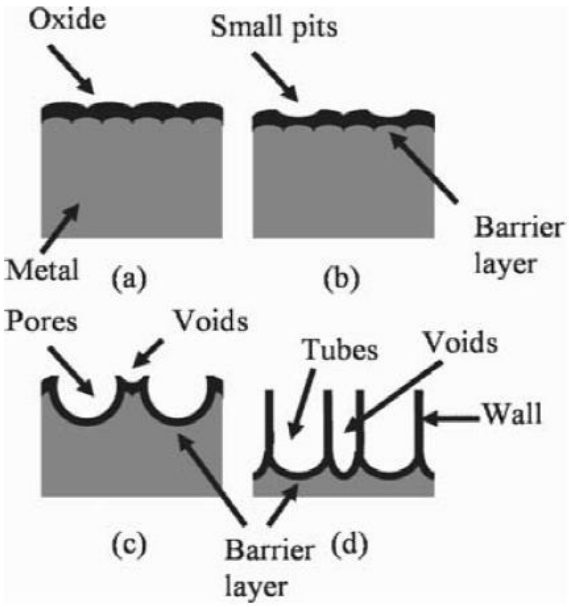

Figure2.9. Schematic diagram for mechanism involved in anodization process.[22]

shown in **Figure 2.9.** Later with field assisted dissolution this pit becomes deep and wide. So depending upon the pH, voltage and duration of anodization length and diameter of tubular nanostructures is decided.[22] *In the present thesis as a part of chapter 3, anodization method is employed for the synthesis of rutile TiO_2 nanoneedles with high aspect ratio of about 10.*

2.4. *Successive Ionic Layer Adsorption and Reaction (SILAR) method*

SILAR method was introduced by Ristov et al. but the name "SILAR" was ascribed by Nicolau et al. in 1985.Silar is very simple, convenient and inexpensive technique. Raw materials used are also cheap and they can be coated on variety of substrates even on large area deposition. It can be done manually or operated by computers. This method is generally used for fabrication of thin films, specifically for metal chalcogenide materials like CdS, CdSe, ZnS, $CuInS_2$. Unlike chemical vapor deposition (CVD) technique it doesn't require high quality target, substrates or high vacuum which is most advantageous aspect of this method. Also it provides feasibility of doping in the system. This method can be performed at room temperature and doesn't undergo localized over heating like radio frequency magnetron sputtering (RFMS).

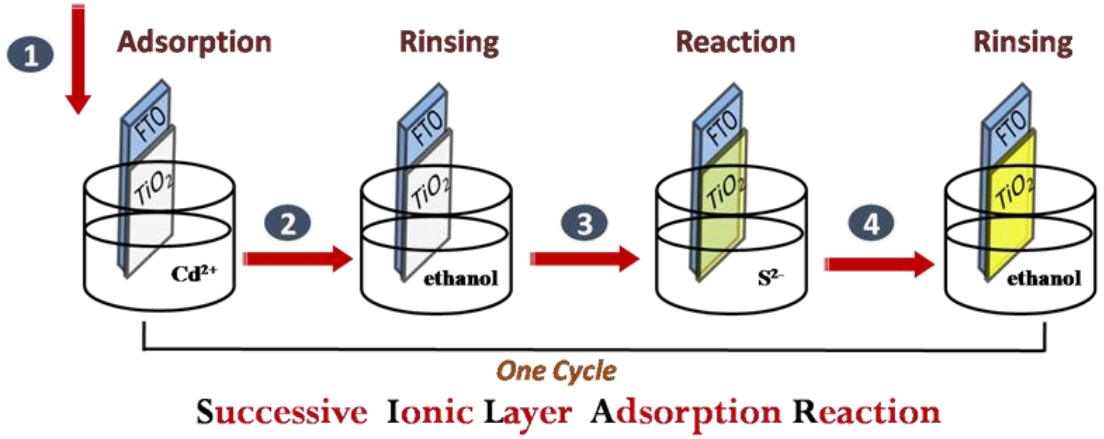

Figure2.10. Schematic diagram for steps involved in SILAR.

SILAR method involves four steps- 1) Dipping the electrode in cationic bath for cationic adsorption from precursor for specific duration, 2) rinsing the electrode with solvent to remove unspecific ad unadhered precursor 3) in situ chemical reaction of cationic precursor with anionic precursor to form the material after dipping the electrode in anionic precursor for same duration.4) again rinsing with solvent to remove unreacted species. These four steps make one SILAR cycle as shown in **Figure 2.10.** and **2.11.**with CdS as an example. Many such successive cycles are

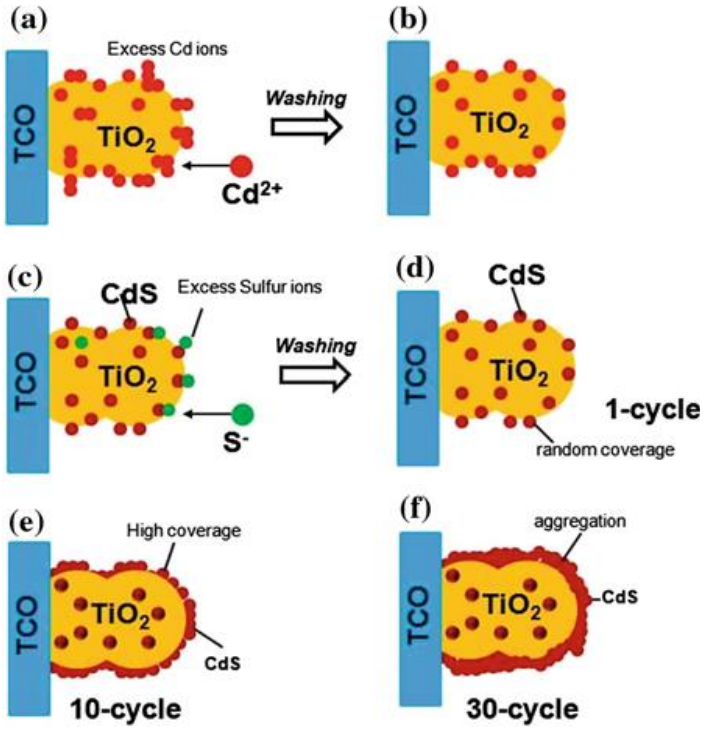

Figure2.11. Schematic illustration of SILAR process with CdS as an example.[23]

performed to deposited material on to the substrate and to increase the thickness of film. In the first step, nucleation starts which is based on the concept of solubility product. When the ionic product exceeds the solubility product then the solution is supersaturated and ions in solution or

on substrate combine to form nuclei. These nucleuses undergo adsorption on the substrate by weak Van-der Waal's forces or chemical attractive forces. There are many unbalanced or residual charges which allow the nuclei to hold the surface of substrate. This adsorption process undergoes sequential reactions to form finally product. Sequential growth of nuclei may form self-assembly to give rise to oriented nanostructures of material. Ternary chaclcogenides obtained by SILAR are generally amorphous in nature which may need post-heat treatment to achieve crystallinity.[24] *In the present thesis as a part of chapter 5, SILAR method is employed for the fabrication of $CuInS_2$ thin film coated on FTO as a counter electrode for DSSC. In Chapter 6, this method is used to load metal chalcogenide quantum dots on TiO_2 as a sensitizer in QDSSC.*

2.5. *Hydrothermal Method*

Stainless steel autoclave **Teflon liner**

Figure2.12.photographs of hydrothermal autoclave with inner Teflon vessel.

Hydrothermal method is used for synthesis of nano crystals under high temperature and pressure in water conditions from substances which are insoluble in ordinary conditions. In such conditions reaction rates are increased by 3 fold. This method was reported first by Karl Emilvon Schafhäutl in 1845 who grew quartz crystal in pressure cooker. Usually there is Teflon liner or vessel as shown in **Figure 2.12.** in which reaction mixture is added .This vessel is inserted in

stainless steel jacket called autoclave and packed tightly with screws. This autoclave is then subjected to high temperature. Crystallite size and shape is dependent on solvent, precursor and temperature. The dielectric constant and density of solvent are important parameters which affect the solvating ability. As the temperature increases and pressure decreases solvating ability increases. The advantage of hydrothermal synthesis is that the materials which are not stable at their melting point can also be grown. Also, this technique can be coupled with microwave, ultra sound, mechano-chemistry, hot pressing to increase the kinetics of reaction.

SECTION III: Characterization techniques

2.6. X-ray Diffraction (XRD)

XRD is most powerful and primary analytical technique used for phase identification of crystalline materials. The break through work of XRD was developed by Bragg's father and son pair in 1913.It is rapid and non-destructive method which determines phase, size, cell parameters, strain and anisotropic growth involved in nanomaterials. Powder form as well as thin films can be analyzed by this technique.

When monochromatic collimating beam of X-rays are incident on sample then they are diffracted by lattice planes of crystallites and the constructive interference for a set of hkl planes diffracting the beam of light at certain angle (θ) for only those diffracted beams whose path difference is integral multiple of wavelength of incident light. Mathematically, condition for constructive inference is given by Bragg's law:

$$2d\sin\theta = n\lambda$$

Where, d is inter planar distance, θ is angle of scattering, n is order of diffraction and λ is

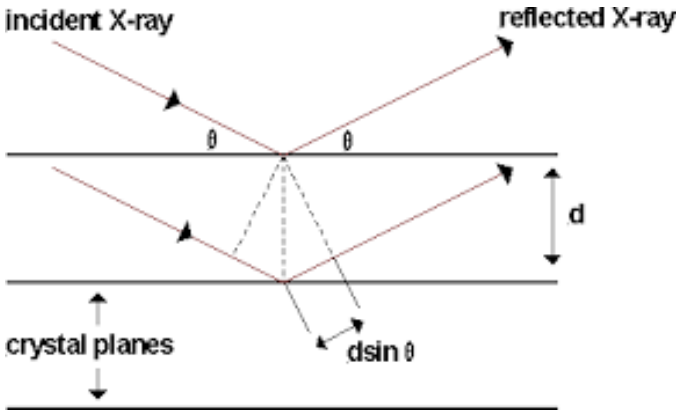

Figure2.13. Schematic for illustration of X-ray diffraction set up.

wavelength of incident angle.

In particularly dealing with nanomaterials, XRD peak broadens as the size decreases or may be strain induced. This is explained by Scherrer formula as:

$$\mathbf{D= \frac{0.9\lambda}{\beta cos\theta}}$$

Where, β is FWHM of XRD peak at angel θ.

Microscopy techniques:

It involves techniques for viewing the sample and obtaining images ranging from µm to nm.

2.7. Scanning Electron Microscopy (SEM):

A beam of electron is produced at the top of microscope by electron gun which is directed towards sample by using different lens in the presence of electromagnetic field as shown in **Figure 2.14.** The top columnar part is under high vacuum to increase free mean path of electron and to direct it efficiently towards the sample. Electron gun used is either thermionic or field emitter. Thermionic gun is generally used for soft samples like polymers and biological samples but gun based on principle of field emission is more reliable in terms of electron brightness

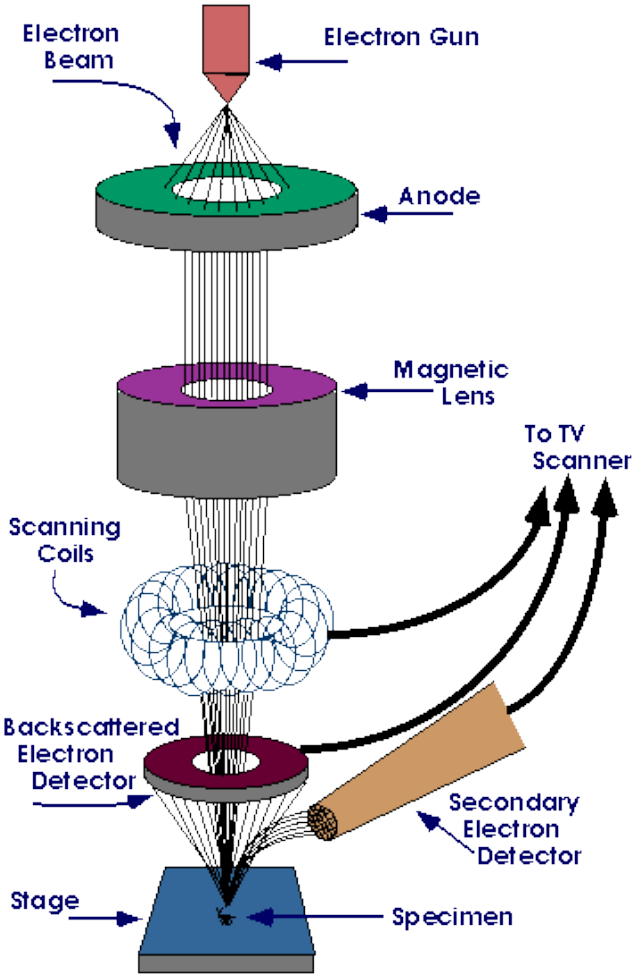

Figure2.14 Schematic diagram of Scanning Electron Microscopy

https://www.purdue.edu/ehps/rem/rs/sem.htm

and spot size. In SEM thermionic based tungsten filament where as in FESEM fields based lanthanuim hexaboride (LaB_6) emitter is used. Electrons are accelerated by the potential of 30 KV in SEM and 3KV in FEEM. When beam of electrons are incident on sample they undergo interactions with sample and give rise to elastic and inelastic events. In elastic event electrons are deflected back due to interaction with nucleus of atom and give rise to back scattered electrons (BSE).In inelastic event electron beam interacts with atoms of specimen and transfer energy to

sample. In these course auger electrons, secondary electrons (SE) and some characteristic X-rays are produced. Signals from secondary and backscattered electrons are acquired and amplified by photomultiplier tube to produce image of topography of sample on the monitor. SEs and BSEs play major role in determining the topography of sample.

Characteristics X-rays produced after transition of electrons from high energy orbital to low energy orbital after removal of electrons from incident beam of electrons can be detected by x-ray detector. This is very useful for identification of elements and mapping of them present in sample.

2.8. Transmission Electron Microscopy (TEM):

The line diagram of TEM is given in **Figure 2.15.**The components of TEM is same as that of SEM difference in working principle and accelerating voltage applied (300kV). Lanthanuim hexaboride (LaB_6) field emitter is used. By using electron energy of several hundred kilovolts the de Broglie wavelength associated with the electron can be reduced to a small fraction of nanometer and hence atomic resolution imaging becomes feasible. With TEM not only shape and size of nanomaterials is determine but the crystal structure, lattice planes and localized defect in nanaometer region can also be analyzed by Selected Area Electron Diffraction (SAED).In TEM also incident beam of electrons interact with sample either elastically or inelastically but the beam of electrons which is transmitted through the sample brings out the image of sample. The transmitted beam is directed through objective, intermediate and projector lens as shown in **Figure 2.15**.to fluorescent screen to produce image. Depending upon the projector lens the TEM is classified as Low resolution TEM or high resolution TEM (HRTEM).In LRTEM projector collects only the central transmitted beam whereas in HRTEM all the types are collected. Due to

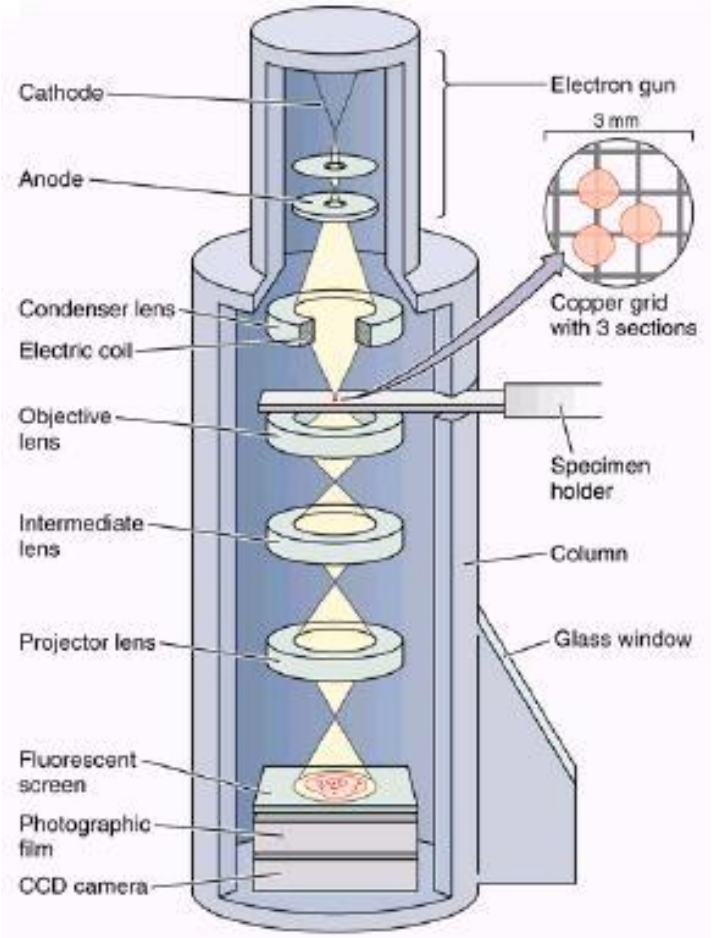

Figure2.15. Schematic diagram of Transmission Electron Microscopy

http://www.ufrgs.br/imunovet/molecular_immunology/microscopy.html

this reason the resolution of Image produced in HRTEM is high and of good quality. Elemental composition of sample can also analyzed by EDAX but in TEM overall composition of sample under consideration can be obtained.

The sample preparation for TEM is vital for obtaining clear and good quality images. Sample is dispersed in particular solvent and drop casted on carbon coated copper grid of 400 mesh size. It is dried and then analyzed under TEM.

Spectroscopy tools:

2.9. Ultraviolet - visible Spectroscopy:

Ultraviolet - visible Spectroscopy (UV-VIS) [25, 26] is vital and non-destructive tool for characterization of optical properties of semiconductors. It deals with absorption/reflectance/ transmittance spectroscopy in UV-Visible region. In this electromagnetic region molecules undergo electronic transition and are related with color of the sample after interaction with light. In solid state physics and in nanomaterials when incident light is greater than the band gap of semiconductor then it absorbs light and UV-VIS spectrum is obtained of absorbed region through spectrometer.

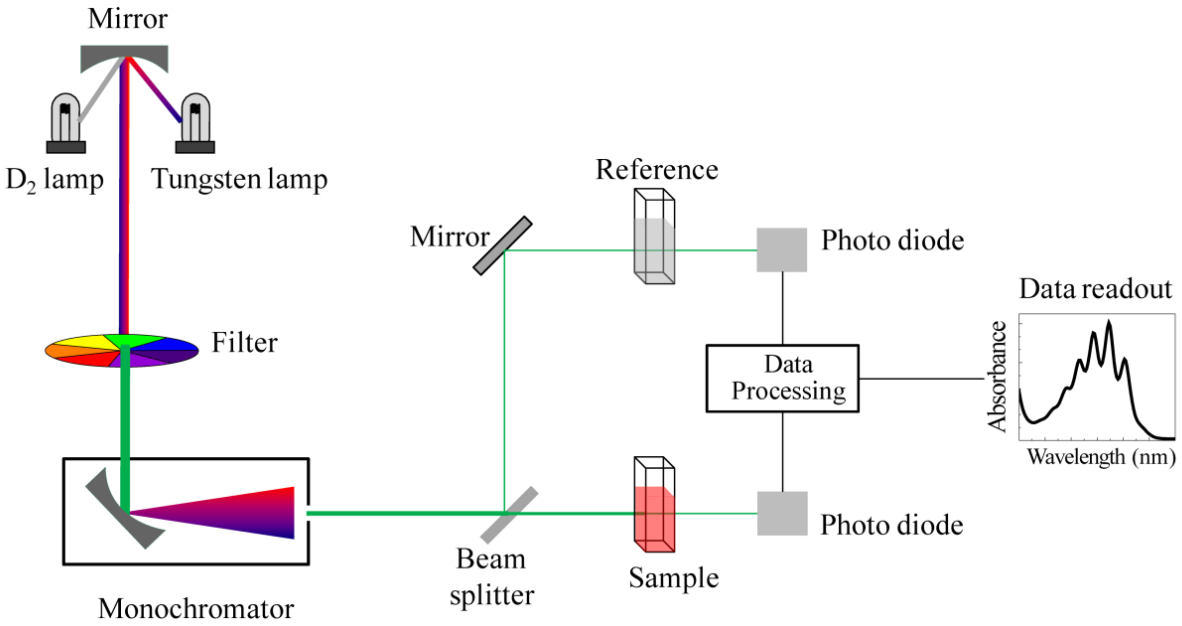

Figure2.16. Schematic diagram of UV-Vis [25]

Spectrometerhttps://en.wikipedia.org/wiki/Ultraviolet%E2%80%93visible_spectroscopy

Instrumentation: The light source used is combination of Deuterium lamp for UV region and halogen or tungsten lamp for visible region to cover entire 200nm to 900nm (**Figure 2.16.**). Specific wavelength of light is selected by monochromatic and then the beam is splitted. One beam is passed through reference where as other through sample. Signals from both of them are analyzed by respective detectors (photomultiplier tube) and the ratio of two output beams is given on monitor.[25]

Principle and Application: UV-VIS spectrometer can be used in three modes: absorbance, transmittance and reflectance. For samples dissolved/dispersed in liquid solvent can be used in absorbance mode. Absorbance is governed by Lambert Beer's Law:

$$I / I_0 = \exp(-\kappa cl) \quad \text{or} \quad I / I_0 = 10^{-\varepsilon cl} = T$$

Where, κ = constant, for particular spectroscopic transition under consideration.

ε = molar absorption coefficient

T = transmittance = I / I_0, ratio of intensity of incident radiation (I_0) to transmitted radiation (I)

Inverting above equation and taking logarithms,

$$I_0 / I = 1_0^{\varepsilon cl} \quad \text{Or} \quad \log (I_0 / I) = \varepsilon cl = A,$$

Where A = absorbance / optical density

Therefore, absorbance is directly proportional to concentration of sample.

In the case of powder samples or films, spectrometer is used in diffused reflectance mode (DRS).To calculate the band gap of semiconductor, tauc plot is obtained from DRS spectrum by following equation:

$$[F(R)h\nu]^{1/n} \propto (h\nu - E_g), \qquad \text{Where, } F(R) = \frac{(1-R)^2}{2R}$$

n= ½ for indirect band gap semiconductor and n=2 for indirect semiconductors. From the plot of $[F(R)h\nu]^{1/n}$ vs hν band gap E_g can be obtained by extrapolating the a straight line tangent to the plot.[26]

2.10. Photoluminescence (PL) Spectroscopy:

PL[27, 28] is measure of spontaneous emission of light which is under optical excitation.PL is highly useful, non-destructive and sensitive characterization technique for nano materials as it provides electrical information and can probe discrete energy levels.PL spectrum provides the information of energy levels, defect systems, surface features, disorders and roughness at interfaces. The intensity of spectrum gives the idea of quality of surface and interfaces. Also the

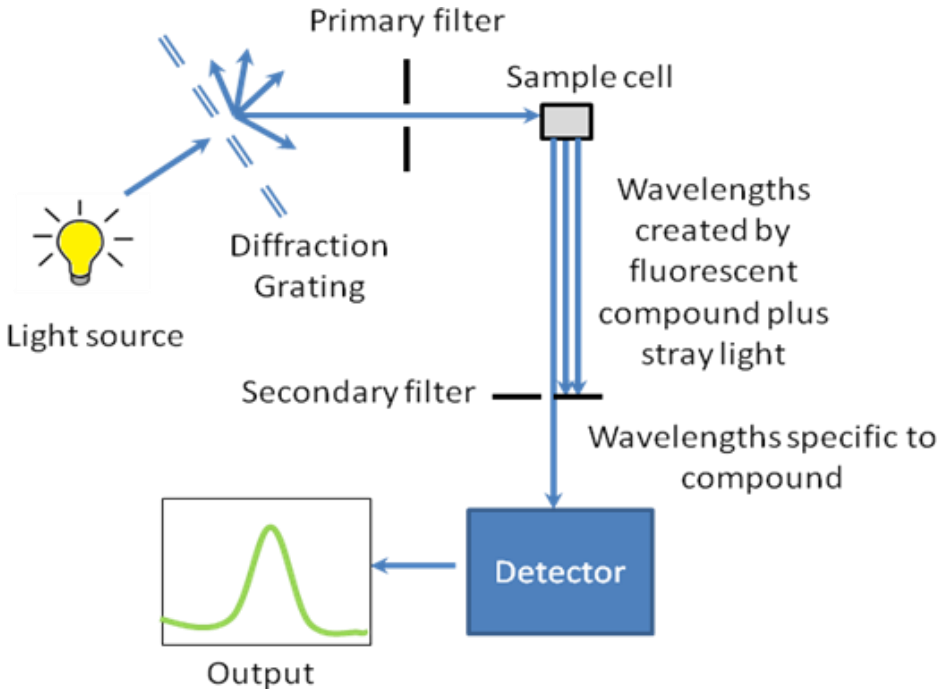

Figure2.17. Schematic diagram of Photoluminescence set up [27]

http://cnx.org/contents/7b4dfcf8-b28e-4148f2f1ff39052669f@13.7:30/Nanomaterials_and_Nanotechnolo

band gap of material can be determined from emitted photons depending upon the presence or absence of non- radiative recombination. Thermally assisted PL yields the information of defect levels and electronic behavior of material with variation in temperature. On the other hand Transient PL intensity gives the life time of charge carrier in the non-equilibrium interfaces and bulk systems.PL is basically a surface technique as PL occurs at surface of material.[28]

Instrumentation: As shown in **Figure 2.17.**PL set up has a light source which is usually xenon arc or mercury vapor lamp which can emit the light of wavelength in UV and visible region. With the help of diffracting gratings and filter specific wavelength of light can be irradiated on sample. From the secondary filter which is placed at 90 angle to the sample, wavelength specific light is allowed to pass through detector. This filter reduces the risk of transmitted, reflected or stray light to pass to detector.[27]

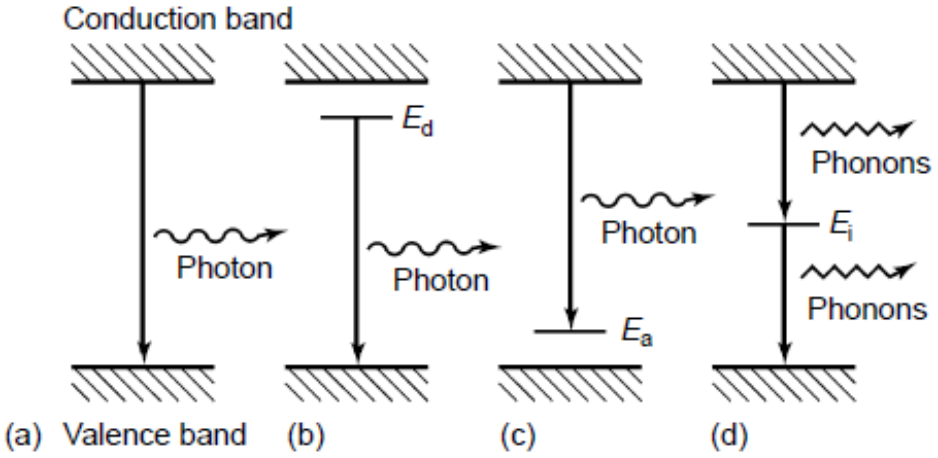

Figure2.18. Schematic diagram of (a-c) radiative path - (a) Band to band (b) donor to CB (c) CB to acceptor, (d) non-radiative path via intermediate states.[28]

In **Figure 2.18.**different path ways of radiative and non radiative decay is given which takes place in semiconductors. It is useful in determination of defect system in semiconductors.

2.11. Fourier Transform Infra –red (FTIR) Spectroscopy:

FTIR [29] technique is used to obtain IR spectrum (800-1200nm) after absorption or emission of IR rays by solid, liquids or gases. The obtained spectrum is finger print of sample which is unique characteristics of that sample only. This makes FTIR spectroscopy a distinctive technique. It utilizes the fact of fourier transform given by J. W. Cooley and J. W. Tukey in 1965 which is a mathematical process required to convert the raw data into spectrum. Therefore this technique is called *fourier transform spectroscopy*. It is fast, highly sensitive and non-destructive technique which gives precise measurement without using external calibration as it has HeNe laser as an

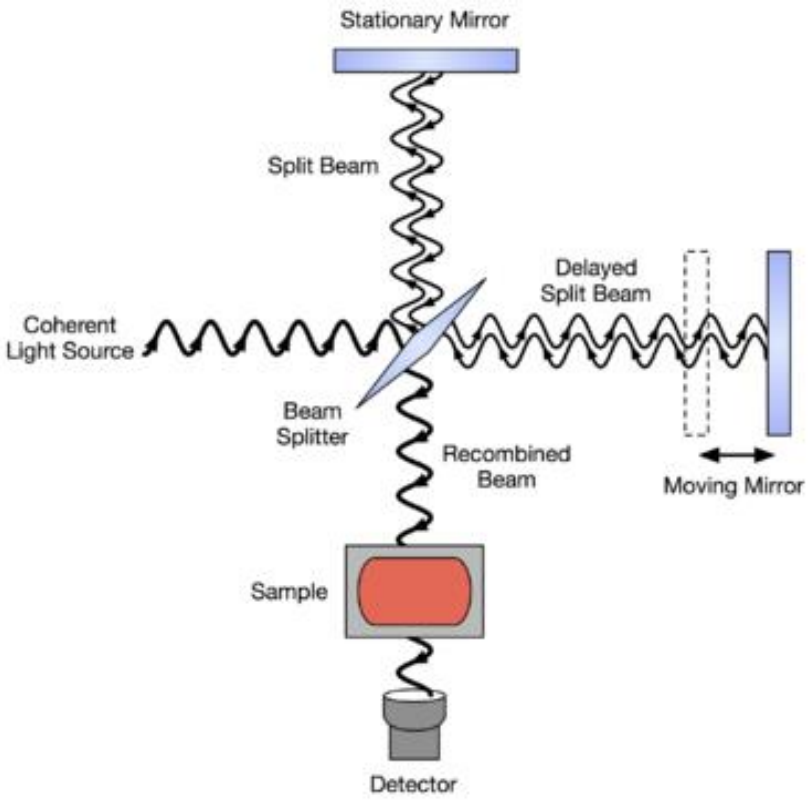

Figure2.19. Schematic diagram of FTIR set up [29]

https://en.wikipedia.org/wiki/Fourier_transform_infrared_spectroscopy

internal wavelength calibration standard. It is used for identification of unknown material, its composition in mixture and surrounding environment

Instrumentation: Infra-red light is emitted by glowing black body radiation which is passed through interferometer where "spectral encoding" takes place. FTIR is based on Michelson interferometer experimental set up. When the radiation is directed towards the beam splitter it splits the beam, out of which 50% is refracted towards a fixed mirror and 50% towards a moving mirror as shown in **Figure 2.19.**Light (50%) from the two mirrors is refracted back to beam splitter and passed to the sample compartment. On leaving the sample compartment light is refocused on detector. The difference in optical path length, i.e. optical path difference (OPD) of two arms of interferometer is called as *retardation.* An interferogram (signal obtained from interferometer) is obtained by varying the retardation and obtaining signals for each change in retardation through the output of detector. Interferogram obtained when no sample is present has maximum value at zero retardation where there is constructive interference of light. But when the sample is present this value changes due to absorption bands of sample. Therefore, the raw data of FTIR has multiple OPD pair values (interferogram) which has to converted into actual spectrum by performing Fourier transformation function(a mathematical process).

Advantage of FT spectrometer is that it gives the information for all the wavelengths is collected simultaneously with high signal to noise ratio.[29]

2.12. Raman Spectroscopy:

Raman [30] is straightforward and non-destructive technique used for identification of materials. This spectroscopy technique deals with vibrational, rotational and other low frequency modes present in the system. It also generates a finger print of molecule like IR spectroscopy which is useful for identification of molecule. In chemistry it gives vibrational information of chemical bond and symmetry of molecule but in solid-state physics it is used to characterize the sample. It also provides the information of crystallite size orientation, symmetry and the strain or defect introduced in the system. The advantage of raman technique lies in requirement of very minute amount of sample due to very small lazer focus spot (1-100 μm dia) without any tedious sample preparation.

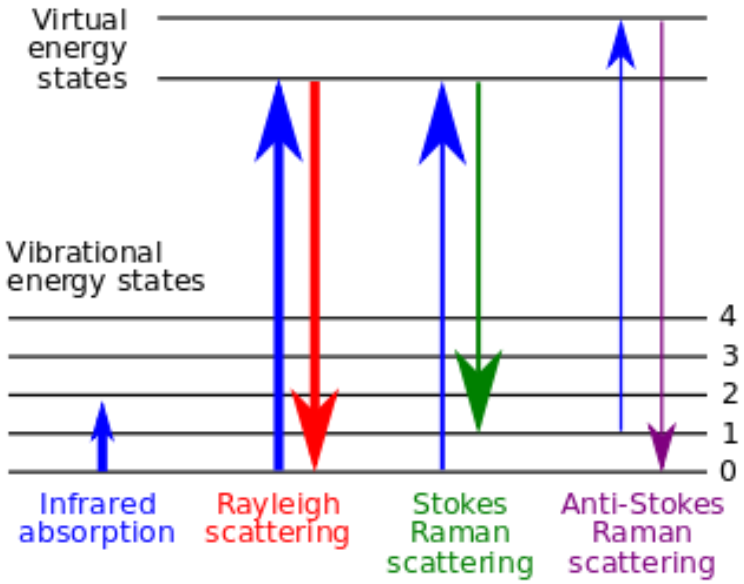

Figure 2.20. Energy level diagram for raman scattering.

Principle and instrumentation: Typically, in this technique sample is illuminated with UV-VIS-IR range monochromatic light from laser which undergoes elastic (Rayliegh) or inelastic (raman)

scattering. Lasers used are HeNe (514nm), Ar (632nm) and diode (nm) which are focused with microscope to a small spot. The electric component of scattered beam from sample perturbs the electron cloud of molecule and excites it to virtue state. So inelastic scattering there is exchange of energy which with photons which decays the vibrational energy level of molecule to higher or

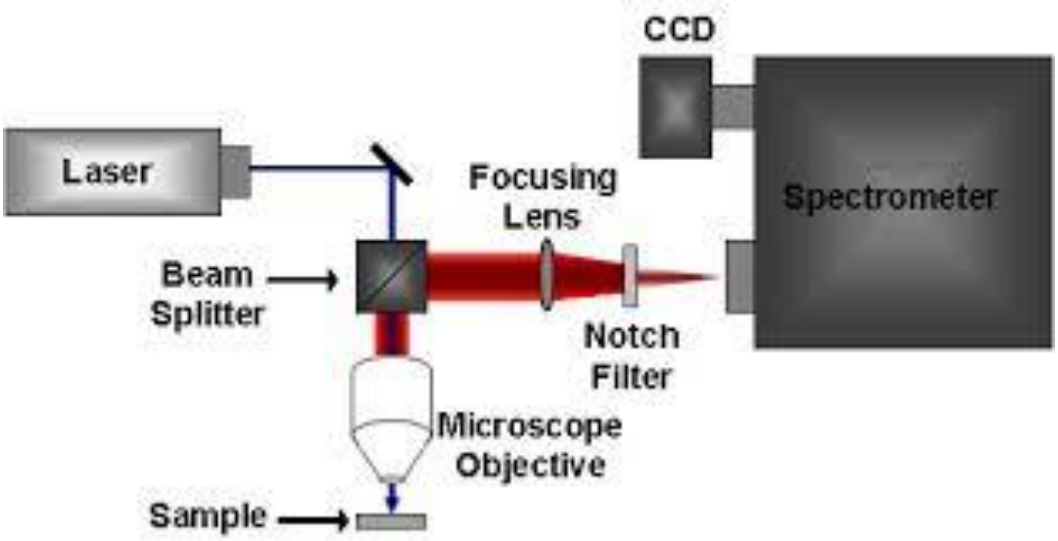

Figure2.21. Schematic diagram of Raman spectrometer.[30]

lowers value than its intial state. The difference in frequency of incident ray and scattered ray is called *Raman shift.* Depending upon the energy lost or gain from the system raman shift is up shifted called as *anti-strokes* and down shifted called as *strokes as shown in* **Figure 2.21.**A plot of detected number of photons verses raman shift gives raman spectrum. Rayliegh scattering from sample is absorbed and only raman scattering is passed to lens and monochromator to Charge Coupled Detector (CCD).[30]

2.13. X-ray Photoelectron Spectroscopy (XPS):

XPS[31] is also known as *Electron Spectroscopy for Chemical Analysis* (ESCA) which provides chemical finger print of surface. It is surface sensitive quantitative spectroscopy technique which is used to determine surface composition, uniformity and contaminant. It also determines the chemical and electronic state of element present in the sample. It is routinely employed for analysis of semiconductors, inorganic compounds, ceramics, glasses, alloys, polymers, wood, paper, bones.

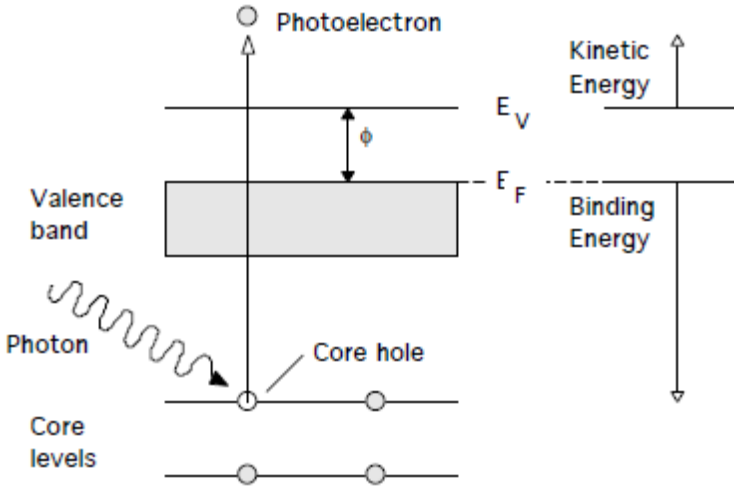

Figure2.22. Principle of XPS

Principle: It is the technique which is based on the principle of *photoelectric effect*. Each atom of the surface has core electron which has characteristics binding energy (B.E.) and this core electron is ejected out of the surface by X-ray beam if the energy of incident photon is greater than the B.E. of electron. The emitted electron is called *photoelectron* that's kinetic energy (K.E.) is measured and B.E. is given by Einstein's equation:

$$h\nu = E_{K.E.} + E_{B.E.} + \phi$$

$$E_{B.E} = h\nu - E_{K.E.} - \phi$$

Where, hν is X-ray photon energy, $E_{K.E}$ is kinetic energy of emitted electron measured by analyzer, ϕ is work function induced by analyzer (4-5eV).

Instrumentation: XPS has a fixed X-ray source, vacuum environment and electron energy analyzer. X-ray energy beam of 10-15KV is obtained by sources Mg Kα (1253.6eV) or Al Kα (1486.6eV).Before exposing sample with X-rays, surface is irradiated with Ar ion gun to remove one atomic layer of surface and to expose fresh sample surface. Electron flood gun of low energy

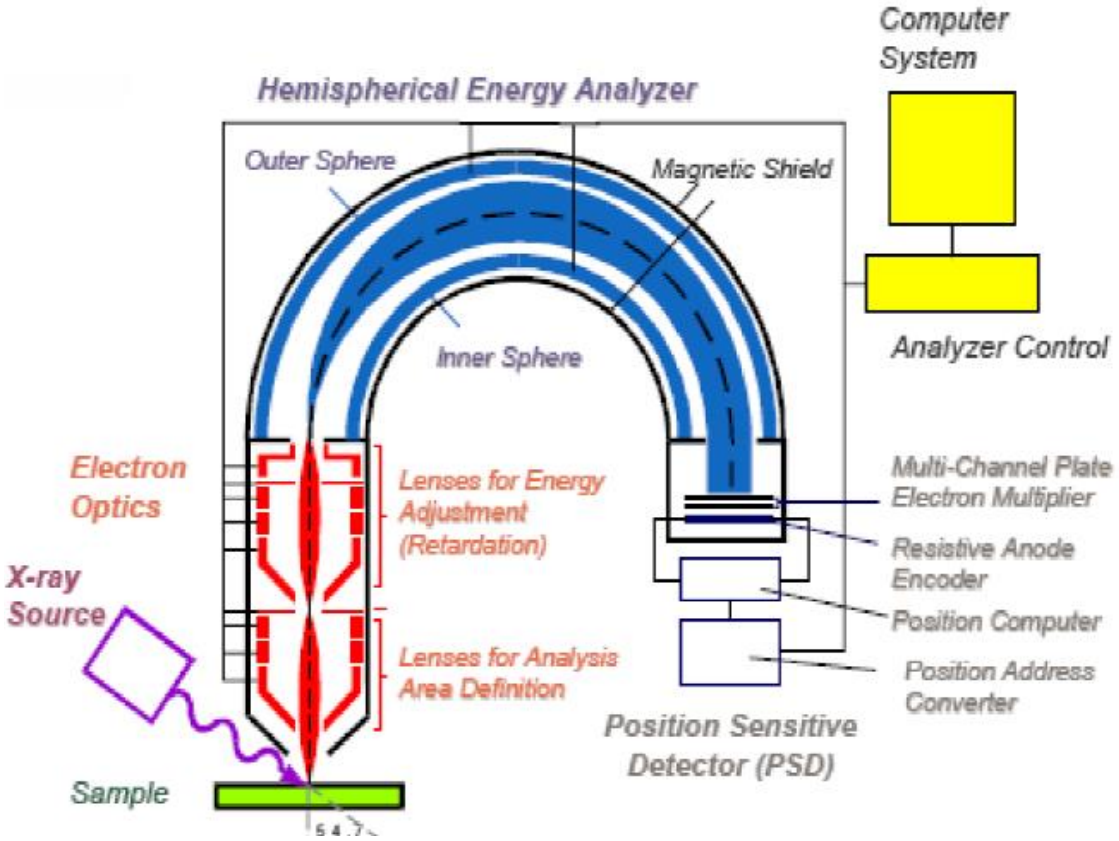

Figure2.23. Instrumentation of XPS [31]

http://www2.cemr.wvu.edu/~wu/mae649/xps.pdf

2-20eV is also used to compensate the charging of sample. When the incident photons ejects out the photoelectron from surface (limit is 3-10nm depth length), it's KE. is measured by hemispherical energy analyzer which is operated under Ulta high vacuum (UHV) 10^{-9} Torr to increase the mean free path of electron which is travelling through analyzer. The analyzer has two plates –inner and outer with opposite charges and operated at high voltage as shown in **Figure 2.23.** Opposite charges repel or attract electrons maintaining them in small orbits. The potential difference between the plates allows only certain energy of photoelectrons to pass through as too slow or fast electrons will crash in plates. So set of electrons of known voltage will produce spectrum.

Interpretation of spectrum: Elements present in particular sample can be **identified** by its characteristics B.E. peak position. BE. of photoelectron depends upon on which level they are emitted. Therefore, formal **oxidation state** of atom present on the surface of sample can be determined. Change in the BE. of peaks due to change in chemical bonding or due to electro negativity effect is called as *chemical shift.* From this chemical shift **chemical and physical environment** of photoelectron can be given. **Electronic effect** such as spin orbital coupling giving rise to doublet peak in XPS spectrum of some element can be analyzed. **Final state effect** giving rise to *shake –up and shake off satellite* peaks indicates the loss of screening of ejected electron. From peak intensity **quantitative elemental analysis** can be done by calculating area under the peak. It gives the **stoitiometric ratio** of elements present on surface. Full width at half maxima (FWHM) of peak determines the change in chemical state or due to physical changes. Charging effect is also responsible for broadening of peak.[31]

2.14. DSSC characterization tool: Solar Simulator

A solar simulator is an instrument which can mimic the spectral distribution in the natural sunlight incident on the earth's surface and hence the instrument is also called *artificial Sun*. The basic purpose of solar simulator is to provide the indoor test facility to characterize solar cells and other optoelectronic devices. The solar simulator typically consists of a **xenon arc lamp** followed by the assembly of mirrors and optical filter for spectral correction as shown in **Figure 2.24a)**. An ellipsoidal reflector around the lamp collects the emission from the lamp, and a

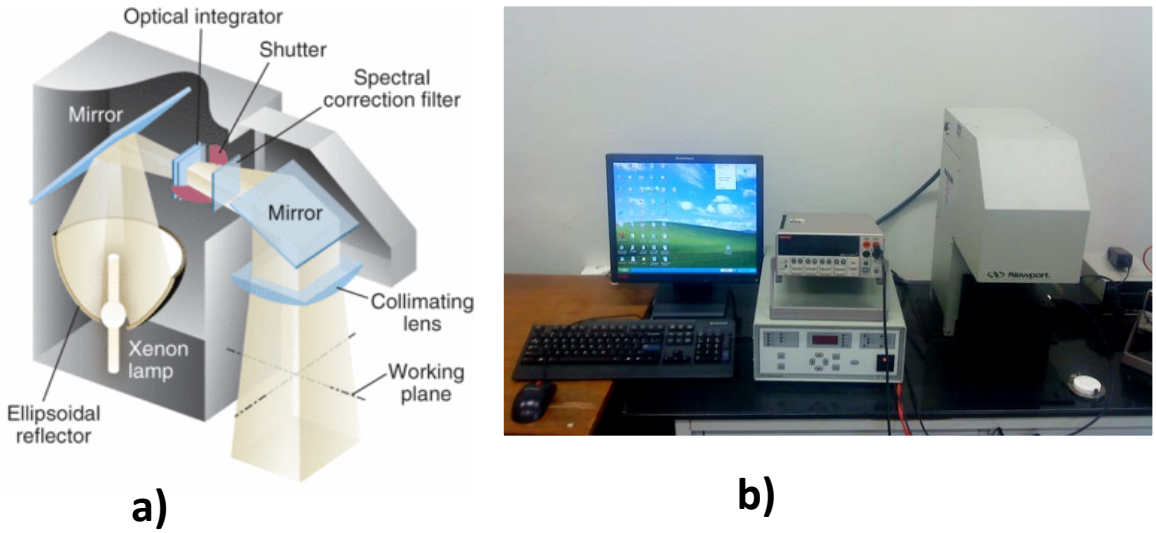

Figure2.24.a) Instrumentation of Solar Simulator [32] b) Newport Solar Simulator at NCL, pune

collection mirror directs the light through a single-blade shutter to an optical integrator that ensures uniformity variations of less than 2% across the simulator's output beam. Depending on the requirement of output illumination area (e.g. 2 × 2 inch to 8 × 8 inch) xenon lamps with different input/output powers (e.g. 250W or 450W) can be used. The intensity of sun light falling on the earth's surface is generally calibrated in terms of Air Mass coefficient which corresponds to the optical path length through the Earth's atmosphere. For instance,in **Figure 2.25.** the air-

mass value AM 1 corresponds to the intensity of solar radiations at the sea level with the sun at the zenith. The number one in AM1 corresponds to the distance equivalent to 'one atmosphere' that is traveled by the solar radiations before reaching the earth's surface. Therefore AM0 corresponds to the solar radiations outside earth's atmosphere. The time for which sun is at zenith is typically less as compared to the time for which it is oblique therefore solar radiations has to travel larger distance than 'one atmosphere' in order to reach the earth's surface under oblique incidence. Therefore a new standard AM 1.5 is defined according to which the solar radiations have to travel 1.5 atmospheres before reaching the earth's surface. Under this

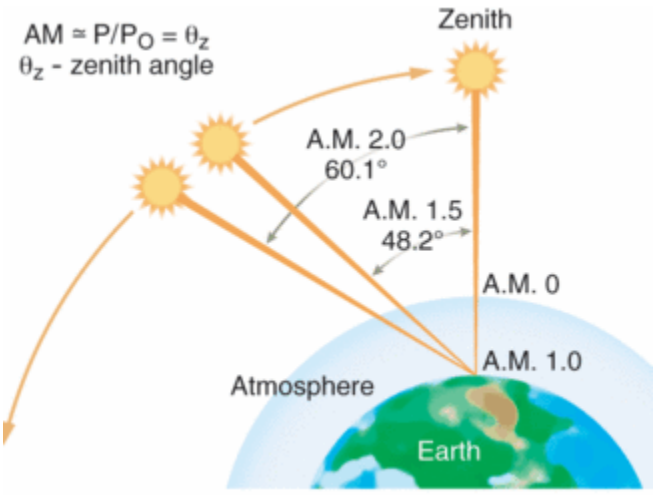

Figure2.25. Air mass calculation for 1Sun measurement [33]

condition the sun is oblique at 48.2^o with respect to zenith. The output intensity of solar simulator is measured using the silicon solar cell whose output current is calibrated for the output intensity. The solar simulator along with the Keithley source and measurement unit forms the solar JV measurement system as shown in the **Figure 2.24b)**.

2.15. References:

1) I. Kartini, D. Menzies, D. Blake, J.C.D. da Costa, P. Meredith, J.D. Riches, G.Q. Lu, *J. Mater. Chem*. **2004**, *14*, 2917-2921.

2) 2) J.R. Durrant, S.A. Haque, E. Palomares, *Coord. Chem. Rev.*, **2004**, *248*, 1247-1257.

3) 3) K. Kalyanasundaram, M. Gratzel, *Coord. Chem. Rev.*, **1998**,*177*, 347-414.

4) 4) K. Zhu, N. Kopidakis, N.R. Neale, J. Lagemaat, A.J. Frank, *J. Phys. Chem. B* **2006**,**110**, 25174 - 251780.

5) S.A. Haque, E. Palomares, B.M. Cho, A.N.M. Green, N. Hirata, D.R. Klug, J.R. Durrant, *J. Am. Chem. Soc.*, **2005**,*127*, 3456-3462.

6) N. Kopidakis, K.D. Benkstein, J. Van de Lagemaat, A.J. Frank, *J. Phys. Chem. B*,**2003**,*107*, 11307-113015.

7) Hattori, H. Goto, *Thin Solid Films*, **2007**,*515*, 8045-8049.

8) J. Xia, N. Masaki, K. Jiang, S. Yanagida, *J. Phys. Chem. C* , **2007**,*111*, 8092-8097.

9) S.-J. Roh, R.S. Mane,S.-K. Min,W.-J. Lee,C.D. Lokhande, S.-H. Han, *Appl. Phys. Lett.*, **2006**,*89*, 253512/1.

10) J. H. Park, J. H. Kim, C. J. Choi, H. Kim, K. S. Ahn, *Molecular Crystals and Liquid Crystals* **2012**, *567*, 19-27.

11) O'Regan, R. R. Haswell, H. J. P. Smit, N. J. Bakker, J. J. T. Smits, J. M. Kroon, J. A. M. van Roosmalen, *Journal of Physical Chemistry B,* **2006**, *110*, 19191-19197.

12) S. Nakade, T. Kanzaki, W. Kubo, T. Kitamura, Y. Wada, S. Yanagida, *Journal of Physical Chemistry B,* **2005**, *109*, 3480-3487.

13) I. Hod and A. Zaban, *Langmuir*, **2014**, 30, 7264−7273.

14) S. V. Kershaw, A. S. Susha and A. L. Rogach, *Chem. Soc. Rev.*, **2013**, 42, 3033-3087.

15) T. L. Li, Y. L. Leea and H. Teng, *Energy Environ. Sci.*, **2012**, 5, 5315–5324.

16) K. T. Kuo, D. M. Liu, S. Y. Chen and C. C. Lin, *J. Mater. Chem.*, **2009**, 19, 6780-6788.

17) H. Lee, M. K. Wang, P. Chen, D. R. Gamelin, S. M. Zakeeruddin, M. Gr€atzel and M. K. Nazeeruddin, *Nano Lett.*, **2009**, 9, 4221–4227.

18) Y. L. Lee, Y S Lo, *Adv Funct Mater*.**2009**, 19,604–9.

19) S. Gorer and G. Hodes, *J. Phys. Chem.*, **1994**, 98, 5338–5346.

20) N. Guijarro, J. M. Campin, Q. Shen, T. Toyod , T. L. Villarreala and R. Gomez, *Phys.Chem. Chem. Phys.*, **2011**, 13, 12024–12032.

21) S. Park, M. K. Son, S. K. Kim, M. S. Jeong, K. Prabakar, and H.-Je Kim, *Korean J. Chem. Eng.*, **2013,** 30, 2088-2092.

22) C. Yao, T J. Webster, *J Nanosci Nanotechnol.*, **2006, 6**, 2682-2692.

23) P. Sudhagar, E. J. J. Pérez, Y. S. Kang and I. M. Seró, *Low-cost Nanomaterials*, Green Energy and Technology, Springer-Verlag London, **2014.**

24) H. M. Pathan and C. D. Lokhande, *Bull. Mater. Sci.*, **2004**, 27, 85–111.

25) Spectrometerhttps://en.wikipedia.org/wiki/Ultraviolet%E2%80%93visible_spectroscopy

26) O. Game, U. Singh, A. A. Gupta, A. Suryawanshi, A. Banpurkar, S. Ogale, *Journal of Materials Chemistry* **2012**, *22*, 17302-17310.

27)http://cnx.org/contents/7b4dfcf8b28e4148f2f1ff39052669f@13.7:30/Nanomaterials_and_Nanotechnolo

28) T. H. Gfroerer, *Encyclopedia of Analytical Chemistry*, R.A. Meyers (Ed.), Ó John Wiley & Sons Ltd, Chichester, **2000,**9209–9231.

29) https://en.wikipedia.org/wiki/Fourier_transform_infrared_spectroscopy.

30) A. R. Barron, *Surface-Enhanced Raman Spectroscopy for the Study of Surface Chemistry*,http://www.cnx.org/contents/f8a19258-739c-43d6-9b26-cc6b9cf70821@1, **2010**.

31) http://www2.cemr.wvu.edu/~wu/mae649/xps.pdf

32) J. Jeong, http://www.laserfocusworld.com/articles/print/volume-43/issue 3/features/photovoltaics-enhancements-enable-solar-simulators-to-shed-lighton-new-photovoltaic-designs.html, **2007.**

33) A. R. Barron, *An Introduction to Solar Cell Technology*,

http://cnx.org/contents/dd0537a2-fb5d-439d-8feb-bf2e50656dae@1, **2011.**

Chapter 3

Room Temperature Synthesis of Rutile TiO_2 Hierarchical Nanoneedle Flower Morphology for Dye Sensitized Solar Cell*

In this work, we present our work on novel synthesis of a hierarchical nanostructure of rutile TiO_2 and its use in Dye Sensitized Solar Cell (DSSC) application. The highlight of this report is the synthesis of rutile TiO_2 at room temperature by using a simple and efficient one step electrochemical process of anodic dissolution. This process employs highly acidic bath of perchloric acid (pH < 2) and a large current density on the surface of titanium foil to form nanoneedle flowers (representing concurrent nano-micro hierarchical morphology) with high shape anisotropy ratio comprising of nanoneedles of ~8 nm diameter and 100 nm length (aspect ratio >10). Such Rutile TiO_2 nanoneedle-assembled flower morphology, when used in a DSSC device, exhibits IPCE of 30% and power conversion efficiency of ~3.6%.

* *The content of this chapter has been published in "**J. Nanosci. Nanotechnol. " 2010,** 10, 5894–5898.*

http://www.aspbs.com/jnn/contents_jnn2010.htm#v10n12

Citation: 18

3.1. Introduction

TiO_2 has two main polymorphic forms - Anatase and Rutile.[1] Out of these, most of the studies have focused on synthesis, phase evolution and 1D structure of anatase phase but crystal growth and mechanism of rutile form of TiO_2 is less common. In optoeletronic applications such as photocatalysis and dye sensitized solar cells also anatase TiO_2 is more favored because of its surface chemistry, higher conduction band edge energy and 10 times higher mobility than rutile TiO_2.[2,3] But rutile is thermodynamically the most stable and has been traditionally used in numerous diverse application sectors because of its good light-scattering[4] and light reflecting properties, high refractive index, non-toxicity, and chemical inertness even in strongly acidic or basic environments.[5] These properties also make the rutile phase attractive for optoelectronic applications such as solar cells despite the fact that it has low electron mobility as compared to anatase phase. *The corresponding studies are still limited possibly due to the need for low cost synthesis, low temperature and shape controlled.*

3.1.3. Need of Room temperature synthesis of rutile TiO_2 phase:

Zhang et al.[6] reported conventional method and the mechanism of rutile TiO_2 synthesis. Rutile TiO_2 is a high temperature phase obtained by calcination of anatase at higher about 600-1200°C depending up on the crystallite size of anatase subjected for calcinations as shown in **Figure 3.1.** At the initial temperature (400-700°C) nuclei growth of rutile TiO_2 initiates and emerges from grain boundaries of anatase but with further increase in temperature (500-1100°C) it spreads throughout the crystal. Calcination at such high temperature unavoidably leads to sintering of crystallite and increases crystallite size which may not be appropriate from DSSC point of view.[7] Also as the temperature increases surface area and porosity decreases which ultimately affect the

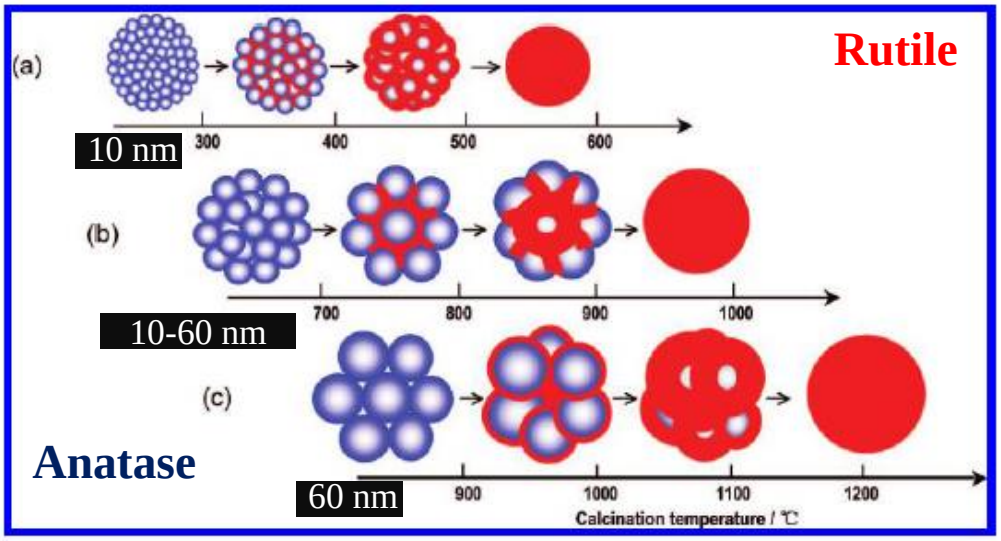

Figure3.1.A proposed scheme for the phase transformation in TiO_2 nanosystem- Anatase to rutile phase depending upon particle size. [6] "Reprinted with permission from (*J. Phys. Chem. C,* **2009**, *113*, 1698-1704). Copyright (2009) American Chemical Society

dye loading and device photocurrent. Moreover if anatase which is subjected for calcination has unique morphology then it gets destroyed at such a high temperature unless templates are used.[8] Some of the researchers tried to overcome this problem by synthesizing rutile phase at lower temperature such as Feng et al.[9] and Liu et al.[10] who employed hydrothermal growth over a temperature range 150°C – 200°C to obtain oriented single crystalline nanorod films to achieve conversion efficiencies of ~5% and 3%, respectively. Moreover, Kaifu Huo et al.[11] have used anodization of Ti foil to synthesize single crystal rutile TiO_2 nanowires at higher temperatures of the order of 600 °C. So achieving rutile phase of TiO_2 at room temperature with hierarchal nanostructure was still a challenge and a future need for scientific community.

In the present work of thesis we report a novel single step room temperature electrochemical (modified anodization i.e., anodic dissolution) process for the synthesis of

phase- pure rutile TiO_2 nanopowder comprising of high aspect ratio nanoneedle flowers. The flowers are shown to self-evolve and detach from the Ti foil surface dynamically under the influence of applied electric field in highly acidic media. Such concurrently nano and micron scale auto-evolved morphology is clearly of interest for dye sensitized solar cell (DSSC) application due to its significance to dye percolation, natural carrier transport pathway formation and light harvesting (submicron flower geometry). It delivered solar power conversion efficiency of 3.6% as photo anode by doctor blading film fabrication method even without significant optimization.

3.2. Experimental Section

3.2.1. Anodization Method

Rutile TiO_2 nanoneedles were synthesiszed by anodization method. It involves two-electrode assembly comprising of Ti foil (Alpha Aesar 99.5% pure, metal basis, thickness 0.5 mm) as anode and Pt foil as cathode, dipped in perchloric acid (1.4 M) mixed in deionized (DI) water.

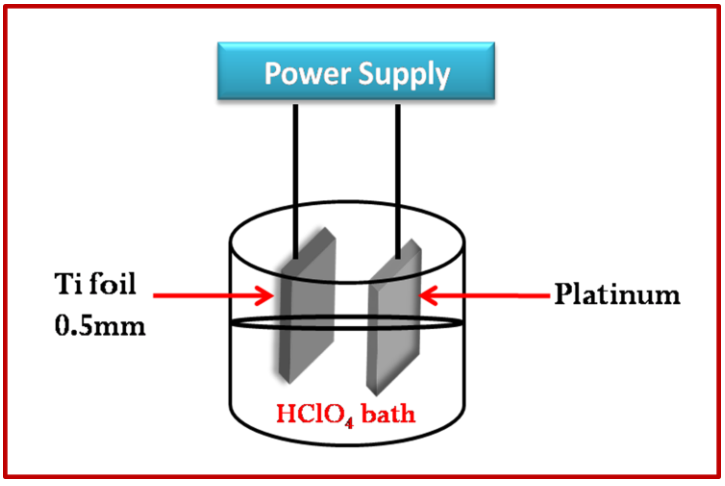

Figure3.2. Schematic diagram of Anodization set up

High voltage stabilized DC power supply was used to apply the field (8V) as depicted by **Figure 3.2.** Highly acidic perchloric bath (pH >1) and voltage promotes etching of Ti metallic foil and it undergoes pitting type of corrosion to form oxide product. Rutile TiO_2 nanoneedle flower powder was found to evolve dynamically from the surface of Ti foil and settle down in the solution in the presence of large current density of the order of 50–100 mA/cm^2.The supernatant bath was then removed and the powder was washed with DI water three times. The powder sample was dried in two conditions: ambient atmospheric conditions and by heat-treatment at 450°C for half an hour. The latter treatment was primarily implemented to test the state of the sample at a temperature, which is used to sinter the doctor bladed nanoparticle film prior to dye sensitization in DSSC experiment.

3.2.2. Fabrication of DSSC.

Detail fabrication of DSSC is given in **Chapter 2 (Section I 2.1.)**.Photoanode of DSSC is prepared from rutile TiO_2 nanoneedle powder (0.2 g) by protocol I and immersed in N3 dye for 24hrs.

3.3. General Characterizations

X-ray diffraction for phase determination was recorded using Philips X'Pert PRO. TGA-DTA (DSC Q600) of ambient dried rutile TiO_2 nanoneedles was done in flowing nitrogen atmosphere within the temperature ranging from room temperature to 900°C. The morphology was characterized by Field-Emission Scanning Electron Microscope (FE-SEM, Hitachi S-4200) and high resolution Transmission electron microscopy (HRTEM, IFEI, Tecnai F30, with 300 KV FEG). Other characterizations such as Fourier transform infrared spectroscopy (FTIR Perkin Elmer Spectra One), diffuse reflectance spectroscopy (DRS Varian, CARY100) were also

employed. The I–V characteristics were measured under irradiation with 100 mW/cm^2 (450 W Xenon lamp, Oriel Instruments) 1 sun AM 1.5 simulated sunlight as a solar simulator in the presence of a water filter, using Kiethley 2400 source. The measurements of incident-photon-to-current conversion efficiency (IPCE) were carried out on 0.27cm^2 active area without bias illumination with respect to a calibrated Melles - Friot silicon diode. IPCE was measured by changing the excitation wavelength (Photon counting spectrometer, ISS Inc.) and Kiethley 2400 source meter. Thickness of electrodes was measured by surface profiler from Dektak 150, Veeco make.

3.4. Results and Discussion:

3.4.1. X-Ray Diffraction (XRD).

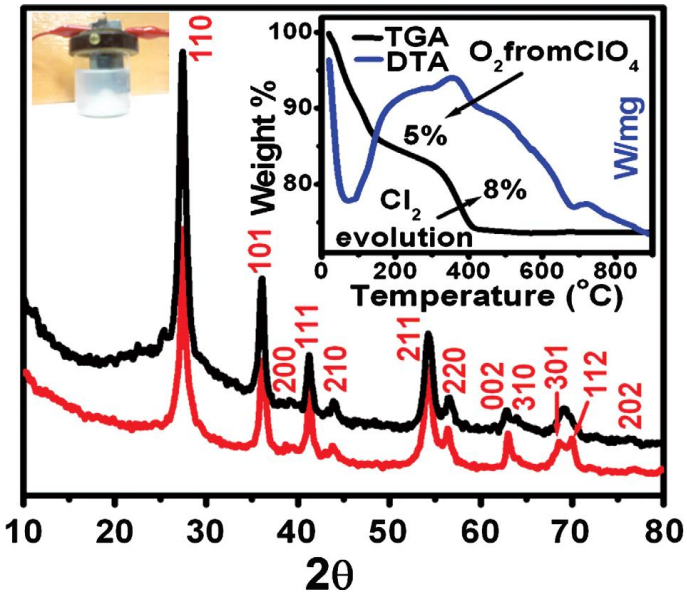

Figure3.3. XRD pattern (red line) of ambient dried TiO_2 and (black line) 450°C heated TiO_2.Inset (left) actual photograph of anodization set up, (right) TGA-DTA

Figure3.6. compares X- Ray Diffraction (XRD) patterns of TiO_2, ambient dried and heat treated at 450°C for half an hour. As can be seen from the patterns, the four major diffraction peaks are identical in the two cases and appear at the 2θ values of 27.39°, 36.18°, 41.20° and 54.38°. These are assigned to the (110), (101), (111) and (211) reflections of rutile TiO_2 (PCPDFWIN # 211 276) respectively. These data indicate that the ambient-dried powder is pure rutile TiO_2 and that this phase form is retained even under the stated heat treatment, which corresponds to the treatment imparted to the corresponding nanoneedles film during solar cell formation for establishing inter-particle electrical contacts and reducing series resistance

3.4.2. Thermogravimetric analysis (TGA-DTA).

Figure3.3. inset depicts Thermogravimetric Analysis (TGA) plot, which shows initial weight loss of 13% up to 150°C due to the removal of adsorbed water on the nanoneedle surface. Within the temperature ranging from 150–320°C the weight loss of 5% is due to the decomposition ofClO^{-4} ions and removal of oxygen molecules. Within the temperature ranging from 320°C – 400°C, the weight loss of 8% is due to chlorine gas evolution from the surface of TiO_2 nanoneedles. After 400°C there is not much significant weightloss, which implies that powder is stable above 400°C. Simultaneously, Differential Thermal Analysis (DTA) was done for the ambient dried rutile TiO_2 powder and it is observed that there is strong signature of endothermic reaction at 100°C due to removal of water molecule from the TiO_2 nanoneedle surface.

3.4.3. Field Emission Scanning Electron Microscopy (FESEM) images.

Figure3.4. presents the Field Emission Scanning Electron Microscopy (FE-SEM) image of the ambient dried rutile TiO2, clearly showing the nano-micro needle flower like morphology. Such

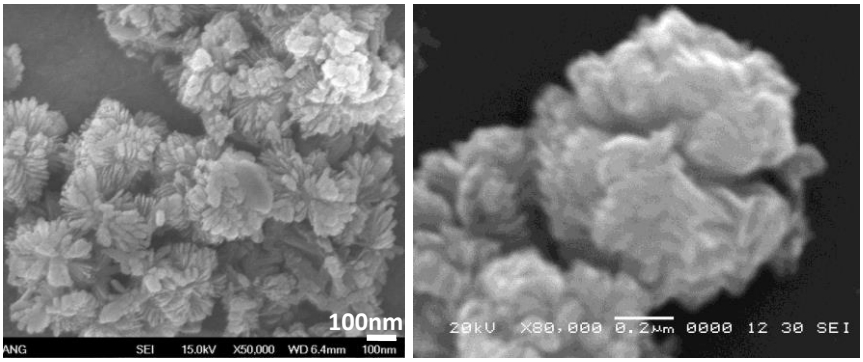

Figure3.4. FESEM images of clustered flower morphology of rutile TiO_2

dense branched hierarchical morphology is of great value in the nanoparticle film formed for solar cell manifestation for reasons of good dye percolation and light harvesting effects.

3.4.4. Transmission electron Microscopy (TEM) images

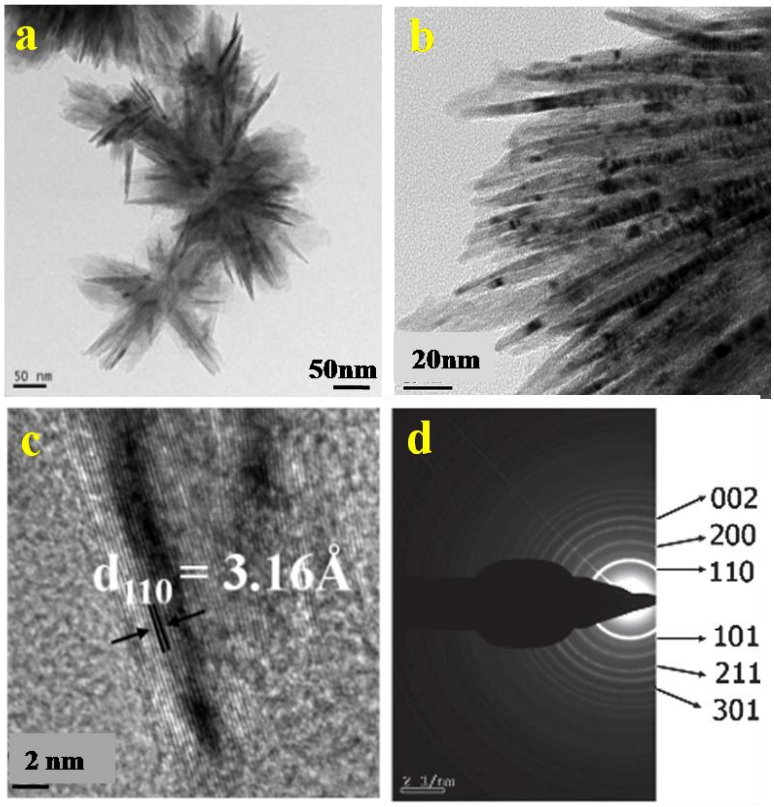

Figure.3.5. a & b TEM images of flower assembly of nanoneedles. **c** HRTEM images of single nanoneedle. **d.** SAED pattern of rutile TiO_2

Figure3.5.a shows the Transmission electron Microscopy (TEM) image of the flower assembly of nanoneedles while **Figure 3.5.b** reveals the needle morphology with uniform diameter of ~8 nm and length of ~100 nm (aspect ratio >10). **Figure 3.5c** depicts High Resolution Transmission electron Microscopy (HRTEM) image of single nanoneedle where d-spacing of 3.16Å is observed which corresponds to 110 plane of Rutile TiO_2.The phase purity of rutile titania was confirmed by selected area electron diffraction (SAED) data. A typical electron diffraction pattern of the ambient dried rutile TiO_2 is depicted in **Figure3.5d.** The d-spacing calculated from the SAED patterns agrees well with the data for rutile titania.

3.4.5. Diffused Reflectance Spectra (DRS).

Figure3.6. shows the Diffused Reflectance Spectra (DRS) of ambient dried and 450°C heat treated rutile TiO_2 powder. A sharp well defined band edge is clearly seen with a band gap of about 3.09 eV and 3.07 eV. This is slightly higher than the band gap of bulk rutile TiO_2 which is

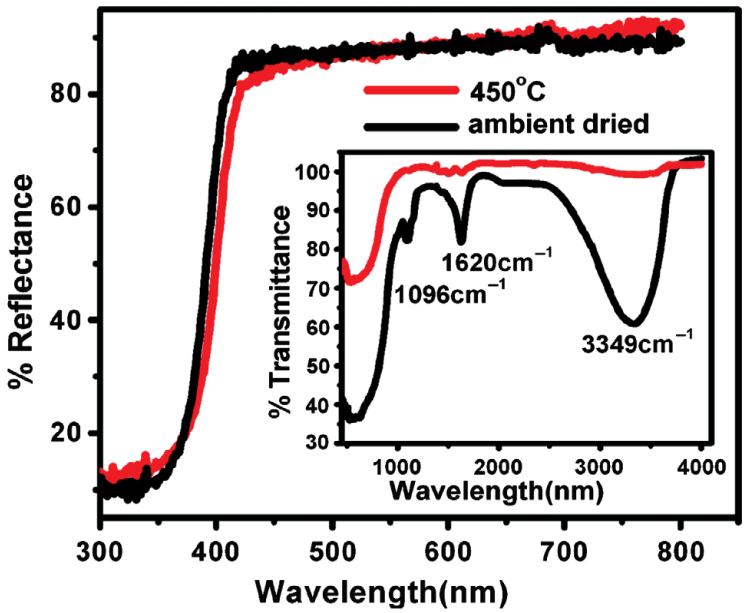

Figure3.6. DRS spectra of ambient dried and 450°C heat treated rutile TiO_2 powder. Inset shows FT-IR spectra of ambient dried and 450°C heat-treated rutile TiO_2.

3eV. Such shift can result from surface capping of ambient dried TiO_2 powder, which in the present case is due to ClO^{-4} ions.[12]

3.4.6. Fourier Transform Infra-red (FTIR) spectra.

The Fourier Transform Infra-red (FTIR) spectra of ambient dried and 450°C heat-treated sample are shown in the inset of **Figure 3.6**. Both the samples show three major and common absorbance regions at 3000–3600 cm^{-1}, 1400–1800 cm^{-1} and 500–1200 cm^{-1}. The two intense vibronic signatures at ~3400 cm^{-1} and ~1600 cm^{-1} originate from the vibration modes of hydroxyl group present for both samples.[13] The O–Ti–O peaks are located at wave numbers between 400 and 1250 cm^{-1}. For ambient dried rutile TiO_2 powder absorption is seen at ~450 cm^{-1} as expected. Room temperature synthesized ambient dried rutile TiO_2 nanoneedle powder shows pronounced peak at 1097 cm^{-1} due to ($ClO4^-$)[14] which is seen to be eliminated by heat treatment at 450°C. This elimination signals the right thermal processing condition for enhancement of inter-needle communication for carrier transport.

3.4.7. Mechanism of nanoneedle formation

During anodization process very high perchoric acidic bath with pH < 1 and high voltage (8V) creates aggressive environment *in situ* for the Ti foil. Perchlorate is not reduced directly at titanium, but it increases the anodic dissolution of titanium. The corrosion product is aquo Ti(III) ions, which are oxidized to Ti(IV) by perchlorate[15]

$$\mathbf{8Ti(III) + ClO_4^- + 8H^+ \rightarrow 8Ti(IV) + Cl^- + 4H_2O}$$

The product of above reaction is Ti(IV) ions, which are reduced at these applied potentials to Ti(III), which again react with perchlorate ions.[15,16] Passivation of titanium occurs as Ti(IV) ions build up in solution and the current density for the Ti(IV) reduction reaction exceeds the critical

$Ti^{0} - 3e \rightarrow Ti(III)$ **electrochemical dissolution reaction**

$8Ti(III) + ClO^{-}_{4} + 8H^{+} \rightarrow 8Ti(IV) + Cl^{-} + 4H_2O$

current density for passivation and results into breakdown of passivating oxide layer. The reduction of perchlorate to chloride is a Ti (III)–Ti (IV) catalyzed process given by the following reaction sequence

$Ti(IV) + e^{-} \rightarrow Ti(III)$ **Electrochemical reduction reaction**

$Ti^{4+} + 2H_2O \rightarrow TiO_2 + 4H^{+}$ **Anodic oxidation**

$4H^{+} + 4e^{-} \rightarrow 2H_2 \uparrow$ **Cathodic reduction**

The plausible overall reaction responsible for the synthesis of rutile TiO_2 is:

$$Ti_{(s)} + ClO_4^- + H_2O \xrightarrow{8V} TiO_{2\,(s)} + H_{2\,(g)} + ClO_4^- + H^+$$

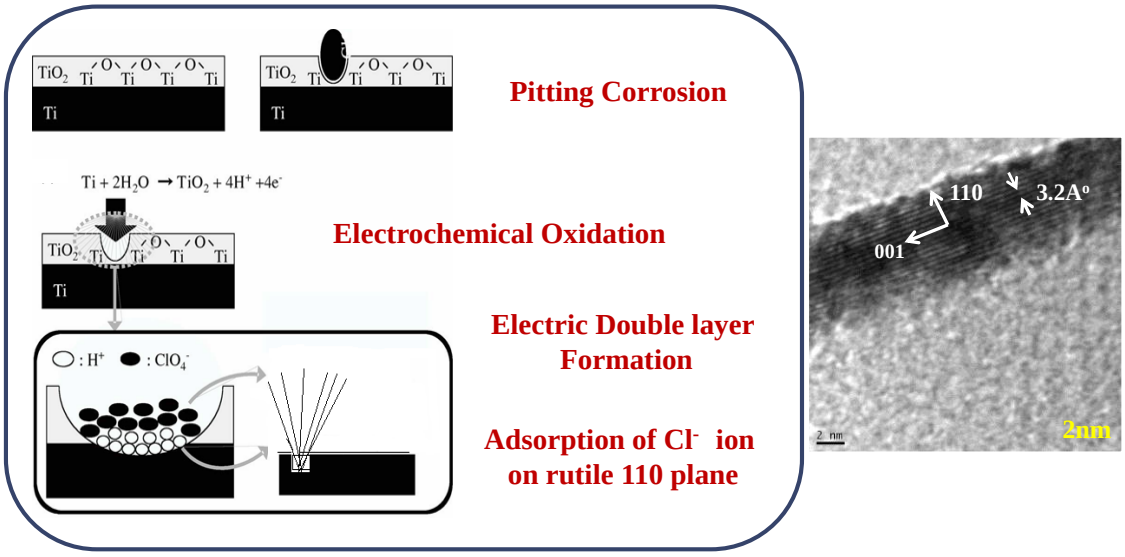

Figure 3.7. Schematic diagram of nanoneedle formation in $HClO_4$ bath. (Right) HRTEM imagedepicting rutile (110) plane and anisotropic growth along 001 direction of nanoneedle

When a high electric voltage is applied between the two electrodes, majority of the H^+ ions move towards the cathode and ClO_4^- ions move towards anode. These ClO_4^- ions form highly aggressive chemical environment on Ti foil surface creating pits as given in **Figure 3.7.**[16] The electrochemical oxidation reaction of Ti occurs at the entire dipped surface of anode causing passivation by forming oxide layer and anodic dissolution starts only at pits where a high-density current flows. This in turn results in the formation of the electric double layer consisting of highly concentrated H^+ and ClO_4^- ion density at the pits.[17] These chloride ions get adsorbed on the (110) plane of rutile TiO_2 suppressing further growth of this plane, resulting into anisotropic growth in (001),that is in c-axis direction and hence TiO_2 nanoneedle formation.[9,18]

3.4.8. Mechanism of rutile nuclei formation

According to ligand field theory, in solution the Ti(IV) ions exist as six-fold coordinated structural units (TiO_6),which undergo condensation to become the octahedra that bond *via* corner and edge-sharing to form the final crystal structure. In the rutile form, TiO_6 octahedra link by sharing an edge along the *c*-axis to form chains which are then interlinked by sharing corner oxygen atoms, whereas in anatase, there is only edge sharing. Thus, the formation of both phases

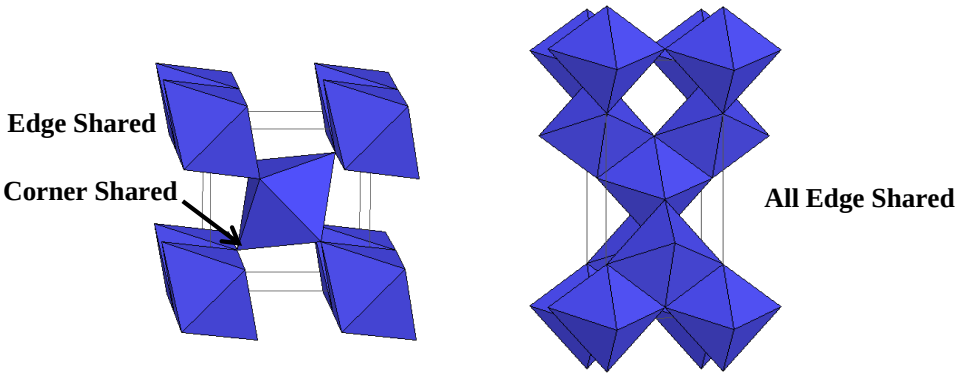

Figure3.8. Octahedra (building block) packing in (left) Rutile TiO_2 (right) Anatase TiO_2[13]

http://ruby.colorado.edu/~smyth/min/tio2.html

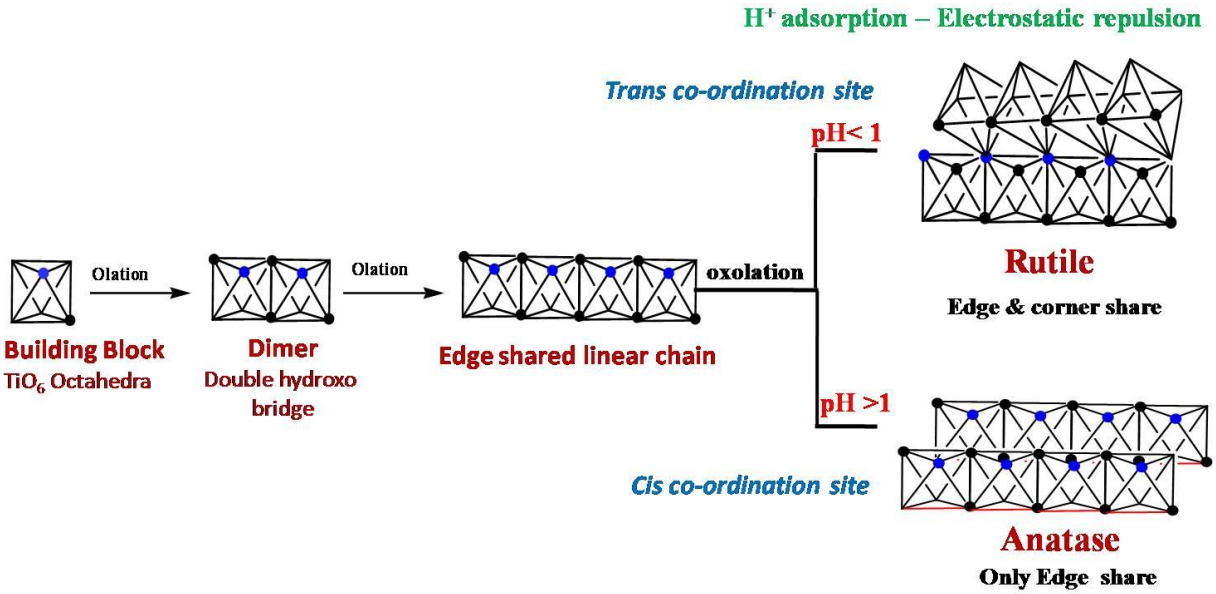

Figure3.9. Schematic diagram of rutile TiO_2 nucleus growth formation

depends on whether –OH or oxo-bridges are formed between the two metal centers during condensation. [13] Condensation to both rutile and anatase starts when the solution activity is high enough to allow further deprotonation and to form zero charge precursors $[Ti(OH)_4(OH_2)_2]$ which undergo two stages of condensation. First, by olation and second by oxolation as shown schematically in **Figure 3.9.** In olation there is elimination of two water molecules having *cis* which lead to $2\mu_2$-OH ions *i.e.* the formation of dimer (double hydroxo bridges, $[Ti_2(OH)_8(OH_2)_2]_0$)[18] which has a tendency to share an edge between the two octahedra leading to a linear chain. *This edge shared linear chain formation is common to both the phases.* [20, 21] After this, nuclei growth depends on acidity feed stock or pH of anodization bath. If pH is > 1 then such two edge shared linear chain come close to share edge and ultimately give rise to

anatase nuclei formation. But if pH < 1 then high H^+ concentration (acidity) which gets adsorbed on TiO_6 octahedra creating electrostatic repulsion between them. Now to minimize this repulsion, two linear shared chain will undergo corner sharing between them and give rise to rutile nuclei formation.[8], [19, 20] From the condensation point of view the dimer undergoes olation where ClO_4^- ions have a tendency to form a symmetric complex which undergoes a type of chlorolysis–oxolation process.[12] In this corner shared TiO_6 the dimers are separated by chlorate anions with each other. This ultimately leads to Ti–O–Ti which is linked through *trans*-oxo bridges (corner sharing) to $2\mu_2$ chains forming the rutile phase and it also stabilizes rutile octahedra internally by connecting one octahedron to another by chlorate bridges.

Thus, through the process of anodic dissolution it was possible to synthesize rutile phase of TiO_2 at room temperature even though it is a high temperature phase with oriented morphology. This is because in strong acidic solution, the condensation rate is slow enough and the formation of the rutile phase is kinetically favored.[7]

3.5. Solar Cell Characterization.

IV characteristics and IPCE spectra of rutile TiO_2 photoanodes is given in **Figure 3.10.** Table1.gives all the IV parameters which indicates that rutile TiO_2 nanoneedles delivered V_{oc} = 0.66V, J_{sc} = 8.83 mA/cm^2 and appreciable power conversion efficiency of 3.6% Also IPCE values obtained as a function of wavelength for rutile TiO_2 is 30%

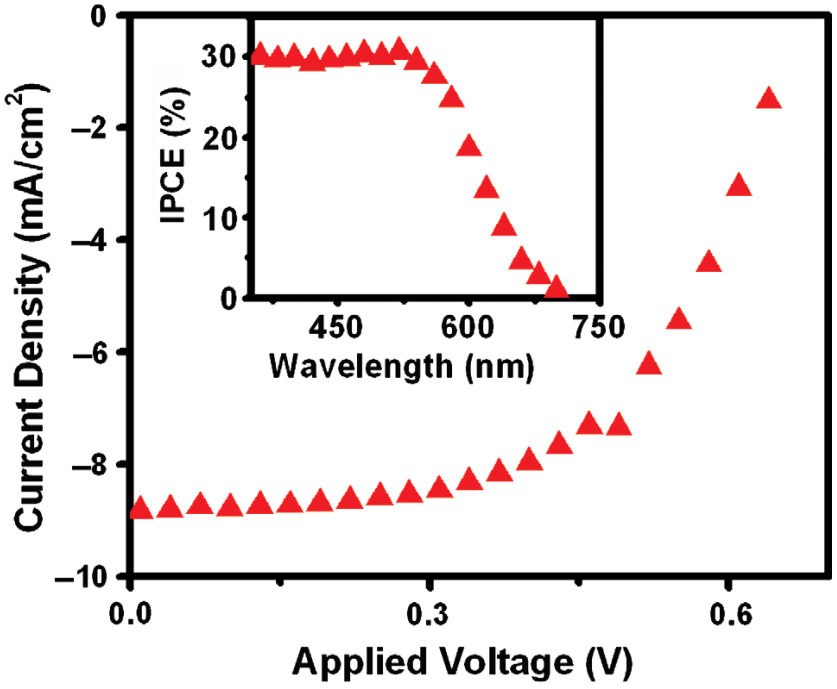

Figure3.10. J–V characteristics and IPCE data (Inset) of ambient dried rutile TiO_2.

Sample name	V_{oc} (V)	J_{sc} (mA/cm^2)	FF (%)	η (%)	IPCE (%)
Rutile TiO_2	**0.66**	**8.83**	**61**	**3.6**	**30**

Table 1.IV characteristics

3.6. Conclusion

In conclusion we have demonstrated a simple and efficient room temperature electrochemical synthesis of (high temperature phase) rutile TiO_2 with hierarchical nano-micro needle-flower morphology. The diameter and length of nanoneedle are ~8 nm and 100 nm (aspect ratio >10), respectively. DSSC based on the corresponding rutile TiO_2 photoanode shows IPCE of 30% and power conversion efficiency of 3.6%.

3.7. References

1) D. R. Coronado, G. R. Gattorno, M. E. E. Pesqueira, C. Cab, R. Coss and G. Oskam, *Nanotechnology*, **2008**, **19**, 145605-145614.

2) N. G. Park, J. v. de Lagemaat, and A. J. Frank, *J. Phys. Chem. B* ,**2000,**104, 8989-8994.

3) L. Kavan, M. Gra1tzel, S. E. Gilbert, C. Klemenz, and H. J. Scheel, *J. Am. Chem. Soc.* **1996**, 118, 6716-6723.

4) K. H. Park, H. Li, M. Dhayal, J. W. Lee, and H. B. Gu, *J. Nanosci. Nanotechnol.* , **2008**, 8, 5252-5256.

5) S. Yang, Y. Liu, Y. Guo , J. Zhao, H. Xu, and Z. Wang, *Mater. Chem. Phys.*,**2002,** 77, 501-506.

6) J. Zhang, Q. Xu, M. Li, Z. Feng, and C. Li, *J. Phys. Chem. C*, **2009**, *113*, 1698–1704.

7) Z. Tang, J. Zhang, Z. Cheng, and Z. Zhang, *Mater. Chem. Phys.*, **2002**, 77, 309-314.

8) H. Cheng, J. Ma, Z. Zhao and L. Qi, Chem. Mater., **1995**, 7, 663-671.

9) X. Feng, K. Shankar, O. K. Varghese, M. Paulose, T. J. Latempa, and C. A. Grimes, *Nano Lett.* , **2008**, 8, 3781-3786.

10) B. Liu and E. S. Aydil, *J. Chem. Soc.,* **2009**,131, 3985- 3990.

11) K. Huo, X. Zhang, J. Fu, G. Qian, Y. Xin, B Zhu, H. Ni, and P. Chu,*J. Nanosci. Nanotechnol.*, **2009**, 9, 3341-3346.

12) M. A. Reddy, M. S. Kishore, V. Pralong, V. Caignaert, U. V. Varadaraju, and B. Raveau, *Electrochem. Commun.*, **2006**, 8, 1299.

13) Mineral structure and property data, University of Colorado http://ruby.colorado.edu/~smyth/min/tio2.html

14) S. López-Romero, J. Castillo-Mendoza, J. Chávez-Ramírez, and J. Muñoz-García, *Revista Matéria,* **2005**,10, 3413-3421.

15) G. M. Brown, *J. Electroanal. Chem.*, **1986**,198, 319-330.

16) N. F. Fahim and T. Sekino, *Chem. Mater*.**2009**, 21, 1967- 1979.

17) K. Nakayama, T. Kubo, and Y. Nishikitani, *Electrochem. solid- state Letts.*,**2008,**11,C23-C26.

18) C. Ribeiro, C. Vila, D. B. Stroppa, V. R. Mastelaro, J. Bettini, E. Longo, and E. R. Leite, *J. Phys. Chem. C,* **2007**,111, 5871-5875.

19) J. P. Jolivet, *Metal Oxide Chemistry and Synthesis: From Solution to Solid State*, John Wiley, Masson Paris, 3rd edn, **1994**, pp. 82–85.

20) J. P. Nikkanen, T. Kanerva and T. Mantyla, *J. Cryst. Growth*, **2007**, 304, 179-183.

21) B. Sun, P. G. Smirniotis, *Catalysis Today*, **2003,** 88, 49–59.

Chapter 4

Chlorate ion mediated rutile to anatase reverse phase transformation in theTiO_2 nanosystem*

Rutile TiO_2 nanoneedles (about 8 nm x 100 nm in size) are synthesized at room temperature by anodization in perchloric acid (pH<1). These are shown to undergo an interesting reverse phase transformation to anatase nanoparticles (about 8 nm) at 300°C only if the chlorate ions are maintained in the ambient medium. When chlorate ions are removed by multiple washing, the rutile phase and the needle morphology are maintained. The mechanism of formation of the ion-stabilized solid and its thermal evolution are discussed. The resultant anatase nanoparticles obtained after phase transformation show 6% power conversion efficiency as photoanode material for DSSC.

The content of this chapter has been published in "Dalton Trans.", 2011,** 40, 11374–11377**.**

Reproduced by permission of The Royal Society of Chemistry (RSC)

http://pubs.rsc.org/en/content/articlelanding/2011/dt/c1dt11288k#!divAbstract

4.1. Introduction

Nanocrystalline TiO_2 has attracted considerable attention during the past decade in view of its applicability as a material for catalyst supports, pigment additives, photocatalysis, nanoporous solar cell architectures, and sensing elements.[1–10]These applications depend strongly on the phase, crystallographic structure, morphology (faceting) and the size of the particles. TiO_2 occurs in three main crystallographic polymorphs ‑ namely anatase, brookite and rutile. Among these rutile is the thermodynamically most stable form, possessing a smaller optical band gap (3.0 eV) as compared to anatase (3.2 eV) and is chemically more stable. In many applications however, the anatase form is preferred as it is an active phase of TiO_2 because of its surface chemistry and higher conduction-band edge energy.[11]

In our previous work[12] we were able to synthesize rutile TiO_2 nanoneedle flowers at room temperature by an electrochemical method in a highly acidic ambient medium (pH <1). This hierarchical morphology with an aspect ratio >10 and surface area about 162 m^2g-1 also yielded 3.6% efficiency in dye sensitized solar cell. In the present work we discuss the consequences of thermal treatment of such nanoneedles at different temperatures, with the presence or absence of the synthetically included chlorate ions in the annealing process.

4.2. Experimental Section

4.2.1 Anodization Method

Synthesis of rutile TiO_2 nanoneedles by anodization method is given in Chapter 3 (section 3.1.).After synthesis the product is taken out of bath and without washing in presence of chlorate ions it is subjected to calcination at 100°C, 200°C and 300°C.

4.2.2. Fabrication of DSSC

Detailed fabrication of DSSC is given in **Chapter 2 (Section I 2.1.)**.Anatase TiO_2 nanoparticles obtained after reverse phase transformation from rutile TiO_2 is used as photoanode material for DSSC. Paste is made by protocol I and immersed in N719 dye for 24 hrs.

4.3. General Characterizations

X-ray diffraction for phase determination was recorded using Philips X'Pert PRO(PAN Analytical diffractometer using Ni-filtered Cu-K$\propto$ radiation, λ=1.541Å),.The morphology was characterized by Field-Emission Scanning Electron Microscope (FE-SEM, Hitachi S-4200) and high resolution Transmission electron microscopy (HRTEM, IFEI, Tecnai F30, with 300 KV FEG). Other characterizations such as Fourier transform infrared spectroscopy (FTIR Perkin Elmer Spectra One), Micro Raman Spectrometry (Horiba Jobin Yuon, 632nm lazer) and Ultraviolet-visible spectrometer (Varian, CARY100) were also employed. The I–V characteristics were measured on 0.25cm^2 active area under irradiation with 100 mW/cm^2 (450 W Xenon lamp, Oriel Instruments) 1 sun AM 1.5 simulated sunlight as a solar simulator in the presence of a water filter, using Kiethley 2400 source. Thickness of electrodes was measured by surface profiler from Dektak 150, Veeco make

4.4. Results and Discussion

4.4.1. X-Ray Diffraction (XRD).

The XRD patterns of the TiO_2 powder synthesized anodically and subjected to calcinations without washing at different temperatures (100°C, 200°C, 300°C) for 2 h each are depicted in **Figure 4.1.** The as-anodized TiO_2 is moist and shows a single major diffraction peak at a 2θ

value of 27.3° which is assigned to the high density plane (110) of rutile TiO_2, albeit with strong disorder (or almost amorphous nature). For this reason it was heated at 100°C for 2 h but still fairly moist due to the tendency of chlorate ions to hold moisture. The corresponding XRD shows rutile (tetragonal) as the main phase having four major diffraction peaks at 2θ values of 27.3°, 36.0°, 41.2°, 54.2° (PCPDFWIN # 78 2485) with a slight shoulder of anatase at 25.3°. The XRD of the 200°C calcined sample shows a mixed phase of rutile and anatase, with the anatase component increasing significantly. The sample calcined at 300°C shows almost pure anatase TiO_2 with 2θ values 25.3°, 37.8°, 48.0°, 53.9°, 55.1° (PCPDFWIN # 78 2486). In the same figure we show the XRD pattern (b) of the as-synthesized powder after multiple washings of the original moist as-obtained powder.

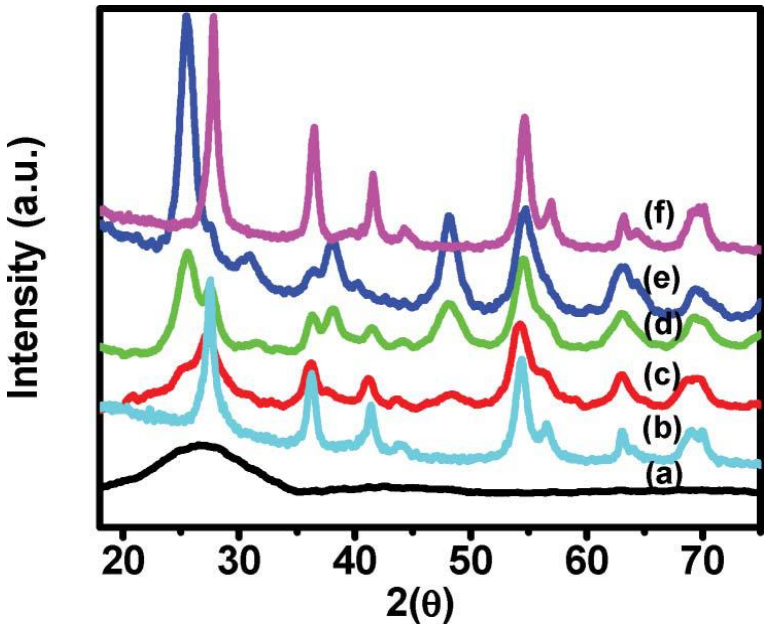

Figure4.1. X-Ray diffraction spectra of as anodized TiO_2 (a), washed sample, (b), unwashed sample heated at (c) 100°C, (d) 200°C, (e) 300°C for 2 h. The data in (f) is for the sample soaked in 1.4 M perchloric acid and annealed at 300°C for 2 h.

In this case all the peaks match completely with the pure rutile phase. Comparison of **Figure.4.1. (a) and (b)** shows that removal of the electrochemically incorporated chlorate ions by multiple washings leads to significant adjustments of TiO_2 octahedra leading to a much better definition of the rutile grain structure (discussed later with reference to **Figure4.7.**). Interestingly, heating of the washed sample (free of chlorate ions as verified by FTIR, shown later in **Figure4.6.**) only leads to the rutile phase and no transformation to anatase is seen for this case. We also used the powder (b) obtained after multiple washings and heated it again to 300°C after soaking it with perchloric acid (different concentrations from 0.3 M to 2 M) to explore whether the transformation can be induced externally by the surface adsorbed chlorate ions. The XRD patterns for all cases are given in **Figure 4.2.** We observed that in each case the phase rutile TiO_2

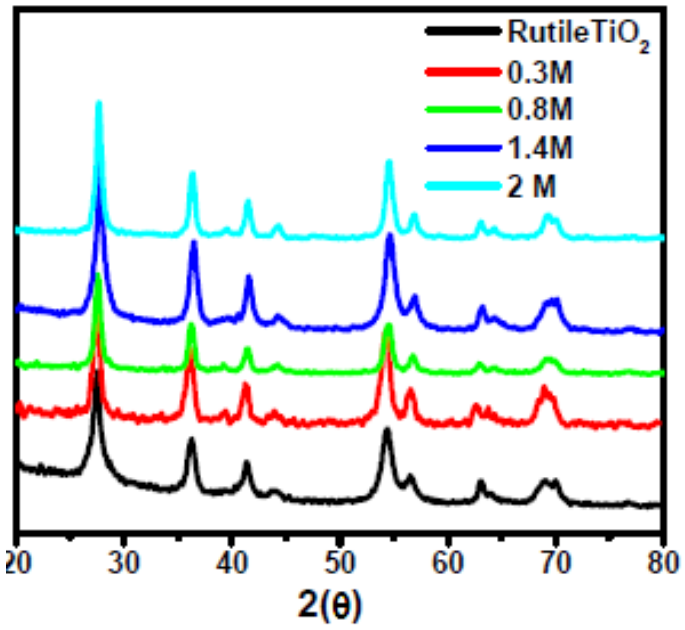

Figure4.2. XRD spectra of washed rutile TiO_2 soaked in different concentration of $HClO_4$ bath and heated at 300°C

was restored.The XRD pattern for a representative case of 1.4M concentration is shown as curve **(f)** in **Figure.4.1**. So even if surface of TiO_2 is partially or fully covered by ClO_4^- ions they are not contributing in surface dependent phase transformation. Thus the chlorate ions responsible for the rutile to anatase transformation are the synthetically (*in situ*) introduced ones, and their removal by washing clearly leads to irreversible changes in the rutile grain conformations.

4.4.2. Raman spectra

The Raman spectra (**Figure 4.3.**) for as-anodized, and annealed sample (100°C, 200°C, 300°C) essentially confirm the results of XRD studies. These data were recorded under illumination of 632 nm laser beam. The as-anodized sample and washed sample showed Raman signals at 450 cm^{-1} and 617 cm^{-1} corresponding to the Eg, A_{1g} Raman modes of rutile, respectively. The peaks are very broad indicating the dynamic disorder of the TiO_6 octahedra.[13, 14] Additionally, there are

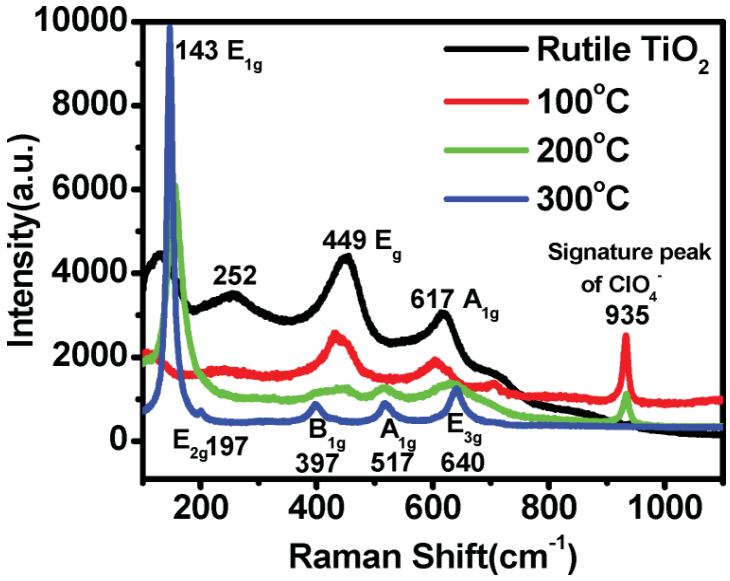

Figure4.3. Raman Spectra of multiply washed nanoneedles, and unwashed samples heated at 100°C, 200°C and 300°C.

second-order scattering features, the most prominent one being at 252 cm^{-1}.[15] In the unwashed sample annealed at 100°C for 2 h there is a red shift in the Eg mode (~15 cm^{-1}) and A_1g mode (~11 cm^{-1}), respectively, due to nonstoichiometric effects at the nanoscale.[16] The peak at 935 cm^{-1} is due to the symmetric stretching mode of ClO_4^- ions[17, 18] which is highly intense in this case. In the unwashed 200°C annealed case the predominant Eg mode of rutile is seen along with the anatase Raman modes implying a mixed phase. The breadth of this main anatase peak (E_{1g}) and its lower intensity signify a tiny particle size. The chlorate ion contribution is seen in this case as well, albeit with reduced intensity. In the unwashed 300°C annealed sample the fairly sharp peaks observed at 143, 197, 397, 517, 640 cm^{-1} represent the established E_{1g}, E_{2g}, B_{1g}, A_{1g}, E_{3g} modes, respectively, for anatase TiO_2.[19] No ClO_4^- ions related peak is present, implying their complete removal.

4.4.3. Transmission electron Microscopy (TEM) images

Figure.4.4a shows the TEM image for the as-anodized sample. The images show a flower assembly of nanoneedles with a uniform diameter of 8 nm and length of ~100 nm (aspect ratio >

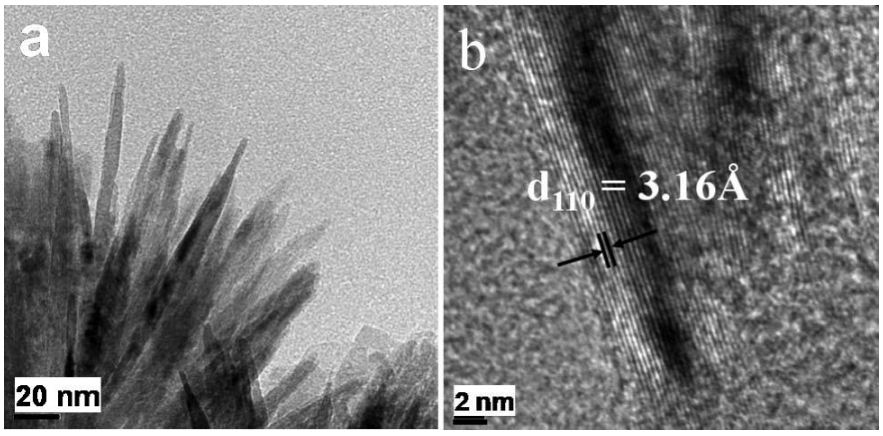

Figure 4.4.a TEM images of Rutile TiO_2 (a) nanoneedles of 100 nm length an ~8 nm diameter. (d) HRTEM image of single needle.

10). **Figure.4.4b** shows the inter-planar *d*-spacing of 3.16A˚, which matches with a (110) plane of rutile TiO_2. **Figure.4.5.a** shows the HRTEM images of the intermediate 200°C annealed case where needles as well as particles are seen. Some of the needles are seen to get transformed into nanoparticles of uniform size 8–10 nm. Image b shows a part of a needle with *d*-spacing 3.1A˚ corresponding to the (110) plane of rutile whereas the particle emanating from the TiO_2 needle shows *d*-spacing 3.6 A˚ corresponding to the (101) plane of anatase TiO_2. The image c for the

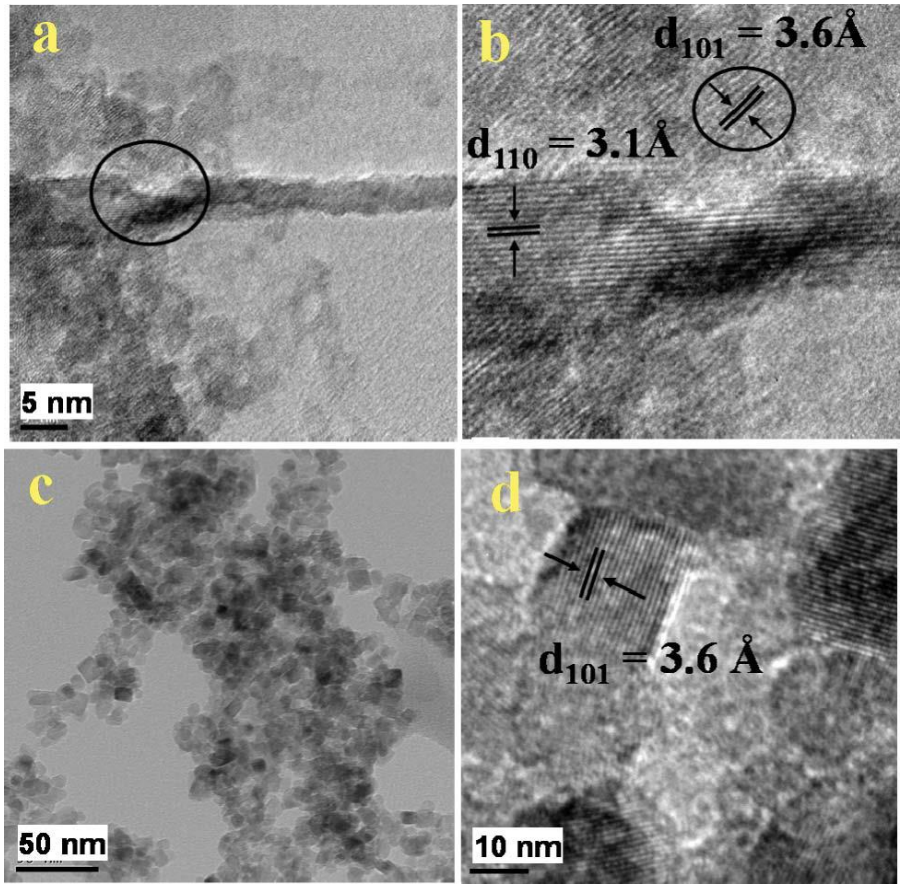

Figure 4.5 (a) HRTEM image for unwashed 200℃ annealed case showing nanoneedles and anatase TiO_2 nanoparticles. (b) shows *d*-spacing of Rutile TiO_2 nanoneedles and anatase TiO_2 nanoparticles. (c) &(d) Unwashed 300°C annealed case with all anatase nanoparticles of 8–10 nm.

unwashed 300°C annealed case shows all particles with uniform size of 8–10 nm with a *d*-spacing of 3.6A˚ (**Figure 4.5d**).

4.4.4. Fourier Transform Infra-red Spectra.

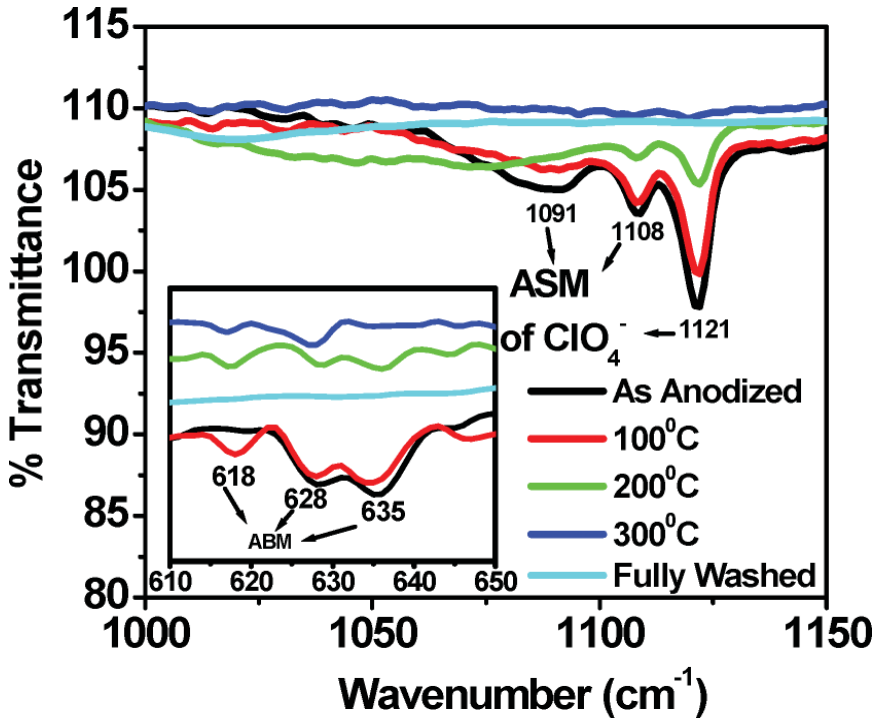

Figure4.6. FTIR spectra of As-anodised sample, unwashed samples annealed at 100°C, 200°C, 300°C for 2 h, and fully washed TiO_2 sample

The FT-IR spectra for the perchlorate containing as-anodized sample and the unwashed calcined samples are shown in **Figure 4.6**.$HClO_4$ is a tetrahedral molecule with normal modes of vibration similar to $KClO_4$ and $NaClO_4$. The asymmetric stretching mode (ASM, v_3) for ClO_4^- ions is in the range of 1050–1170 cm^{-1}(triply degenerate) whereas the asymmetric bending mode (ABM, v_4, triply degenerate) is at 630 cm^{-1}.[20–22] Chabanel *et al.* conclude that interaction between cations and perchlorate ions results in a change or lowering in the symmetry ofClO_4^-

ions. This causes band splittings of the degenerate vibrations, *i.e.* v_3 and v_4. In our case the v_3 band has split in three components, namely 1091 cm^{-1}, 1108 cm^{-1}, 1121 cm^{-1} and the v_4 band into 618 cm^{-1}, 628 cm^{-1}, 635 cm^{-1} indicating the strong interaction of ClO_4^- ions with Ti^{4+} cation. Here ClO_4^- group prefers C_{2v} symmetry and is in the bridging position.[17] Also the reduced intensity of bands with annealing implies their progressive removal.

4.4.5. Mechanism of reverse phase transformation

There are several reports [23–25] on the usual phase transformation of anatase to rutile TiO_2 by bcoarsening of anatase nanoparticlesto a definite size of *ca*. 14 nm but reverse phase transformation is the least studied. Since in the present case the synthetically incorporated chlorate ions (the same discussed in Chapter 3) appear to play a critical role, it is important to analyse and discuss the basic growth process in some detail.

According to ligand field theory, in solution the Ti(IV) ions exist as six-fold coordinated structural units (TiO_6),which undergo condensation to become the octahedra that bond *via* corner and edge-sharing to form the final crystal structure. In the rutile form, TiO_6 octahedra link by sharing an edge along the *c*-axis to form chains which are then interlinked by sharing corner oxygen atoms, whereas in anatase, there is only edge sharing. Thus, the formation of both phases depends onwhether –OH or oxo-bridges are formed between the two metal centers during condensation. Condensation to both rutile and anatase starts when the solution activity is high enough to allow further deprotonation and to form zero charge precursors $[Ti(OH)_4(OH_2)_2]$ which undergo two stages of condensation. First,by olation and second by oxolation as shown schematically in **Figure 4.7**. In olation there is elimination of two water

molecules having *cis* configuration, which lead to $2\mu_2$-OH ions *i.e.* the formation of dimer (double hydroxo bridges, $[Ti_2(OH)_8(OH_2)_2]^0$)[26] which has a tendency to share an edge between the two octahedra leading to a linear chain. This edge sharing is also promoted by high H+ concentration (acidity) as it gets adsorbed on TiO_6 octahedra creating electrostatic repulsion between them. To minimize this repulsion, they arrange themselves as linear chains which is common for both phases of TiO_2.[14,27] After this the dimer undergoes olation where ClO_4^- ions have a tendency to form a symmetric complex which undergoes a type of chlorolysis–oxolation process.[28] In this corner shared TiO_6 the dimers are separated by chlorate anions with each other. This ultimately leads to Ti–O–Ti which is linked through *trans*-oxo bridges (corner sharing) to $2\mu_2$ chains forming the rutile phase and it also stabilizes rutile octahedra internally by connecting one octahedron to another by chlorate bridges. Thus, through the process of anodic dissolution it

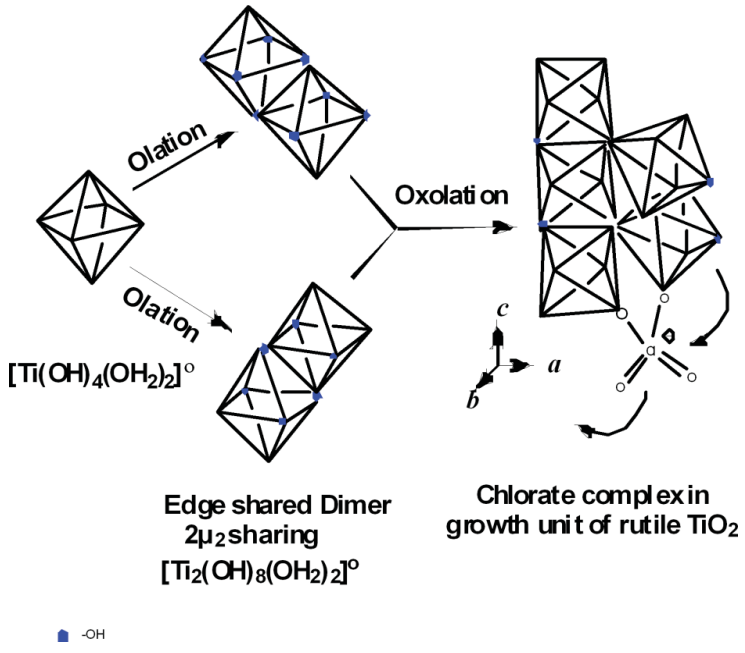

Figure4.7. Schematic diagram of proposed mechanism indicating growth nuclei of rutile TiO_2 synthesized electrochemically (aquo ligand is unlabelled here).

was possible to synthesize rutile.

The *synthetically included* chlorate ions can get eliminated by both the processing protocols namely: (a)multiple washings alone, or, (b) direct annealing without washing, as depicted by the left and right routes, respectively, in the cartoon shown in **Figure 4.8**. However, the phase (and shape) evolution occurs quite differently in the two cases. In the case of multiple washings the removal occurs at room temperature, hence, although some rutile grain growth clearly occurs (Compare the XRD data of **Figure4. 1a)** and **b)** thermal energy is not available for significant and brisk drying shrinkage (due to chlorate removal) and related densification of the needle. Thus the nanoneedle maintains its formas well as the

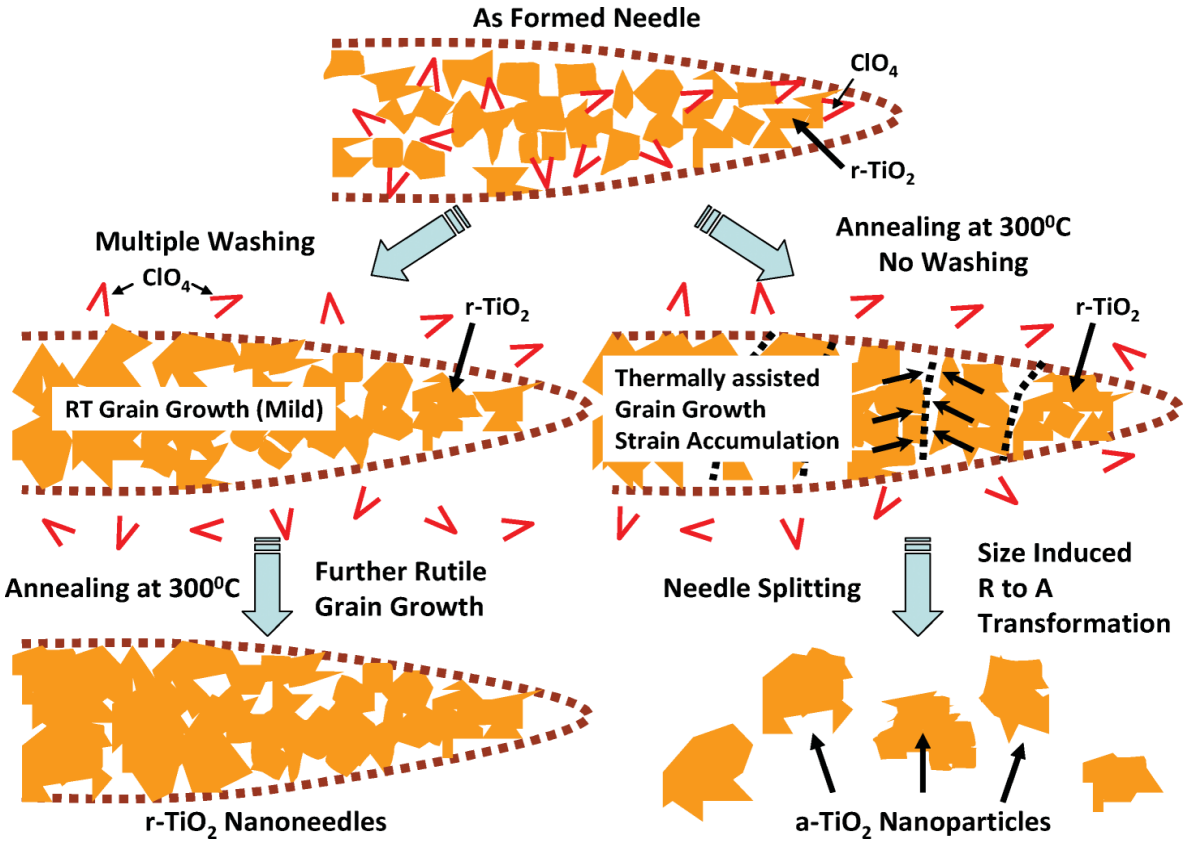

Figure4.8. Cartoon of the proposed mechanism for the growth of rutile nanoneedles and anatase nanoparticles, r-TiO_2 stands for rutile TiO_2, a-TiO_2 stands for anatase TiO_2, R to A transformation implies rutile to anatase transformation.

rutile phase, with the stresses associated with the shrinkage distributed rather homogeneously. Upon heating such needles at higher temperature, the stresses can be gradually relaxed with further densification and the rutile phase is maintained. When on the other hand the as-grown needle mass (moist phase) is directly heated at 300°C without any washing, the removal of chlorate ions is brisk with the temperature also providing for considerable densification and enhanced grain growth, leading concurrently to accumulation of stresses as shown in the cartoon (black arrows). This leads to rupture of the needles into tiny nanoparticles (*ca*. 10 nm), which then undergo size induced rutile to anatase transformation. It is reported that in a nanosystem, the thermodynamically favored phase is anatase, especially when the particle size is below about 11 nm.[24, 30, 31] If the pellet made by adding an organic binder is directly heated to high temperature, cooperative internal transport occurring before binder removal leads to stress inhomogeneities and cracking. On the other hand, if calcination is done, the densification is gradual and controlled, and the pellet holds its shape without cracking. In conclusion, we show that synthetically incorporated chlorate ions play a critical role in the formation of nanoneedles of the *high temperature* rutile TiO2 phase at *room temperature* as well asin the unique reverse *rutile to anatase* nano phase transformation under annealing at 300 ◦C following a specific protocol. We believe that the issue of ion-stabilized solid state and its specific thermal evolution could be employed to engineer specific phases and morphological forms.

4.5. Solar Cell Characterization.

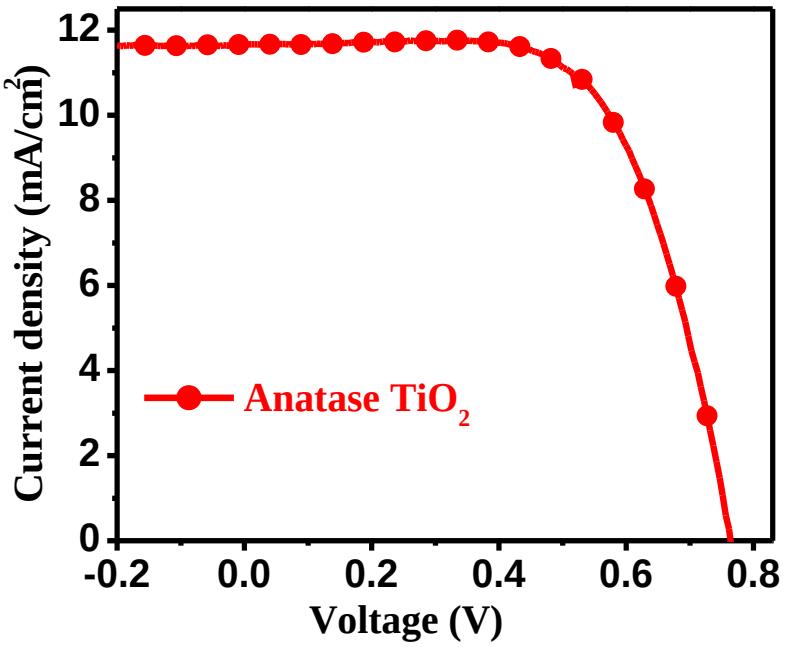

Figure4.9. J–V characteristics of ambient anatase TiO_2

Sample name	V_{oc} (V)	J_{sc} (mA/cm^2)	FF (%)	η (%)
Anatase TiO_2	**0.76**	**11.83**	**65**	**6.0**

Table 1.IV characteristics

IV characteristics of anatase TiO_2 is given in **Figure 4.9.** Table1.gives all the IV parameters which indicates that anatase delivered V_{oc} = 0.76V, J_{sc} = 11.83 mA/cm^2 and appreciable power conversion efficiency of 6%.

4.6. Conclusion:

In conclusion, we show that synthetically incorporated chlorate ions play a critical role in the formation of nanoneedles of the *high temperature* rutile TiO_2 phase at *room temperature* as well as in the unique reverse *rutile to anatase* nanophase transformation under annealing at 300°C following a specific protocol. We believe that the issue of ion-stabilized solid state and its specific thermal evolution could be employed to engineer specific phases and morphological forms. Also the anatase TiO_2 obtained after reverse phase transformation delivered a appreciable solar to power conversion efficiency of 6% whem employed as photanode material of DSSC.

4.7. References

1) M. C. J. Bradford and M. A. Vannice, *Appl. Catal., A*, **1996**, 142, 73-96.

2) X. Chen and S. S. Mao, *Chem. Rev.*, **2007**, 107, 2891-2959.

3) C. W. Dunnill and I. P. Parkin, *Dalton Trans.*, **2011**, 40, 1635-1640.

4) M. Liu, L. Piao, W. Lu, S. Ju, L. Zhao, C. Zhou, H. Lia and W. Wang, *Nanoscale*, **2010**, 2, 1115-1117.

5) B. O Regan and M. Gr¨atzel, *Nature*, **1991**, 353, 737-740.

6) M. Gratzel, *Nature*, **2001**, 414, 338-344.

7) Y. Qu, W. Zhou, K. Pan, C. Tian, Z. Ren, Y. Dong and H. Fu, *Phys. Chem. Chem. Phys.*, **2010**,12, 9205-9212.

8) S. Muduli, O. Game, V. Dhas, A. Yengantiwar and S. B. Ogale, *Energy Environ. Sci.*, **2011**, 4, 2835-2839.

9) C. Garzella, E. Comini, E. Tempesti, C. Frigeri and G. Sberveglieri, *Sens. Actuators, B,* **2000**, 68, 189-196.

10) P. Hu, G. Du, W. Zhou, J. Cui, J. Lin, H. Liu, D. Liu, J. Wang and S. Chen, *ACS Appl. Mater. Interfaces*, **2010**, 2, 3263-3269.

11) N. G. Park, J. Lagemaat and A. J. Frank, *J. Phys. Chem. B*, **2000**, 104, 8989-8994.

12) R. S. Hyam, R. K. Bhosale, W. Lee, S. H. Han, B. Hannoyer and S. B. Ogale, *J. Nanosci. Nanotechnol.*, **2010**, 10, 5894-5898.

13)V. Swamya and B. C. Muddle, *Appl. Phys. Lett.*, **2006**, 89, 163118, 3pages.

14) H. Cheng, J. Ma, Z. Zhao and L. Qi, *Chem. Mater.*, **1995**, 7, 663-671.

15)S. P. S. Porto, P. A. Fleury and T. C. Damen, *Phys. Rev.*, **1967**, 154, 522-526.

16) T. Mazza, E. Barborini, P. Piseri and P.Milani, *Phys. Rev. B: Condens. Matter Mater. Phys.*, **2007**,75, 045416, 5pages.

17) M. Chabanel and K. Touaj, *J. Chem. Soc., Faraday Trans.*, **1996**, 92, 4207-4213.

18) I. R. Lewis and H. G. M. Edwards, *Handbook of Raman Spectroscopy,* New York, 1st edn, **2001**, vol.28, pp. 701.

19) S. Muduli, W. Lee, V. Dhas, S. Mujawar, M. Dubey, K. Vijayamohanan, S. H. Han and S. B. Ogale, *ACS Appl.Mater. Interfaces*, **2009**, 1, 2030-2035.

20) L. Wittenkeller, W.Lin, C. Diven, A. Ciaccia, F. Wang and D. M. Freitas, *Inorg. Chem.*, **2001**, 40, 1654-1662.

21) S. L. Romero, J. C. Mendoza, J. C. Ram´ırez and J. M. Garcia, *Revista Mat´eria*, **2005**, 10, 413-418.

22) Y. Chen, Y. H. Zhang and L. J. Zhaoa, *Phys. Chem. Chem. Phys.*, **2004**, 6, 537-542.

23) J. Zhang, Q. Xu, M. Li, Z. Feng and C. Li, *J. Phys. Chem. C*, **2009**, 113, 1698.

24) H. Zhang and J. F. Banfield, *J. Mater. Chem.*, **1998**, 8, 2073-2076.

25) Y. Sun, T. Egawa, L. Zhang and X. Yao, *Jpn. J. Appl. Phys.*, **2002**, 41, L945-L948.

26) J. P. Jolivet, *Metal Oxide Chemistry and Synthesis: From Solution to Solid State*, John Wiley, Masson Paris, 3rd edn **1994**, pp. 82–85.

27) J. P. Nikkanen, T. Kanerva and T. Mantyla, *J. Cryst. Growth*, **2007**, 304, 179-183.

28) D. R. Coronado, G. R. Gattorno, M. E. E. Pesqueira, C. Cab, R. Coss and G. Oskam, *Nanotechnology*, **2008**, 19, 145605-145614.

29) Z. Tang, J. Zhang, Z. Cheng and Z. Zhang, *Mater. Chem. Phys.*, **2003**, 77, 314-317.

30) H. Zhang and J. F. Banfield, *J. Phys. Chem. B*, **2000**, 104, 3481-3487.

31) M. I. Zaki, G. A. H. Mekhemer, N. E. Fouad, T. C. Jagadale and S. B. Ogale, *Mater. Res.Bull.*, **2010**, 45, 1470-1475.

Chapter 5

Nanophase $CuInS_2$ nanosheets/CuS composite grown by the SILAR method leads to high performance as a counter electrode in dye sensitized solar cells*

In this work, we report synthesis of binary suifide $CuInS_2$ (CIS) and its composite with CuS as a counter electrode material for Dye sensitized Solar Cell (DSSC) to replace the presently used precious and therefore high cost metal platinum. Pure phase CIS nanosheets are synthesized on TiO_2 coated FTO by the simple technique of Successive Ionic Layer Adsorption Reaction (SILAR) followed by annealing at 500°C. Annealing at a lower temperature of 250°C is found to yield CuS nanoparticles in addition to the CIS phase. The CIS–CuS composite is found to have a synergistic effect on the catalytic performance towards the reduction of tri-iodide, yielding a power conversion efficiency of 6.3% as compared to pristine CIS case (5%) or CuS case (3.5%). The possible reasons behind the high performance of the composite are elucidated using cyclic voltammetry (CV) measurements and electrochemical impedance spectroscopy (EIS).

*_The content of this chapter has been published in "**RSC Adv.", 2014**, 4, 21989-21996._**.**

Reproduced by permission of The Royal Society of Chemistry (RSC)

http://pubs.rsc.org/en/content/articlelanding/2014/ra/c4ra01740d#!divAbstract

5.1. Introduction

As one of the most promising alternatives for traditional silicon solar cells, dye-sensitized solar cells (DSSCs) have attracted tremendous scientific and industrial attention in the past two decades, owing to their low cost, simple fabrication, and high efficiency.[1] A typical DSSC has a sandwich structure with a photoanode comprising a TiO_2 nanoparticle film sensitized by dye molecules, an electrolyte containing the iodide – triiodide (I^-/I_3^-) redox couple, and a counter electrode (CE) catalyzing the reduction of I_3^- to I^-. Usually, platinum is the best material for catalyzing the reduction of I_3^- due to its superior conductivity, electrocatalytic activity, and stability. However, as a noble metal, low abundance ratio and high cost prevent Pt from being used for DSSCs, which has stimulated great efforts to explore and evaluate substitutes for Pt in order to reduce the overall cost and simultaneously retain the performance of DSSC. Towards this end many alternatives like carbon based material, conducting polymers, and metallic nano-materials have been and are being investigated.[2–5]

Transition metal sulfides such as CoS, NiS, SnS appear to be particularly interesting in this context due to their unique catalytic, optical and electrical properties.[6–8] Multimetal sulfides too are excellent candidates in photovoltaic applications due to their direct band gap and high absorption coefficient of more than 10^5 cm^{-1}. A synergistic mechanism involving various metal elements also renders a higher catalytic activity in such semiconductors. $CuInS_2$ (CIS) is one such bi-metallic sulfide which has not yet been fully explored in the DSSC counter electrode context except for a few interesting recent works. For example, Yang et al.[9] and Liu et al.[10] used hydrothermally and solvothermally synthesized CIS nanosheets and CIS nanoflakes respectively as counter electrode in DSSCs, which exhibited an efficiency of 6%. Composites of CIS have

also being explored. For instance, Zhang et al.[11] reported CIS/PEDOT: PSS composite to increase the adhesion and conductivity of counter electrodes giving an efficiency of 6.5%. Most recently sponge-like $CuInS_2$ is synthesized by solvothermal method and its composite is made with graphene which gave the power conversion efficiency of 6.18% but only $CuInS_2$ gave 3.31% efficiency.[12]

In our work we have synthesized the bimetallic sulfide in situ by the facile, well known and easily scalable Successive Ionic Layer Adsorption Reaction (SILAR) method which when used as counter electrode showed an efficiency of 6.3% in DSSC. To the best of our knowledge, this is for the first time any ternary sulfide is synthesized by SILAR as a counter electrode for DSSC. Here initially grown films were amphorous in nature and when calcined at 500°C yield pure crystalline $CuInS_2$ nanosheets. These CIS nanosheets when used as counter electrode in DSSC gave an efficiency of 5%. But when calcined below 500°C, an efficiency of 6.3% was obtained. Interestingly, our findings based on thorough Raman, X-ray diffraction and multiple characterizations reveal the presence of tiny nanocrystals of CuS, which can defy coarse level characterizations, may in fact be the key to its higher performance as counter electrode material when calcined below 500°C. Thus even when one is claiming a single phase condition based on broad level characterization, the material could be a nano-composite, giving synergistic effect on counter performance. We specifically point out that the two materials are not purposely mixed in any off stoichiometry ratio but the specific constitution results only from specific controlled thermal annealing.

SILAR is a very simple and inexpensive method to grow semiconductor nanocrystals even for large area applications on various substrates without any special restrictions. Moreover

the thickness and composition of the film grown can be controlled easily and accurately by changing the cycle numbers and the immersing processes/sequences. More importantly, since competitive adsorption between different metal ions is caused by a significant difference in solubility products, it is hard to deposit ternary or quaternary metal sulfides in a single solution comprising of two or more cations by the SILAR method. Therefore multiple and sequential (alternate) dippings in solutions of different cations are required. Interestingly this helps in careful control of stoichiometry while at the same time allowing nanophase growth. With this approach we have successfully achieved graphene like 2D layered morphology of metal chalcogenide (CIS) which is an emerging potential material for applications in energy storage (Li ion intercalaction), catalysis, photovoltaics etc.

5.2. Expermental Section

5.2.1. Synthesis: SILAR Method

Before depositing CIS on FTO (F: SnO_2) substrates they are cleaned (given in **Chapter 2, Section 2.1.1.**) and spin coated with TiO_2 (Solaronix HT/SC) at 3000 rpm for 60 s and annealed at 450°C for 15 min. Such TiO_2 films were given $TiCl_4$ treatment by immersing them in $TiCl_4$ solution at 70°C for 30 min followed by annealing at 450°C for 30 min. After this $CuInS_2$ was deposited by modified SILAR method on TiO_2 coated substrates.[13] Briefly, the above mentioned substrates were dipped sequentially in aqueous solutions of 0.1 M $In_2(Cl)_3$ for 60 s, and S ion precursor solution (0.075 M Na_2S, with a pH equal to 11.3 adjusted by a buffer solution of 0.1 M KH_2PO_4 and 0.1 M NaOH) for 150 s. This was followed by dipping in 0.01 M $CuCl_2$ aqueous solution for 20 s, and again in S ion precursor solution for 150 s. Between each dip, the films were rinsed with de-ionized water for 30 s to remove excess precursors and dried in air before

the next dipping. Such an immersion procedure is termed as one cycle for copper indium sulfide deposition, and this immersion cycle was repeated several times (8–20) until the desired amount of $Cu_xIn_yS_z$ quantum dots (QDs) were incorporated. To increase the crystallinity of SILAR-deposited $CuInS_2$, samples were annealed at different temperatures (250°C and 500°C) in a split-tube furnace under sulfur atmosphere/Ar gas for 30 min at a ramp of 2°C min^{-1}. CuS is also prepared by SILAR by immersing TiO2 coated FTO in $CuCl_2$ (0.1 M) and Na_2S (0.1 M) for 1 min.

5.2.2. Fabrication of DSSC

Detailed fabrication of DSSC is given in **Chapter 2 (Section I 2.1.).**Commercially available anatase TiO_2 nanoparticle powder (Sigma Aldrich, ~25nm) was used as photoanode material and paste is prepared by protocol II. CIS, CuS and CIS-CuS composite was used as counter electrode. Platinium was employed as a standrad counter electrode for comparison.

5.3. General Characterizations

Phase formation was established by X-ray diffraction (XRD, Philips X0 Pert PRO). The Raman spectra were measured with 632 nm laser by a LabRAM HR800 (JY Horiba). Surface morphology of the samples and elemental mapping was studied using field emission scanning electron microscope (FESEM, FEI Quanta 200 3D), high solution transmission electron microscope (HRTEM, tecnai 300 (T-30)) was applied to investigate the detailed nanostructure of different counter electrodes. The current density–voltage (J–V) characteristics of DSSCs were measured under 100 mW cm^2 irradiation (150 W xenon lamp, Oriel Instruments), 1 sun AM1.5, simulated sunlight (solar simulator) on active area of 0.25 cm^2. The cyclic voltammetry was measured on the three-electrode system carried out at scan rate of 100 mV s^{-1} with Ag/AgCl as

the reference electrode, Pt foil as the counter electrode and thermally deposited Pt/CIS/ CIS–CuS composite as the working electrode. The electrolyte used for this study was 10 mM LiI, 1 mM I_2 and 0.1 M $LiClO_4$ in acetonitrile. Electrochemical impedance spectroscopy (EIS) of the CEs was recorded using AUTOLAB PGSTAT 30 and performed on dummy cells with a symmetric sandwich-like structure between two identical electrodes, that is, CE/electrolyte/CE under dark conditions. The CEs used for testing in this paper are for fabricating the DSCs. The frequency range was varied from 105 Hz to 0.01 Hz. Thickness of electrodes was measured by surface profiler from Dektak 150, Veeco make.

5.4. Results and Discussion:

5.4.1. X-Ray Diffraction (XRD).

Figure5.1. shows the XRD data of as-grown CIS films, films annealed at 250°C and that annealed at 500°C. The XRD curve in **Figure 5.1. (a)** is of as-grown CIS films which show no peaks of CIS except peaks of FTO substrate are seen. This indicates that the as grown CIS films are amorphous in nature. The XRD pattern in **Figure 5.1. (b)** refers CIS Films annealed at 500°C. It shows peaks at $2\theta = 28.1°$, 46.8°, and 54.5°. When matched with (JCPDS no. 85-1575) it confirms that these peaks can be indexed to the (112), (220), and (312) planes of $CuInS_2$ indicating crystalline pure tetragonal phase.[10] But when the films were annealed at 250°C, **Figure5.1. (a)** not only the three main peaks of CIS with slight shift were observed but also occurrence of additional three peaks was noted. These additional three peaks belonged to hexagonal CuS with peak positions at 29.4°, 31.6°, and 48.0° corresponding to the (102), (103),(110) planes. Thus the sample annealed at 250°C showed mixed phase of CIS–CuS. The

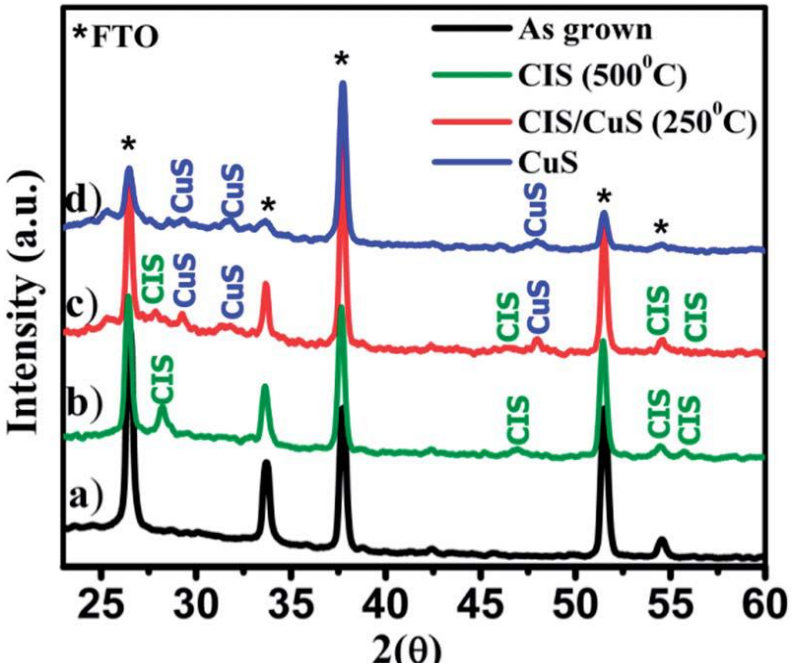

Figure5.1. XRD data for (a) as grown copper indium sulfide (CIS). (b) CIS annealed at 500°C. (c) CIS annealed at 250°C (d) CuS.

phase equilibria between different components depend on temperature and the formation of the phases is controlled by the kinetics of diffusion of the constituent elements in the intermediate phases. In the present case, sub-phases (such as In_2S_3, $CuIn_5S_8$ or CuS) of Cu, In and S occur at the low temperature of 250°Cover the experimental reaction time and the temperature is not high enough to overcome diffusive processes. On the other hand, at the elevated temperature of 500°C the diffusive kinetics are accelerated and these sub phases can react to form single phase CIS over comparable processing time reaching global phase equilibrium at that temperature. Thus, the observed phase formation is a two-step process wherein sub-phases form at lower temperature and with further increase in temperature these phases react and form a single phase compound. **Figure5.1. (d)** shows the XRD pattern of pure CuS deposited by the same method.

The CuS peaks in this case match well with the CuS peaks in the composite CIS–CuS annealed at 250°C.

5.4.2. Raman spectra

Chalcopyrite and sulfide based nanomaterials have very close and similar 2(θ) positions in XRD, hence to have much more clear scenario of phase formation a careful Raman spectroscopy study is considered essential. CIS has two possible metastable phases, i.e., the Cu–Au (CA)-ordered phase, and the chalcopyrite (CH) phase. Raman spectroscopy is very effective in distinguishing between these two phases. Due to low formation energies, CA-ordered phase and CH phase co-exist at room temperature as stable phase. But, CA-ordered phase is known to be related with decrease of grain size and increase of defects in grains at lower temperature and is unstable at higher temperature. [14–16] In **Figure5.2.** we present the Raman spectra for the sample annealed at 500°C (a) and the one annealed at 250°C (b). For comparison purpose the spectrum for pure CuS sample is also shown (c). Remarkable differences are seen between the cases of samples annealed at the two different temperatures. Most significantly, it is noted that the 250°C annealed sample shows co-existence of CIS and CuS phases, while the one annealed at 500°C shows presence of single phase CIS. This is glaringly brought out by the signature in the domain of 450– 500 cm^{-1}; the well-known CuS A_{1g} signature at 472 cm^{-1}.[15–17] Another CuS signature at 263 cm^{-1} is also present in the 250°C annealed sample.

In pure CIS (500°C) case A_1 mode of CH phase is clearly observed at 292 cm^{-1} whereas in the case of the composite (250°C) the A_1 mode is broader and split into CH- and CA ordering which appear at 293 cm^{-1} and 305 cm^{-1}, respectively.[14, 15] It is also to be noted that the full width at half maximum (FWHM) values of the 292 cm^{-1} and 305 cm^{-1} lines are (11 cm^{-1})

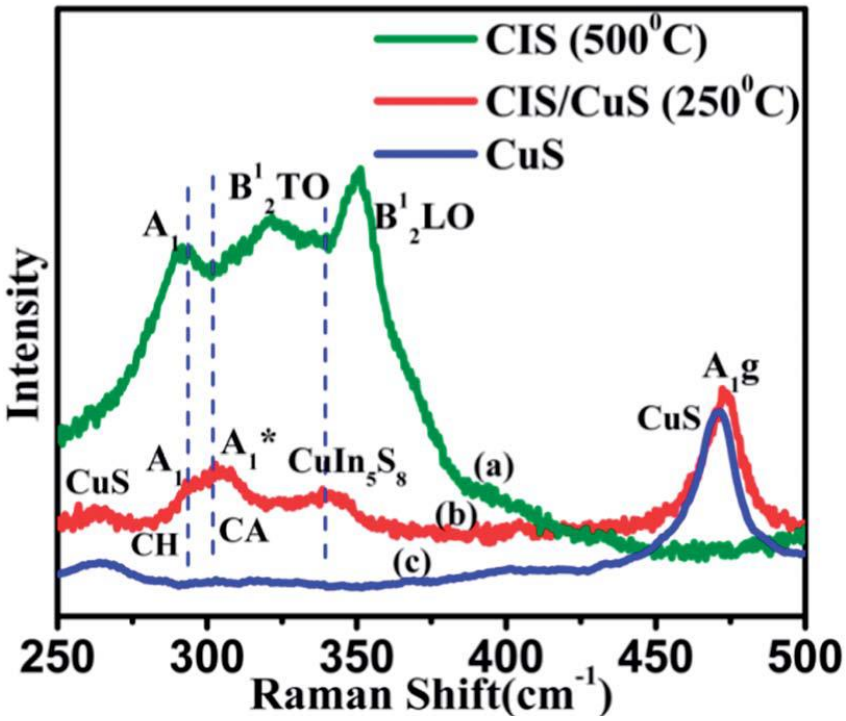

Figure5.2. Raman spectra of CIS film (a) annealed at 500°C (b) annealed at 250°C and (c) pure CuS film.

and (17 cm^{-1}) than that reported for large single crystal[18] which is very much similar with graphene like samples and this is very well reflected in TEM images shown in **Figure 5.9.**Broadening of the Raman bands suggests that the lateral dimensions of these layers are in the nano regime.

The intensity of A_1 mode at 292 cm^{-1} in 250°C case is lower than A*1 mode due to increase in the Cu/In-ratio. Interestingly, the peak of 305 cm^{-1} from A_1* mode of CA ordering is dominant in the case of 250°C annealed sample and is totally absent in the pure CIS (500°C annealed case) as it is unstable at higher temperature. This result implies that the sulfurized metallic film at 500°C is formed with nearly perfect CH ordering of CIS with no secondary phase of Cu_xS and In_2S_3.[15] The 322 cm^{-1} (B_2^1 TO) and 351 cm^{-1} (B_2^1 LO) are also from CH

ordering. [19] It is reported that b-In_2S_3 shows peaks at 323 cm^{-1} and 363 cm^{-1} [15] which are not seen in both the cases. But in indium rich phase, $CuIn_5S_8$ is indicated by broad signal at around 341 cm^{-1} [16]which co exists with CIS at 250°C. This $CuIn_5S_8$ phase is not possible to distinguish in XRD due to very close 2(θ) positions of CIS and $CuIn_5S_8$ but can be elucidated with higher sensitivity primarily by Raman spectroscopy as shown.[20]This peak gets totally vanished in the case of the 500°C annealed sample as $CuIn_5S_8$ gets chemically transformed into CIS with the help of CuS.[15, 16] Nanoporous film of TiO_2 (thickness 40 nm) used for SILAR is not detected in XRD but is seen in Raman at 148 cm^{-1}.

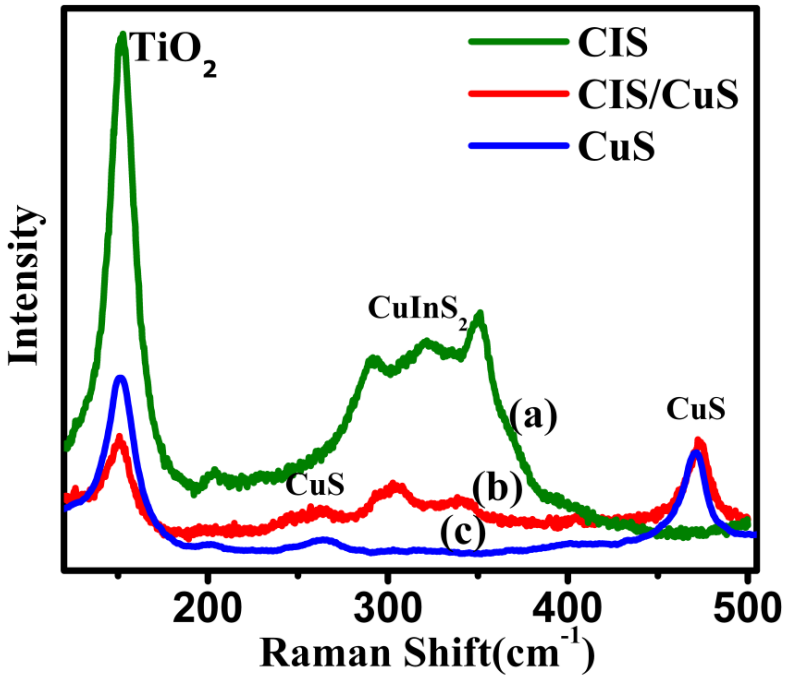

Figure5.3. Raman spectra of CIS film (a) annealed at 500^0C (b) annealed at 250^0C and (c) pure CuS film

5.4.3. Field Emission Scanning Electron Microscopy (FESEM) images.

When CIS is directly deposited on bare FTO (without coating of TiO_2) by SILAR method, agglomeration of irregular nanoparticles with random growth is seen as shown in FESEM images (**Figure 5.4)**.Also visually less amount of CIS material is deposited which has poor

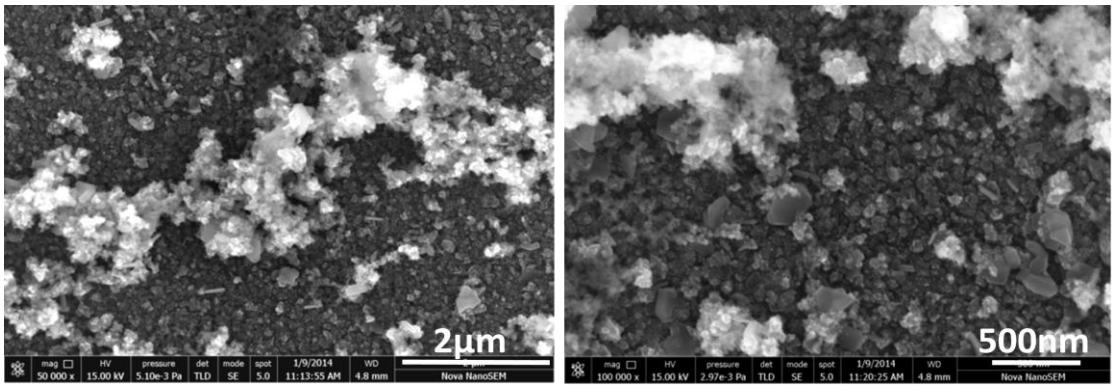

Figure5.4. FESEM images of CIS on FTO without TiO_2

adhesion. To increase the adhesion and coverage of material on substrate, a thin and uniform layer of TiO_2 was spin coated on FTO (synthesis details given in **Section 5.2.1**) as shown in FESEM image, **Figure 5.5.**

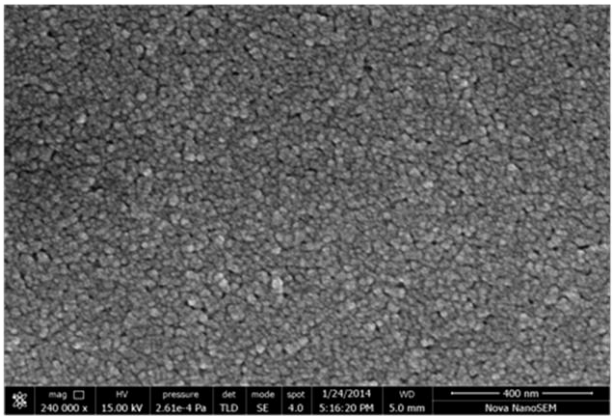

Figure 5.5.FESEM Image of TiO_2 film coated on FTO

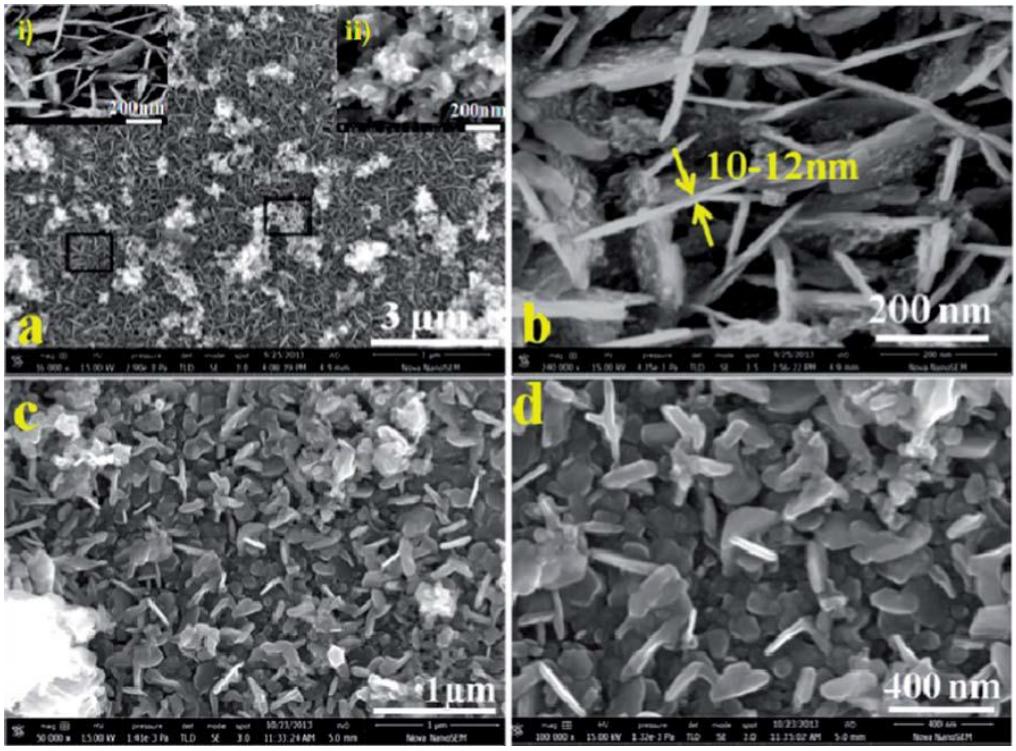

Figure5. 6. FESEM images of (a) CIS–CuS composite with insets showing two distinct surface features, (b) CIS–CuS thin nanoplates and their typical thickness, (c) and (d) CIS nanosheets under two magnifications.

When CIS and CIS-CuS deposited on TiO_2 coated FTO substrate then not only adhesion and coverage of the material was seen to increase but also distinct nanostructured morphology was obtained as shown in **Figure 5.6.Figure 5. 6. (a)** and **(b)** shows the images for the film (0.1–1.2 µm) obtained by annealing at 250 °C while **Figure 5. 6. (c)** and **(d)** shows the images for the sample annealed at 500°C. These establish that the films comprise of uniform and compact nanosheets which are vertically oriented and interconnected, forming multiple semiconducting channels. In DSSCs, the catalytic reactions take place on the surface of the counter electrodes, thus it is credible that the

morphologies of catalytic materials will have an obvious influence on the catalytic reaction. Such a hierarchical architecture not only facilitates transfer of carriers from their surface to the conducting FTO substrate but also endows a large surface area for sufficient light harvesting in

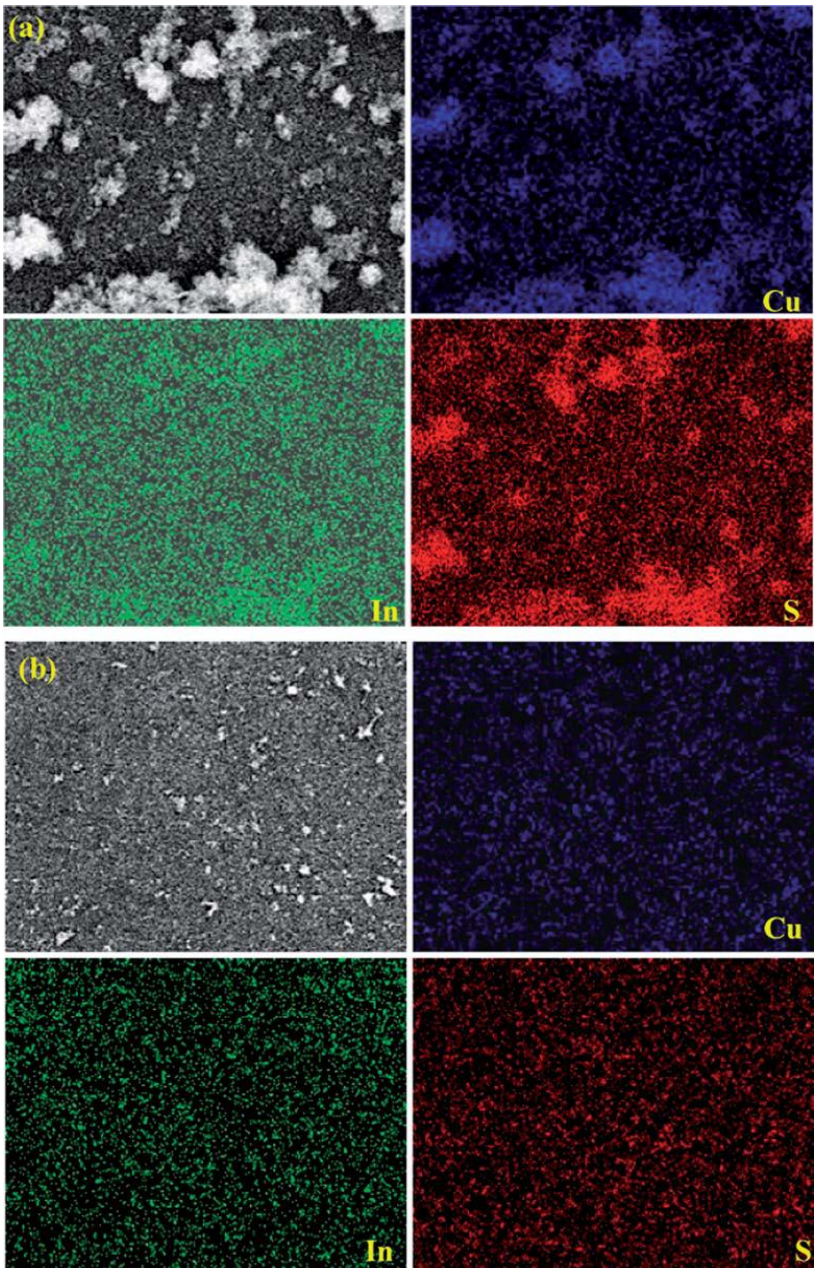

Figure5.7. Elemental mapping of (a) CIS–CuS composite, (b) CIS

optoelectronic applications. We measured the BET surface area for all the three cases although the measurement of BET surface area on thin films is non-trivial. The surface area values for CIS–CuS and CuS were obtained as ~13 m^2 g^{-1} and ~3 m^2 g^{-1}, respectively. The area measured for the single phase CIS case realized at 500°C was below the detection limit of our instrument. This may be due to densification and grain growth which occurs at such high temperature, thereby reducing the surface area significantly.

Separately, we found that as the number of SILAR cycles used are increased from 8 to 20, the thickness of nanosheets increases. **Figure 5.6. (b)** represents the case of 16 cycles and the corresponding nanoplate width is seen to be 10–12 nm. In the composite case (250°C annealed sample), aggregation of CuS nanoparticles (inset ii) is seen to be embedded on CIS nanosheets which is clearly seen in the elemental mapping (**Figure 5.7.(a)**) whereas in the 500°C annealed case only CIS nanosheets with no other secondary phase are seen in **Figure 5. 7.(b)**. These nanosheets are fused together due to annealing effect as seen in **Figure 5.6. (c)** and **(d)**. Only CuS prepared by SILAR also shows nanoparticle assembly in the form of sea-corals as shown in **Figure 5.8.**

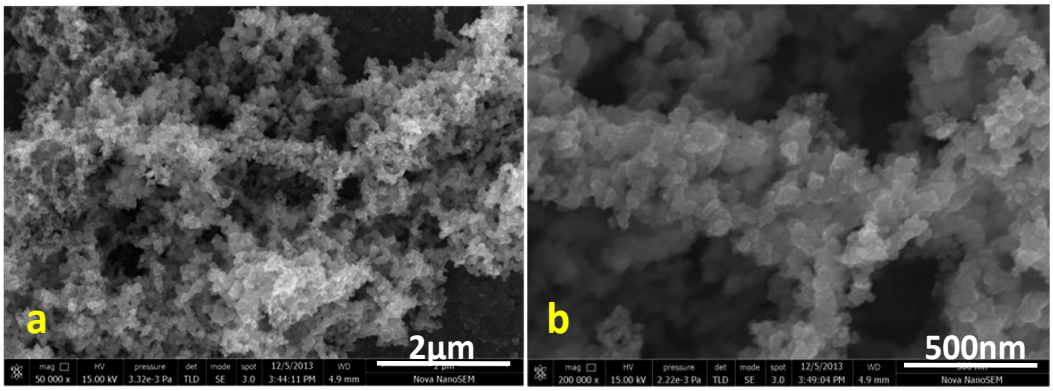

Figure 5.8. CuS on TiO_2 coated FTO

5.4.4. Transmission electron Microscopy (TEM) images

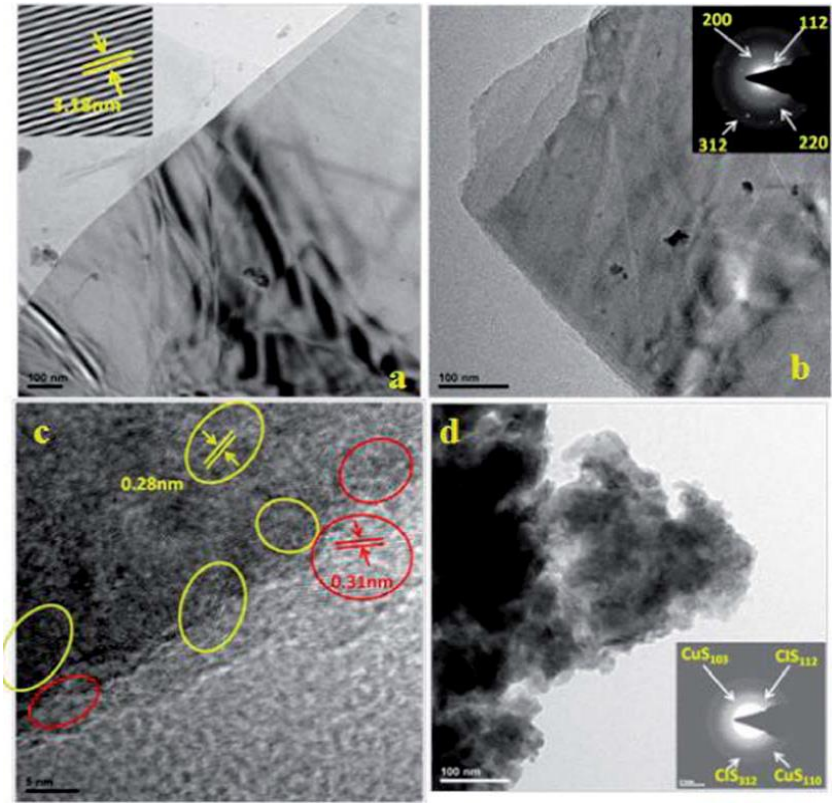

Figure5.9. HRTEM images of (a and b) CIS and (c and d) CIS–CuS composite.

The TEM images of the CIS sample annealed at 500°C are shown in **Figure5.9. (a and b)**. These reveal graphene like 2D morphology with stacked nanosheets. The bent contour lines in the TEM image are possibly caused either by buckling in the nanosheet introduced in the process of TEM sample preparation or by electron-beam-induced thermal strain during the characterization process. The lattice spacing of about 0.319 nm can be measured from the HRTEM image which corresponds to the (112) lattice plane spacing of $CuInS_2$. The selected area electron diffraction (SAED) pattern confirms that the nanosheet is polycrystalline with planes corresponding to pure

CIS. The HRTEM image of the 250°C annealed composite case shown in **Figure 5.9.c)** reveals that CIS nanosheets (d-spacing 0.31 nm) are decorated with CuS (d-spacing 0.28 nm) nanoparticles of ~5 nm. The SAED pattern gives two sets of signals: one set gives (112) and (312) of CIS whereas the other gives (103) and (110) of CuS.

5.4.5. Mechanism of CIS nanosheet formation

To study the formation mechanism of CIS nanosheets, only FTO and FTO coated TiO_2 were studied in detail, the latter to also concurrently investigate the role of TiO_2 nanoparticles in the specific morphology evolution. A schematic diagram for the proposed mechanism of nanosheets is shown in **Figure 5.10**. The thin film of TiO_2 increases the roughness of surface and thereby the adhesive anchoring of CIS nanosheets on it. Also hydrophilicity of TiO_2 surface promote nucleation as the hydroxyl groups present on the TiO_2 surface bond with metal cations, such as Cu^{2+} and $In^{3+}$and control random crystal aggregation.[21] When this TiO_2 modified FTO is dipped in solutions for SILAR process, it undergoes heterogenous nucleation. In SILAR, ions from precursors go ion-by-ion adsorption directly on the substrate forming CIS nuclei. Thus the reactants are transported from the solution to the solution/substrate interface, leading to the deposition on the substrate and further crystal growth. Therefore, it is more convenient for the nucleation and adhesion of $CuInS_2$ seeds on the rough TiO_2 surface, due to the lower interfacial energy between the substrate and the solution. A control experiment was also performed without coating of TiO_2 on FTO which gave rise to poor coverage of material on FTO. Moreover FESEM images (**Figure 5.4.**) revealed that there is formation of CIS nanoparticle clusters with random growth. This is due to the lesser hydrophilic property of FTO than TiO_2. Thus TiO_2 not only promotes adhesion of CIS film but also gives rise to unique morphology of nanaosheets.

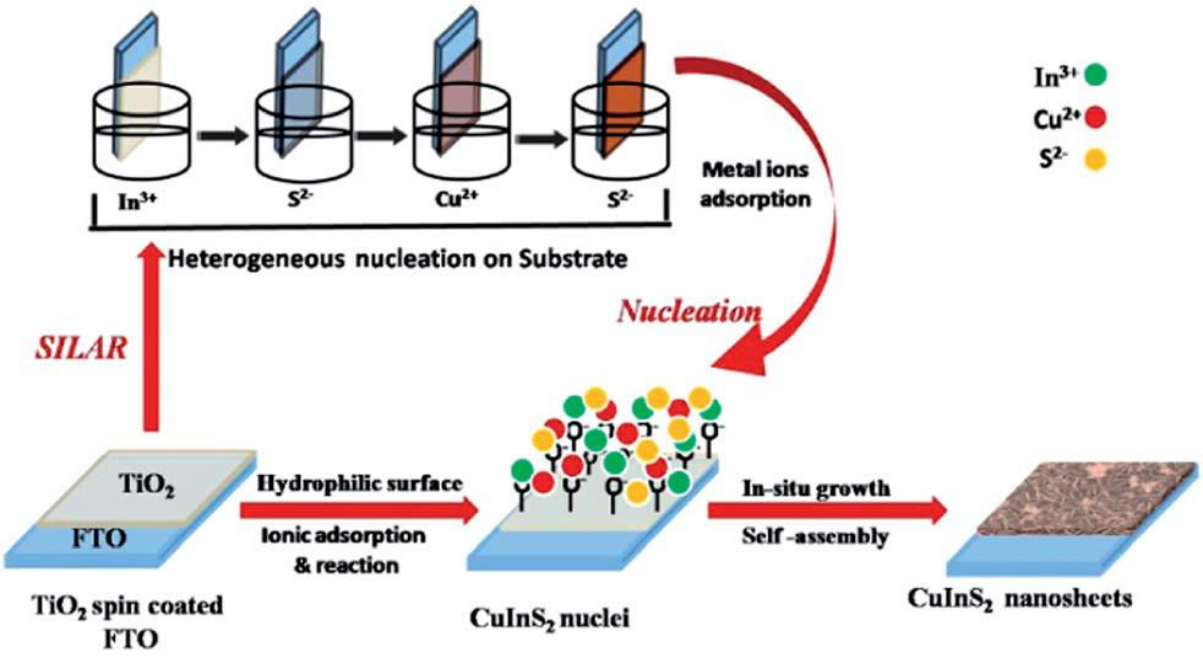

Figure5.10. CIS nanosheet formation in SILAR.

With further increase in the SILAR cycles, crystal growth continues by consumption of more reactants. Thus the morphology is strictly dependent on the concentration of reactants and dipping time of substrates in solutions. After the nucleation step, CIS nuclei undergo *in situ* anisotropic growth process forming thin nanosheets perpendicular to substrate. This phenomenon could be explained by 'evolutionary selection'' mechanism proposed by Van der Drift [22,23] which means that only the facets with the highest growth rate and perpendicular to the growth surface would be favorable to the crystal growth. This concurrent growth of a large number of CIS nanosheets form a net or mesh like system to reduce the surface energy of the system. With further increase in the cycles these coalescence of nanosheets undergoes self-assembly process to form channels of nanoplates interconnected with each other. This is evident from the TEM images in **Figure 5.9.** where uniform plate-like structures display clear nanosheet edges. As prepared CIS is amorphous in nature. Upon annealing at 250^{o}C some of the unreacted ions of Cu

and from solution or ions from stoichiometric CIS, oozing out of the film cause CuS aggregation. It is well known that the solution method is based on surface chemistry through changing the interfacial tension to control the structure and morphology of the products, but at higher temperature the chemical kinetics of diffusion of dissolved reactants is enhanced.[23] Therefore the higher temperature could induce secondary nucleation favoring dissolution of unreacted ions and of thinner nanosheets to form thicker ones according to the nucleation–dissolution–recrystallization mechanism. During this mechanism binary products may come out giving rise to temperature induced composite. In 500^{o}C case same is the situation but it is an ideal temperature reported by many reports, where all the unreacted ions diffuse to form pure chalcopyrite CIS with no secondary phase. From the FESEM image (**Figure 5.6.c**) it is clear that nanosheets are more fused compared to the 250^{o}C annealed case due to grain boundary diffusion.

5.4.6. Electrochemical analysis

For use as counter electrodes in DSSCs these CIS and CIS–CuS composite counter electrodes must show good catalytic activity towards I^-/I_3^- redox reaction. Cyclic voltammetry technique allows qualitative assessment of the electrode kinetics towards this redox couple. [24] CIS and CIS–CuS composite counter electrodes with different SILAR cycles (8 cycles to 20 cycles) were subjected to cyclic voltammetry analysis. In the case of the counter electrodes, two pairs of redox peaks, I and II, representing sequential redox reactions of different iodide species are seen, corresponding to the reactions

$$I_3^- + 2e^- \leftrightarrow 3I^- \quad (1) \qquad I_3^- \leftrightarrow I_2 + I^- \quad (2)$$

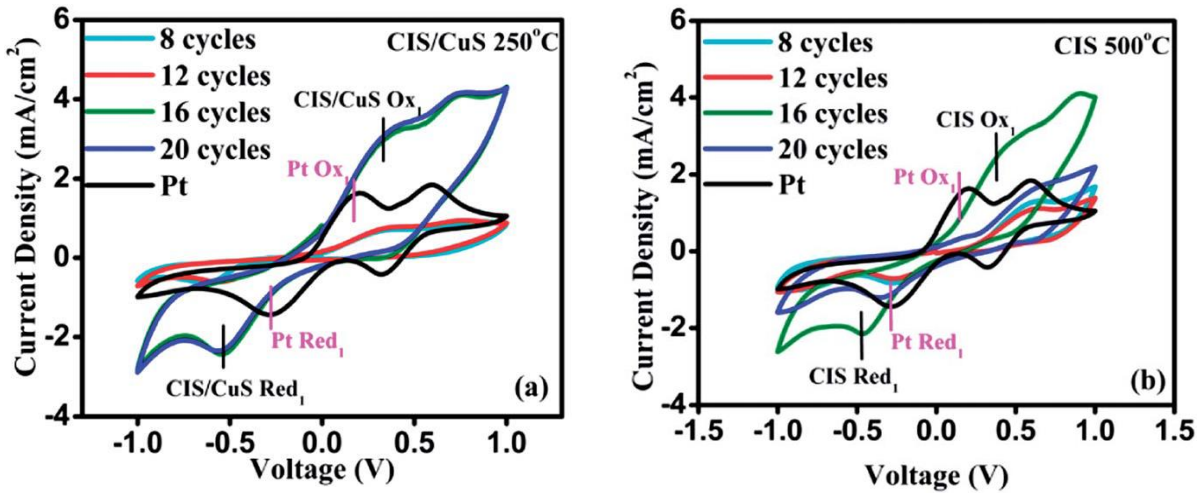

Figure 5.11. Cyclic voltammetry data of (a) CIS–CuS composite (b) CIS counter electrodes.

The peak current density helps to evaluate the catalytic activity of the CE, and thus a higher peak current density infers better catalytic activity. The counter electrodes (CEs) fabricated with 16 cycles of both CIS and CIS–CuS composite showed highest current density as compared to other cycles in **Figure 5.11.(a)** and **(b)**. The peak currents of reduction reactions on different electrodes were noted to follow the order: CIS–CuS > CIS > Pt. Also a shift in the reduction potential towards more negative potential of CIS (-0.28 to -0.38) and CIS–CuS (-0.28 to -0.45), indicates that the oxidized iodide species formed by scavenging photo-excited holes of the dye are easily reduced and regenerated of the electrodes. Besides this the separation of the anodic and the cathodic peak potentials, peak to peak separation (Epp) of CIS, CIS–CuS and Pt CE was also calculated. The Epp value for Pt counter electrode is 475 mV. The Epp is inversely proportional to the catalytic activity of counter electrode towards the redox species. As seen from the **Figure 5.11.(a)** and **(b)** the Epp is lower for all the cases with CIS–CuS composite as compared to pure CIS. Of all the cycles, for the 16 cycle case, both CIS and CIS–CuS composite counter

electrodes show higher current density and lower Epp value indicating better catalytic activity towards I^-/I_3^- reduction. The average Epp for all cases in CIS–CuS composite is 820 mV while it is 870 mV for CIS. Thus the CIS–CuS composite CEs are better towards reduction of iodide–triiodide compared to CIS. CV of pure CuS (16 SILAR cycles) was also recorded which shows lower performance as compared to CIS and CIS–CuS composite.

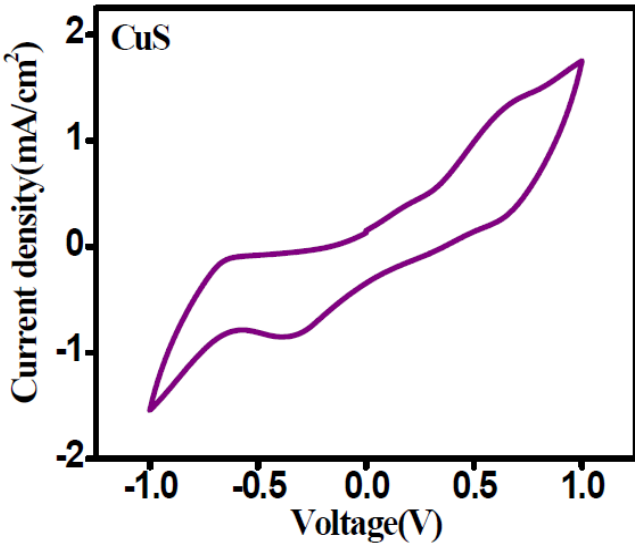

Figure5.12. Cyclic voltammetry data of CuS counter electrode

5.4.7. Photovoltaic performance

After the cyclic voltammetry (CV) analysis, the cells based on the pristine $CuInS_2$ nanosheet counter electrode and temperature induced composite (CIS–CuS) were also studied with respect to different SILAR cycles (8-20) and their effect on photovoltaic performance as shown in **Figure 5.13.** and **Figure 5.14.** respectively. **Table 1** and **Table 2** summarizes the IV parametersfor the CIS nanosheet based counter electrode and CIS-CuS nanosheets /nanoparticle

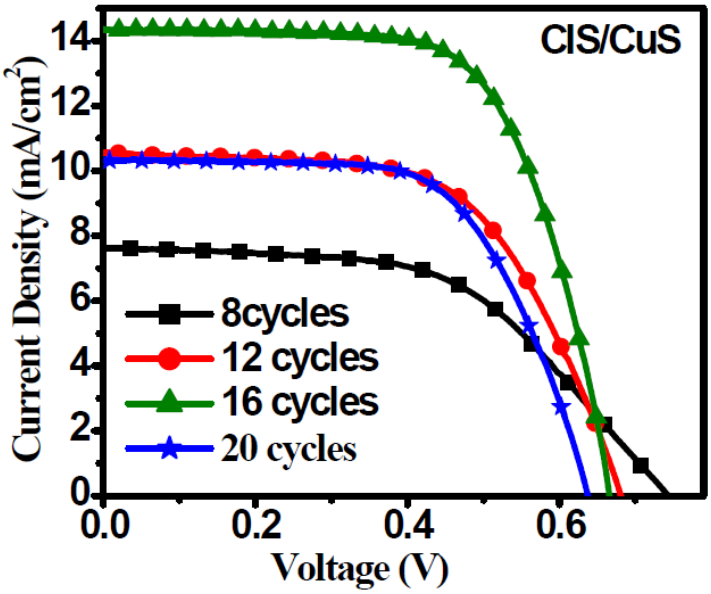

Figure 5.13.I-V data of CIS/CuS as counter electrodes at different SILAR cycles

Sample	V_{oc} (V)	J_{sc} (mA/cm^2)	FF (%)	Efficiency (%)
8cycles	0.74	7.6	54	3.2
12 cycles	0.68	10.5	60	4.6
16 cycles	0.70	14.4	66	6.3
20 cycles	0.64	10.2	63	4.5

Table 1.I–V parameters of CIS/CuS counter electrodes with different SILAR cycles

composite based counter electrode respectively. Out of these 16 SILAR cycled CEs showed the best performance given in **Figure 5.15.** and IV parameters summarized in **Table 3**. All the counter electrodes with 8–12 cycles show lower short circuit current density and a lower fill factor compared to 16 cycles. This is probably because the film is too thin to provide enough catalytic sites for I_3^- reduction. With a continued increase in SILAR cycles, the efficiency

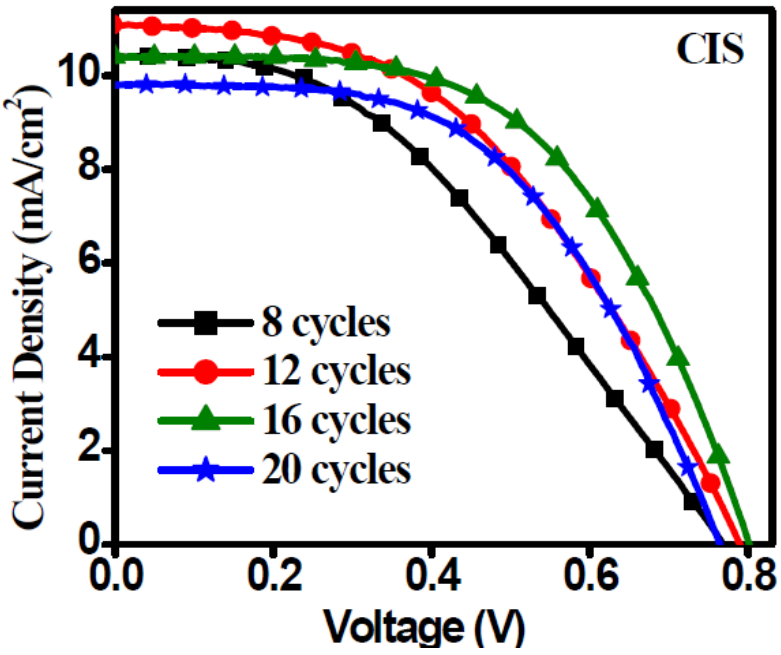

Figure 5.14.I-V data of CIS as counter electrodes at different SILAR cycles

Sample	V_{oc} (V)	J_{sc} (mA/cm^2)	FF (%)	Efficiency (%)
8cycles	0.76	10.4	40	3.5
12 cycles	0.78	11.0	46	4.4
16cycles	0.80	10.5	55	5.0
20 cycles	0.76	9.8	53	4.3

Table 2.I–V parameters of CIS counter electrodes with different SILAR cycles

becomes lower, which can be attributed to higher resistance arising from the thicker $CuInS_2$ film. An efficiency of 6.3% was obtained with the 250°C annealed case of CIS–CuS composite counter electrode while 5% efficiency was obtained with CIS. This is to be compared to 7.5%

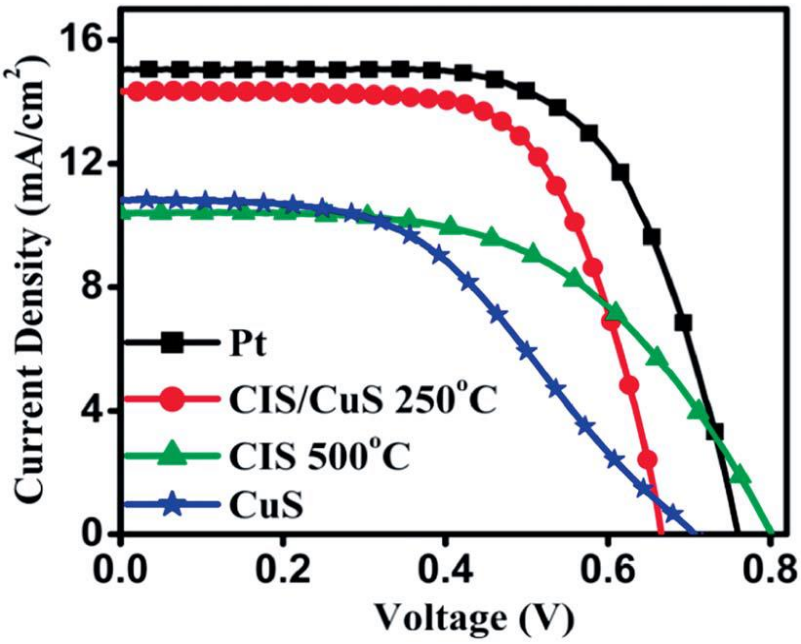

Figure 5.15.I–V data of counter electrodes with 16 SILAR cycles

Name	V_{oc} (V)	J_{sc} (mA/cm^2)	FF (%)	Efficiency (%)
Pt	**0.76**	**15.04**	**65.7**	**7.5**
CIS/CuS 250°C	**0.67**	**14.4**	**66.0**	**6.3**
CIS 500°C	**0.8**	**10.5**	**55.0**	**5.0**
CuS	**0.71**	**10.8**	**46.2**	**3.5**

Table 3.I–V parameters of all counter electrodes with 16SILAR cycles

efficiency obtained with platinum counter electrode. To verify the effect of CuS as counter electrode, 16 SILAR cycles of CuS were deposited on TiO_2 coated FTO and this electrode was also tested as counter electrode in DSSC. This CuS counter electrode gave an efficiency of 3.5%

with low current density, open circuit voltage and fill factor as compared to its composite with CIS. Higher current density obtained in the composite case is due to its superior catalytic activity as also seen in the cyclic voltammetry analysis. The interconnected nanosheets morphology with CuS on top of it gives good accessibility to the electrolyte with large number of catalytically active sites. The fill factor of this CIS– CuS composite is slightly more than that of Pt which proves that the adhesion (electronic anchoring) and conductivity of this composite is optimal and provides good contact of electrolyte. The only reason for somewhat lower efficiency in the case of composite is its low current density which can be attributed to its relatively weaker catalytic properties as compared to Pt. In the case of pristine CIS the cause for low efficiency may be due to fusion of the CIS nanosheets thus lowering the electrolyte accessible area and thereby the catalytic effectiveness. The low efficiency in case of only CuS counter electrode is of course its poor catalytic activity. Thus the nanocomposite electrode comprising of CIS nanosheets incorporated with CuS renders a synergistic effect as compared with either a pristine $CuInS_2$ or CuS electrode. All these results confirm that this nanocomposite can greatly improve the performance of CE.

5.4.8. Stability data

The stability of solar cells with such CIS–CuS based counter electrodes is a concern. As shown in **Figure 5.16.** and **Table 4**, the cell stability is clearly not impressive in this case. However, it was seen to improve with a thin passivation layer of ZnS, also grown by SILAR method. In order to protect the counter electrodes from corrosion of iodine a surface passivation layer of ZnS (0.2M) was deposited on the CIS/CuS (250°C annealed) counter electrode (the best performer) by SILAR method. It can be seen that the stability of the ZnS coated electrode is better than

the one without ZnS. Inset shows the I-V data which reflects the effect of ZnS coating on the device performance. The ZnS coated counter electrode device shows slightly lower efficiency but enhanced stability. More work on using ALD grown passivation layers which can lead to uniform conformal coatings is needed to push the stability further.

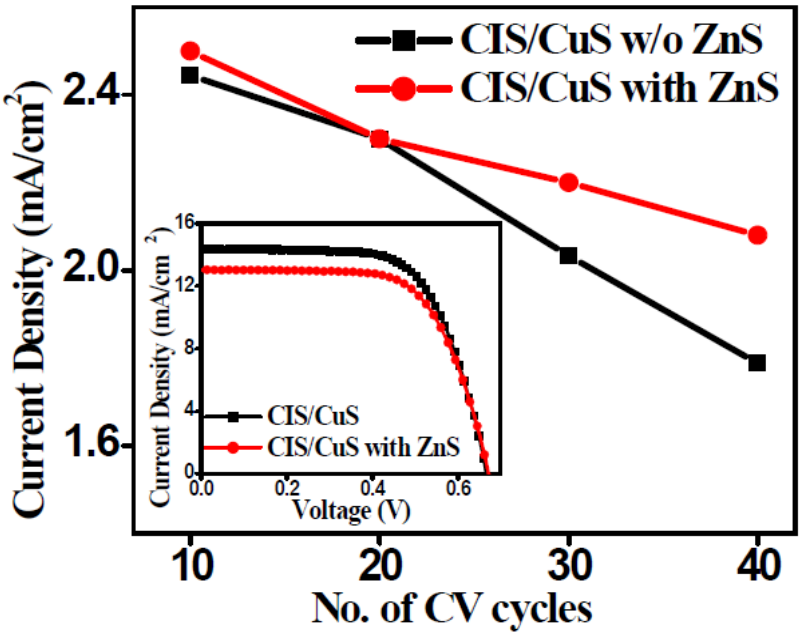

Figure 5.16. Stability data with I-V data as inset of CIS/CuS counter electrode with and without ZnS layer

Name	V_{oc} (V)	J_{sc} (mA/cm²)	FF %	η %
CIS/CuS	0.67	14.4	66.3	6.3
CIS/CuS with ZnS	0.67	13.0	66.4	5.8

Table 4.I–V parameters of counter electrodes with with and without ZnS layer

5.4.9. Electrochemical impedance analysis

In order to further elucidate catalytic properties of counter electrodes, electrochemical impedance spectroscopy (EIS) analysis was carried out with symmetric cells fabricated with two identical

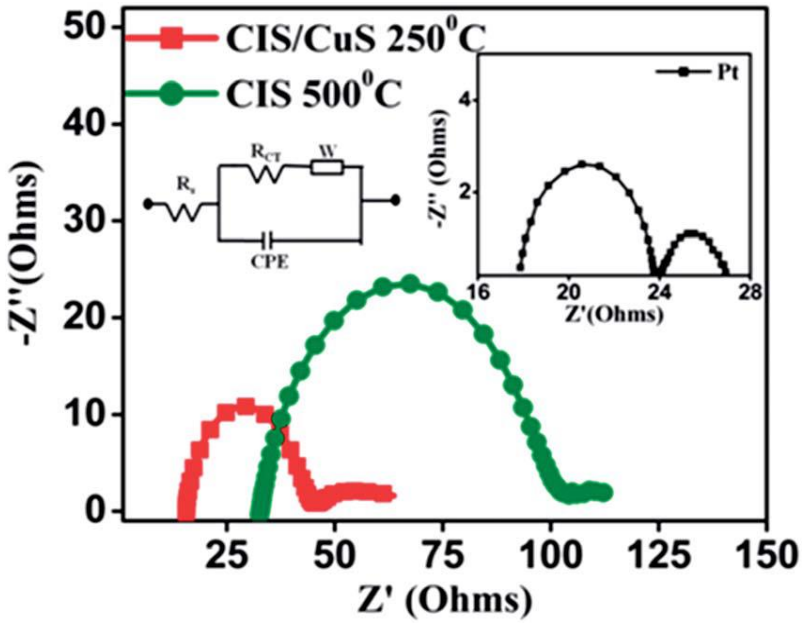

Figure5.17. Nyquist plot of counter electrodes with 16 SILAR cycles

electrodes. In Nyquist plots, the high frequency intercept on the real axis (Z' axis) represents the series resistance R_s while the semicircle region in the high-frequency range is mainly determined by both the charge-transfer resistance R_{ct} and the in parallel capacitance C at the electrolyte-counter electrode interface. **Figure 5.17.** shows the Nyquist plot for pristine CIS, CIS–CuS composite along with the data for Pt counter electrode (inset). The R_{ct} which determines the catalytic activity of the counter electrode is lowest for Pt as seen in the inset. This R_{ct} value is around 29.4 ohms for CIS–CuS composite electrode and 69.2 ohms for pristine CIS counter electrode. R_{ct} is inversely proportional to the catalytic activity of the electrode, thus the CIS–CuS

composite electrode is better for catalyzing the I^-/I_3^- redox shuttle. This effect is well reflected in the efficiency data as seen in **Figure 5.15**. R_s involves series resistance of FTO, adhesion ofcounter electrode material on FTO as well as the contact resistance which is higher in case of CIS counter electrode (32 ohms) as compared to CIS–CuS composite case (~15 ohms) as well as Pt. This is due to better conductivity of CIS–CuS composite electrodes as introduction of CuS decreases the series resistance of thin film. Thus it is clear from impedance data as well that CIS– CuS composite is better counter electrode for DSSC.

5.4.10. Tafel Polarization Curve

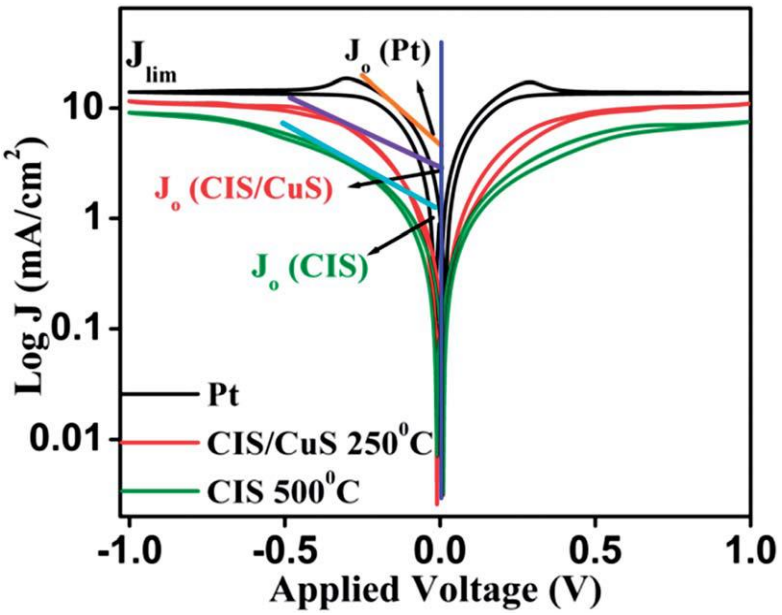

Figure5.18. Tafel curve for Pt, CIS–CuS and CIS counter electrodes

Another technique to analyze the catalytic properties of the counter electrodesis by measurement of Tafel polarization curve. **Figure 5.18** shows the Tafel plot for Pt, CIS–CuS composite and pristine CIS. These measurements were also carried out in a symmetric cell assembly at a scan

rate of 50 mV s^{-1}. The Tafel curve is usually divided into three regions the lower potential zone is called the polarization zone, the middle region with steep slope is the Tafel zone which determines the catalytic activity of the electrode, and the third zone is the diffusion zone which determines the diffusion of ions in the electrode. In the Tafel zone the intersection of the tangent to the cathodic branch with the equilibrium (zero) potential ordinate is J_o, which is the exchange current density.The comparison indicates that the CIS–CuS is more effective in catalyzing the reduction of I_3^- than CIS. J_o is inversely proportional to R_{ct} from the equation:

$$J_o = RT/nFRct,$$

where R is constant, T is temperature, n is the number of electrons involved in reaction, and R_{ct} is the charge transfer resistance. A higher J_o for Pt and CIS–CuS counter electrodes implies a lower value of R_{ct} in the impedance measurement. Another parameter to be extracted from Tafel plot is the limiting current density J_{lim} which describes the diffusion of I_3^- ions in the counter electrode. From the graph it is clear that the diffusion of I_3^-ions in the CIS–CuS composite is higher than that of pristine CIS.

5.4.11. Diffusion Co-efficient Calaculation

To further analyze the diffusion of I_3^- ions in various counter electrodes Randles–Sevcik equation was used.[25] Here the anodic peak current values for CIS, CIS–CuS composite and only CuS were recorded at different scan rates to calculate the diffusion coefficients of I_3^- in these electrodes. **Figure 5.19** shows a linear relationship of anodic peak current density with the square root of scan rate for the cases of interest. These data show that the redox reaction is largely dependent on the diffusion of ions in counter electrode. The diffusion coefficient is

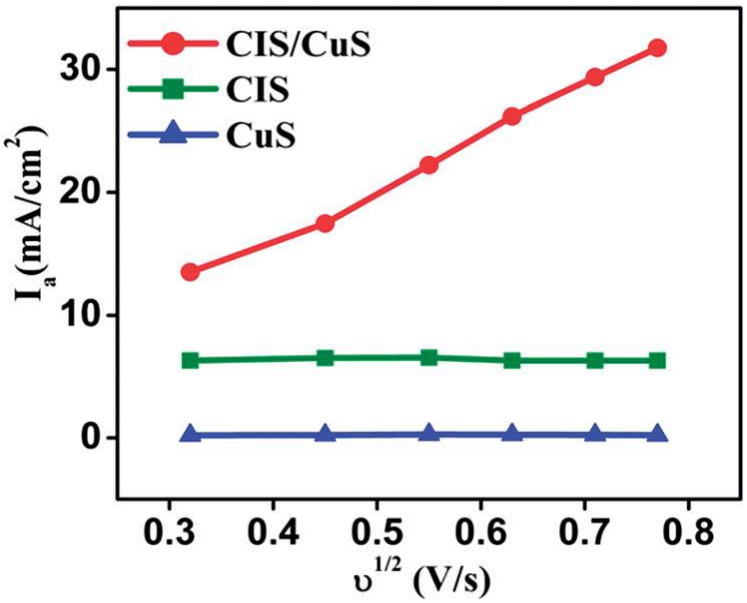

Figure5.19. Plot of anodic peak current versus square root of scan rate.

directly proportional to the limiting current density as seen from the equation:

$$I_p = KnFAC \times (nF/RT)n^{1/2}D_o^{1/2}$$

where K is the constant (2.69×10^5); A is the area of the electrode; n = 2, the number of electrons contributing the charge transfer; F is Faraday's constant; C* is the bulk concentration of tri-iodide species. The calculated diffusion coefficients for the three electrodes are CIS (1.14×10^{-7} cm^{-2} s^{-1}), CIS–CuS (1.16×10^{-6} cm^{-2} s^{-1}) and only CuS (1.93×10^{-10} cm^{-2} s^{-1}). This clearly proves that the diffusivity of ions in the CIS–CuS electrode is better as compared to CIS and only CuS. This can be attributed to increased internal porosity due to some CuS segregating on the top surface of the CIS nanosheet film as seen in FESEM images. This leads to an increased contact between the counter electrode material and the electrolyte.

5.5 Conclusion

We have synthesized single phase $CuInS_2$ (CIS) nanosheets on TiO_2 coated FTO by Successive Ionic Layer Adsorption Reaction (SILAR) followed by annealing at 500°C. Annealing at a lower temperature of 250°C yields a morphology comprising of CuS nanoparticles on CIS nanosheets. When examined as counter electrode for dye sensitized solar cell, the CIS–CuS composite isfound to render a synergistic effect on catalytic performance toward the reduction of tri-iodide, yielding a power conversion efficiency of 6.3% as compared to pristine CIS (5%) or CuS (3.5 %). In addition to various physical property characterizations, the possible reasons behind the higher performance of the nano-composite are elucidated by employing cyclic voltammetry (CV) measurements and electrochemical impedance spectroscopy (EIS).

5.6. References

1) B. O'Regan and M. Gr¨atzel, *Nature*, **1991**, 353, 737–740.

2) C. Wang, F. Meng, M. Wu, X. Lin, T. Wang, J. Qiu and T. Ma, *Phys. Chem. Chem. Phys.*, **2013**, 15, 14182–14187.

3) R. Gokhale, S. Agarkar, J. Debgupta, D. Shinde, B. Lefez, A. Banerjee, J. Jog, M. More, B. Hannoyerc and S. Ogale, *Nanoscale*, **2012**, 4, 6730–6734.

4) L. Bay, K. West, B. Winther-Jensen and T. Jacobsen, *Sol. Energy Mater. Sol. Cells*, **2006**, 90, 341–351.

5) H. Xu, X. Zhang, C. Zhang, Z. Liu, X. Zhou, S. Pang, X. Chen, S. Dong, L. Zhang, P. Han, X. Wang and G. Cui, *ACS Appl.Mater. Interfaces*, **2012**, 4, 1087–1092.

6) G. R. Li, J. Song, G. L. Pan and X. P. Gao, *Energy Environ. Sci.*, **2011**, 4, 1680–1683.

7) H. C. Sun, D. Qin, S. Q. Huang, X. Z. Guo, D. M. Li, Y. H. Luo and Q. B. Meng, *Energy Environ. Sci.*, **2011**, 4, 2630–2637.

8) X. Chen, Y. Hou, B. Zhang, X. Yang and H. Yang, *Chem. Commun.*, **2013**, 49, 5793–5795.

9) J. Yang, C. Bao, J. Zhang, T. Yu, H. Huang, Y. Wei, H. Gao, G. Fu, J. Liuac and Z. Zouab, *Chem. Commun.*, **2013**, 49,2028–2030.

10) Y. Liu, Y. Xie, H. Cui, W. Zhao, C. Yang, Y. Wang, F. Huangand N. Daic, *Phys. Chem. Chem. Phys.*, **2013**, 15, 4496–4499.

11) Z. Zhang, X. Zhang, H. Xu, Z. Liu, S. Pang, X. Zhou, S. Dong, X. Chen and G. Cui, *ACS Appl. Mater. Interfaces*, **2012**, 4, 6242–6246.

12) M. Liu, G. Li and X. Chen, *ACS Appl. Mater. Interfaces*, **2014**, 6, 2604–2610.

13) J. Wu, W. Jiang and W. Liao, *Chem. Commun.*, **2010**, 46, 5885–5887.

14) J. Alvarez-Garcia, B. Barcones, A. P´erez-Rodr´ıguez, A. Romano Rodr´ıguez, J. Morante, A. Janotti, S. Wei and R. Scheer, *Phys. Rev. B: Condens. Matter Mater. Phys*., **2005**, 71, 054303, 9pages.

15) D. Lee and J. Kim, *Thin Solid Films*, **2010**, 518, 6537–6541.

16) E. Rudigier, B. Barcones, I. Luck, J. T. Colin, A. P´erez- Rodr´ıguez and R. Scheer, *J. Appl. Phys.*, **2004**, 95, 5153–5158.

17) M. Ishii, K. Shibata and H. Nozaki, *J. Solid State Chem*., **1993**,105, 504–511.

18) H. Matte, A. Gomathi, A. Manna, D. Late, R. Datta, S. Pati and C. Rao, *Angew. Chem., Int. Ed.*, **2010**, 49, 4059–4062.

19) M. Trushin, T. Arguirov, M. Kittler, W. Seifert, A. Klossek, T. Bernhard, W. Gerlach-Blumenthal, A. Tober and M. Schwabe, *Phys. Status Solidi A,* **2013**, 210, 222–225.

20) H. Azimi, T. Heum¨uller, A. Gerl, G. Matt, P. Kubis, M. Distaso, R. Ahmad, T. Akdas, M. Richter, W. Peukert and C. Brabec, *Adv. Energy Mater.*, **2013**, 3, 1589–1596.

21) S. Peng, Y. Wu, P. Zhu, V. Thavasi, S. Ramakrishna, S. Mhaisalkar, *J. Mater. Chem.*, **2011**, 21, 15718-15726.

22) V. Drift, "Evolutionary Selection,A Principle Governing Growth Orientation in Vapour-Deposited Layers". *Philips Res. Rep.***1967**, 22, 267-288.

23) S. Peng, P. Zhu, V. Thavasi, S. Mhaisalkar , S. Ramakrishna, *Nanoscale* ,2011, **3**, 2602-2608.

24) R. Crompton and C. Banks, Understanding Voltammetry, World Scientific Publishing Co. Pte. Ltd, Singapore,2007.

25) P. Sudhagar, S. Nagarajan, Y. Lee, D. Song, T. Son, W. Cho, M. Heo, K. Lee, J. Won and Y. Kang, ACS Appl. Mater. Interfaces, 2011, 3, 1838–1843.

Chapter 6

Colloidal $CuInS_2$/CdS sensitizer for Quantum dot sensitized solar Cell

In this chapter, we report ternary chalcogenide Colloidal Quantum Dots (CQD) of $CuInS_2$ (CIS) as a promising sensitizer for Quantum Dot Sensitized Solar Cell (QDSSC). Thioglycollic acid assisted aqueous based colloidal solution of CIS QDs is prepared by a simple solution process. To improve stability of the colloidal solution and interfaces involved in QDSSC, a thin passivation layer of CdS is introduced *in situ*. This increased the stability of solution up to two months and showed five times enhancement in solar power conversion efficiency due to increased V_{oc} and J_{sc} of the device. The passivated CdS layer also acted as a buffer layer for appropriate tuning of band alignment between CIS and TiO_2. In another case, additional CdS coat is formed by Successive Ionic Layer Adsorption Reaction (SILAR) method. This hybrid sensitized photoelectrode has given an overall power conversion efficiency of 3% in QDSSC as a result of improved light harvesting. Thus the two systems, CIS and CdS, have a synergistic effect on the solar cell performance.

6.1. Introduction.

Dye Sensitized Solar Cells (DSSC) are proving to be an interesting alternative to the traditional forms of silicon solar cells.[1] The ruthenium based organic dyes used in DSSC plays a crucial role in the device performance, but they degrade with time and are expensive.[2] Hence Quantum Dots have emerged as a promising sensitizer system for the development of the so-called "Quantum Dot Sensitized Solar Cell (QDSSC)". QDs have unique optical and electronic properties such as size dependant tunability of band gap[3, 4], high absorption co-efficient[5], and delivery of hot electrons.[2]Also, they are robust and easy to process. Moreover, multiple exciton generation[6, 7] in QDs have pushed the QDSSCs theoretical power conversion efficiency of devices up to 44% as compared to the current Shockley-Queisser limit of 31% [8, 9]. (Detailed components and working of QDSSCs is given in **Chapter 1** (**section 1.10.**)

Up till now most of the focus in QDSSC has been on metal chalcogenides such as PbSe, CdS, CdSe, CdTe, InP, InAs, PbS.[6, 10-15]All these QDs individually deliver about 1-2% solar efficiency with polysulfide electrolyte, which is very low as compared to the DSSC efficiency. Due to this researchers have been interested in using multilayered cascade structure or co-sensitizers such as CdS/CdSe which could increase the efficiency to 4.15%.[16] In spite of all these appealing photovoltaic performances of QDs they have an major drawback of toxicity. These QD sensitizers have cadmium, lead and arsenic, and these systems disintegrate easily leading to bioaccumulation of heavy metal ions in the biological systems. Owing to this health and environmental risk their large scale commercial production is not feasible. Hence elimination of harzdous precursors and eco-friendly environment is of prime focus. In this direction, recently I-III-VI semiconductor $CuInS_2$ has emerged as alternative to toxic metal ions.

$CuInS_2$ is also of particular interest as it has a direct band gap (1.5eV) with high absorption co-efficient (10^5) in visible to near infra-red region.[17] Several methods are available for synthesis of $CuInS_2$ such as thermal, [18] photochemical, [19] decomposition of single precursor and thermolysis,[20] and hot injection of organometallic precursors[21]. Such methods are straight forward but need expensive starting materials which may be toxic and their synthesis is cumbersome. Also simple one step solution processible solvothermal method [22] is available but it leads to increased particle size of CIS beyond the quantum size effect limit.

Teng et al [23] reported that photoelectrochemical performance of sensitized TiO_2 depends on size of CIS QDs and thickness of the layer with which it is passivated. The present literature indicates that well dispersed QDs of ternary chacogenides is still a challenge. Early attempts to use CIS in liquid based QDSSC delivered only 1% of power conversion efficiency.[24] This is due to the leakage of current and interfacial recombination between TiO_2/QD/electrolyte. To improve this situation the notion of an interface buffer layer was introduced using materials such as Cu_2S and ZnSe which improved the device efficiency to 2.52%.[25] P V Kamat group also used CdS as a buffer layer in electrophoretically deposited CIS based QDSSC and showed a remarkable efficiency of 3.9% due to improved hole scavenging ability.[26] Recently, Teng et al. [27]made a breakthrough in CIS QD-CdS solar cell by achieving an efficiency of 4.2%. However, CIS synthesized by solvothermal method in their work involves three complicated and uneconomical processes like synthesis of QD, ligand exchange, and linker assisted assembling of QD on to TiO_2.

In this work, we report a simple novel aqueous-based synthesis method for colloidal $CuInS_2$ QDs of 3nm size which can be assembled in one step on the TiO_2 surface. To improve the stability of CQDs and the interface between TiO_2/CIS/electrolyte a thin passivation layer of CdS is introduced by $CdCl_2$ treatment during *in situ* growth, where CdS acts as the buffer layer. Incorporation of the buffer layer has tremendous effect on the solar performance as it improves unmatched band alignment and suppresses interfacial recombination. Also it increases the stability of colloidal solution up to 2 months due to passivation of surface states/defects of bare CIS. Furthermore, QDSSc device conversion efficiency is improved to 3% by assembling additional CdS by SILAR method where it acts as a sensitizer. Overall CIS and CdS have synergistic effect on the QDSSC performance.

6.2. Experimental Section

6.2.1. Thioglycolic acid assisted aqueous synthesis of CIS and CIS /CdS

$CuInS_2$ (CIS) QDs were synthesized at room temperature by thioglycolic acid (TGA) assisted aqueous method, which were passivated by CdS. This colloidal solution was stable up to 2 months at room temperature. Briefly, $Cu(CH_3COO)_2.2H_2O$ (0.2mmol) and $InCl_3.4H_2O$ (0.3mmol) were dissolved in N_2 saturated 150ml D.I. water. While stirring TGA 170µl is added drop wise. The pH of the solution is maintained at 4 by addition of 1 mol/L NaOH. After 10 mins Na_2S (0.5mmol) is added swiftly by rapid stirring. The solution is kept stirring for 2hrs during which its colour changes to dark brown. Subsequently, $CdCl_2.2H_2O$ (0.1mmol) is added while rapid stirring and the colour of solution changes to dark red. Here a thin layer of CdS is formed which passivates the surface of CIS and increases its life span even at room temperature.

The solution is evaporated to 30ml in rotary evaporator and used further for sensitization of TiO_2 photoanode.

6.2.2 Fabrication of QDSSC.

Detailed fabrication protocol of QDSSC is given **Chapter 2 (Section I 2.2.)**

a) Ex - situ sensitization of the TiO_2 film: QDs are ex-situ sensitized by immersing TiO_2 film in CIS and CIS/CdS colloidal QD (CQD) solution for 24 hrs. A color change is seen in the TiO_2 film after sensitization as shown in **Figure 6.4.**

b) Sensitization by SILAR method: CQD sensitized TiO_2 film is further sensitized by CdS QDs by Successive Ionic Layer Adsorption Reaction (SILAR). In SILAR, the ionic solution of Cd^{2+} and S^{2-} is prepared by dissolving precursors $Cd(NO_3)_2$(0.1M) and Na_2S (0.1M) in methanol. In the first step, the TiO_2 film is dipped in Cd^{2+} solution for 1 min where cadmium ions get adsorbed in mesoporous TiO_2 film. In the second step, the film is taken out and rinsed with methanol. Subsequently, the film is dipped in S^{2-} solution for 1min where it instantly reacts with Cd^{2+} ions to form *in situ* CdS QDs on TiO_2 film itself. Again it is rinsed with methanol to eliminate un-adhered QDs which forms the fourth step. These four dipping steps form one *SILAR cycle*. Such nine SILAR cycles are repeated to obtain uniform coverage of QDs on TiO_2.After this all the electrodes are given ZnS treatment.

6.3. General Characterization

EDAX is studied using field emission scanning electron microscope (FESEM, FEI Quanta 200 3D). High resolution Transmission electron microscopy (HRTEM, IFEI, Tecnai F30, with 300 KV FEG) is used for imaging QDs. Light absorption properties of QD sensitized electrodes were

measured by diffuse reflectance spectroscopy (DRS Varian, CARY100). Photoluminescence spectra were obtained on Fluoromax-4, Spectroflurometer (HORIBA scientific). The I–V characteristics were measured under irradiation with 100 mW/cm^2 (450 W Xenon lamp, Oriel Instruments) 1 sun AM 1.5 simulated sunlight as solar simulator in the presence of a water filter, using Kiethliey 2400 source employing 0.16cm^2 as active area. The thickness of electrodes was measured by surface profiler from Dektak 150, Veeco make.

6.4. Results and Discussion:

6.4.1. CQD Characterization

Energy Dispersive Absorption X-ray (EDAX) given in **Figure 6.1 a)** confirms the presences of elements Cu, In and S in approximate ratios whereas **b)** confirms the presences of Cu, In and S along with Cd element. Excess sulfur atomic ratio is seen in both the CQDs which are due to sulfur contribution from TGA used during synthesis. Morphology of $CdCl_2$ treated CIS CQDs was confirmed by HRTEM as given in **Figure 6.2**. It indicates the average particle size of around 3-4nm with d-spacing of 0.32nm which corresponds to CIS 112 plane. No CIS/CdS core shell

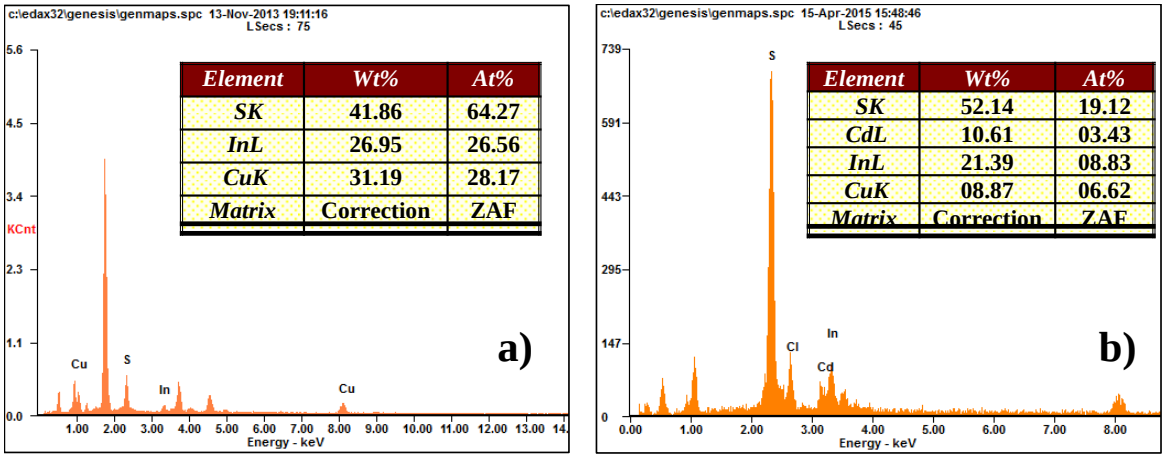

Figure6.1. EDAX of a) $CuInS_2$ CQD b) $CuInS_2$/CdS CQD

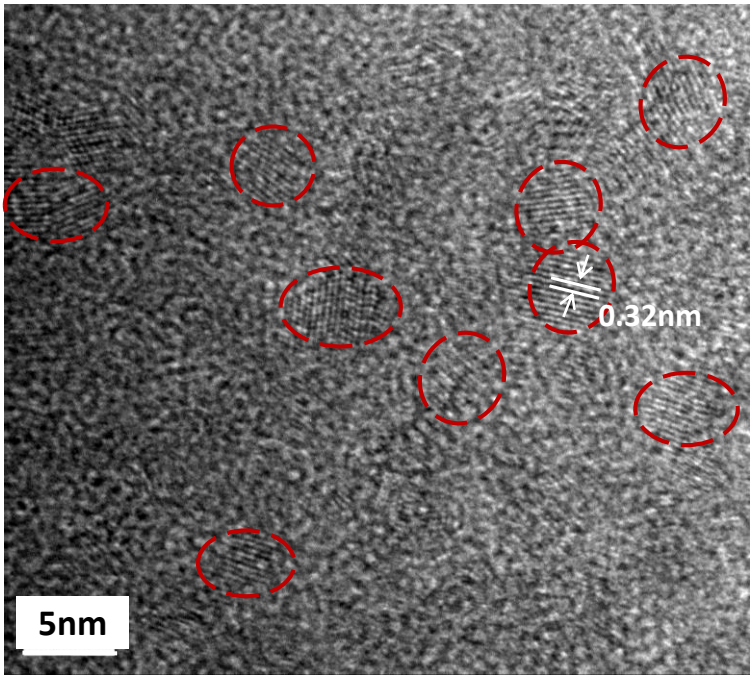

Figure6.2 HRTEM image of CIS/CdS CQD

contrast or lattice constant is seen in HRTEM indicating a passivation layer of CdS on CIS CQDs due to $CdCl_2$ treatment.

6.4.2. Optical Characterization

6.4.2.1. Photoluminescence (PL)

The colours of the CIS and CIS/CdS CQDs solutions are shown in the inset of **Figure 6.3.** Addition of $CdCl_2$ *in situ* during synthesis created a thin passivation layer of CdS over CIS CQDs which increased the PL intensity tremendously as compared to bare CIS, as shown in photoluminescence spectra (**Figure 6.3.).** This is due to the fact that QDs have surface traps and defects which give rise to non-radiative recombination centers, thereby decreasing the PL intensity. Also, defects make the surface of CQD sensitive after air exposure and affect the stability adversely. Hence to increase the stability of QDs, their surface is passivated by any

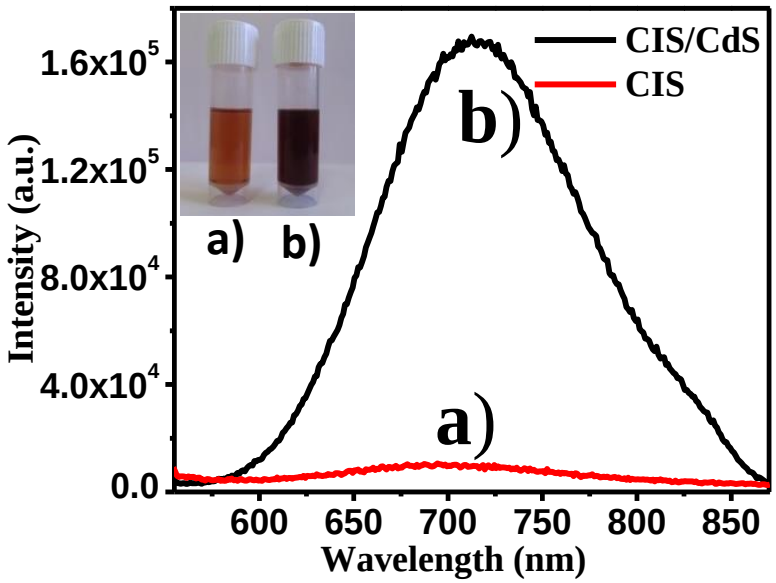

Figure6.3. Photoluminescence of a) CIS and b) CIS/CdS CQD

inorganic shell like CdS.[28] With the CdS passivation layer not only the stability of CIS CQD is increased up to two months compared to bare CIS CQD but also the PL intensity has enhanced greatly due to passivation of surface defects.

Using passivated CIS as the sensitizer in QDSSC inhibits interfacial recombination as the surface defects can act as trap sites for free electrons and decrease their life time. Also this layer acts as the barrier for leakage of current from TiO_2/CQD/electrolyte interface and thereby increases the current density of device.[29]

6.4.2.2. Diffuse Reflectance Spectra (DRS)

Figure 6.4 shows the actual photographs and DRS of the TiO_2 photoanode with different QD sensitizers. Bare TiO_2 shows absorption only in UV region (< 380). When bare TiO_2 is sensitized by single CdS, absorption onset occurs approximately at 500nm whereas with single CIS layer onset occurs at 570nm. But when CIS /CdS CQDs both in colloidal solution are used for sensitization, the photoanode showed increased absorption intensities in visible region as well as

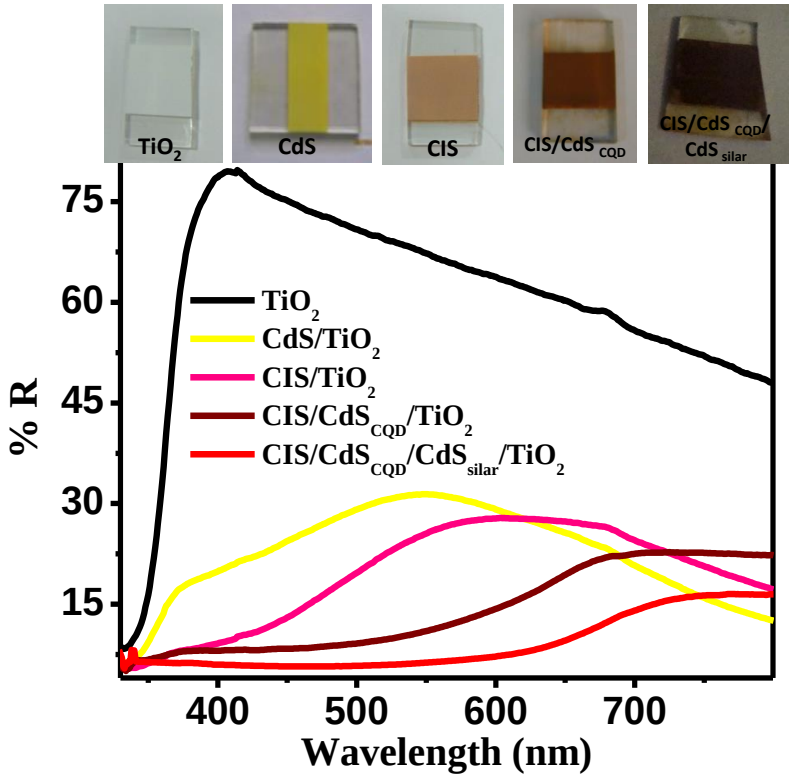

Figure 6.4.DRS of TiO_2 photoanode with different QD sensitizers

a red shift in the absorption onset (620nm) as compared to single ones.

This is due to the narrowing of the effective band gap as the band edges of CIS and CdS are too close that they reduce the confinement effect.[27] Further external addition of CdS QDs by SILAR method extends greatly the absorption onset to 720 nm making them a promising sensitizer in QDSSC.

6.5. Solar Cell Characterization.

The photovoltaic performance of various QD sensitized TiO_2 photoanodes was evaluated from the I-V characteristics as given in **Figure 6.5.** and **table 1**. When TiO_2 is sensitized with CIS QD very low (0.5%) power conversion efficiency is obtained which is ascribed to serious recombination between QD and polysulphide electrolyte.

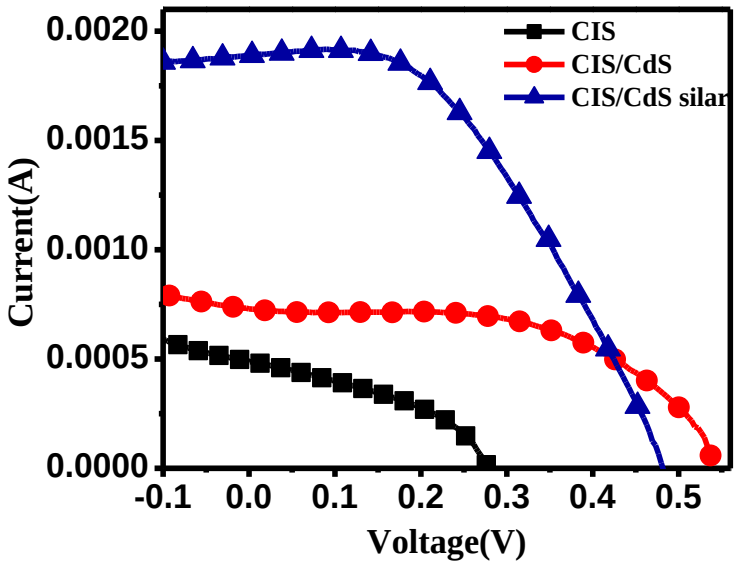

Figure 6.5.IV characteristics of different QD sensitized photoanode

Sample name	V_{oc} (V)	I_{sc} (mA)	J_{sc} (mA/cm^2)	FF %	Efficiency %
CIS CQD	0.29	0.5	4.15	40	0.5
CIS CQD/CdS $_{buffer}$	0.54	0.7	7.23	56	2.4
CIS $_{CQD}$/CdS$_{buffer}$/CdS SILAR	0.48	1.9	12	45	3.0

Table 1.IV parameters of QDSSC device

When CdS shell is introduced on CIS CQD dramatic increment in V_{oc} (from 0.29 V to0.54 V) and J_{sc} (4 to 7.23 mA/cm^2) is observed. In principle, V_{oc} is the potential difference between the Fermi level which is near conduction band (CB) and the redox potential of polysulphide electrolyte. Here CdS shell acts as a buffer layer to improve the mismatch in the band alignment between CIS and TiO_2. When light is incident on CIS it is excited and electron hole pairs are generated. These electron hole pairs are efficiently separated in CB of CdS and VB of CIS

respectively. Thus electrons are effectively transferred to CB of TiO_2 assisting accumulation of electrons. This causes upward shift of TiO_2 CB to negative potentials resulting in higher V_{oc}. Higher V_{oc} is the indication that thin passivation layer of CdS around CIS acts as a buffer layer as shown in **Figure 6.6.** Introduction of CdS shell not only passivates surface defects (which can act as recombination centres) of CIS but also inhibits interfacial recombination, as it acts as barrier between TiO_2/QD/electrolyte interface. Overall, the tuned band alignment, efficient electron transfer to TiO_2 and suppressed interfacial recombination are responsible for such major enhancement of photocurrent.

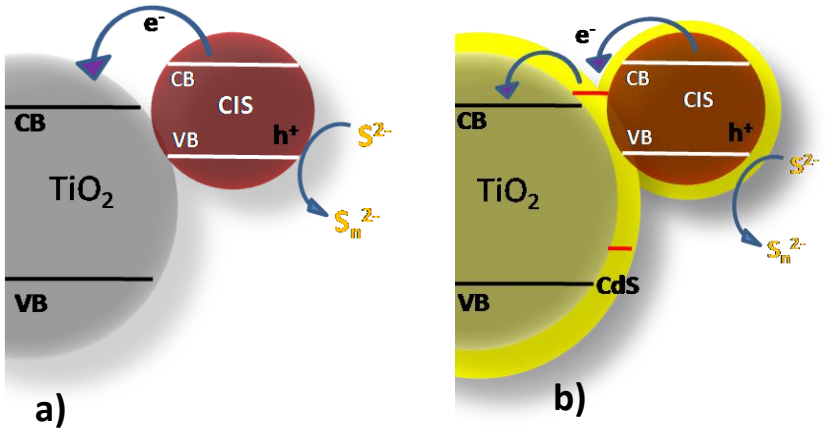

Figure6.6. Schematic diagram of band levels, electron transfer and hole extraction involved in a) TiO_2/CIS without buffer layer of CdS, b) TiO_2/CIS with buffer layer of CdS.

When further CdS is deposited on TiO_2/CIS/CdS buffer electrode by SILAR method no enhancement in V_{oc} is observed but J_{sc} is increased from 7 to12 mA/cm^2 with 3% of power conversion efficiency. This improvement in photocurrent is attributed to extended light harvesting over the 500-800 nm region as seen from the DRS data. Here newly introduced CdS

plays the role of the sensitizer along with CIS. Also it is observed that the hole scavenging ability of CIS is poor in QDSSC but it can be extracted efficiently when the CdS sensitizer level is introduced as shown in **Figure 6.6.b).** Thus, this hybrid sensitizer has synergistic effect on the QDSSC performance.

6.6. Conclusion

Highly dispersed stable water-based colloidal solution of $CuInS_2$ is synthesized by TGA assisted method. To improve the stability of CIS and interfaces involved in QDSSC, CdS passivation layer is introduced around CIS. CdS acts as a buffer layer and enhances the power conversion efficiency of CIS sensitized system from 0.5% to 2.4%. This major increment is due to the passivation of surface defect states of CIS and suppression of interfacial recombination. It also helps in improving the mismatch between the band alignments and hole extraction ability of CIS. Furthermore addition of CdS by SILAR enhances the solar efficiency to 3% due to extended absorption region in the visible. Thus, CIS and CdS have synergetic effect on solar cell performance.

6.7. References:

1) Grätzel, M. *Acc. Chem. Res.,* **2009**, 42, 1788−1798.

2) A.J. Nozik, *Physica,* **2002,** E 14, 115 – 120.

3) P. K. Snatra, P. V. Kamat, *J. Am. Chem. Soc.,* **2012**, 134, 2508−2511.

4) I. Moreels, K. Lambert, D. Smeets, D. De Muynck, T. Nollet, JC. Martins, F. Vanhaecke , A. Vantomme , C. Delerue , G. Allan , Z. Hens, *ACS Nano.,***2009**, 3: 3023-3030.

5) W. Yu, L. H. Qu, W. Z. Guo, X. G Peng, *Chem. Mater.*, **2003**, *15*, 2854–2860.

6) R. D. Schaller and V. I. Klimov, Phys. Rev. Lett., **2004**, 92, 186601, 1-4.

7) A J. Nozik, *Nano Lett.*, **2010**, 10, 2735–2741.

8) W. Shockley, H. J. Queisser, *J. Appl. Phys.* ,**1961**, 32, 510−519.

9) V. I. Klimov, *J. Phys. Chem. B,* **2006,** 110, 16827–16845.

10) Y. L. Lee, C. H. Chang, *J. Power Sources* **2008**, *185*, 584-

11) O. Niitsoo, S. K. Sarkar, C. Pejoux, S. Ru¨hle, D. Cahen, G. Hodes, *J. Photochem. Photobiol., A* **2006**, 181, 306-313.

12) J. H. Bang and P. V. Kama, *ACS Nano ,* **2009,** 3, 1467–1476.

13) A. Zaban, O. I. Micici, B. A. Gregg, A. J. Nozik, *Langmuir*, **1998**, 14, 3153-3156.

14) P Yu, K. Zhu, AG. Norman, S. Ferrere, AJ. Frank, AJ. Nozik, *J Phys Chem B,* **2006**, 110, 25451-25454.

15) R. Plass, S .Pelet, J. Krueger, M. Gratzel, U. Bac,. *J Phys Chem B,* **2002**, 106, 7578 -7580.

16) Y.L. Lee and Y.S. Lo, *Adv. Funct. Mater.*, **2009**, 19, 604–609.

17) G. Xu, S. Ji, C. Miao, G. Liu and C. Ye, *J. Mater. Chem.*, **2012**, 22, 4890–4896.

18) S. L. Castro, S. G. Bailey, R. P. Raffaelle, K. K. Banger and A. F. Hepp, *Chem. Mater.*, **2003**, 15, 3142–3147.

19) J. J. Nairn, P. J. Shapiro, B. Twamley, T. Pounds, R. von Wandruszka, T. R. Fletcher, M. Williams, C. Wang and M. G. Norton, *Nano Lett.,* **2006**, 6, 1218–1223.

20) D. P. Dutta and G. Sharma, *Mater. Lett.* , **2006**, 60, 2395–2398.

21) D. Pan, L. An, Z. Sun, W. Hou, Y. Yang, Z. Yang and Y. Lu, J. Am. *Chem. Soc*., **2008**, 130, 5620–5621.

22) T. L. Li and H. Teng, *J. Mater. Chem.,* **2010**, 20, 3656–3664.

23) T. L. Li, Y. L. Lee and H. S. Teng, *J. Mater. Chem.,* **2011**, 21, 5089-5098.

24) K. T. Kuo, D. M. Liu, S. Y. Chen and C. C. Lin, *J. Mater. Chem*., **2009**, 19, 6780-6788.

25) J.-Y. Chang, Li F. Su, C.H. Li, C.C. Chang and J.M. Lin, *Chem. Commun.,* **2012**, 48, 4848-4850.

26) P. K. Santra, P. V. Nair, K. G. Thomas and P. V. Kamat, *J. Phys. Chem. Lett.* **2013**,4, 722 − 729.

27) T. L. Li, Y. L. Leea and H. Teng, *Energy Environ. Sci.*, **2012**, 5, 5315–5324.

28) H. McDaniel, N. Fuke, J. M. Pietryga, and V. I. Klimov, *J. Phys. Chem. Lett.* **2013**,4, 355−361.

29) J.Y. Chang, J. Mo Lin, Li. F. Su, and C. F. Chang, *ACS Appl. Mater. Interfaces*, **2013**, 5,8740 − 8752.

Chapter 7

$NiS_{1.97}$: A New Efficient Water Oxidation Catalyst for Photoelectrochemical Hydrogen Generation

In the present chapter $NiS_{1.97}$, a sulfur deficient dichalcogenide in nanoscale form is reported as unique and efficient photoelectrochemical (PEC) catalyst for H_2 generation by water splitting. Phase pure $NiS_{1.97}$ nanomaterial is obtained by converting nickel oxide into sulfide by controlled sulfurization method, which is otherwise difficult to establish. The ordered defect states (sulfur vacancies) in this material increase the carrier density and in turn lead to favorable band line-up with respect to redox potential of water, rendering it to be an effective photoelectrochemical catalyst. The material exhibits a remarkable PEC performance with hydrogen evolution equivalent of 1.25 mA/cm^2vs NHE at 0.68V in neutral pH, which is almost 1000 times superior as compared with that of the stoichiometric phase of NiS_2. The latter is well known to be a co-catalyst but not as a primary PEC catalyst.

******The content of this chapter has been published in* ***ACS Appl. Mater. Interfaces,*** **2015,** *7* (36), 20053–20060.

7.1. Introduction:

Hydrogen is recognized to be a highly promising fuel for the future.[1] Existing methods of hydrogen production on the commercial scale are neither economical nor clean, thereby defeating the very purpose for which we seek hydrogen energy technology.[2, 3, 4, 5] There is thus a real and express need for exploring clean and efficient ways of H_2 generation. Towards this end, solar-driven water splitting is a very attractive proposition. During the last decade a large number of material systems, mostly belonging to metal nitride and oxide families, have been studied and demonstrated to render fairly good efficiencies and stability.[1,6] However, in the interest of even higher and commercially viable efficiencies, search is needed to be expanded to other promising classes of materials.

Metal dichalcogenides with pyrite structure (MX_2, where M=Fe, Co, Ni, Mo, X=S, Se) are interesting materials to examine in this context because they are earth abundant, relatively inexpensive and have long term stability in both the acidic and basic media.[7, 8] They also have a unique combination of optical and electronic properties that are suitable for the stated application. Most of dichacogenides absorb the visible solar spectrum with high absorption coefficient and their electronic structure (energy gaps and optical emissions) can be tuned continuously by changing their stoichiometry, dimensionality, and size (quantum size effects). Moreover, their short carrier diffusion times, photochemical stability and electrical conductivity make them potentially appropriate candidates for efficient H_2 generation.[9]

From the metal sulfide family, cobalt sulfide (CoS) has been demonstrated to be an effective electrochemical as well as a photoelectrochemical (PEC) catalyst for H_2 generation.[10] However, from the metal disulfide (dichalcogenide) family, materials such as CoS_2, [11] FeS_2, [12] MoS_2 [13] and

NiS_2[14] have only been studied as electrocatalysts and not as a single light absorber PEC catalyst for water splitting. NiS_2 has proved to be a particularly effective electrocatalyst. It is a Mott-insulator with a band gap 0.3-0.8 eV and its surface is intrinsically metallic.[15] Pang et al.[14] have reported microwave assisted synthesis of NiS_2nanospheres exhibiting enhanced photocatalytic performance for H_2 generation by employing Erythrosin Yellow system as the main photon absorber and triethanolamine as a sacrificial agent. Similarly, Yin et al.[16] have reported noble metal free NiS_2 nanoparticles as a co-catalyst for the g-C_3N_4 system wherein the corresponding loading was shown to improve the photocatalytic H_2 generation rate by inhibiting recombination of the photo-generated charge carriers. In none of these works NiS_2 has been examined or reported as a photoelectrode for PEC water splitting possibly because of the incompatibility of its band structure vis a vis the water redox potentials.

We set out to synthesize this material in the form of a nanosystem so as to examine whether any property features could be tuned to render it effective in the context of the said objective of hydrogen evolution. When we synthesized NiS_2 nanoparticles by the hydrothermal method, metallic nickel Ni (0) contribution was revealed to be present in the surface layer by X-ray Photoelectron Spectroscopy (XPS). This material did not show any notable photoelectrochemical (PEC) water splitting. In order to get rid of the Ni (0) we sulfurized the sample and obtained NiS_2 phase. This sulfurized catalyst showed a slight gain in water splitting current density (about 7 $\mu A/cm^2$) but still not so significant. Interestingly, when we adopted another route to make NiS_2 film by first making NiO film by doctor blading followed by sulfurization, we obtained single phase $NiS_{1.97}$ which showed a dramatic increase in the current density of water splitting (over 1.25 mA/cm^2).

In this chapter we demonstrate for the first time a new facet of the Nickel disulfide system, namely its efficacy as a photo-electro chemical catalyst, but only for its sulfur deficient phase $NiS_{1.97}$. We show that when synthesized under halogen vapor transport method, the sulfur deficient $NiS_{1.97}$ phase can be stabilized which has a favorable flat band potential and band line-up for water splitting as compared to NiS_2. It not only gives highly impressive PEC performance but a very good stability as well. Furthermore, this work highlights the role of surface defect states (non-stoichiometry) in rendering an efficient water splitting performance due to pinning of Fermi level, improved charge transport, and increased visible light absorption.

7.2. Experimental section:

7.2.1.Synthesis of HYD-NiS_2: NiS_2 was synthesized by modified hydrothermal process following previous reports[16] wherein it was used in PEC experiments but only as co-catalyst. Typically 0.1g Nickel acetate was dissolved in 70 ml D.I. water followed by addition of 8g thiourea in 100ml Teflon lined autoclave. Inside it, washed FTO was inserted vertically with conducting side facing towards the wall of autoclave at a slight slanting angle. The autoclave was kept at 140°C for 8hrs. After cooling at room temperature the films were rinsed with water and dried in oven.

7.2.2.Synthesis of HYDS-NiS_2: The surface layer of the above mentioned hydrothermally synthesized HYD-NiS_2 sample was observed to have a strong contribution of Ni (0) state as confirmed from XPS (**Figure 7.7.**) even though XRD showed pure NiS_2 phase. To remove or reduce the density of this Ni (0) surface state the HYD-NiS_2 sample was sulfurized to convert the material fully into sulfide form by heating in a furnace at 500°C for 1/2h at a ramp rate of

3°C/min under the presence of sulfur source by using Ar as a carrier gas.The NiS_2 sample thus obtained after sulfurization is abbreviated as "HYDS-NiS_2"

7.2.3. Synthesis of SUL-$NiS_{1.97}$: Synthesis of SUL-$NiS_{1.97}$ involved three steps as follows:

7.2.3.1.Synthesis of $Ni(OH)_2$: In a typical experiment, 0.01mol of $NiCl_2.6H_2O$ was dissolved in 30mL distilled water under magnetic stirring for 15min to form a homogeneous solution at room temperature, and then 0.03mol of NaOH dissolved in 15ml D.I. water was added drop-wise to the above solution. The as-formed green colored Ni $(OH)_2$ precipitate was washed with 1 litre of D.I. water. To this washed precipitate 0.01mol NaOH dissolved in 30ml D.I. water is added. Thisfinal solution was then transferred into a 50mL Teflon-lined stainless steel autoclave, sealed and maintained at 160°C for 20 hrs, followed by natural cooling to room temperature.

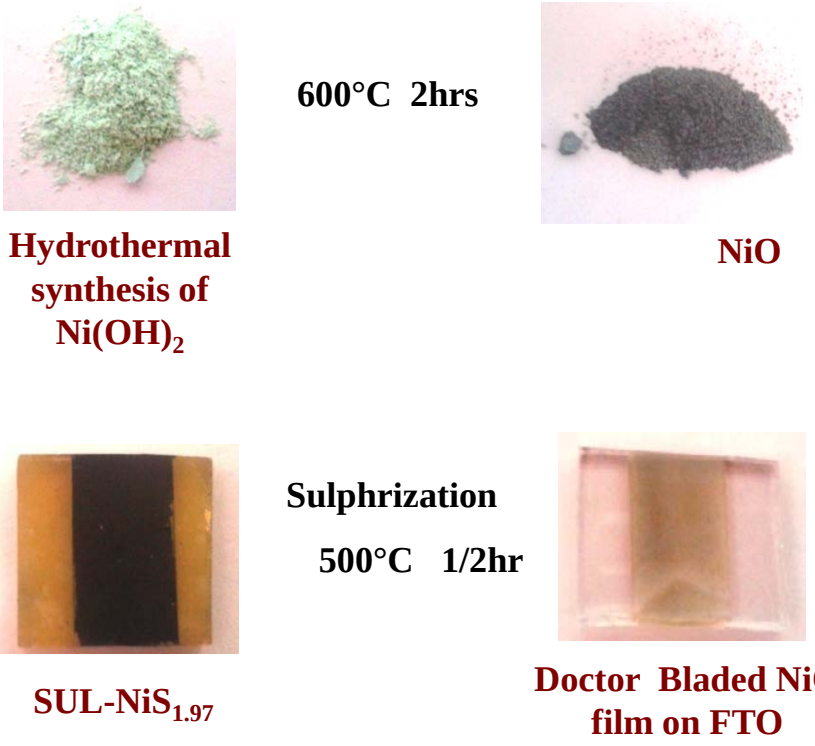

Figure7.1. Synthesis protocol for SUL-$NiS_{1.97}$

The product was collected, washed several times with distilled water and absolute ethanol, and dried at 60°C in air.

7.2.3.2. Synthesis of NiO: The obtained $Ni(OH)_2$ powder was calcined at 600°C for 2hrs at a ramp rate of 10°C /min to obtain grey colored NiO powder, as shown in **Figure 7.1.** From this powder (0.2g) paste was prepared in a mortar by adding Triton X-100 and PEG. This paste was coated on FTO by doctor blading method followed by heating at 450°C for 1hr to obtain a film of thickness around 1-1.5µm.

7.2.3.3. Sulfurization of NiO: NiO was sulfurized by the same parameters as mention earlier and the obtained sample was abbreviated as SUL-$NiS_{1.97}$. The doctor bladed NiO film was kept inside a split-tube furnace connected to a sulfur source, for sulfurization at 500°C for half hr at a ramp rate of 3°C/min. The sulfur source was in the form of thioacetamide which was heated at 200^0C and the vapor was carried into the furnace by using Ar as the carrier gas. The films were then taken out of the furnace when cooled down to room temperature naturally.

7.3. Characterization:

Phase of powders Ni $(OH)_2$ and NiO along with all sulfide electrodes (on FTO) was confirmed by X-ray diffraction (XRD, Philips X' Pert PRO). Light absorption properties of sulfide electrodes were measured by diffuse reflectance spectroscopy (DRS Varian, CARY100). Photoluminescence spectra were obtained on Fluoromax-4, Spectroflurometer (HORIBA scientific). Surface analysis was done by X-ray Photoelectron Spectroscopy (XPS)"Phi 5000 versa probe 2",equipped with a mono-chromatic Al K α (1486.6 eV) X-ray source and a hemispherical analyzer. Morphology of the samples was studied using field emission scanning electron microscope (FESEM, FEI Quanta 200 3D). N_2 gas adsorption−desorption

measurements were performed using Quadrasorb automatic volumetric instrument at 77 K. The thickness of electrodes was measured by surface profiler from Dektak 150, Veeco. Mott−Schottky plots were recorded at a scan rate of 10 mV/s in Na_2SO_4 neutral solution indarkness at a frequency of 10 kHz.

The photoelectrochemical (PEC) measurements of sulfide electrodes were carried out in a three-electrode system using AUTOLAB PGSTAT 30. The photoanode material coated on FTO with 0.25 cm^2 area served as the working electrode, platinum foil as the counter electrode, and Ag/AgCl as the reference electrode in a 0.1 M Na2SO4 electrolyte (pH 7.4) under simulated sunlight illumination at100 mW/cm^2 from a 400 W xenon lamp. The measured potentials vs Ag/AgCl were converted to the standard hydrogen electrode (NHE) scale according to the Nernst equation:

$$E_{NHE} = E_{Ag/AgCl} + 0.1976\ V$$

where, E_{NHE} is the converted potential vs NHE, $E_{Ag/AgCl}$= 0.1976 V at 25°C, and $E_{Ag/AgCl}$ is the experimentally measured potential against the Ag/AgCl reference. To confirm that the photocurrents observed in the PEC cell are really due to PEC water splitting, we constructed a sealed and inert PEC system.

Chronoamperometry measurements (stability profile) were per- formed using a two-electrode method under the bias of 1.1 V up to 60 min. The amounts of O_2 and H_2 generated from the two compartments of the PEC systems were detected and quantified by headspace gas analysis with an Agilent 7890A Series Gas Chromatograph (GC) equipped with a 5°A molecular sieve column. Thermal conductivity detector (TCD) equipped GC was used. The two-electrode PEC system was kept in darkness initially for 30 min (control experiment), and then the photoanode

was exposed to light from a solar simulator (100 mW/cm^2). The O_2 and H_2 were collected from anodic and cathodic compartments of the PEC cell, respectively, through a tightly sealed septum. Readings were recorded through GC at a 10 min interval.

7.4. Results and discussion:

7.4.1. X-ray diffraction:

The hydrothermally synthesized film exhibits 2θ values at 31.8°, 35.6°, 39.2°, 45.6°, and 53.8° as shown in **Figure 7.2.**which match well with JC-PDF 80-0375 data reported for NiS_2.Due to the thin film character of this hydrothermally synthesized sample, the FTO peaks are

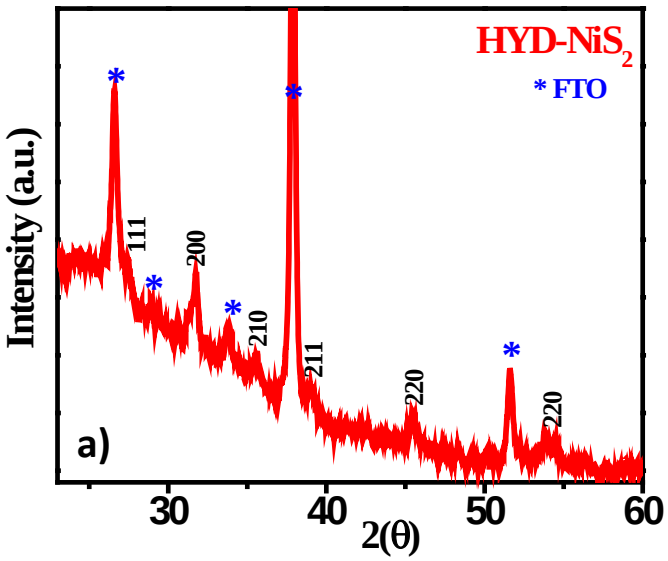

Figure7.2. XRD patterns for HYD-NiS_2

more intense than the NiS_2 peaks.No Ni (0) contribution/peak is seen. However, as seen from the x-ray photoelectron spectroscopy (XPS) data forthe same sample (**Figure 7.7.**) a strong contribution of Ni (0) is noted, which required ex situ sulfurization. When HYD-NiS_2 sample was ex situ sulfurized to convert the Ni (0) surface to sulfide, the XRD of this sample (abbreviated as HYDS-NiS_2) shown in **Figure 7.3.c** is found to be almost similar to the HYD-

NiS_2. The 2(θ) values are 27.5°, 31.7°, 35.5°, 39.0°, 45.5° and 53.8° which match with JC-PDF 80 0375 indicating pure NiS_2 phase. However, as discussed later with the help of XPS result, the ex situ sulfurization reduced the Ni(0) contribution dramatically, as desired. The peaks marked by a * correspond to the FTO substrate. Due to the thin film character of this HYDS-NiS_2 sample, the FTO peaks are more intense than the NiS_2 peaks.

The third sample for the experiment, namely $NiS_{1.97}$ in nanoparticulate form, was obtained by the procedure explained in the experimental section starting from $Ni(OH)_2$ which was converted to NiO followed by sulfurization of the NiO film. XRD pattern shown in **Figure7.3.a** matches

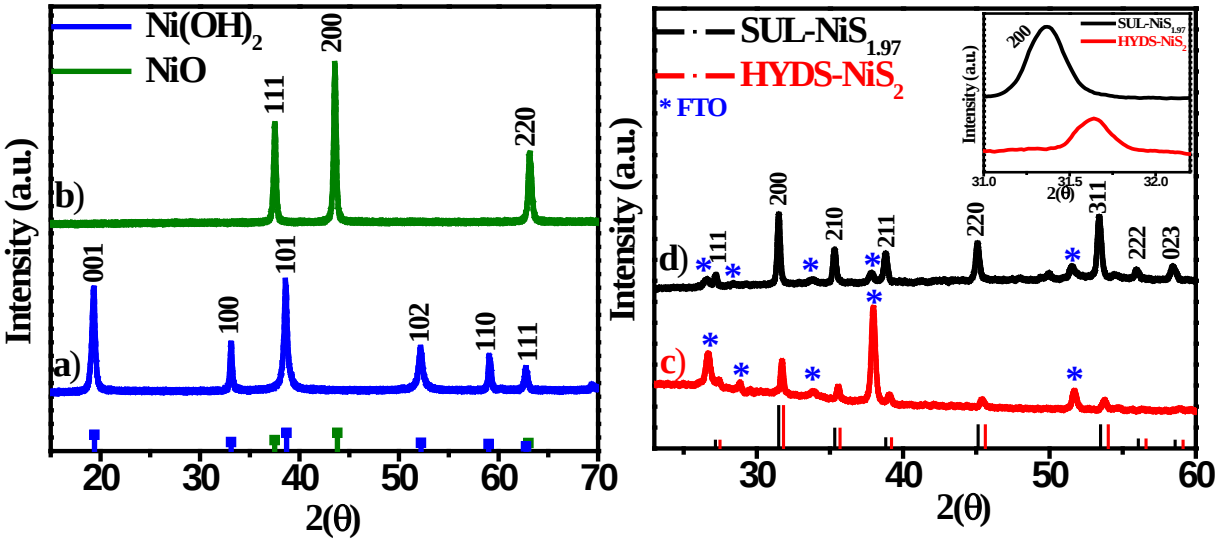

Figure7.3. XRD pattern of (a)Ni $(OH)_2$ (b) NiO (c) HYDS-NiS_2 and (d) SUL-$NiS_{1.97}$.

very well with the JC-PDF data 73-1520 reported for $Ni(OH)_2$ with 2θ values at 19.3°, 32.9°, 38.5°, 52.1°, 58.9° and 62.8°. The XRD pattern of **Figure 7.3.b** is of the powder obtained after calcination of $Ni(OH)_2$ at 600°C and it matches very well with JC-PDF-750269 representing the cubic NiO phase with 2θ values at 37.1°, 43.2° and 62.1°.

Thermal sulfurization of the doctor-bladed NiO film led to an XRD pattern as shown in **Figure7.3d.** The peaks appearing at 2θ values of 31.4°, 35.3°, 38.6°, 45.0° and 53.4° can be uniquely identified with the sulfur deficient $NiS_{1.97}$ phase (JC-PDF 330754 data). It may be noted that the peaks corresponding to the SUL-$NiS_{1.97}$ phase are clearly down shifted (as shown in the inset) respect to the peak positions corresponding to the stoichiometric NiS_2 phase, confirming expanded lattice (larger lattice parameters) due to sulfur deficiency.

7.4.2. Diffuse Reflectance Spectroscopy (DRS):

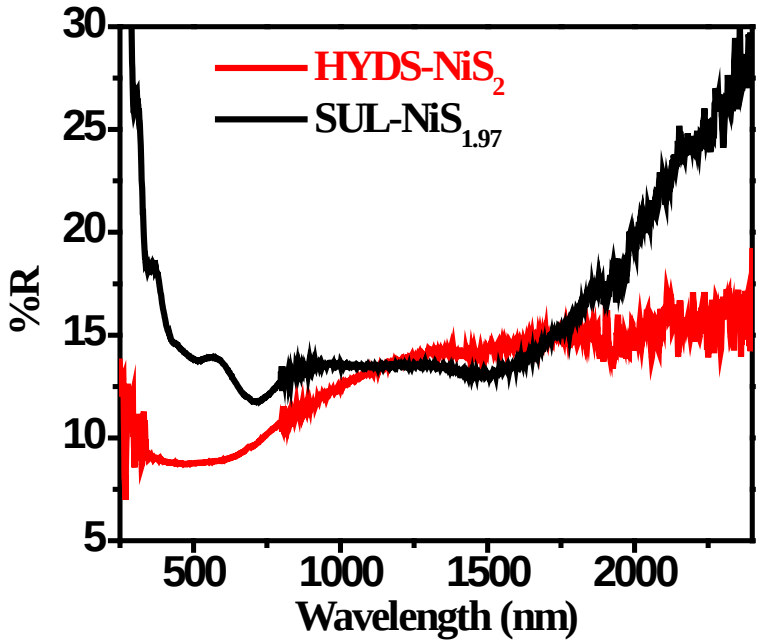

Figure7.4. DRS of SUL-$NiS_{1.97}$ and HYDS-NiS_2

The DRS of SUL-$NiS_{1.97}$ and HYDS-NiS_2 is given in **Figure 7.4.**whichshows absorption over the whole visible and infra-red region. The optical structure of the DRS is clearly more well-defined in the case of SUL-$NiS_{1.97}$.

The band gaps of $NiS_{1.97}$ and HYDS-NiS_2 were estimated using Tauc plots given in **Figure 7.5.**based on the diffuse reflectance spectroscopy (DRS) data. From the Tauc's plots the band

gap of HYDS-NiS_2 is found to be 0.8eV, as expected, and that of SUL-$NiS_{1.97}$ is found to be higher, namely 1.32 eV. The higher band gap of SUL-$NiS_{1.97}$ can be ascribed to changes in the electronic structure of NiS_2 due to large concentration of ordered sulfur vacancies. Notably the corresponding changes in the electronic state density are seen to occur in the energy range of 1.5-2 eV due to defects resulting from non-stoitiometric nature of $NiS_{1.97}$.[17]

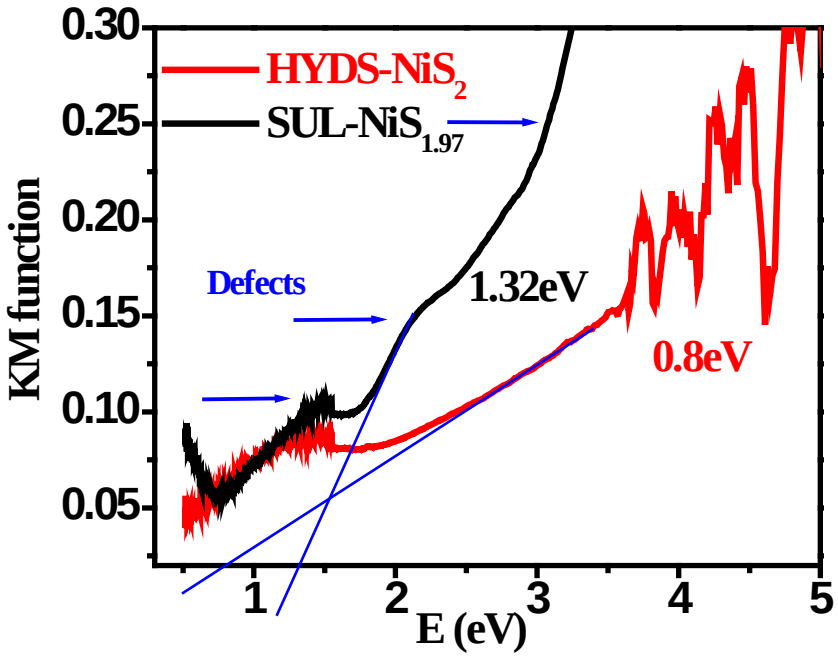

Figure7. 5. Tauc plots for SUL -$NiS_{1.97}$ and HYDS- NiS_2

7.4.3. Photoluminescence spectroscopy (PL):

The presence of defects (S-vacancy states) in the SUL-$NiS_{1.97}$ sample can be further elucidated by room temperature photoluminescence (PL) spectroscopy. When the sample is excited at 380 nm, an emission peak is obtained at 418 nm, as shown in **Figure 7.6.**This peak can be strictly attributed to the sulfur vacancy or interstitial sulfur lattice defects.[18] Another broad peak is located at 428 nm (shown in inset) and the presence of such separated multiple peaks are an

indication of structural defects within the sample due to electronic transitions, as discussed in the literature.[17, 19] These peak positions are seen in both the samples indicating the same surface features but the intensity of PL peak in case of SUL-$NiS_{1.97}$ is much reduced as compared to HYDS-NiS_2 indicating greater concentration of defects. The reduced PL intensity in diachalcogenide family (WS_2 and $MoSe_2$) has been investigated by Piemyoo et al. [20] and Wanget al.[21] respectively. These authors have shown that defects, particularly anion (S) deficiency in

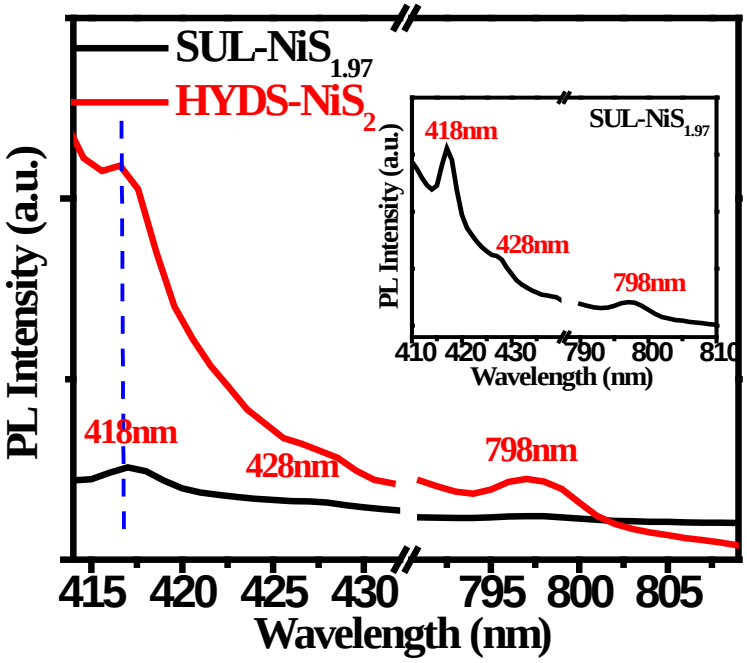

Figure7.6. Photoluminescence (PL) spectra for SUL-$NiS_{1.97}$ and HYDS-NiS_2

the system, is the primary reason for quenching in intrinsic PL because such defects act as non-radiative recombination sites. It is reported by Tongay et al.[22] that the sulfur vacancy creates energy levels near the band edges in the dichacogenide family and such defect-induced levels arising from non-stichiometry in the crystal system can influence the location of the Fermi level and thereby the PEC performance.[23] Also a broad peak of low intensity is seen at 798 nm which can be attributed to intra-band transitions in the $NiS_{1.97}$ band structure.[19]

7.4.4. X-ray photoelectron spectroscopy (XPS):

Although the XRD pattern confirms the presence of pyrite phase, evaluation of surface chemistry (valence states) and the composition are of utmost importance in the context of the present work as these specifically control the phenomenon of photo-catalysis.

Figure7.7.(a) gives the Ni 2p XPS spectra of HYD- NiS_2 sample. Peak at 853.2eV and 870eV is indication of Ni^{2+} state of $2p_{3/2}$ and $2p_{1/2}$ main lines respectively.[24] A huge peak at 852.0eV is present indicating large amount of Ni (0) state at surface.[25] Due to this reason the sample was

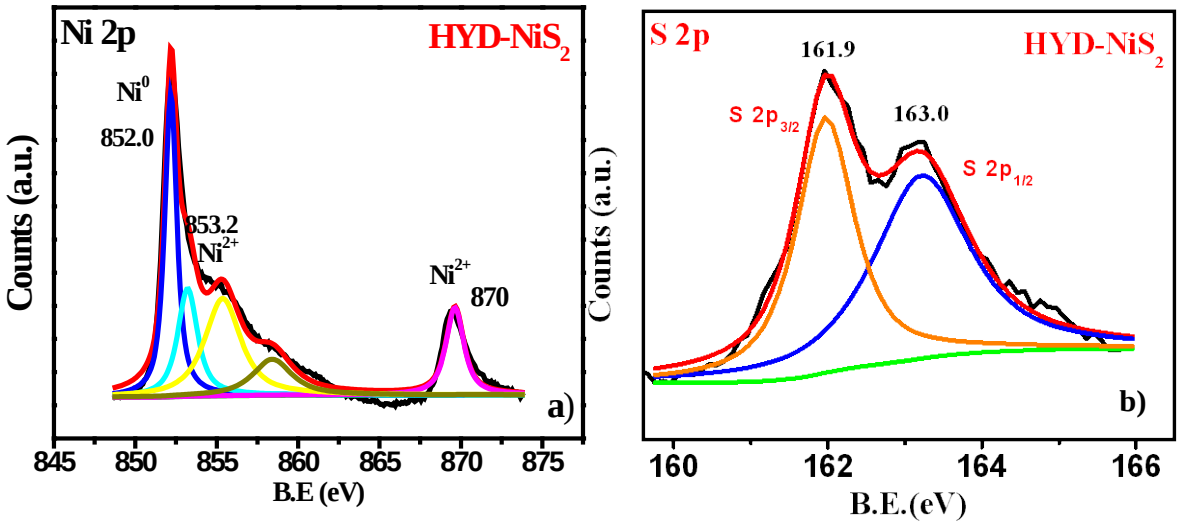

Figure7.7. XPS spectrum of HYD-NiS_2: a) Ni 2p contribution, b) S2p contribution

subjected to thermal sulfurization so as to convert surface Ni (0) to sulfide. Peak at 855.0eV is associated with some organic impurity peak. Two broad peaks at 161.9eV and 163.0eV is attributed to S $2p_{3/2}$ and S $2p_{1/2}$ lines in S2p spectra of HYD-NiS_2 sample given in **Figure7.6.(b)**[24, 25, 26]

Figure 7.8.a shows the Ni 2p XPS spectrum of HYDS-NiS_2 sample. The peaks at 854.1eV and 872eV represent the Ni^{2+} state ($2p_{3/2}$ and $2p_{1/2}$ main lines). The two shake up-satellite peaks are found at 860eV and 879eV, respectively, for each of the emission lines of Ni 2p. [24] One more small peak at 851.7eV is present indicating small amount of Ni (0) state at surface. [25] As stated

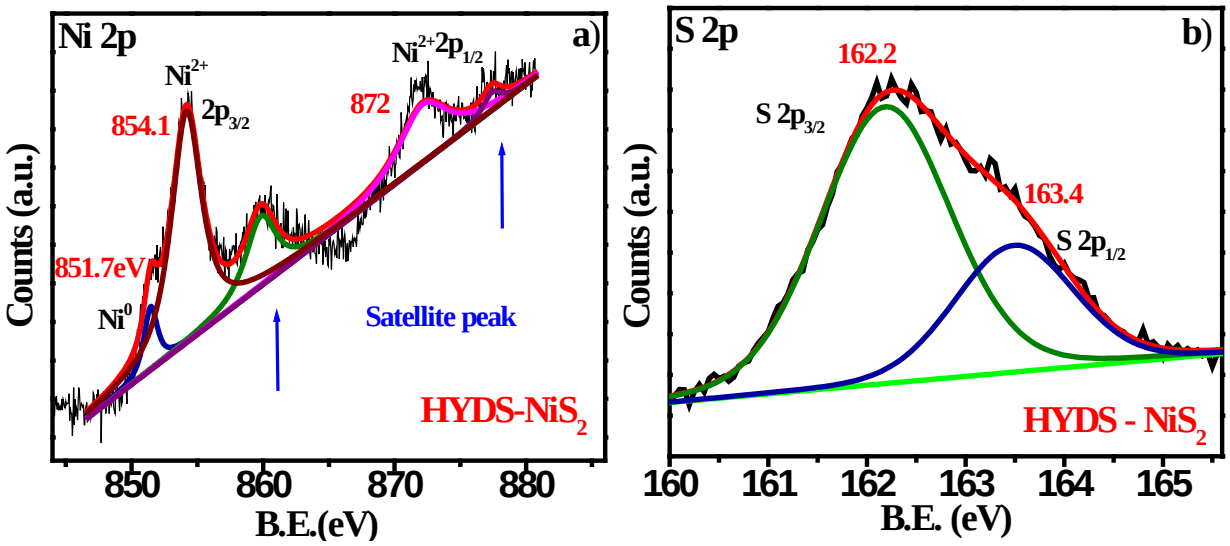

Figure7.8. XPS spectra for HYDS-NiS_2 :(a) Ni 2p contribution, (b) S 2p contribution

earlier, this peak is present as a major contribution in the XPS spectrum of the HYD-NiS_2 sample. After sulfurization this contribution is reduced significantly, as desired. The sulfur contribution to the XPS spectrum of the HYDS-NiS_2 sample is given in **Figure 7.7.b**. The two broad peaks at 162.2eV and 163.4eV are attributed to the S $2p_{3/2}$ and S $2p_{1/2}$ contributions. These indicate the presence of S_2^{2-} type of species (dimer of sulfur) which is bonded to Ni^{2+}. [24, 25, 26]

Figure 7.9.ashows the XPS spectrum for the $NiS_{1.97}$nanoparticulate sample (SUL-$NiS_{1.97}$). The peaks at 853.6 eV and 871.5 eV once again correspond to Ni $2p_{3/2}$ and Ni $2p_{1/2}$ contributions, respectively, representing the Ni^{2+} state. Interestingly, no discernible Ni (0) contribution is seen

in this sample even though there is sulfur deficiency.**Figure 7.9.b** shows the sulfur contribution to the XPS spectrum of the SUL-$NiS_{1.97}$ sample. In this case the two peaks are again observed at 162 and 163 eV, corresponding to $S2p_{3/2}$ and $S2p_{1/2}$ binding energies, but

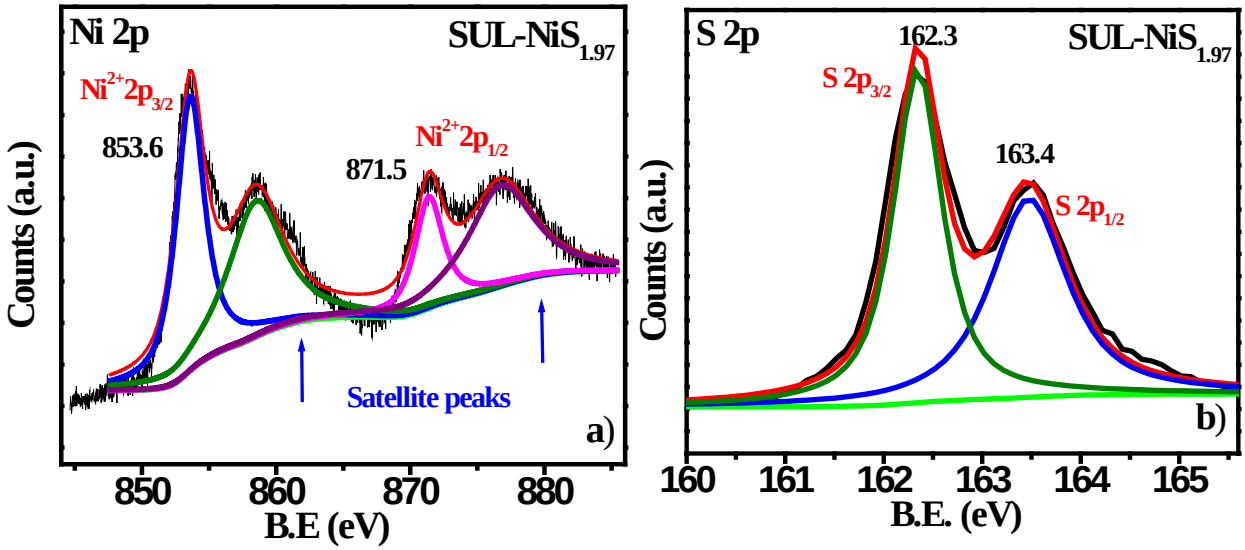

Figure7.9.XPS spectra of SUL-$NiS_{1.97}$:(a) Ni 2p contribution, (b) S 2p contribution

they are significantly sharper than their counterparts in the case of HYDS-NiS_2 sample (**Figure 7.8b**). This indicates that the surface quality of the $NiS_{1.97}$ sample in terms of the uniformity of stoichiometry and possibly the crystalline quality is superior to that of HYDS-NiS_2. The Ni:S atomic ratios calculated from the corrected peaks obtained from the respective XPS spectra also show a significant difference. Here it may be noted that the depth scale of the XPS probe is about 5-10 nm and therefore the ratios in the case of naomaterials are not too precise, but can only give a semi-qualitative picture. The HYDS-NiS_2 sample showed the Ni: S ratio to be 1:2.4 indicating full sulfurization, whereas the SUL-$NiS_{1.97}$ sample showed the Ni : S ratio to be 1:1.7 confirmingsignificant deficiency of sulfur. Such deficiency leads to defect states that can cause

the decrease of PL intensity, as indeed seen in our case (**Figure 7.6.**). It is reported by Wang et al.[27] that such sulfur deficiency (SV_s) on the surface acts as electron donor and Induces localized (defect) states in the band gap. This in turn increases the carrier/donor density of the system which ultimately has a strong effect on pinning of the Fermi level.

7.4.5. Field emission Scanning Electron microscopy (FESEM):

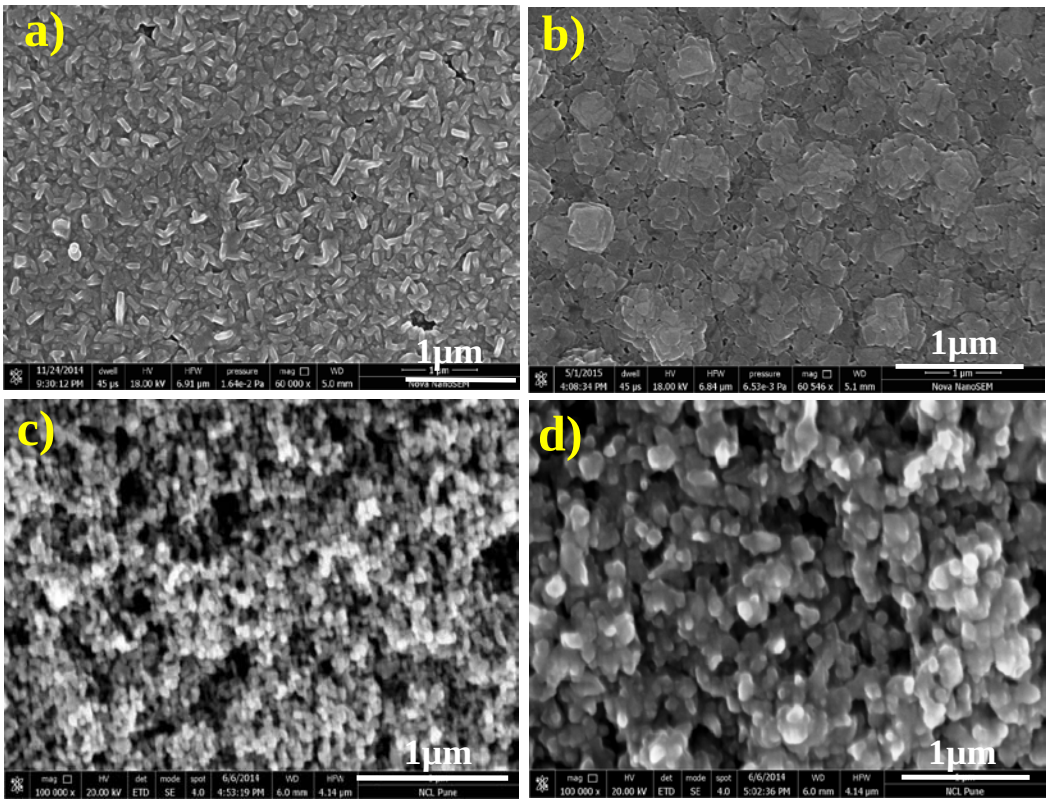

Figure7.10. FESEM images of (a) HYD- NiS_2,(b) HYDS - NiS_2 ,(c) NiO, (d) SUL-$NiS_{1.97}$

In **Figure7.10.**the FESEM images of the photoanodes HYD-NiS_2, HYDS-NiS_2, NiO and SUL-$NiS_{1.97}$ are given. In the image of **Figure 7.10.a** corresponding to the hydrothermally synthesized film a granular morphology is seen which is much more compact. When this sample is thermally sulfurized the obtained HYDS-NiS_2 again shows a compact film of regularly fused nanoparticles

as seen from FESEM image of **Figure 7.10.b.** The FESEM image of NiO film is included specifically to show the morphology evolution upon sulfurization. In **Figure 7.10.c** agglomerates of NiO nanoparticles of the size 50-60 nm are seen. This film when sulfurized gives SUL-$NiS_{1.97}$ with increased grain size of ~120 nm, as shown in **Figure 7.10.d.**The corresponding film is seen to be much more porous which is beneficial for electrolyte contact, as the foremost thumb rule for catalysis is the contact of the photocatalyst with the electrolyte/water.

7.4.6. Photoelectrochemical (PEC) measurement:

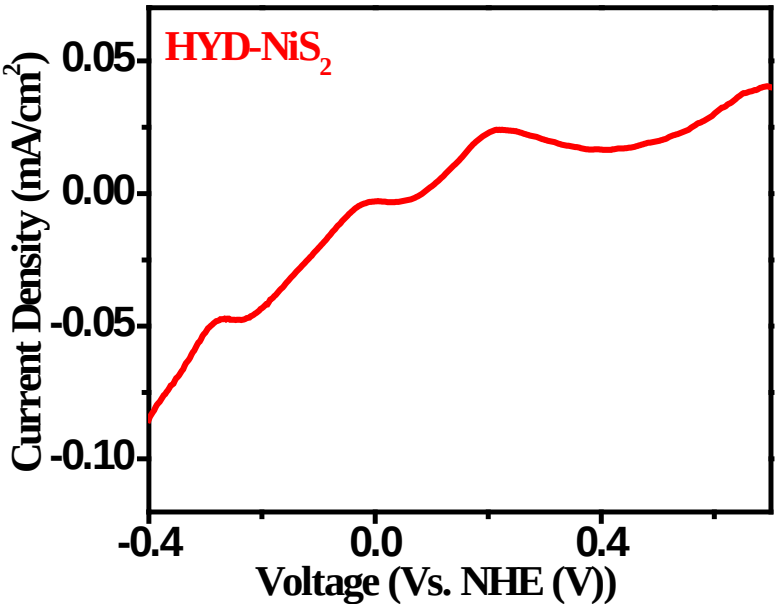

Figure7.11. Photoelectrochemical measurement (J-V scans) of HYD-NiS_2

The data of the PEC measurements (J-V scans) the sample HYD-NiS_2 shows almost no photo effect (**Figure 7.11.**) but the sulfurized HYDS-NiS_2 sample showed a weak performance reflected by a current density of about 7µA/cm^2 (see inset to **Figure 7.12.**). Most interestingly

however, the sulfide photoanode SUL-$NiS_{1.97}$ obtained by sulfurization of doctor bladed NiO film shows a remarkable photocurrent density of about1.25 mA/cm^2 at 0.68 V vs NHE.

Obtaining sulfide based materials through sulfurization process is not so trivial as parameters like inert gas flow, concentration of sulfur source, heating ramp, cooling rate are needed to be controlled as they directly affect the PEC performance. Here we have obtained photoanode with

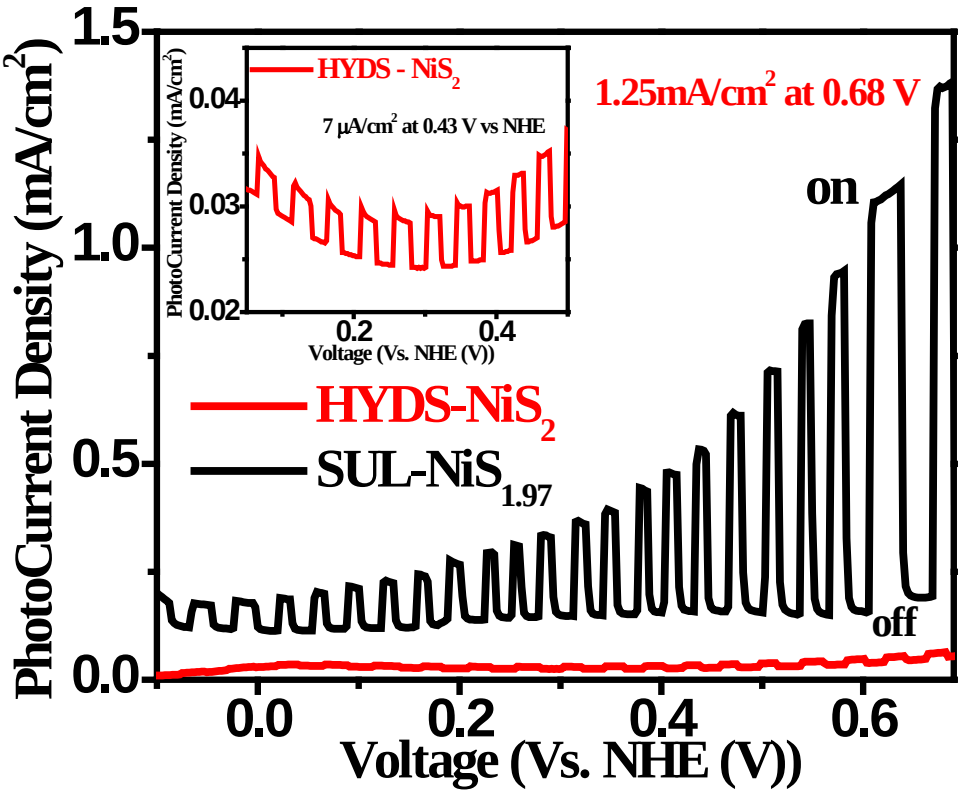

Figure 7.12. Photoelectrochemical measurement (J-V scans) data for SUL- $NiS_{1.97}$ and HYDS-NiS_2 (Inset is enlarged view)

performance from 0.5 to2.0 mA/cm^2. In **Figure 7.13.**PEC performance of champion cell is given where 2mA/cm^2 of photocurrent density is obtained at 0.68V vs NHE.

It is important to emphasize that the SUL-$NiS_{1.97}$ sample shows the stated impressive performance as a main PEC catalyst without any additional co-catalyst in neutral pH with a low applied bias of 0.68V.

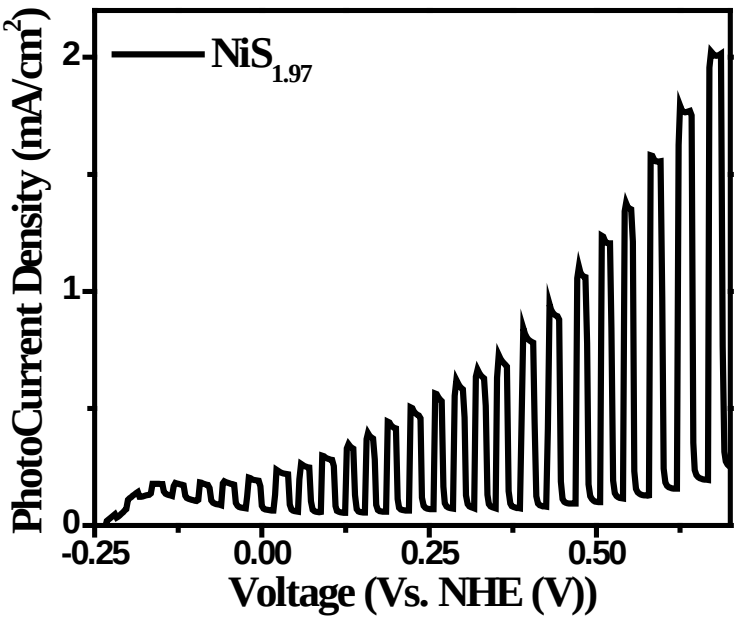

Figure7.13. Photoelectrochemical measurement (J-V scans) of Champion cell

7.4.7. Mott Schottky analysis:

To bring out and elucidate the possible reasons for such high PEC performance and its possible correlation to the defect induced electronic states, Mott Schottky analysis was done. First, the plot given in **Figure 7.14.**shows a positive slope for both the sulfide electrodes indicating their n-type semiconductor character. Second, the Flat band (fb) potential estimated from the x-intercept of the linear portion of the Mott Schottky plots, indicates that the Fb-potential of $NiS_{1.97}$ is -0.33V and that of HYDS-NiS_2 is 0.09V. The Fb-potential of HYD-NiS_2 is 0.29V (**Figure 7.15.**).

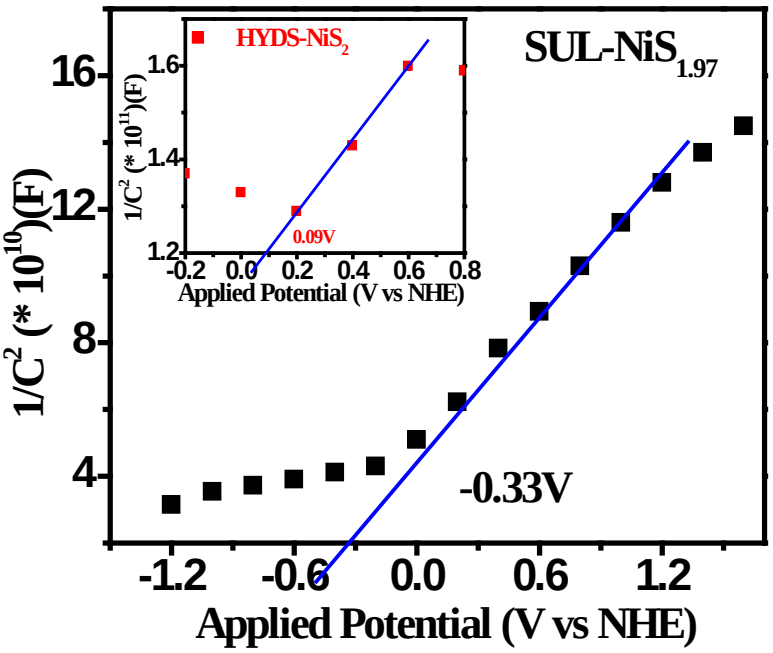

Figure7.14. Mott Schottky plots of SUL-$NiS_{1.97}$ and HYDS-NiS_2 (Inset)

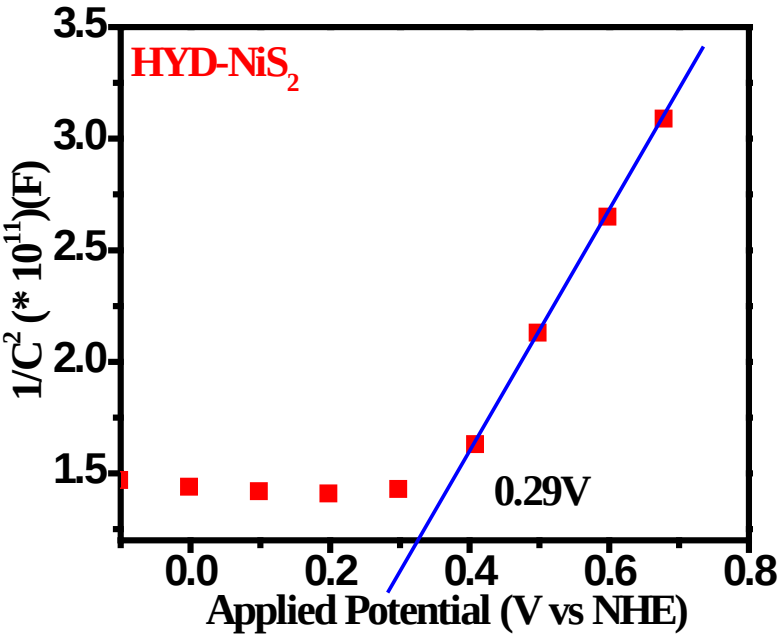

Figure 7.15. Mott Schottky plot of HYD-NiS_2

From the flat band potential and the band gap calculated from the Tauc's plot approximate energy levels were determined which could reveal a clear picture as to why $NiS_{1.97}$ shows two to three orders of magnitude superior photocatalytical activity as a single absorbing anode material as compared to NiS_2. This is clearly because the conduction-band edge of SUL-$NiS_{1.97}$ is just above the hydrogen-evolution potential, and the edge of the valence band lies below the oxygen-.

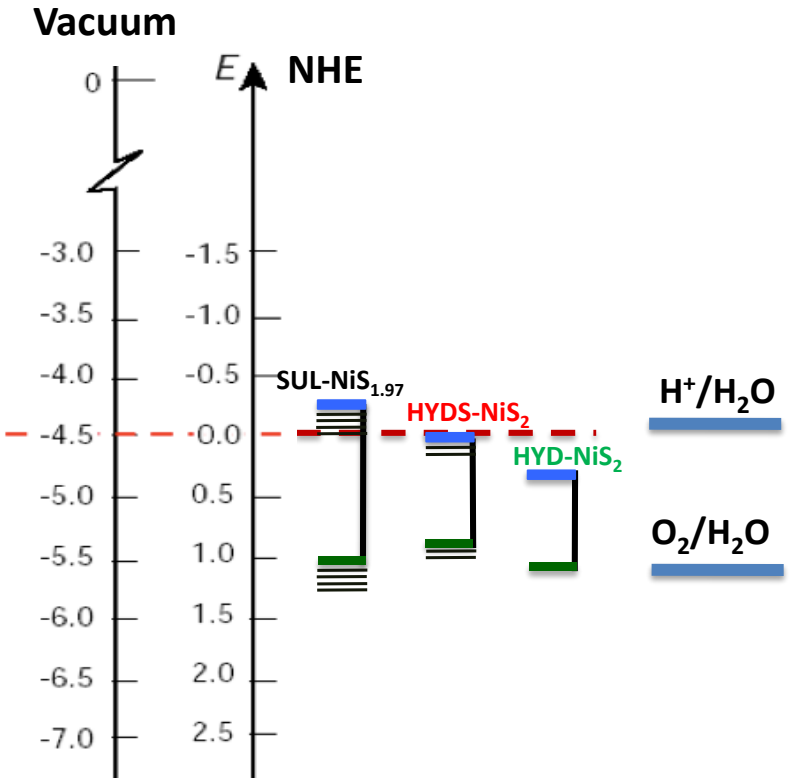

Scheme1. Schematic diagram of Energy levels of photoanodes.

evolution potential of water as shown schematically in **Scheme 1.** This makes the charge transfer reactions for water splitting feasible Also the introduced defect levels below the band edges must be electronically active to perform charge transfer and redox reactions in water. On the other hand the hydrothermally synthesized and sulfurized HYDS-NiS_2 sample and the only hydrothermally synthesized sample do not have such desirable band alignment to facilitate the

water splitting process. The HYDS-NiS_2 sample has some degree of advantage in this respect as compared to the HYD-NiS_2 sample and as such shows a degree of water splitting which is totally absent for the HYD-NiS_2 case. Notably, the hydrothermally synthesized but unsulfurized sample HYD-NiS_2 has much more positive conduction band edge which has established it as an efficient co-catalyst instead of PEC catalyst.

From the Mott-Schottky plots, we calculated the slopes for two samples, which are inversely proportional to the carrier density values. The charge carrier density can be calculated from equation (1) as follows.[28]

$$N_d = (2/e_0 \varepsilon \varepsilon_0)[d(1/C_2)/dV]^{-1} \quad (1)$$

Here N_d is carrier density, C is capacitance (F/cm^2), e_0 was the electron charge, ε is the dielectric constant, and ε_0 is permittivity of vacuum. The dielectric constant of NiS_2 is 6.52.[29]The calculated carrier density value for HYD-NiS_2 is $4.4*10^{17}cm^{-2}$, HYDS-NiS_2 is $2.7*10^{18}cm^{-2}$ and SUL-$NiS_{1.97}$ is $3.6*10^{18}$ cm^{-2}. The SUL-$NiS_{1.97}$ sample clearly has a considerably higher carrier density than the other two NiS_2 samples. These data provides a direct evidence that increased donor density in the SUL-$NiS_{1.97}$ sample is due to S-vacancy which is also consistent with the PL and XPS analyses. This increased donor density causes upward shift of Fermi level making the levels favorable w.r.t. to the redox potential of water as also seen in the case of TiO_2 system.[30] Moreover, this increased donor density also promotes band bending at the surface.[31] This band bending along with the induces defect levels facilitate better charge separation and transport across the electrode/electrolyte interface making $NiS_{1.97}$nanosystem to be an efficient photoelectrochemical catalyst operating at lower bias voltage in neutral pH without need of any co-catalyst.

7.4.8. Stability data and Faradiac Efficiency

Figure 7.16 shows the chronoamperometry data (stability profile) for the SUL-$NiS_{1.97}$ sample which exhibits an almost stable current density of 0.83 mA/cm2 for 60 min when bias of 1.1 V is applied between the working and counter electrode. This stability profile (in terms of current density) was used for theoretical calculation of the expected gas evolution rates. Figure 7.17.compares the theoretically expected and experimental found (by GC analysis) quantities

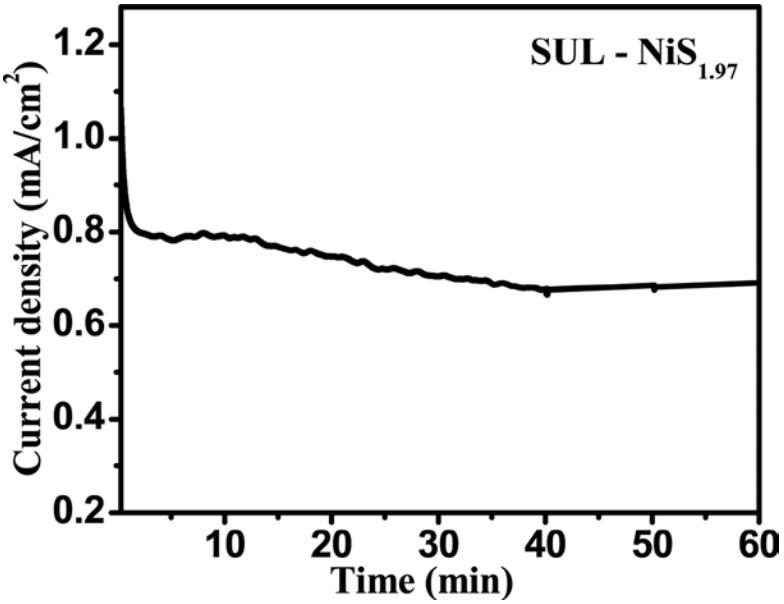

Figure7.16. Stability data of SUL-$NiS_{1.97}$

of hydrogen and oxygen evolved as a function of time. The ratio of the measured and calculated gas evolution rates gives the Faradiac efficiency at 1.1 V. The efficiency is close to about 65% for oxygen, but is relatively lower (about 40−45%) for hydrogen evolution. This suggests some losses by side or back reactions along with thermal losses. This efficiency could be improved by further optimization of the catalyst material, the applied bias and by passivating the catalyst surface to inhibit deleterious (side) reactions.

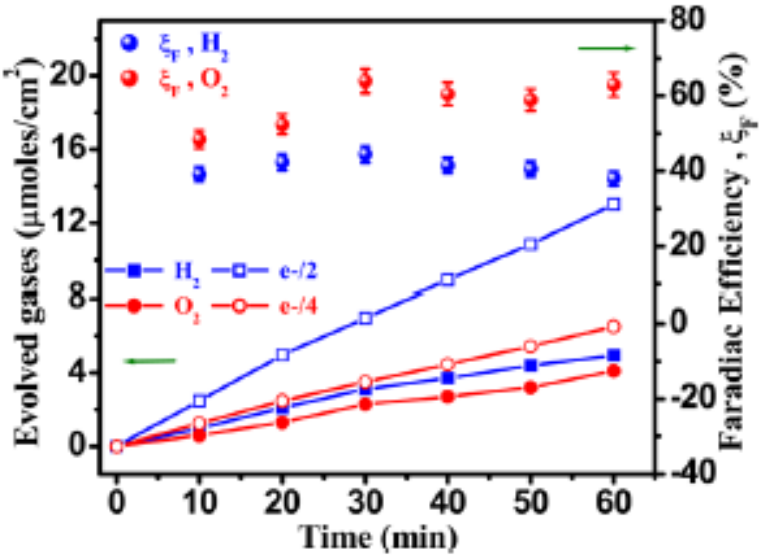

Figure7.17. Theoretical and measured gas production rates of (□) H_2, (○) O_2 and (■) H_2, (●) O_2, respectively, along with (spheres) the Faradiac efficiency for SUL-$NiS_{1.97}$.

7.5. Conclusion:

From dichalcogenide family the sulfur deficient $NiS_{1.97}$ phase is established for the first time as a highly efficient photoelectrochemical (PEC) catalyst for water splitting. This phase is realized following a specific synthetic protocol and thermal sulfurization method. The ordered S-vacancy mediated single phase material renders electronic states which yield a positioning of the Fermi level and the conduction/valence bands vis a vis the water redox levels, which are favorable for water splitting. This leads to a remarkable orders of magnitude superior water splitting performance of $NiS_{1.97}$ over NiS_2, the latter established only as a co-catalyst uptill now. This study brings out a defect engineering strategy for tuning the properties of (di) chalcogenides photoanodes for enhancing the water splitting ability, and in a broader context, for enhancing their applicability to other optoelectronic property domains.

7.6. References:

1) T. Bak, J. Newton, M. Rekas, C.C. Sorrell, *Int. J.Hydrogen Energy.*,**2002,** 27, 991 – 1022.

2) R. M.Navarro, M. A. PeÇa, J. L. G. Fierro, *Chem. Rev.*,**2007**, 107, 3952-3991.

3) Palo, D. R.*Chem. Rev.*,**2007,** 107, 3992−4021.

4) J. R. Rostrup-Nielsen, J. S. Sehested, J. K. Nrskov, *Adv. Catal.*, **2002**, 47, 65- 139.

5) J. O' M. Bockris, *Int. J. Hydrogen Energy*.**2002**, 27,731- 740.

6) R.M. N. Yerga, M. C. A. Galvan, F. Valle, J.A. V. Mano, J. L. G. Fierro, *ChemSusChem.***2009**, 2, 471 – 485.

7) D. Kong, J. J. Cha, H. Wang, H. R. Leec, Cui, Y. *Energy Environ. Sci.*, **2013,** 6, 3553–3558.

8) M. S. Faber, R. Dziedzic, M. A. Lukowski, N. S. Kaiser, Q. Ding, S. Jin,*J. Am. Chem. Soc*.**2014**, 136, 10053−10061.

9) N. Singh, G. Jabbour, U. Schwingenschlog, *Eur. Phys. J. B,* **2012**, 85, 392,1-4pg.

10) Y. Sun, C.Liu, D. C. Grauer, J. Yano, J. R. Long, P. Yang, C. J. Chang, *J. Am. Chem. Soc*.**2013**,135, 17699−17702.

11)M. S.Faber, M. A. Lukowski, Q. Ding, N. S. Kaiser, S. Jin, *J. Phys. Chem. C* **2014**, 118, 21347−21356.

12) P.Du, R. Eisenberg, *Energy Environ. Sci.*, **2012**, 5, 6012–6021.

13) Z. Chen, A. J.Forman, T. F.Jaramillo, *J. Phys. Chem. C*. **2013**, 117, 9713−9722.

14) H. Pang, C. Wei, X.Li, G.Li, Y.Ma, S.Li, J.Chen , J. Zhang, *Sci Rep*, **2014**, 4, 3577 1-8.

15) K. D. M. Rao, T. Bhuvana, B. Radha, N. Kurra, N. S. Vidhyadhiraja, G. U. Kulkarni, *J. Phys. Chem. C*.**2011**, 115, 10462–10467.

16) L.Yin, Y.P.Yuan, S.W.Cao, Z. Zhanga, C. Xue, *RSC Adv*.**2014**, 4, 6127–6132.

17) E. C. Linganiso , S. D.Mhlanga , N. J. Coville , B.W. Mwakikunga, *Journal of Alloys and Compounds*.**2013**, 552, 345–350.

18) Y.Li, H.Wang, H. Zhang, P.Liu, Y. Wang, W.Fang, H. Yang, Y.Lie,H. A Zhao, *Chem. Commun* .**2014,** 50, 5569-5571.

19) R. Akbarzadeh, H. Dehghani, F. Behnoudnia, *Dalton Trans*., **2014**, 43, 16745–16753.

20) N. Peimyoo, J. Shang, C. Cong, X. Shen, X. Wu, K. L. Yeow, T. Yu, *ACS Nano,***2013**, 7, 10985–10994.

21) X. Wang, Y. Gong, G. Shi, W. L. Chow, K. Keyshar, G. Ye, R. Vajtai, J. Lou, Z. Liu, E. Ringe, B. K. Tay, P. M. Ajayan, *ACS Nano,* **2014**, 8, 5125–5131.

22) S. Tongay, J. Suh, C. Ataca, W.Fan, A. Luce, J. S. Kang, J. Liu, C. Ko, R. Raghunathanan, J. Zhou, F. Ogletree, J. Li, J. C.Grossman,J. Wu, *Sci Rep*.**2013,** 3, 2657, 1-4.

23) Y. Goswami, Advances in Solar Energy", Vol 17,American Solar Energy Society, Inc., Boulder, CO, London, **2007**, page 179.

24) S.L. Yang, H. B. Yao, M. R. Gao, S. H. Yu, *Cryst Eng Comm*, **2009**, 11, 1383–1390

25) A. Galtayries, J. Grimblot, *Surf. Interface Anal.***1995**, 23, 171-179.

26) R. S. C. Smart,W. M.Skinner, A. R. Gerson, *Surf. Interface Anal.***1999**, 28, 101–105.

27) H. Qiu, T. Xu, Z. Wang, W. Ren, H. Nan, Z. Ni, Q.Chen, S. Yuan, F. Miao, F.Song, G. Long, Y. Shi, L.Sun, J. Wang,X. Wang, *Nat. Comm.*, **2013**, 4, 2642, 1-6.

28) Y. Ling, G.Wang, D. A.Wheeler, J. Z.Zhang, Y. Li, *Nano Lett.***2011**,11, 2119.

29) J. S. Anand, R. K. M. Rajan, A. A. M. Zaidan, *Reports in Electrochemistry*. **2013**, 3, 25–29.

30) Y. H. Hu, *Angew. Chem. Int. Ed.***2012**, 51, 12410 – 12412.

31) H. Cui, W. Zhao, C. Yang, H.Yin, T. Lin, Y. Shan, Y. Xie, H. Gua, F. Huang, *J. Mater. Chem. A*, **2014**, 2, 8612–8616.

Chapter 8

Summary and Future work

In this chapter, we present a summary of the research work reported in this thesis with concluding remarks, followed by a brief statement regarding the future scope for research in this field.

8.1. Summary.

Growing energy demand for the developments and the environmental risks from the present non-renewable energy sources has inspired scientists worldwide to perform intense research on alternative clean and renewable energy sources. Amongst the possible renewable energy resources "solar energy" has a great potential for fulfillment of present energy demands in eco-friendly and sustainable manner. With the emergence of nanotechnology, new functional nanomaterials with novel properties are being continuously developed. This has given rise to a new breed of device systems for energy harvesting, storage and conservation.

Dye sensitized solar cell architecture is an interesting example of nanomaterials based solar cell design to harvest solar energy in fairly efficient manner at low cost and even on flexible substrates. Solar energy can also be utilized for splitting of water by the photoelectrochemical (PEC) method using nanomaterials platforms for the generation of hydrogen fuel. The foremost purpose of employing nanomaterials along with use of renewable source of energy is to make optoelectronic devices efficient, yet cost effective. In this direction, we have focused and studied nanostructures of earth abundant metal oxides and chalcogenides for DSSC and PEC applications.

1. We have demonstrated efficient room temperature electrochemical synthesis of (high temperature phase) rutile TiO_2 with hierarchical nano needle-flower morphology with diameter and length of nanoneedles of ~8 nm and 100 nm (aspect ratio >10), respectively. The DSSC device based on the corresponding nanostructure of rutile TiO_2 photoanode showed appreciable IPCE of 30% and a power conversion efficiency of 3.6%.

2. We have also studied in detail the formation of rutile TiO_2 nanoneedles by anodization process and its size induced reverse phase transformation to anatase nanoparticles. These resultant nanoparticles showed about 6% power conversion efficiency as photoanode material for DSSC.

3. We have focused on synthesis of ternary metal chalcogenide $CuInS_2$ nanosheets by SILAR method and their composite with the CuS nanoparticles as counter electrode material for DSSC to replace highly expensive and less abundant noble metal platinum. The composite showed remarkable power conversion efficiency of 6% due to synergistic effect of the two materials.

4. In the DSSC device generally used sensitizers are organometallic dyes which are highly expensive and unstable. We have attempted to replace these successfully with low cost and highly disperse metal chalcogenide colloidal quantum dots of $CuInS_2$. To improve the stability of CIS QDs and interfaces involved in QDSSC, CdS passivation layer is introduced *in situ* around CIS. Furthermore, CdS by SILAR method is also coated externally to photoanode to improve the hole extraction ability of CIS and mismatch between the band levels. With such kind of assembly and synergetic effect of CIS and CdS in QDSSC, efficiency of about 3% is achieved.

5. We have engineered sulfur deficient metal chalcogenide, $NiS_{1.97}$ as an efficient photoelectrochemical (PEC) catalyst for hydrogen generation by solar driven water splitting. The ordered S-vacancy mediated single phase material renders electronic states that were able to position/pin the flat band potential favorably with respect to redox potentials of water. This leads to a remarkable PEC performance of 1.25 mA/cm^2 vs NHE at 0.68V in neutral pH. This performance of $NiS_{1.97}$ as a PEC catalyst is far superior in orders of magnitude than NiS_2 phase which is established only as a co-catalyst up till now.

8.2. Future scope of the work.

1. In the case of clean and renewable energy technologies the cost effectiveness is the central issue which needs to be addressed upfront because without this large scale implementation of any novel concepts of energy harvesting, storage and conservation is not feasible. Thus use of low cost, earth abundant materials along with low cost materials and device processing technologies must be given primary emphasis.

2. Recent breakthrough in the field of sensitized solar cell domain came almost after two decades of research in the form of solid state "pervoskite solar cells" which have captured the attention of the world as the next generation solar cell with very impressive efficiency of 20%. This development has given way to novel materials science and new device physics. We see the following areas of research opportunities in this field for the near future:

a) Metal oxide-pervoskite interface is similar to conventional p-n junction solar cell which is free of liquid electrolyte. In such kind of junction doped metal oxides have a positive effect over undoped one in terms of band matching and enhanced charge transfer. Therefore, study of various dopants in metal oxide nanoparticle systems can be crucial for scientific progress.

b) Recently, mesoporous one dimensional nanostructures of metal oxides (as seen in the Chapter 3 of the present thesis) are proven to be beneficial for better loading of perovskite nanocrystals. Therefore, use of engineered metal oxide nanostructures in perovskite cells is of current interest.

3. Transition metal chalcogenides with 2-D layered structure have applicability in a wide range of applications. The lower dimensionality not only brings in new property portfolio due to the nature of electronic density of states, but the materials issues related to morphology in such systems are also amenable to interesting manipulation with specific consequences for property features. We see the following research opportunities for these materials in the years ahead:

a) The expensive hole transporting material (HTM) spiro-MEOTAD used in pervoskite solar cell needs immediate replacement with cheap and earth abundant materials to establish cost-effective devices. In this direction p-type materials like NiO, CuI, PbS $CuInS_2$ can be efficient candidate.

b) 2-D layered structure of transition metal chalcogenide can enable them to serve as efficient hosts for interaction of molecules. This property can make them viable for Li ion battery. For instance layered sulfides materials like MoS_2, TiS_2 and VS_2 can be employed.

3. Solar driven water splitting generates a clean and sustainable energy source, namely hydrogen. Photo-electrochemical (PEC) water splitting is certainly advantageous over electrochemical water splitting due to the requirement of lower applied bias in the former. However, unassisted water splitting using various tandem assemblies of nanomaterials based photoelectrodes and/or photovoltaic (PV) cells have been an area interest lately. One such example is the dual absorber system which utilizes an n-type semiconductor as anode and a p-type as cathode whose band gaps and alignments are such that the electrochemical potential developed by this assembly in electrolyte is self-sufficient to split water. Therefore, n-type metal oxides TiO_2, Fe_2O_3, $BiVO_4$

and p-type NiO,Cu_2O,$CuInS_2$ or metal chalcogenide sensitized metal oxide can be efficient candidate as electrode materials.

In summary, it can be concluded that there are many interesting research directions that have opened up lately due to the rapid progress in the fields of nanotechnology and advanced functional materials which promise great results in the clean energy sector. With the success of research along these lines we can perhaps hope to have a clean, green and sustainable living for the mankind.

List of Publications

1. Rajeshkumar Hyam, **Reshma Bhosale,**Wanjoo Lee, S. H. Han, Bèatrice Hannoyer and Satishchandra Ogale*****. *Room Temperature Synthesis of Rutile TiO_2 Hierarchal Nanoneedle Flower Morphology for DSSC,* ***J. Nanosci. andNanotechnol****.,* **2010,** 10,5894–5898.(**Authors have equal contribution**).
2. **Reshma Bhosale,***Rajesh Hyam, P Dhanya and Satishchandra Ogale*****, *Chlorate ion mediated rutile to anatase reverse phase transformation in TiO_2 nanosystem,* ***Dalton Trans.***, **2011**, 40, 11374–11377.
3. **ReshmaBhosale,***Shruti Agarkar, Ishita Agrawal, Rounak Naphade, Satishchandra Ogale*****, *Nanophase $CuInS_2$nanosheets/CuS composite grown by the SILAR method leads to high performance as a counter electrode in DSSC,****RSC Adv.****,****2014,** 4, 21989–21996.
4. **ReshmaBhosale,***Sarika Kelkar, Golu Parte, Rohan Fernandes, Dushyant Kothari and Satishchandra Ogale*****. *$NiS_{1.97}$: A New Efficient Water Oxidation Catalyst for Photoelectrochemical Hydrogen Generation****, ACS Appl. Mater. Interfaces,*** **2015,** *7* (36), 20053–20060.
5. John Mallows, Miquel Planells, Vishal Thakare, **Reshma Bhosale**, Satishchandra Ogale * & Neil Robertson *, *p-type NiO Hybrid Photodetector****, ACS Appl. Mater. Interfaces (under revision),2015.***

Patent Granted

- **Reshma Bhosale**, Rajeshkumar Hyam, Dr. Satishchandra Ogale. *One step electrochemical process for the synthesis of pure rutile titanium dioxide nanoneedles.*

PATENT GRANTED, 1) EP2376386 B1, CSIR No: 2008-NF-0227

2) IN 269059

Poster Award

- **Reshma Bhosale**, Rajeshkumar Hyam, Dr. Satishchandra Ogale. *Room temperature electrochemical synthesis of Rutile TiO_2 nano-needles: Properties, phase transformation and DSSC application.*

IUMRS-ICEM best poster presentation award 2010, Korea.